Geoscience BC

Energy & Water

SUMMARY OF ACTIVITIES

2020

GEOSCIENCE BC
SUMMARY OF ACTIVITIES 2020:
ENERGY AND WATER

Geoscience BC Report 2021-02

Front cover photo and credit: Drilling and installation of a groundwater monitoring well in northern winter conditions near Hudson's Hope, northeastern British Columbia (M. Goetz, 2019).

Foreword

Geoscience BC is pleased to once again present results from our ongoing projects and scholarship recipients in our annual *Summary of Activities* publication. Papers are published in two separate volumes: *Minerals*, and this volume, *Energy and Water*. Both volumes are available in print and online via www.geosciencebc.com.

Summary of Activities 2020: Energy and Water

This volume, *Summary of Activities 2020: Energy and Water*, contains 16 papers from Geoscience BC–funded projects or scholarship recipients that are within Geoscience BC's strategic focus areas of energy (including oil and gas, and geothermal) and water. The papers are divided into four sections, based on Geoscience BC's strategic objectives of

1) Facilitating Responsible Natural Resource Development,

2) Advancing Science and Innovative Geoscience Technologies,

3) Enabling Clean Energy, and

4) Understanding Water.

In the 'Facilitating Responsible Natural Resource Development' section, there are seven papers, the first three dealing with furthering our understanding of induced seismicity in the Kiskatinaw Seismic Monitoring and Mitigation Area (KSMMA*)*. The paper by Monahan et al. paper provides an update on new shear-wave velocity (V_s) data acquired to categorize and map surface sediments with respect to their effect on ground-motion amplification. Salvage et al. expound on the unique opportunity of using a dense seismographic network to monitor background seismicity during a quiescent period attributed to the COVID-19 pandemic. Continuing work by Wang et al. on earthquake-triggering mechanisms attributable to hydraulic fracturing suggest that a moment magnitude (M_w) 4.6 event occurred on a pre-existing fault with a significant amount of preloaded tectonic strain.

The next four papers focus primarily on novel techniques, such as multivariate analysis and machine learning or source parameter inversions, that may aid in understanding seismic susceptibility and mitigation techniques. Amini and Eberhardt, in their first phase of work, apply different machine-learning algorithms to determine the relative importance of several geological and operational parameters in relation to the triggering of induced seismicity. Mehrabifard and Eberhardt investigate the dependence of induced-seismicity magnitudes on differential stress and pore pressure of using supervised machine learning. Roth et al. discuss preliminary results from source parameter inversions of induced seismic events from the KSMMA area. The last paper in this section is from one of our scholarship recipients, Wozniakowska, and Eaton. Their paper analyzes the seismogenic-activation potential of the Montney Formation.

The 'Advancing Science and Innovative Geoscience Technologies' section includes four papers. The first, by Hayes et al., looks at wastewater disposal in the maturing Montney play of northeastern BC, while Chalmers et al. and Silva and Bustin discuss hydrogen sulphur sources in the Montney and Doig formations, respectively. In the last of the four papers, Chevrot et al. model fluid migration and distribution in the Montney Formation.

In the 'Enabling Clean Energy' section, Grasby et al. give an update on this summer's continuing research into the geothermal-resource potential of the Garibaldi volcanic belt in southwestern BC.

Lastly, in the 'Understanding Water' section, four papers deal with water research in the Peace Region. The first paper, by Allen et al., is an activity report on the installation of a purpose-built groundwater-monitoring network that is characterizing groundwater methane in the region. The Van De Ven et al. paper reports on a multidisciplinary experiment at the Hudson's Hope Field Research Station—the controlled release of natural gas into a confined aquifer. The paper by Lapp et al. gives an overview of a unique Pilot Collaborative Water Monitoring Program aimed at gathering Western-based science along with Traditional Knowledge at multiple river sites. The section concludes with Goetz and Beckie discussing groundwater recharge in a confined paleovalley setting.

Geoscience BC Energy and Water Publications 2020

In addition to the two *Summary of Activities* volumes, Geoscience BC releases interim and final products from our projects as Geoscience BC reports and maps. The following three Energy and Water reports were published in 2020:

- Sixteen technical papers in the **Geoscience BC Summary of Activities 2020: Energy and Water** volume (Geoscience BC Report 2021-02)

- **The Garibaldi Volcanic Belt Geothermal Energy Project: Mount Meager 2019 Field Report,** by S.E. Grasby, S.M. Ansari, R. Bryant, A. Calahorrano-DiPatre, Z. Chen, J.A. Craven, J. Dettmer, H. Gilbert, C. Hanneson, M. Harris, F. Hormozzade, J. Liu, D. Montezadian, M. Muhammad, J.K. Russell, R.O. Salvage, G. Savard, V. Tschirhart, M.J. Unsworth, N. Vigouroux-Caillibot, G. Williams-Jones and A.R. Williamson (Geoscience BC Report 2020-09)

- **Statistical Assessment of Operational Risks for Induced Seismicity from Hydraulic Fracturing in the Montney, Northeast BC,** by A. Fox, S. McKean and N. Watson (Geoscience BC Report 2020-12)

All releases of Geoscience BC reports, maps and data are published on our website and are announced through our website and e-mail updates. Most final reports and data can also be viewed or accessed through our Earth Science Viewer at https://gis.geosciencebc.com/esv/?viewer=esv.

Acknowledgments

Geoscience BC would like to thank all authors and reviewers of the *Summary of Activities* for their contributions to this volume. COVID-19 has made this a challenging year for both field programs and laboratory research, and Geoscience BC is grateful for the perseverance of our researchers and scholarship recipients in continuing their projects during the past nine months.

RnD Technical is also acknowledged for its work in editing and assembling both volumes. As well, Geoscience BC would like to acknowledge the Province of British Columbia and our project funding partners for their ongoing support of public geoscience, and express our appreciation for the leaders and volunteers in British Columbia's mineral exploration, mining and energy sectors who support our organization through their guidance, use and recognition of the data and information that we collect and distribute.

Carlos Salas
Executive Vice President & Chief Scientific Officer
Geoscience BC
www.geosciencebc.com

Contents

Shear-Wave Velocity Studies of Near-Surface Deposits in the Fort St. John–Dawson Creek Area, Northeastern British Columbia (NTS 093P, 094A)

P.A. Monahan, Monahan Petroleum Consulting, Victoria, British Columbia, pmonahan@shaw.ca

B.J. Hayes, Petrel Robertson Consulting Ltd., Calgary, Alberta

M. Perra, Petrel Robertson Consulting Ltd., Calgary, Alberta

Y. Mykula, Petrel Robertson Consulting Ltd., Calgary, Alberta

J. Clarke, Petrel Robertson Consulting Ltd., Calgary, Alberta

C. Gugins, Frontier Geosciences Inc., North Vancouver, British Columbia

C. Candy, Frontier Geosciences Inc., North Vancouver, British Columbia

D. Griffiths, Frontier Geosciences Inc., North Vancouver, British Columbia

O. Bayarsaikhan, Frontier Geosciences Inc., North Vancouver, British Columbia

O. Jones, Frontier Geosciences Inc., North Vancouver, British Columbia

U. Oki, Metro Testing + Engineering Ltd., Fort St. John, British Columbia

Introduction

Seismicity in northeastern British Columbia (BC) has recently increased significantly due to hydraulic fracturing and water disposal by the petroleum industry (Atkinson et al., 2016; Kao et al., 2018; Roth, 2020). Most of these events are small, but rare events up to magnitude (M) 4.6 have occurred (Babaie Mahani et al., 2017a, b, 2019). Ground motions for the largest events are at the lower bound of possible damage, in the range of modified Mercalli intensity (MMI) VI (Worden et al., 2012; Babaie Mahani and Kao, 2018; Babaie Mahani et al., 2019).

As part of an investigation of the potential for amplification of seismic ground motions, shear-wave (V_S) data for near-surface geological deposits have been acquired at 28 sites in the Fort St. John–Dawson Creek area of northeastern BC. This area is in the southern part of the Montney gas play area, which is currently the most active gas play in BC and is being extensively developed by hydraulic fracturing in horizontal wells. A M4.6 induced event occurred in this area in November 2018 (Babaie Mahani et al., 2019). The objective of this paper is to summarize the results of the V_S data acquisition and to present a V_S model of the shallow

geological deposits. Other aspects of this project are described by Monahan et al. (2020).

Ground-Motion Amplification

Ground-motion amplification due to shallow geological conditions can be estimated by the time-averaged V_S in the upper 30 m (V_{S30}, harmonic mean), with amplification susceptibility increasing as V_{S30} decreases (Table 1; Kramer, 1996; Building Seismic Safety Council, 2003; Finn and Wightman, 2003; National Research Council, 2015).

Amplification can also be due to resonance in the soil column, where the dominant period of the ground motions is the same as the dominant site period. Amplification due to resonance was also suspected in the region by Monahan et al. (2019).

Regional Geology

The project area is located in the western part of the Alberta Plateau (Holland, 1976), and extends from Fort St. John to Dawson Creek and from the Alberta border west to the Pine and Moberly rivers (Figure 1). The plateau is incised by valleys, up to 280 m deep, of the Peace River and its major tributaries, the Kiskatinaw, Pine, Moberly, Pouce Coupé and Beatton rivers. Adjacent to these valleys, low relief benches form the plateau surface, and these extend up smaller valleys into the hilly uplands that lie farther from the rivers. In the uplands in the western part of the project

Table 1. National Earthquake Hazards Reduction Program (NEHRP) Site classes, also adopted by the National Building Code of Canada (Building Seismic Safety Council, 2003; National Research Council, 2015). Susceptibility ratings from Hollingshead and Watts (1994).

Site Class	General description	Definition by V_{S30}	Susceptibility rating
A	Hard rock	$V_{S30} > 1500$	Nil
B	Rock	$760 < V_{S30} < 1500$	Very low
C	Very dense soils and soft rock	$360 < V_{S30} < 760$	Low
D	Stiff soils	$180 < V_{S30} < 360$	Moderate
E	Soft soils	$V_{S30} < 180$	High

area, hilltops are up to 900 metres above sea level (m asl) in elevation and the local relief is up to 200 m. The topography of the uplands becomes more subdued toward the east, where hilltops are up to 700 m asl in elevation and local relief is 50 m.

Bedrock at surface consists of gently easterly dipping, relatively soft Cretaceous sedimentary rocks (Irish, 1958; Stott, 1982; McMechan, 1994; Plint, 2000). The principal geological units exposed from northwest to southeast across the project area are, in ascending order, the Shaftesbury Formation, which consists of marine shale; the Dunvegan Formation, which consists of marine and nonmarine sandstone, conglomerate and shale; the Kaskapau Formation, which consists of marine shale, with sandstone members in its lower part; and the Cardium Formation, which consists of marine and nonmarine sandstone, conglomerate and shale. The upper 5 to 30 m of bedrock is commonly weathered to clay, particularly the shale intervals, and the upper surface is commonly glaciotectonized (Monahan et al., 2019, 2020).

At least three glaciations occurred during the Quaternary in this area (Mathews, 1978; Hartman and Clague, 2008; Hickin et al., 2015, 2016a, b). Deposits of the last two glacial and adjoining nonglacial periods show a repetitive pattern of fluvial incision and deposition during nonglacial intervals, followed by deposition of glaciolacustrine silt as drainageways were blocked by advancing Laurentide ice, and finally, by till during the glacial maximum. Fluvial incision cut deeper following each glaciation, so that modern valleys of the Peace River and its major tributaries are incised through the older Quaternary deposits into bedrock.

Deposits of the latest glaciation, during the Late Wisconsinan, are the best known (Mathews, 1978, 1980; Hartman and Clague, 2008; Hickin et al., 2015, 2016a, b). Both Cordilleran and Laurentide ice extended into the area, but the maximum extents of each appear to have been out of sync. West of the project area, Cordilleran till has been reported interbedded with advance-phase glaciolacustrine deposits (glacial Lake Mathews; Hartman et al., 2018). However, the advance-phase glaciolacustrine deposits are overlain by

clay-rich till deposited by Laurentide ice. The ice sheets appear to have coalesced, but in the latter stages, Laurentide till appears to have been overridden locally by Cordilleran ice (Hickin et al., 2016b). As Laurentide ice retreated, drainage was again blocked, resulting in widespread deposition of glaciolacustrine silt, clay and very fine sand of glacial Lake Peace. Following drainage of this lake, fluvial incision resumed and continued into the Holocene.

Sediments older than the last glacial maximum are restricted to Quaternary river valleys (paleovalleys) that underlie benches adjacent to the major rivers and some smaller valleys. They are exposed only in the valley walls of the Peace River and its tributaries. Elsewhere, only Late Wisconsinan till, retreat-phase deposits and Holocene sediments occur at the surface. These units occur in specific geomorphic settings (Mathews, 1978; Reimchen, 1980; Hartman and Clague, 2008; Hickin et al., 2015; Monahan et al., 2019). The uplands are underlain mainly by till with a veneer of glaciolacustrine silt and clay. Topography in the uplands is largely controlled by bedrock, which is locally exposed and generally within a few metres of the surface in the western parts of the project area. However, in the uplands of more subdued relief in the eastern part of the project area, till commonly forms a blanket up to 30 m thick. The low relief benches, between the uplands and deeply incised major valleys, are underlain by retreat-phase glaciolacustrine and related deposits, which are 10 to 15 m thick adjacent to the major rivers and between 5 and 50 m thick in smaller valleys. Where these deposits overlie older Pleistocene deposits in paleovalleys, the total Quaternary thickness locally exceeds 200 m. Terraces on the walls of major valleys are underlain by late stage Wisconsinan glaciofluvial sand and gravel representing the earliest phases of postglacial fluvial incision and are up to 30 m thick. Modern fluvial sand and gravel occupies river valley bottoms.

Within the upland areas, the valleys of smaller streams have gently sloping floors and are underlain by glaciolacustrine sediments, into which the modern streams have now incised. The degree of incision increases markedly as these streams approach the major valleys. Boundaries between
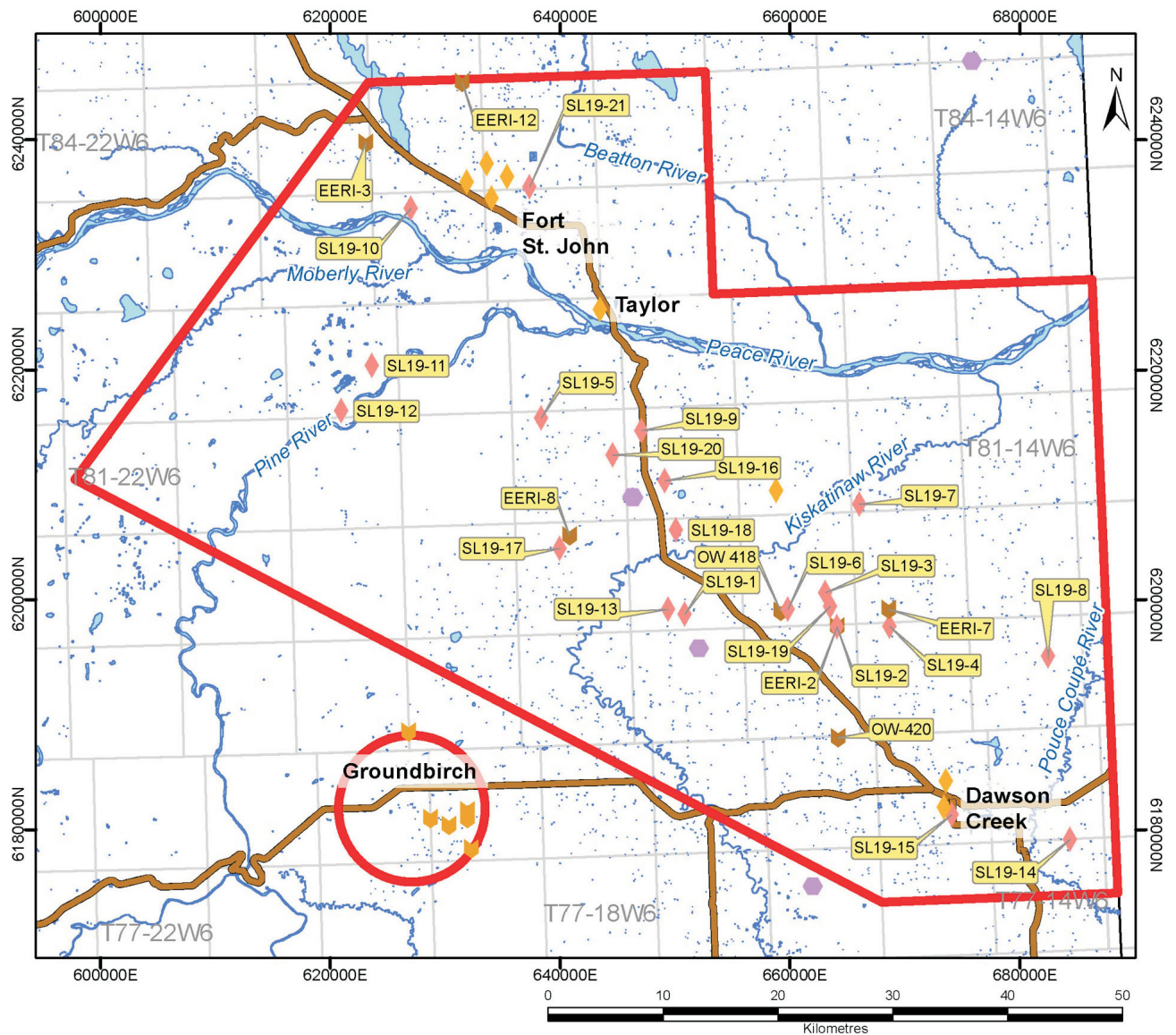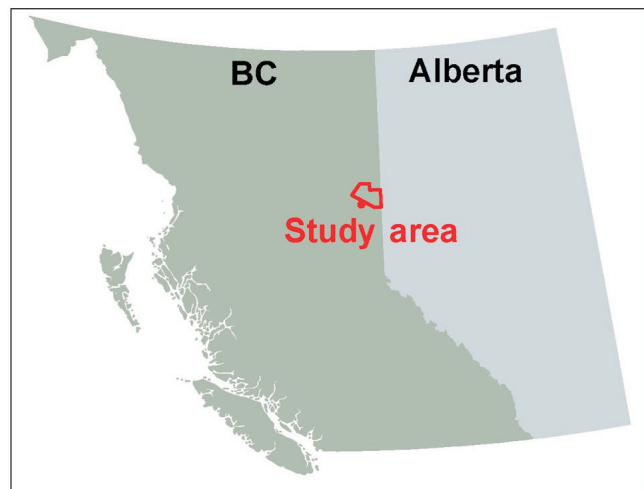
Figure 1. Spatial distribution of sites where shear-wave velocity (V_S) data were acquired in the Fort St. John–Dawson Creek area, northeastern British Columbia. Site details are found in Tables 2 and 3. The previous study noted is that by Monahan et al. (2019). Abbreviations: MASW, multichannel analysis of surface waves; VSP, vertical seismic profiling. UTM Zone 10N, NAD 83.

the upland areas and adjacent glaciolacustrine benches and valley bottoms are commonly marked by distinct breaks in slope. However, these breaks in slope are not as clear in the areas of subdued topography in the east.

Acquisition of V_S Data

Shear-wave velocity (V_S) data have been acquired at 28 sites, by downhole logging in existing boreholes using the vertical seismic profiling (VSP) method, and by multichannel analysis of surface waves (MASW), a non-invasive surface technique that generates a V_S profile along a 100 m transect. These two methods are described by Arsenault et al. (2012) and Phillips and Sol (2012), respectively. The data were acquired by Frontier Geosciences Inc.

The VSP logs were acquired in seven boreholes, and the results are summarized in Table 2. Five of the boreholes were drilled by the Energy and Environment Research Initiative (EERI) as part of a regional groundwater monitoring project by the University of British Columbia (Cahill et al., 2019; Ladd et al., 2019, 2020), and the other two are Province of BC groundwater observation wells (OW; Kelly and Janicki, 2013). In addition to V_S, P-wave velocity (V_P) data were obtained at all sites, and gamma-ray logs were run in EERI-2, and -3, and OW 418 and 420 to correlate with gamma-ray logs in nearby petroleum wells. The EERI boreholes have polyvinyl chloride (PVC) casing, whereas the OW have steel casing to the approximate top of bedrock, and PVC casing below. Descriptive logs of the OW are also available in the BC Ministry of Environment and Climate Change Strategy's groundwater wells and aquifers database (GWELLS; BC Ministry of Environment and Climate Change Strategy, 2020). Figure 2 shows the logs of OW 418, which was the deepest borehole logged. Note that the gamma-ray signal is somewhat attenuated in the steel-cased interval. In addition to those illustrated here, the logs for EERI-2 and -3 are shown in Monahan et al. (2020, Figures 3, 4).
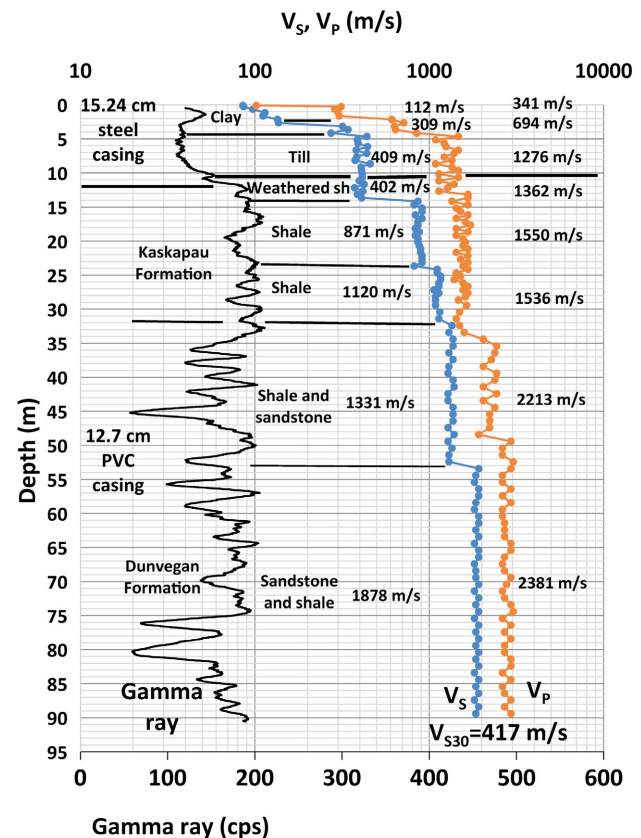
Figure 2. Borehole logs for Observation Well 418 (groundwater wells and aquifers database [GWELLS] well tag number 104709; BC Ministry of Environment and Climate Change Strategy, 2020), located on gently sloping upland hillside. Gamma-ray, shear-wave velocity (V_S) and P-wave velocity (V_P) data. Average V_S and V_P posted for each interval. Lithological log and descriptions modified from those of Kelly and Janicki (2103) and GWELLS to match gamma-ray and velocity logs. Note downward increase in V_S below the weathered interval. Note also, attenuation of gamma-ray signal in steel-cased interval. Top of bedrock picked in this interval based on driller's log and the lower and less serrate gamma-ray signature of Quaternary till compared to Cretaceous shale. Upper part of Dunvegan Formation from 32 to 75 m correlates with the basal A-X member of the Kaskapau alloformation of Plint (2000). Gamma-ray scale at bottom. The average shear-wave velocity in upper 30 m (V_{S30}) is 417 m/s at the site (Site Class C). Abbreviations: cps, counts per second; PVC, polyvinyl chloride; sh, shale.

Table 2. Summary of vertical seismic profiling (VSP) data in pre-existing boreholes. All co-ordinates are in UTM Zone 10N, NAD 83. Locations of boreholes shown on Figure 1. Abbreviations: GWELLS, BC Ministry of Environment and Climate Change Strategy's groundwater wells and aquifers database; OW, observation well; V_{S30}, average shear-wave velocity in upper 30 m; WTN, well tag number.

Borehole	Easting	Northing	Elevation (m asl)	Depth penetrated (m)	Depth to bedrock (m)	V_{S30} (m/s)	Site Class	Setting	Reference
EERI-2	664116	6197620	747	45	26.7	271	D	Gentle upland hillside	Cahill et al., 2019; Monahan et al., 2020
EERI-3	623071	6239713	737	55	26	276	D	Valley bottom	Cahill et al., 2019; Monahan et al., 2020
OW 418	659177	6198989	699	91	10	417	C	Gentle upland hillside	Kelly and Janicki, 2013 (GWELLS WTN 104709)
OW 420	664197	6187988	776	44	22.5	370	C	Gentle upland hillside	Kelly and Janicki, 2013 (GWELLS WTN 104711)
EERI-7	668605	6199167	790	33	5.5	360	C-D	Gentle upland hilltop	Ladd et al., 2019, 2020
EERI-8	640811	6205544	824	32	2.5	415	C	Steep upland hilltop	Ladd et al., 2019, 2020
EERI-12	631468	6245003	691	32	19	500	C	Steep upland hillside	Ladd et al., 2019, 2020

Table 3. Summary of multichannel analysis of surface wave (MASW) data. All co-ordinates are in UTM Zone 10N, NAD 83. Depth to bedrock is interpreted from gamma-ray log in adjacent petroleum well or borehole, except for those where the depth to bedrock was interpreted from the MASW profile (indicated with an asterisk).

Test site	Seismic station/ wellsite/location	Elevation (m asl)	Easting	Northing	Depth penetrated (m)	Depth to bedrock (m)	V_{S30} (m/s)	Site Class	Setting	Reference
SL19-1	MONT1, South of Parkland Rd	719	650841	6198716	38		253 ±4	D	Minor valley bottom - glaciolacustrine	Monahan et al., 2020
SL19-2	EERI 2	747	664110	6197627	34	26.7	228 ±7	D	Gently sloping upland hillside	Cahill et al., 2019; Monahan et al., 2020
SL19-3	Proprietary seismic station, 11-11-80-16W6[1]	722	663081	6200612	36		345 ±14	D	Steep upland hillside	
SL19-4	MG05, 16-32-79-15W6	794	668701	6197690	30		233 ±13	D	Gentle upland hilltop	Monahan et al., 2020
SL19-5	MONT8	685	638350	6215777	36	>36*	246 ±16	D	Gently sloping upland hillside	
SL19-6	MG03, 14-4-80-16W6	699	659839	6199174	30	50.5	268 ±15	D	Edge of minor valley bottom - glaciolacustrine	
SL19-7	MG04, 6-6-81-15W6	681	666039	6208315	32	77.7	221 ±5	D	Glaciolacustrine bench above Kiskatinaw River	
SL19-8	MG02, 13-23-079-14W6	641	682467	6195094	32	67.2	238 ±15	D	Glaciolacustrine bench	
SL19-9	MG01, 16-30-81-17W6	721	647093	6214696	30	102.8	192 ±17	D-E	Valley bottom, glaciolacustrine organic soils at surface	Hansen, 1950; Farstad et al., 1965; Lord and Greene, 1986
SL19-10	GSBC BH 2017-1	652	627001	6234050	32	>53.6	303 ±8	D	Glaciolacustrine bench above Peace River	Levson and Best, 2017
SL19-11	Wilder Gas Plant, 10-14-82-20W6, near MONT6	622	623627	6220351	30		309 ±32	D	Glaciolacustrine bench above Pine River	
SL19-12	Terrace above Pine River	514	620944	6216406	30		292 ±5	D	Glaciofluvial terrace above Pine River	
SL19-13	West end Parkland Rd	762	649412	6199166	30		384 ±34	C-D	Upland hilltop	
SL19-14	MG10, Patterson Rd, Briar Ridge	793	684376	6179103	30	18*	287 ±18	D	Gentle slope near upland hilltop	
SL19-15	Northern Lights College, Dawson Creek Campus	661	674114	6181275	30	13*	386 ±20	C	Minor valley bottom - glaciolacustrine	
SL19-16	226 Rd	837	649114	6210336	30		371 ±23	C-D	Gentle upland slope near hilltop	
SL19-17	Station 15, 11-28-80-18	797	639975	6204452	30	5*	499 ±31	C	Steep slope	Babaie Mahani and Kao, 2018
SL19-18	Lebell Road	699	650083	6206051	30		273 ±6	D	Glaciolacustrine bench	
SL19-19	West Doe Gas Plant, 2-11-80-16W6	703	663492	6199398	30	15*	338 ±13	D	Edge of minor valley bottom - glaciolacustrine	
SL19-20	Station 9, 11-24-81-18W6	772	644574	6212594	30	48.2	259 ±18	D	Gentle upland slope	Babaie Mahani and Kao, 2018
SL19-21	Airport Road, Fort St. John	683	637354	6235899	30		349 ±9	D	Gentle upland terrane	

[1] L.S. 11, Sec. 11, Twp. 80, Rge. 16, W 6th Mer.

The MASW profiles were acquired at 21 sites, and the results are summarized in Table 3. Of these, 11 were acquired at seismograph stations, in order to assess site effects: six are in the McGill University Dawson–Septimus Induced Seismicity Study network (MG01 to MG05 and M10; McGill University, 2020), two are in the Geological Survey of Canada–BC Oil and Gas Commission Induced Seismicity Study network (MONT1, MONT8; Natural Resources Canada, 2020), two are industry stations included in the study by Babaie Mahani and Kao (2018; stations 9 and 15), and one is a proprietary industry station. Six MASW profiles were acquired at residences (two co-located with seismograph stations), to calibrate the residents' experiences with induced earthquakes (MASW SL19-1, -12, -13, -14, -16, -18). Six MASW profiles were located adjacent to sites where geotechnical or scientific borehole data had been obtained, in order to refine the V_S model of the shallow geological materials (MASW SL19-2, -10, -11, -15, -17, -21). One MASW, SL19-2, was done adjacent to EERI-2 in order to compare the two techniques.

The total depths investigated on the MASW profiles are between 30 and 38 m. The V_S data are determined at multiple geophones on each profile (typically 39), so that V_{S30} was calculated at each geophone, and the V_{S30} mean and standard deviation could be calculated for the entire profile (Table 3). Note that the mean V_{S30} shown in Table 3 is the time-averaged velocity in the top 30 m of the soil column at all geophones. The depths to bedrock reported are either interpreted from adjacent petroleum industry gamma-ray logs or other borehole data, or interpreted from the MASW data. An example of a MASW profile and adjacent borehole data are shown in Figure 3a, b.

V_S Model of Shallow Geological Deposits

The V_S data acquired for this project have been used to prepare a V_S model of the shallow geological deposits in the project area, and builds on a V_S model developed previously for the entire Montney play area (Monahan et al., 2019). The new model incorporates V_S data acquired for the previous study, including six VSP logs in the Groundbirch area, twelve MASW profiles (Figure 1), and three dipole sonic logs in Geoscience BC boreholes drilled in 2017. Four of the MASW profiles and all the dipole sonic logs are from outside of the current project area and not shown on Figure 1. All data from the previous study were reinterpreted for the new model. The data have been supplemented by V_S data acquired by others, comprising nine seismic cone penetration tests (SCPT) at four sites, and four MASW tests at one site. Most of the latter data are proprietary. Of the five sites, only one is outside of the area shown in Figure 1.

To develop the model, the V_S data points were correlated with specific stratigraphic units. In computing the average

V_S (V_{SAV}) for each unit, data were time-averaged to be consistent with the calculation of V_{S30}. For the borehole V_S data, published core descriptions and wireline log data are sufficient to confidently assign V_S data points to specific stratigraphic units (Figures 2, 4, 5). Core descriptions for these boreholes are by Hickin et al. (2016a; Groundbirch), Levson and Best (2017; Geoscience BC 2017 boreholes), and Goetz (Cahill et al., 2019; Ladd et al., 2019; EERI boreholes).

However, for the MASW profiles, only data from those adjacent to geotechnical or scientific boreholes were used—that is, all of the MASW profiles from Monahan et al. (2019) and six of the MASW profiles acquired for this study. In these, only intervals from the closest geophone to the borehole that could be equated with specific stratigraphic intervals in the boreholes were used in the V_S model (e.g., Figure 3). Data from deeper than the bottom of the adjacent borehole were excluded, except in cases where bedrock had been confirmed in the borehole.

The V_S model is summarized in Table 4. The ranges shown on the table are the lowest and highest interval values rather than from individual data points. Ranges of standard penetration test (SPT) blowcount (N) values for each stratigraphic unit were derived from geotechnical borehole data collected as part of the project (Monahan et al., 2020). The SPT blowcount is the number of hammer blows required to drive a sample tube 305 mm (1 ft.), and is a measure of the strength and consolidation of the deposits. The test is usually terminated after 50 blows, which is referred to as 'refusal'. The new V_S model is generally similar to that previously described by Monahan et al. (2019), but differs from the earlier model in two important aspects—the greater range of V_S for tills and weathered bedrock (shale and sandstone; Monahan et al., 2020).

Holocene and Retreat-Phase Deposits of the Last Glaciation

Holocene alluvium was tested at one MASW site on the Sikanni Chief River, north of the project area (Monahan et al., 2019; SL2-2), where the V_{SAV} is 196 ±14 m/s in 11 m of interbedded gravel, sand and silt. Based on a comparison with Holocene fluvial deposits elsewhere, this is likely to be representative of these deposits in the Fort St. John–Dawson Creek area.

Retreat-phase deposits of the last glaciation show a pattern of increasing V_S with grain size. The V_{SAV} increases from 214 ±55 m/s in glaciolacustrine silt, clay and very fine sand (25 sites), to 299 ±45 m/s in glaciolacustrine and glaciodeltaic sand with minor gravel (six sites), and to 364 ±91 m/s in glaciofluvial gravel and sand (one site). The last mentioned site is located on a glaciofluvial terrace and the gravel and sand is overlain by 7 m of thick silt. The V_{SAV}
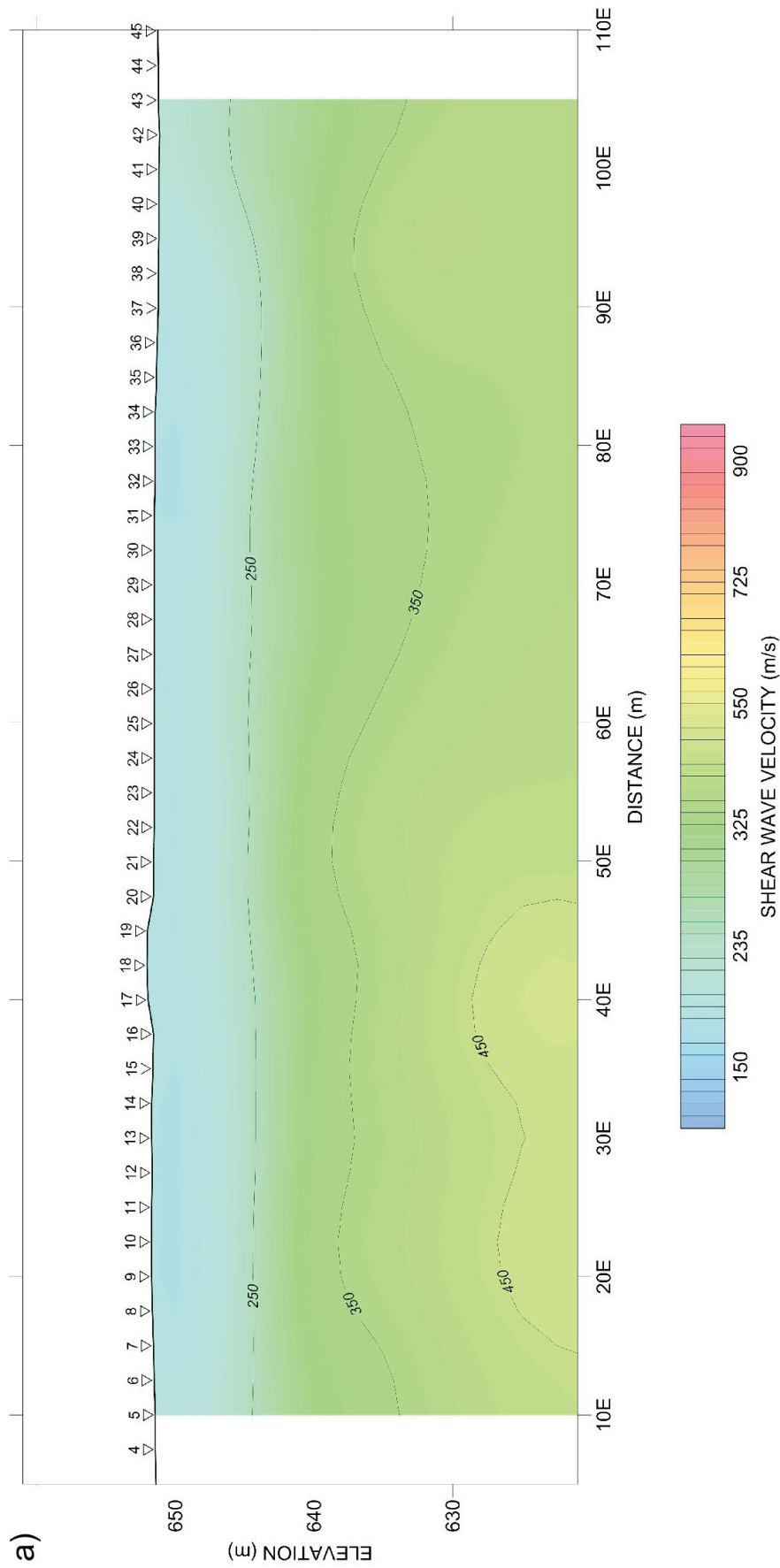
Figure 3. Multichannel analysis of surface waves (MASW) at SL19-10 at Geoscience BC borehole 2017-12 (Levson and Best, 2017), located on a glaciolacustrine bench above the Peace River. **a)** MASW profile. Numbers along the top of the profile are geophone locations. Abbreviation: E, east.
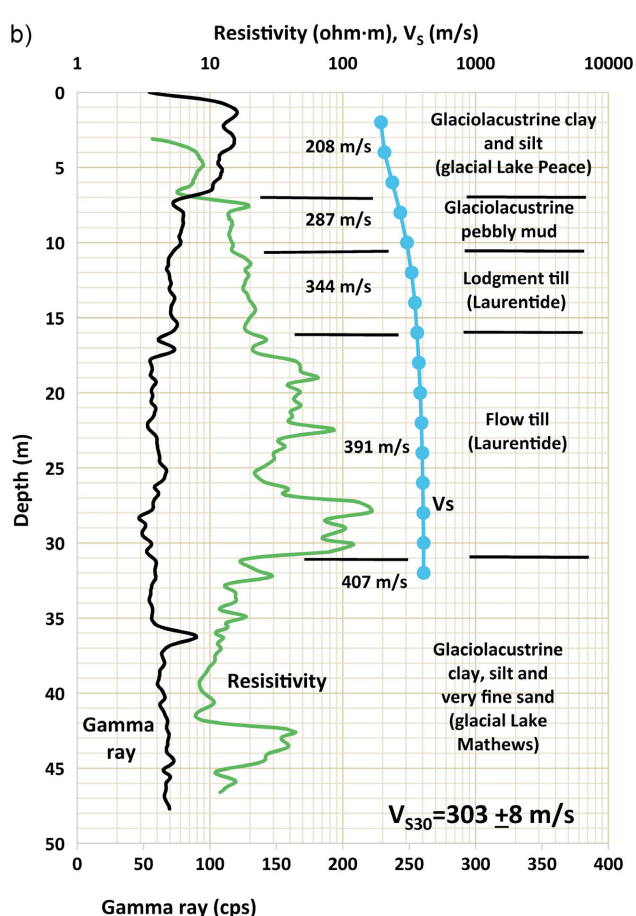
Figure 3 (continued). Multichannel analysis of surface waves (MASW) at SL19-10 at Geoscience BC borehole 2017-12 (Levson and Best, 2017), located on a glaciolacustrine bench above the Peace River. **b)** Borehole gamma-ray and resistivity logs and shear-wave velocity (V_S) trace at geophone 24 (627001E, 6234050N, UTM Zone 10N, NAD 83), the closest to the borehole. Average V_S is posted for each interval. Gamma-ray and resistivity logs by Weatherford International plc, core description from Levson and Best (2017). The average shear-wave velocity in upper 30 m (V_{S30}) is 303 ±8 m/s at the site (Site Class D).

Figure 4. Borehole log for EERI-12. Shear-wave velocity (V_S) and P-wave velocity (V_P) data. Average V_S and V_P are posted for each interval. Core description by Goetz (in Ladd et al., 2019). Note that the V_S increases downward through the diamict (i.e., till) as clast size increases. The V_S increase at 12.5 m is interpreted to represent the downward change from meltout to lodgment till. An alternate interpretation is that each V_S interval represents a till of a different age. The average shear-wave velocity in upper 30 m (V_{S30}) is 500 m/s at the site (Site Class C).

of these deposits together is 326 ±94 m/s. Pebbly silt intervals interbedded with glaciolacustrine sediments are 3 to 7 m thick and have a V_{SAV} of 301 ±29 m/s (three sites; e.g., Figure 3b).

Retreat-phase glaciolacustrine silt, clay and very fine sand are widespread and described in many geotechnical boreholes. The SPT N values are generally between 2 and 20 for these deposits.

Tills

Till occurs in 42 intervals at 30 sites and has a V_{SAV} of 343 ±176 m/s. However, the till intervals can be subdivided into those interpreted to be Late Wisconsinan, which occur at surface or directly below the Late Wisconsinan retreat-phase deposits, and those that occur deeper in the section and are interpreted to be older.

Accordingly, till intervals at 28 sites are interpreted as Late Wisconsinan and have a V_{SAV} of 321 ±134 m/s, with a wide range from 135 to 790 m/s. In most borehole logs, the differentiation between meltout, flow and lodgment till was not made by the person logging the core. However, these interpretations were made by Hickin et al. (2016a) and Levson and Best (2017) in their core descriptions (e.g., Figure 3); and in two of the EERI borehole logs the distinction between meltout and lodgment till can be inferred from an abrupt downward increase in V_S in an otherwise continuous till sequence (Figure 4). Following these interpretations, Late Wisconsinan meltout till occurs at two sites with V_{SAV} of 224 ±52 m/s, flow till occurs at two sites with V_{SAV} of 377 ±42 m/s, and lodgment till at eight sites with V_{SAV} of 422 ±151 m/s. Undifferentiated tills at 20 sites have a V_{SAV} of 295 ±110 m/s. Significantly, the range of V_{SAV} in till in the thick till blanket encountered in many upland sites in the eastern part of the project area overlaps with that of gla-
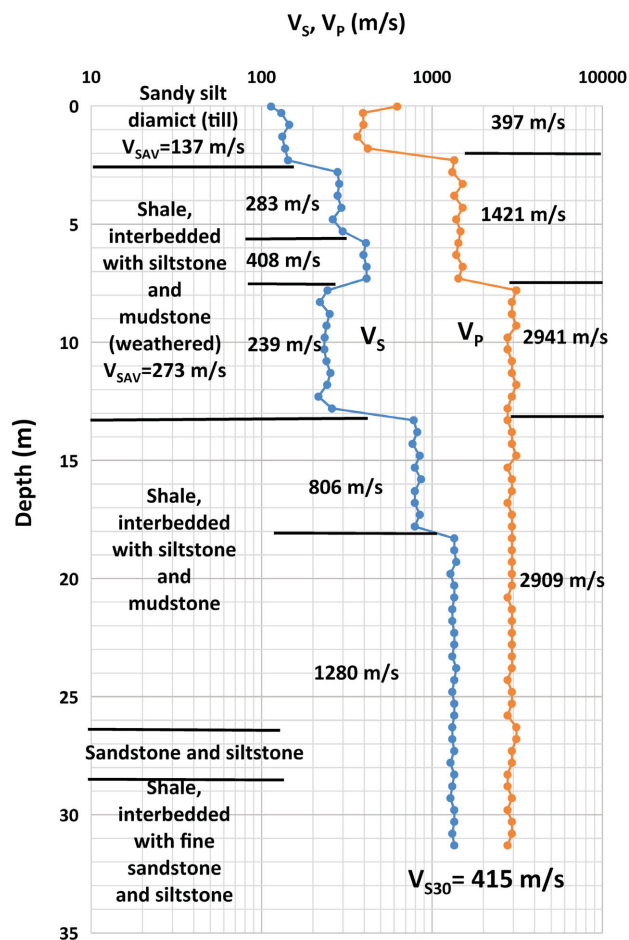
Figure 5. Borehole log for EERI-8, located on steep upland hilltop. Shear-wave velocity (V_S) and P-wave velocity (V_P) data. Average V_S and V_P are posted for each interval. Core description by Goetz (Ladd et al., 2019). Note weathered bedrock interval is 10.5 m thick with an average shear-wave velocity (V_{SAV}) of 273 m/s. The average shear-wave velocity in upper 30 m (V_{S30}) is 415 m/s at the site (Site Class C).

Figure 6. Proprietary data from a geotechnical investigation at a gently sloping upland site, provided courtesy of an oil and gas operator. Data shown are shear-wave velocity (V_S) and tip resistance (qt) from a seismic cone penetration test (SCPT). Standard penetration test (SPT) blowcount (N) and lithological data are from an adjacent borehole. Average V_S in the SCPT is 219 m/s. Based on a correlation of N with V_S, the average V_S of the section down the bottom of the borehole is estimated to be 224 m/s, and estimated average shear-wave velocity in upper 30 m (V_{S30}) is 312 m/s, assuming bedrock V_S of 900 m/s from the base of the hole down to 30 m (Site Class D). This estimate is an upper bound one, as the one bedrock N value (30) indicates that the bedrock surface is weathered, and the estimated V_{S30} will be less if a thick weathered interval is present.

ciolacustrine silt (e.g., Figure 6). In geotechnical boreholes, the range of SPT N values in Late Wisconsinan tills is typically between 10 and >50 (i.e., refusal).

Tills interpreted to be older than the last glacial maximum occur at four sites, and have a V_{SAV} of 660 ±132 m/s. Lodgment till occurs at three sites with a V_{SAV} of 709 ±100 m/s, and flow till occurs at two sites with a V_{SAV} of 572 ±111 m/s (Hickin et al., 2016a; Levson and Best, 2017; Monahan et al., 2019).

The range of V_{SAV} in tills is likely related to varying degrees of glacial compaction and clast and clay content, with the latter increasing and decreasing V_S, respectively. Although till provenance controls lithology, and Laurentide tills are clay rich (Mathews, 1978), there are insufficient data to assess the control of provenance on till V_S.

Advance-Phase Deposits of the Last Glaciation and Earlier Deposits

Deposits older than the Late Wisconsinan glacial maximum are represented at 10 sites. These have higher V_{SAV} than retreat-phase and Holocene deposits due to glacial compaction, and display less grain-size control of V_S. Glaciolacustrine clay, silt and very fine sand occur at six sites, with a V_{SAV} of 426 ±26 m/s; glaciolacustrine and glaciodeltaic silty sand and sand occur at five sites, with a V_{SAV} of 527 ±188 m/s; and glaciofluvial and fluvial sand and gravel occur at seven sites with a V_{SAV} of 519 ±117 m/s.

Table 4. Shear-wave velocity (V_S) model of near-surface geological deposits in the Fort St. John–Dawson Creek area. Numbers in brackets in environment and lithology columns are the number of sites represented. Bracketed standard penetration test (SPT) blow-count (N) values are inferred, not observed. Ranges in V_S are highest and lowest interval averages, rather than individual data points.

Period	Unit	Environments	Lithology	SPT N	V_S average (range, m/s)
Holocene	Alluvium		Silt, sand and gravel (1)	14–25 (>50?)	196 ±14 (180–250?)
Pleistocene	Late Wisconsinan glaciation retreat phase	Glaciofluvial terrace	Gravel and sand (1) (with overlying silt V_{SAV} 326 ±94)		364 ±91 (260–400)
		Glaciolacustrine	Silt, clay and very fine sand (25)	2 to 20	214 ±55 (135–330)
			Pebbly silt (3)		301 ±29 (285–340)
		Glaciolacustrine, glaciodeltaic	Sand and gravel (6)	(20 to 50)	299 ±45 (250–370)
		Tills (28 sites) V_{SAV} 321 ±134 (135–790)	Flow till (2)		377 ±42 333–465
			Meltout till (2)		224 ±52 (135–260)
	Late Wisconsinan glaciation maximum		Undifferentiated till (20)	10 to >50	295 ±110 (135–600)
			Lodgment till (8)		422 ±151 (260–790)
	Late Wisconsinan advance phase and earlier glacial and nonglacial deposits	Glaciolacustrine	Clay, silt and very fine sand (6)	15 to >50	426 ±26 (360–460)
		Glaciolacustrine, glaciodeltaic	Silty sand and sand (5)	(>50)	527 ±188 (400–860)
		Glaciofluvial and fluvial	Gravel and sand (7)	(>50)	519 ±117 (420–840)
		Tills	Till, flow and lodgment (4)	(>50)	660 ±132 (490–830)
Cretaceous	Cardium, Kaskapau, Dunvegan and Shaftesbury fm.	Weathered shale and sandstone (16)		30 to >50	522 ±232 (240–1200)
		Shale (7)		>50	962 ±198 (725–1280)
		Interbedded sandstone and shale (9)		>50	1179 ±411 (725–1878)

Bedrock

Bedrock V_S was recorded at 18 sites. Weathered intervals at the top of bedrock occur at 16 sites and were either directly reported on borehole logs (e.g., Figure 5) or interpreted on MASW profiles by steep downward V_S increases before levelling off at a high V_S, with the latter being interpreted as unweathered bedrock (e.g., Figure 7). Weathered intervals are up to 36 m thick, with an average of 15 m and a V_{SAV} of 522 ±232 m/s.

Relatively unweathered bedrock is represented at 11 sites. Shale intervals have generally lower V_{SAV} than intervals of interbedded sandstone and shale. The V_{SAV} for these intervals are 962 ±198 m/s and 1179 ±411 m/s, respectively. However, V_S continues to increase downward from the weathered zone, as shown in OW 418, where V_{SAV} in-creases downward from 871 m/s at 14 to 24 m depth in Kas-kapau Formation shale to 1878 m/s between 53 and 90 m in the Dunvegan Formation sandstone and shale (Figure 2). This downward increase is likely due to the gradually decreasing effects of weathering below the upper highly weathered interval, the closure of fractures due to greater overburden stress and the effect of increased overburden stress itself.

V_{S30} by Geomorphological Setting

Figure 8 shows the distribution of V_{S30} by geomorphological setting at sites in the Fort St. John–Dawson Creek area. Those sites on modern alluvium, glaciofluvial terraces and glaciolacustrine benches and minor valley floors are generally in Site Class D, as would be expected as these deposits are generally relatively thick and/or overlie
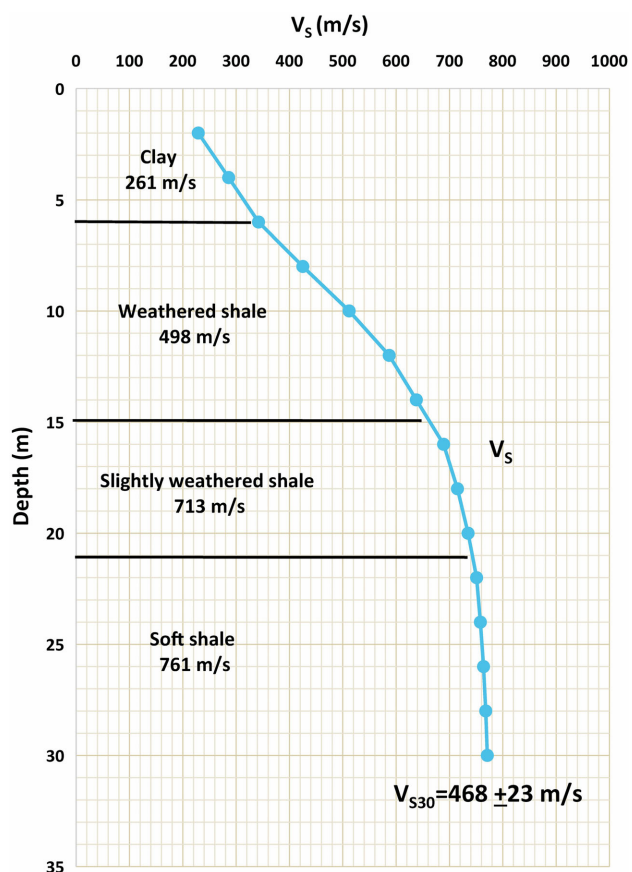
Figure 7. Shear-wave velocity (V_S) trace from multichannel analysis of surface waves (MASW) at test site SL-4, from previous study (Monahan et al., 2019), and lithological data from adjacent proprietary borehole. Site located at hilltop site of gentle topography in Dawson Creek. The V_S trace is at geophone 28, the closest to the borehole (673711E, 6184226N, UTM Zone 10N, NAD 83). Average V_S is posted for each interval. Borehole log reports weathered shale down to 15 m, but the V_S trace suggests that the effects of weathering extend down to ~21 m. Relatively unweathered bedrock is interpreted below 21 m where the V_S values level off at high values. The average shear-wave velocity in upper 30 m (V_{S30}) is 468 ±23 at the site (Site Class C).

older Quaternary deposits. At the two glaciolacustrine sites in Site Class C, which are located in minor valleys, bedrock is interpreted to be shallow (<20 m) on the MASW profiles. Site Class in the upland sites ranges from B to D and overlaps with the glaciolacustrine sites where thick tills with V_S comparable to glaciolacustrine deposits occur. This is particularly so in the uplands of subdued topography in the eastern part of the project area. However, V_{S30} increases as depth to bedrock decreases, so in the steeper upland areas of the western part of the project area, where thin tills overlie bedrock, sites are likely to be in Site Class C.

The relationship between V_{S30} and depth to bedrock is shown in Figure 9. Generally, sites where depth to bedrock exceeds 15 m are in Site Class D. Upland sites which deviate from this trend are associated with very high till velocities (e.g., EERI-12, Figure 4), or thick weathered bedrock intervals (e.g., EERI-7, -8; Figure 5).

The steeper upland areas, where bedrock is shallow and Site Class C predominates, are primarily underlain by sandstone units of the Dunvegan Formation and sandstone members of the Kaskapau Formation. These units are more resistant to erosion than shale of Kaskapau Formation, which underlies most of the upland areas of subdued topography in the eastern part of the project area, where thicker till overlies bedrock and Site Class D is widespread.

However, significant amplification of seismic ground motions may also occur due to resonance where the depth to bedrock is less than 15 m. Amplification of induced seismicity at the Groningen gas field in the Netherlands is greatest where Holocene deposits are thin (<~20 m), less so where they are thick, and the least where the Holocene is absent (van Ginkel et al., 2019).

Conclusions

The project data confirm that, in the Fort St. John–Dawson Creek area, the shear-wave velocity of the clay-rich Late Wisconsinan till is commonly comparable to that of the Late Wisconsinan retreat-phase glaciolacustrine clay, silt and fine sand. Consequently, where thick till occurs in the upland areas of subdued topography, such as in the eastern part of the area, the average shear-wave velocity in the upper 30 m (V_{S30}) is similar to that of glaciolacustrine sites, and is assigned to Site Class D. In upland areas of steeper topography, where thinner tills overlie bedrock, Site Class C predominates. As a result, depth to bedrock is a better predictor of V_{S30} than whether till or glaciolacustrine deposits occur at surface, and a depth of 15 m approximates the boundary between Site classes C and D. This depth may vary depending on the presence of denser till or a thick weathered bedrock interval with low velocity, which would increase or decrease, respectively, the bedrock depth of the Site Class C–D boundary.

However, amplification of seismic ground motions may also occur due to resonance where the depth to bedrock is less than 15 m. To assess this, future work in this project will include analysis of recorded ground motions at sites where the depth to bedrock is known.

Acknowledgments
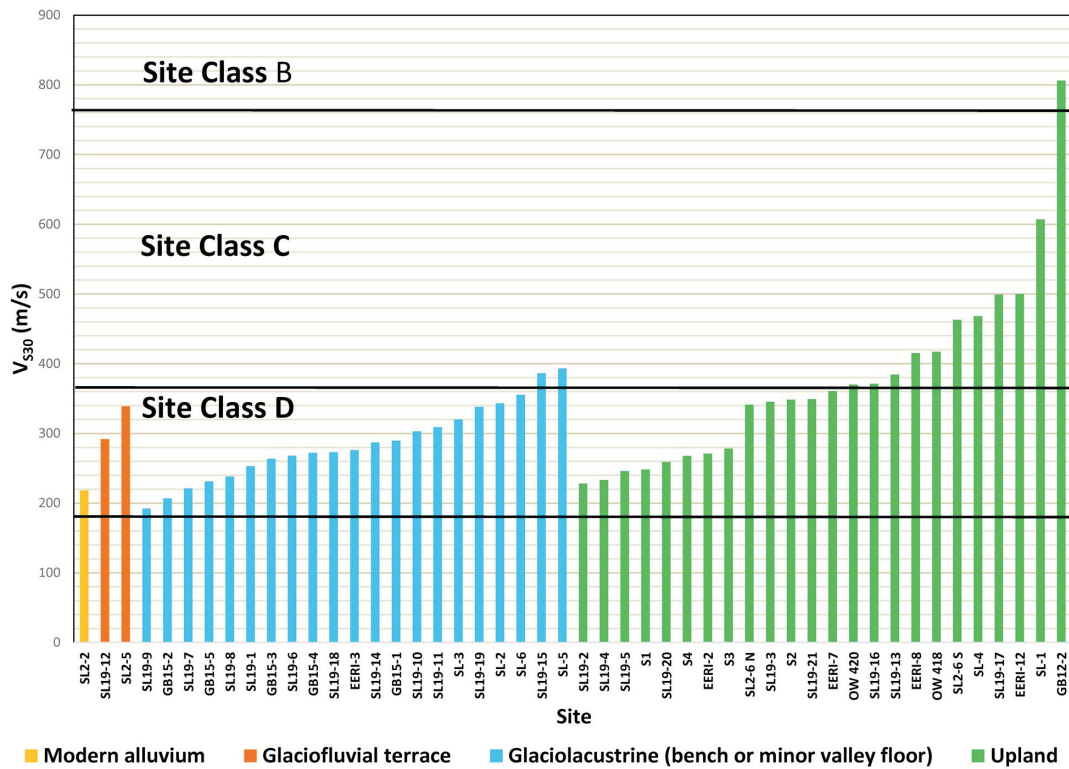
Figure 8. The average shear-wave velocity in the upper 30 m (V_{S30}) by geological setting for sites in the Fort St. John–Dawson Creek area. Only site SL2-2 is located outside of the project area; it represents a modern alluvium site. Site details are shown in Tables 2 and 3; sites SL-1 to SL-6, SL2-2, SL2-5, SL2-6 N, SL2-6 S, GB12-2 and GB15-1 to GB-15-5 are from a previous study by Monahan et al. (2019); data from tests S1 to S4 are proprietary. Note range of V_{S30} in upland setting extends into Site Class D, overlapping with V_{S30} of the other settings represented.
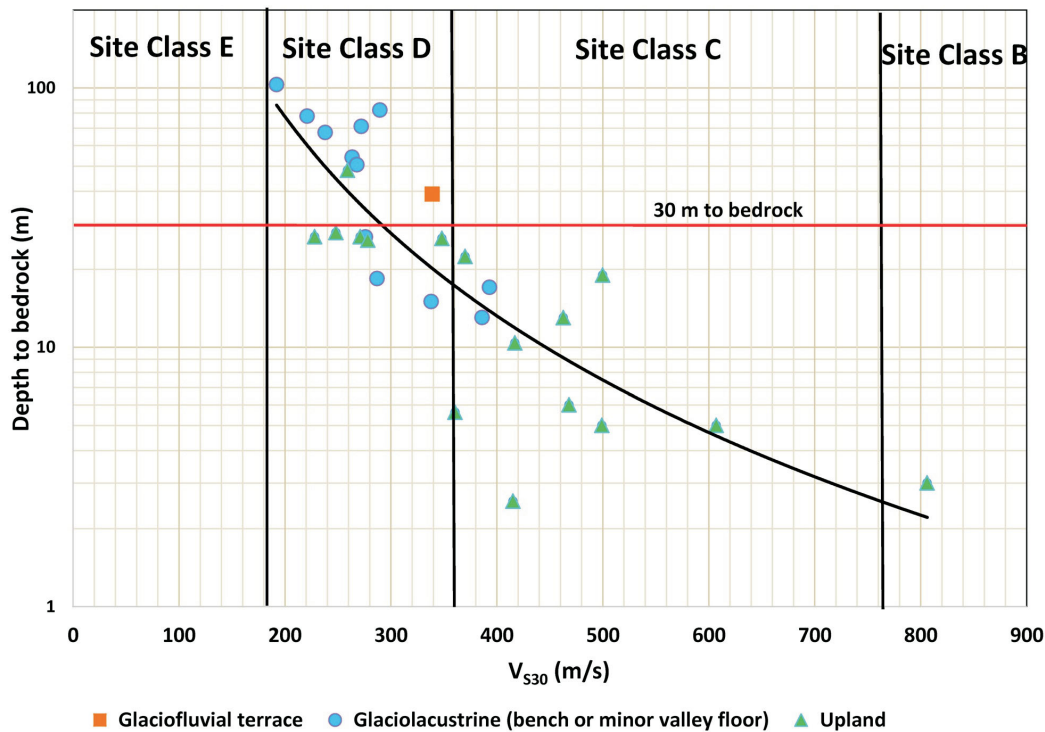
Figure 9. Plot of average shear-wave velocity in the upper 30 m (V_{S30}) versus depth to bedrock for sites in the Fort St. John–Dawson Creek area. Only sites where bedrock is confirmed in the boreholes are shown. Power trendline is for all points, R^2=0.69. Note that for sites where bedrock is deeper than 30 m, shear-wave velocity values below 30 m do not contribute to V_{S30} calculation.

References

Arsenault, J.-L., Hunter, J.A. and Crow, H.L. (2012): Shear wave velocity logs from vertical seismic profiles; *in* Shear Wave Velocity Measurement Guidelines for Canadian Seismic Site Characterization in Soil and Rock, J.A. Hunter and H.L. Crow (ed.), Geological Survey of Canada, Open File 7078, p. 123–138, URL <https://doi.org/10.4095/291753>.

Atkinson, G.M., Eaton, D.W., Ghofrani, H., Walker, D., Cheadle, B., Schultz, R., Shcherbakov, R., Tiampo, K., Gu, J., Harrington, R.M., Liu, Y., van der Baan, M. and Kao, H. (2016): Hydraulic fracturing and seismicity in the Western Canada Sedimentary Basin; Seismological Research Letters, v. 87, no. 3, p. 1–17, URL <https://www.desmogblog.com/sites/beta.desmogblog.com/files/Hydraulic%20Fracturing%20and%20Seismicity%20in%20the%20Western%20Canada%20Sedimentary%20Basin.pdf> [November 2020].

Babaie Mahani, A. and Kao, H. (2018): Ground motion from M 1.5 to 3.8 induced earthquakes at hypocentral distance <45 km in the Montney play of northeast British Columbia, Canada; Seismological Research Letters, v. 89, no. 1, p. 22–34, URL <https://doi.org/10.1785/0220170119>.

Babaie Mahani, A., Kao, H., Atkinson, G.M., Assatourians, K., Addo, K. and Liu, Y. (2019): Ground-motion characteristics of the 30 November 2018 injection-induced earthquake sequence in northeast British Columbia, Canada; Seismological Research Letters, v. 90, no. 4, p. 1457–1467, URL <https://doi.org/10.1785/0220190040>.

Babaie Mahani, A., Kao, H., Johnson, J. and Salas, C. (2017a): Ground motion from the August 17, 2015, moment magnitude 4.6 earthquake induced by hydraulic fracturing in northeastern British Columbia; *in* Geoscience BC Summary of Activities 2016, Geoscience BC, Report 2017-01, p. 9–14, URL <http://www.geosciencebc.com/i/pdf/SummaryofActivities2016/SoA2016_BabaieMahani.pdf> [October 2017].

Babaie Mahani, A., Schultz, R., Kao, H., Walker, D., Johnson, J. and Salas, C. (2017b): Fluid injection and seismic activity in the northern Montney play, British Columbia, Canada, with special reference to the 17 August 2015 Mw 4.6 induced earthquake; Bulletin of the Seismological Society of America, v. 107, p. 542–552, URL <https://doi.org/10.1785/0120160175>.

BC Ministry of Environment and Climate Change Strategy (2020): Groundwater wells and aquifers (GWELLS) database; BC Ministry of Environment and Climate Change Strategy, URL <https://apps.nrs.gov.bc.ca/gwells/> [September 2020].

Building Seismic Safety Council (2003): NEHRP recommended provisions for seismic regulations for new buildings and other structures (FEMA 450), part 1: provisions (2003 edition); prepared for the Federal Emergency Management Agency, 338 p., URL <http://www.nehrp.gov/pdf/fema450-provisions.pdf> [October 2017].

Cahill, A.G, Beckie, R.D., Goetz, M., Allen, A., Ladd, B., Welch, L., Kirste, D., Mayer, B. and van Geloven, C. (2019): Characterizing dissolved methane in groundwater in the Peace Region, northeastern British Columbia, using a regional, dedicated, groundwater monitoring well network; *in* Geoscience BC Summary of Activities 2018: Energy and Water, Geoscience BC, Report 2019-02, p. 105–122, URL <http://cdn.geosciencebc.com/pdf/SummaryofActivities2018/EW/2017-002_SoA2018_EW_Cahill_DissolvedMethane.pdf> [November 2020].

Farstad, L., Lord, T.M., Green, A.J. and Hortie, H.J. (1965): Soil survey of the Peace River area in British Columbia; University of British Columbia, British Columbia Department of Agriculture and Canada Department of Agriculture, Research Branch, British Columbia Soil Survey Report No. 8, 114 p., URL <http://www.env.gov.bc.ca/esd/distdata/ecosystems/Soils_Reports/bc8_report.pdf> [November 2020].

Finn, W.D.L. and Wightman, A. (2003): Ground motion amplification factors for the proposed 2005 edition of the National Building Code of Canada; Canadian Journal of Civil Engineering, v. 30, p. 272–278, URL <https://cdnsciencepub.com/doi/pdf/10.1139/l02-081> [November 2020].

Hansen, H.P. (1950): Postglacial forests along the Alaska Highway in British Columbia; Proceedings of the American Philosophical Society, v. 94, no. 5, p. 411–421.

Hartman, G.M.D. and Clague, J.J. (2008): Quaternary stratigraphy and glacial history of the Peace River valley, northeast Brit-

ish Columbia; Canadian Journal of Earth Sciences, v. 45, p. 549–564, URL <https://cdnsciencepub.com/doi/pdf/10.1139/E07-069> [November 2020].

Hartman, G.M.D., Clague, J.J., Barendregt, R.W. and Reyes, A.V. (2018): Late Wisconsinan Cordilleran and Laurentide glaciation of the Peace River Valley east of the Rocky Mountains, British Columbia; Canadian Journal of Earth Sciences, v. 55, no. 12, p. 1324–1338, URL <https://doi.org/10.1139/cjes-2018-0015>.

Hickin, A.S., Best, M.E. and Pugin, A. (2016a): Geometry and valley-fill stratigraphic framework for aquifers in the Groundbirch paleovalley assessed through shallow seismic and ground-based electromagnetic surveys; BC Ministry of Energy, Mines and Low Carbon Innovation, BC Geological Survey, Open File 2016-5, 46 p., URL <http://cmscontent.nrs.gov.bc.ca/geoscience/PublicationCatalogue/OpenFile/BCGS_OF2016-05.pdf> [November 2020].

Hickin, A.S., Lian, O.B. and Levson, V.M. (2016b): Coalescence of late Wisconsinan Cordilleran and Laurentide ice sheets east of the Rocky Mountain Foothills in the Dawson Creek region, northeast British Columbia, Canada; Quaternary Research, v. 85, p. 409–429, URL <https://doi.org/10.1016/j.yqres.2016.02.005>.

Hickin, A.S., Lian, O.B., Levson, V.M. and Cui, Y. (2015): Pattern and chronology of glacial Lake Peace shorelines and implications for isostasy and ice-sheet configuration in northeastern British Columbia, Canada; Boreas, v. 44, p. 288–304, URL <https://doi.org/10.1111/bor.12110>.

Holland, S.S. (1976): Landforms of British Columbia – a physiographic outline; BC Ministry of Energy, Mines and Low Carbon Innovation, Bulletin 48, 138 p., URL <https://www2.gov.bc.ca/gov/content/industry/mineral-exploration-mining/british-columbia-geological-survey/publications/bulletins> [November 2020].

Hollingshead, S. and Watts, B.D. (1994): Preliminary seismic microzonation assessment for British Columbia; prepared for Resources Inventory Committee, Earth Sciences Task Force, 109 p.

Irish, E.J.W. (1958): Charlie Lake, West of Sixth Meridian, British Columbia; Geological Survey of Canada, Preliminary Map 17-1958, scale 1:253 440, 1 sheet, URL <https://doi.org/10.4095/106866>.

Kao, H., Hyndman, R., Jiang, Y., Visser, R., Smith, B., Babaie Mahani, A., Leonard, L., Ghofrani, H. and He, J. (2018): Induced seismicity in western Canada linked to tectonic strain rate: implications for regional seismic hazard; Geophysical Research Letters, v. 45, 12 p., URL <https://doi.org/10.1029/2018GL079288>.

Kelly, J. and Janicki, E. (2013): Drilling and construction of Provincial Observation Wells in the Montney play area, Dawson Creek, British Columbia 2011; BC Ministry of Environment and Climate Change Strategy, BC Ministry of Energy, Mines and Low Carbon Innovation, 84 p., URL <http://a100.gov.bc.ca/pub/acat/public/viewReport.do?reportId=36194> [November 2020].

Kramer, S.L. (1996): Geotechnical Earthquake Engineering; Prentice-Hall, Inc., Upper Saddle River, New Jersey, 653 p.

Ladd, B., Cahill, A.G., Goetz, M., Allen, A., Welch, L., Mayer, B., van Geloven, C., Kirste, D. and Beckie, R.D. (2020): Installation of a purpose-built groundwater monitoring well network to characterize groundwater methane in the Peace Region, northeastern British Columbia (NTS 093P/09–16, 094A/01–08); in Geoscience BC Summary of Activities 2019: Energy and Water, Geoscience BC, Report 2020-02, p. 131–144, URL <http://www.geosciencebc.com/i/pdf/SummaryofActivities2019/EW/Project%202017-002_EW_SOA2019.pdf> [November 2020].

Ladd, B., Goetz, M., Allen, A., Kirste, D. and Beckie, R.D. (2019): Characterizing dissolved methane in groundwater in the Peace Region, Northeast BC, using a regional, dedicated groundwater monitoring well network, EERI Monitoring Well Installation Project (EERI MWIP), drilling campaign #3– review; The University of British Columbia, Energy and Environment Initiative, unpublished internal report, 20 p.

Levson, V. and Best, M. (2017): Northeast BC sonic drilling project, physical logs descriptions and interpretations; Geoscience BC, Geoscience BC Report 2017-16, 35 p., URL <http://cdn.geosciencebc.com/project_data/GBCR2017-16-CoreDescriptionsInterpretations.pdf> [November 2020].

Lord, T.M. and Green, A.J. (1986): Soils of the Fort St. John-Dawson Creek area, British Columbia; Canada Department of Agriculture, British Columbia Soil Survey Report No. 42, 81 p., URL <http://www.env.gov.bc.ca/esd/distdata/ecosystems/Soils_Reports/bc42_report.pdf> [November 2020].

Mathews, W.H. (1978): Quaternary stratigraphy and geomorphology of the Charlie Lake (94A) map-area, British Columbia; Geological Survey of Canada, Paper 76-20, 25 p., includes Map 1460A, scale 1:250 000, URL <https://geoscan.nrcan.gc.ca/starweb/geoscan/servlet.starweb?path=geoscan/downloade.web&search1=R=104544> [November 2020].

Mathews, W.H. (1980): Retreat of the last ice sheets in northeastern British Columbia and adjacent Alberta; Geological Survey of Canada, Bulletin 331, 22 p., URL <https://geoscan.nrcan.gc.ca/starweb/geoscan/servlet.starweb?path=geoscan/downloade.web&search1=R=102160> [November 2020].

McGill University (2020); McGill Dawson–Septimus Induced Seismicity Study; International Federation of Digital Seismograph Networks, URL <https://www.fdsn.org/networks/detail/XL_2017/> [November 2020].

McMechan, M.E. (1994): Geology and structure cross section, Dawson Creek, British Columbia; Geological Survey of Canada, Map 1858A, scale 1:250 000, URL <https://doi.org/10.4095/203491>.

Monahan, P.A., Hayes, B., Perra, M., Mykula, Y., Clarke, J., Galambos, B., Griffiths, D., Bayarsaikhan, O. and Oki, U. (2020): Amplification of seismic ground motion in the Fort St. John–Dawson Creek area, northeastern British Columbia; in Geoscience BC Summary of Activities 2019, Geoscience BC, Report 2020-02, p. 1–12, URL <http://www.geosciencebc.com/i/pdf/SummaryofActivities2019/EW/Project%202018-052_EW_SOA2019.pdf> [November 2020].

Monahan, P.A., Levson, V.M., Hayes, B.J., Dorey, K., Mykula, Y., Brenner, R., Clarke, J., Galambos, B., Candy, C., Krumbiegel, C. and Calderwood, E. (2019): Mapping the susceptibility to amplification of seismic ground motions in the Montney play area of northeastern British Columbia; Geoscience BC Report 2018-16, 65 p., URL <http://cdn.geosciencebc.com/project_data/GBCR2018-16/GBCR2018-16-NEBC_Amplification_Report.pdf> [November 2020].

National Research Council (2015): National Building Code of Canada; National Research Council, Ottawa, v. 1, 708 p.

Natural Resources Canada (2020): Geological Survey of Canada–BC Oil and Gas Commission Induced Seismicity Study; International Federation of Digital Seismograph Networks, URL <https://www.fdsn.org/networks/detail/1E_2018/> [November 2020].

Phillips, C. and Sol, S. (2012): Multichannel analysis of surface waves (MASW) technique for hazard studies; *in* Shear Wave Velocity Measurement Guidelines for Canadian Seismic Site Characterization in Soil and Rock, J.A. Hunter and H.L. Crow (ed.), Geological Survey of Canada, Open File 7078, p. 62–66, URL <https://doi.org/10.4095/291753>.

Plint, A.G. (2000): Sequence stratigraphy and paleogeography of a Cenomanian deltaic complex: the Dunvegan and lower Kaskapau formations in subsurface and out crop, Alberta and British Columbia, Canada; Bulletin of Canadian Petroleum Geology, v. 48, p. 43–79, URL <https://doi.org/10.2113/48.1.43>.

Reimchen, T.H.F. (1980): Surficial geology, Dawson Creek, West of the Sixth Meridian, British Columbia; Geological Survey of Canada, Map 1467A, scale 1:250 000, URL <https://doi.org/10.4095/120060>.

Roth, M.P., Verdecchia, A., Harrington, R.M. and Liu, Y. (2020): High-resolution imaging of hydraulic-fracturing-induced earthquake clusters in the Dawson–Septimus area, northeast British Columbia, Canada; Seismological Research Letters, v. 91, p. 2744–2756, URL <https://doi.org/10.1785/02202-00086>.

Stott, D.F. (1982): Lower Cretaceous Fort St. John Group and Upper Cretaceous Dunvegan Formation of the foothills and plains of Alberta, British Columbia, and District of Mackenzie and Yukon Territory; Geological Survey of Canada, Bulletin 328, 124 p., URL <https://doi.org/10.4095/119100>.

van Ginkel, J., Ruigrok, E. and Herber, R. (2019): Assessing soil amplifications in Groningen, the Netherlands; First Break, v. 37, p. 33–38.

Worden, C.B., Gerstenberger, M.C., Rhoades, D.A. and Wald, D.J. (2012): Probabilistic relationships between ground-motion parameters and modified Mercalli intensity in California; Bulletin of the Seismological Society of America, v. 102, p. 204–221, URL <https://doi.org/10.1785/0120110156>.

Real-Time Monitoring of Seismic Activity in the Kiskatinaw Area, Northeastern British Columbia (NTS 093P, 094A)

R.O. Salvage, University of Calgary, Calgary, Alberta, rebecca.salvage1@ucalgary.ca

J. Dettmer, University of Calgary, Calgary, Alberta

T.H.A. Swinscoe, University of Calgary, Calgary, Alberta

K. MacDougall, University of Calgary, Calgary, Alberta

D.W. Eaton, University of Calgary, Calgary, Alberta

M. Stacey, Nanometrics Seismic Monitoring Services, Ottawa, Ontario

M. Aboud, Nanometrics Seismic Monitoring Services, Ottawa, Ontario

T.-S. Kang, Pukyong National University, Busan, South Korea

S. Kim, Chungnam National University, Daejeon, South Korea

J. Rhie, Seoul National University, Seoul, South Korea

Introduction

Over the past decade, hydraulic fracturing and wastewater disposal operations have significantly increased in the Western Canada Sedimentary Basin (WCSB) due to development of a number of distinct resource plays, including the Montney. Due to the temporal and spatial correlation of increased seismicity with increased operations in this area, this trend is generally attributed to anthropogenic causes, although very few hydraulic fracturing operations (0.3%) are actually linked to seismic activity with moment magnitudes (M_W) >3 (Rivard et al., 2014; Atkinson et al., 2016). In recent years, northeastern British Columbia (BC) has experienced an increasing number of felt seismic events during active development within the Montney play. This led the British Columbia Oil and Gas Commission (BCOGC) to implement a special order in 2018 (BC Oil and Gas Commission, 2018) within the area now known as the Kiskatinaw Seismic Monitoring and Mitigation Area (KSMMA; Figure 1). This order required operators to undertake a pre-assessment of the seismic hazard, fully inform residents in the area of upcoming operations and monitor seismic activity in real-time before, during and after completions. Of particular importance was the introduction within the KSMMA of the cessation of operations following an event with a local magnitude (M_L) of ≥ 3.0 (BC Oil

and Gas Commission, 2018), which is lower than the M_L 4.0 threshold that is standard elsewhere in BC (e.g., Babaie Mahani and Kao, 2020).

Although the KSMMA is heavily monitored for seismic activity by individual companies undertaking resource development, limited real-time public data were available to better understand exactly how and why this area is so susceptible to induced seismicity, how faults are activated during hydraulic fracturing operations and why low magnitude events (M_L <2) are often felt by residents. Although a number of larger felt events have occurred within the KSMMA (e.g., November 30, 2018, near Fort St. John), the majority of seismic events have magnitudes <2, meaning that they were difficult to study with the sparse public seismic monitoring networks. Consequently, in early 2020, 13 new broadband seismometers and 2 accelerometers were installed within the KSMMA to enhance the monitoring capabilities of ongoing operations, improve risk assessments and inform mitigation strategies (Figure 1). The installation of such a dense monitoring network aims to enhance the understanding of the generation of felt seismicity due to fluid injection, in particular, the physical processes governing fault (re)activation and arrest, the role of aseismic processes and the management of risk and mitigation strategies related to such events. This is not only important for the operators undertaking hydraulic fracturing experiments in this area, but also for regulators and the general public so that they can improve best practices for safer operations.
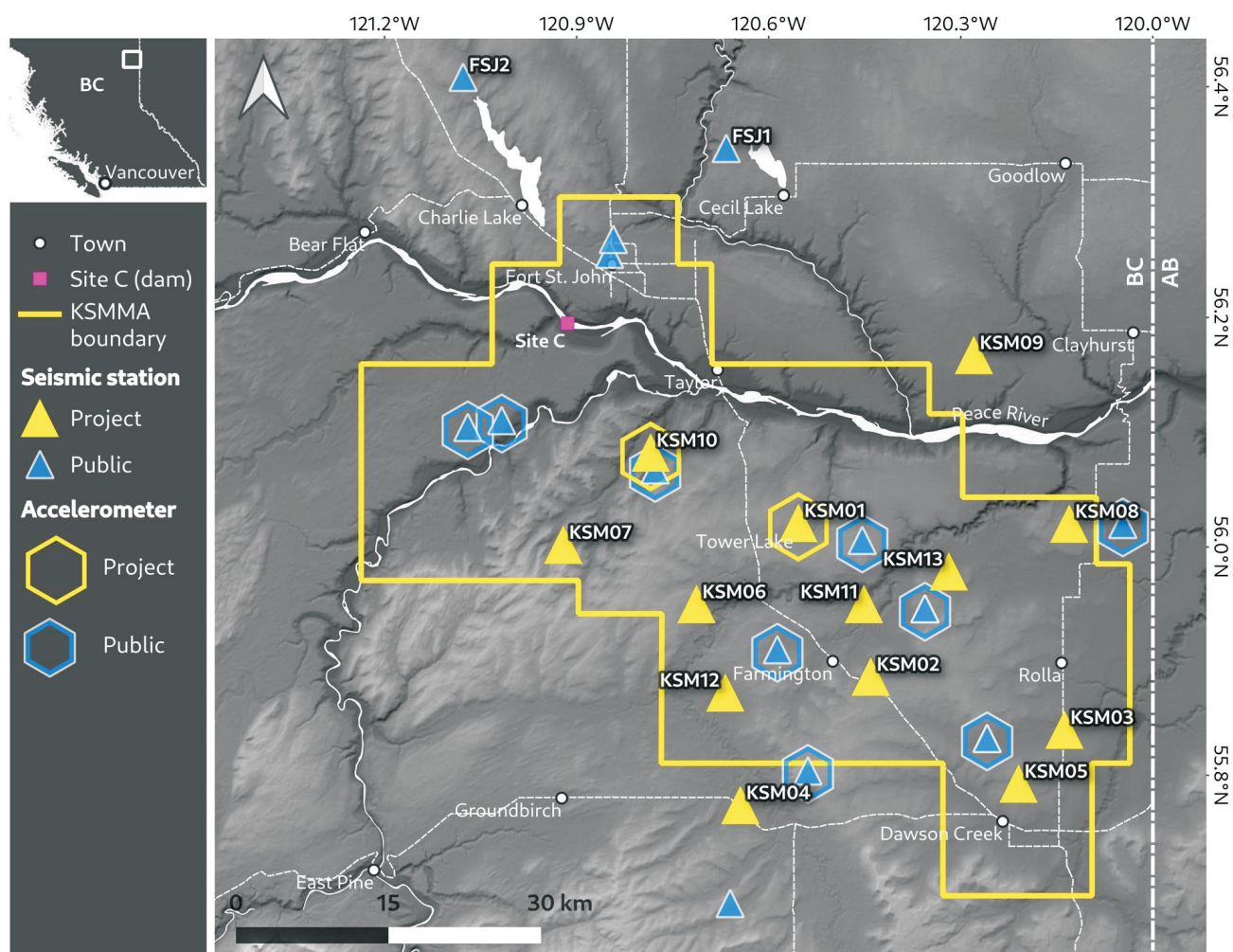
Figure 1. Installed seismic monitoring stations within the Kiskatinaw Seismic Monitoring and Mitigation Area (KSMMA; yellow border), northeastern British Columbia. Yellow stations denote those from a new Earth-System Observing Network–Réseau d'Observation du Système Terrestre (EO) dense array network installed for this project; blue stations are previously installed public stations, managed by Natural Resources Canada (Geological Survey of Canada) and the University of Calgary. Stations FSJ1 and FSJ2 are also part of the EO network but were installed in 2018. Station FSJ1 was decommissioned on August 26, 2020, but is shown for completeness as its data has been used in seismic analyses. Elevation data from Shuttle Radar Topography Mission (U.S. Geological Survey, 2014). WGS 84/ Pseudo-Mercator, World Geodetic System 1984 datum.

Network Design and Installation

With increasing operations within the KSMMA over the past decade, the number of public monitoring stations has also increased. Prior to the installation of this new dense array, nine public sensors maintained by Natural Resources Canada (NRCan; Geological Survey of Canada) existed within the KSMMA (Figure 1), along with six co-located accelerometers poised to better capture higher levels of ground motion from larger seismic events. Therefore, it was important that the installation of the new dense array complemented the locations of the existing stations. In particular, it was noted that most of the public stations were positioned within a corridor orientated to the northwest, with large gaps in spatial coverage in the northern KSMMA (close to the Site C dam), and in the central area near Tower Lake and in the southwest near Farmington.

Ten broadband seismic stations (Nanometrics Trillium T120 seismometers with Taurus digitizers) were loaned to the University of Calgary for this project by a geothermal research group in South Korea led by T.-S. Kang, S. Kim and J. Rhie. Nanometrics Seismic Monitoring Services (Nanometrics) upgraded the existing firmware on these systems and provided solar power, communication systems and interconnect cables to ensure all systems were fully operational. Furthermore, Nanometrics provided an additional three broadband sensors and two accelerometers (Nanometrics Titan) for the project, as well as undertaking the installation and maintenance of the network. Installation began in January 2020, with four broadband stations and an accelerometer being successfully installed. The remaining stations were installed in March and May 2020. This dense array network adds to two previously installed

stations by the University of Calgary in 2018 in the EON-ROSE (Earth-System Observing Network–Réseau d'Observation du Système Terrestre [EO]) seismic network in this area.

Sensors were installed at existing well sites (Figure 2) through the generous support of four independent companies. The primary aim of the network was to expand monitoring capabilities in the KSMMA, in particular in the northeastern and southwestern parts of the area where prior public monitoring was sparse. However, difficulties relating to the availability of suitable sites (i.e., sites not associated with active well pads and/or having good telecommunication strength) and actual accessibility to sites meant that it was not possible to place sensors in a truly optimum spatial array. In particular, it was not possible to place sensors close to the Site C dam, an area of sparse coverage. For this reason, a decision was made to place two sensors outside of the KSMMA (KSM04 and KSM09, Figure 1) to optimize the aperture of the array, even though these sensors are at a greater distance from ongoing operations than is ideal. Stations KSM01 and KSM10 are centrally located and both have a co-located accelerometer alongside the seismometer. The sites of the accelerometers were chosen due to their proximity to the most recent seismicity in the area, in particular a number of felt events that have occurred close to Tower Lake and Farmington (Figure 3).

Continuous seismic data from the EO network can be downloaded directly from the Incorporated Research Institutions for Seismology (IRIS) website (https://ds.iris.edu/ds/nodes/dmc/) following an initial 91 day embargo period reserved for researchers at the University of Calgary and the project partners. Data are released on a 24-hour basis for all stations within the network.

Data Processing

Nanometrics is providing continuous data acquisition, archiving and standard data processing of data from the EO network, as well as incorporating data from the existing public stations in the area. This represents a significant in-kind contribution to this project to produce an accurate and well-maintained catalogue of seismic events during the recording period. The Nanometrics workflow includes event detection, event location analysis and determination of magnitudes, both automatic and through manual inspection by a trained analyst. In March 2020, Nanometrics further supplemented this workflow by deploying AI Analyst advanced processing techniques to augment the automatic processing of data. The full catalogue, including phase pick information and waveform data, as well as the continuous seismic data are provided to researchers so that they can undertake their own analysis of the seismicity.

Firstly, seismic events are detected from the incoming continuous seismic data using a simple short-term average over
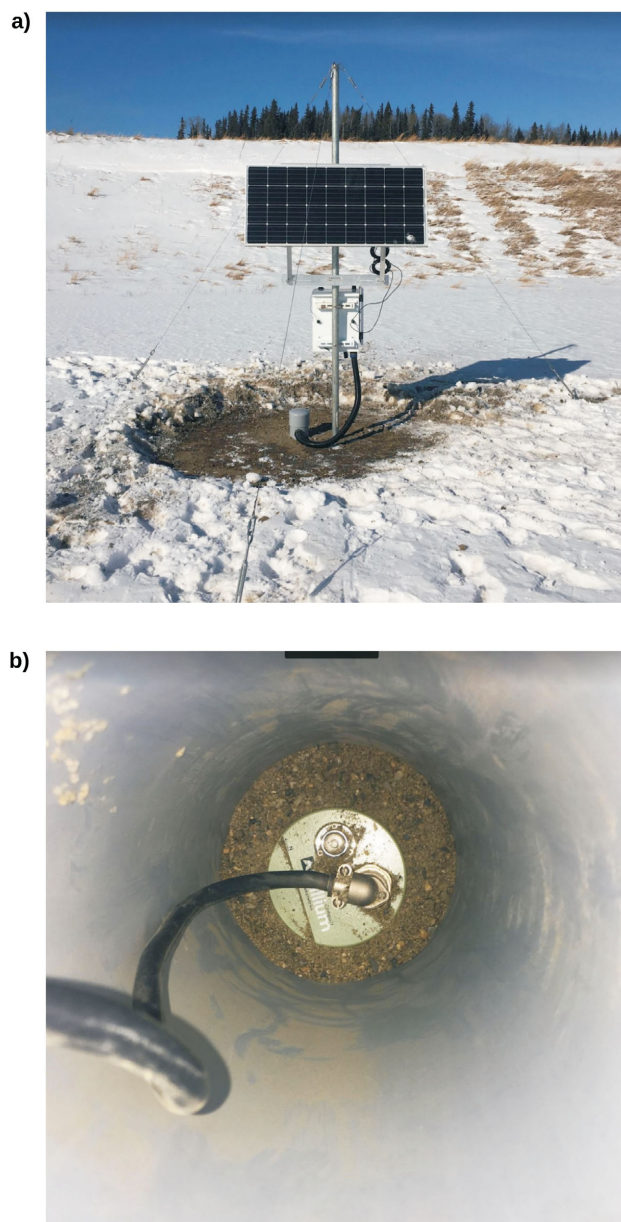
Figure 2. **a)** Example of the footprint of a single seismic monitoring station, showing solar power panels and the top of the short borehole containing the seismometer (Nanometrics Trilium T120). The digitizer (Nanometrics Taurus) and other electronics (e.g., cables, modem, etc.) are housed within the light grey box halfway up the solar panel pole. **b)** Example of the depth of borehole (~30 cm) containing the buried seismometer. Sensors were buried just below the surface to reduce surface noise (e.g., meteorological, traffic, etc.).

long-term average (STA/LTA) triggering algorithm, followed by a separate template-matching algorithm using continuously retrained modules that classify noise from events and remove unwanted signals. Then, the AI Analyst uses the support vector machine (SVM)-learning technique to identify phase arrivals in continuous real-time waveform streams. These phase arrivals are identified by training an SVM model on historical data, as it is a supervised machine-learning approach. By converting the waveforms
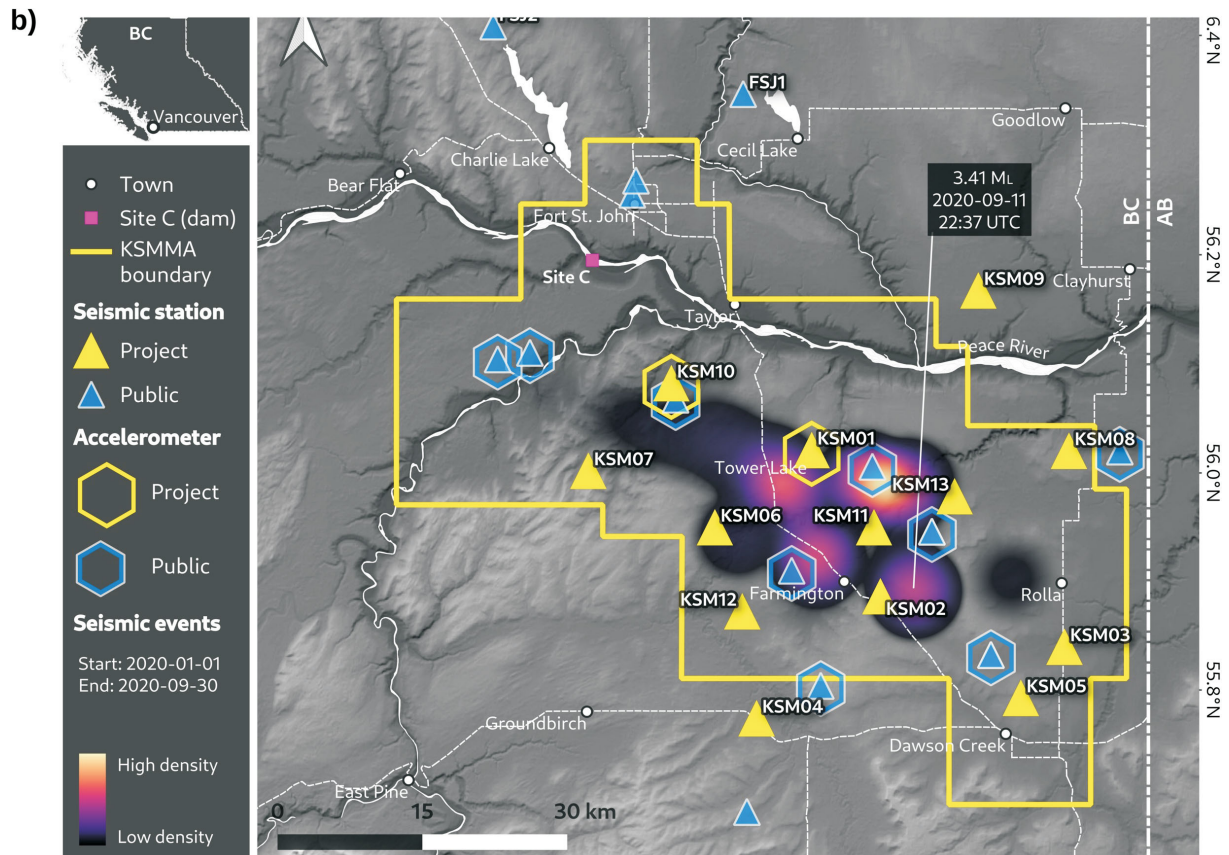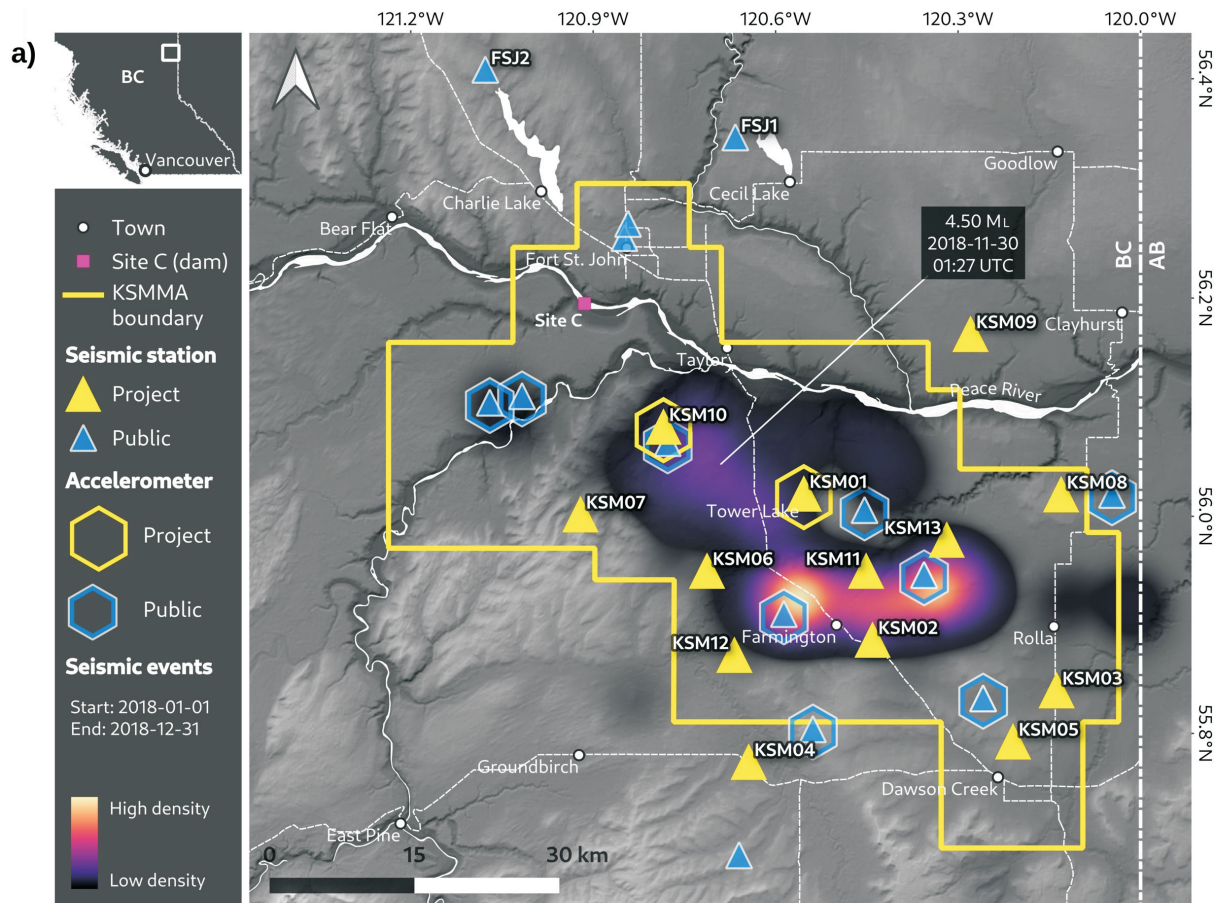
Figure 3. Spatial locations of seismicity concentrations within the Kiskatinaw Seismic Monitoring and Mitigation Area (KSMMA). Higher density of seismic events is indicated by brighter colours; lower density by darker colours; and no seismicity by grey. **a)** Seismic events recorded by Natural Resources Canada between January 1 and December 31, 2018 (data from Visser et al., 2020). Note: although the new dense array was not installed at this time, it is shown on the map for reference. The largest event in 2018, occurring on November 30 north of Tower Lake, is shown (M_L 4.50). **b)** Seismic events recorded on the newly installed Earth-System Observing Network–Réseau d'Observation du Système Terrestre (EO) network (and incorporating data from public stations) from January 22 to September 30, 2020 (data from Nanometrics Seismic Monitoring Services, 2020). The largest magnitude event in 2020, occurring on September 11 east of Farmington, is indicated (M_L 3.41). Stations FSJ1 and FSJ2 are also part of the EO network but were installed in 2018. Station FSJ1 was decommissioned on August 26, 2020, but is shown for completeness as it was used in seismic analysis prior to this. Elevation data from Shuttle Radar Topography Mission (U.S. Geological Survey, 2014). WGS 84/ Pseudo-Mercator, World Geodetic System 1984.

into over 250 features using quantities such as time and band-normalized spectrograms, a model is generated that can associate the features with P and S phases (or conversely, with noise). These can then be extracted from real-time waveforms, provided the model is applied to a network of very similar topology and geographic area for which it was trained. Additionally, the phase extraction from real-time data can be used to derive confidence measures in the phases/events detected, as well as to identify and exclude regional events. Once phases have been identified, a beamforming grid-search approach is used to identify event locations and times based on the highest likelihood P-S separation times observed at all contributing stations.

Event locations are further refined using a double-differencing algorithm (Figure 4) to produce high-precision locations. This uses parameters such as a one-dimensional (1-D) velocity model for the area and cross-correlation specific thresholds, and some parameters relating to event pairing. It reduces errors associated with the velocity model and pick placement by relocating events to minimize a) the travel time differences between co-located event pairs and b) the pick time differences between cross-correlated waveforms from co-located event pairs. A precision estimate is then derived by bootstrapping the input catalogue and quantifying the resultant hypocentre distribution. The 1-D velocity model used has been specially derived for the KSMMA (provided by the BCOGC) based on sonic logs (compressional and shear) and formation tops, and calibrated using events detected on local networks from a number of operators within the KSMMA.

Local magnitudes (M_L) are calculated using a form of the Hutton and Boore (1987) magnitude formula, which was developed for events in southern California that are detected on stations with up to 100 km epicentral distance. This scale is based upon the Wood-Anderson conversion of seismic sensors using the peak S-wave amplitude measurement.
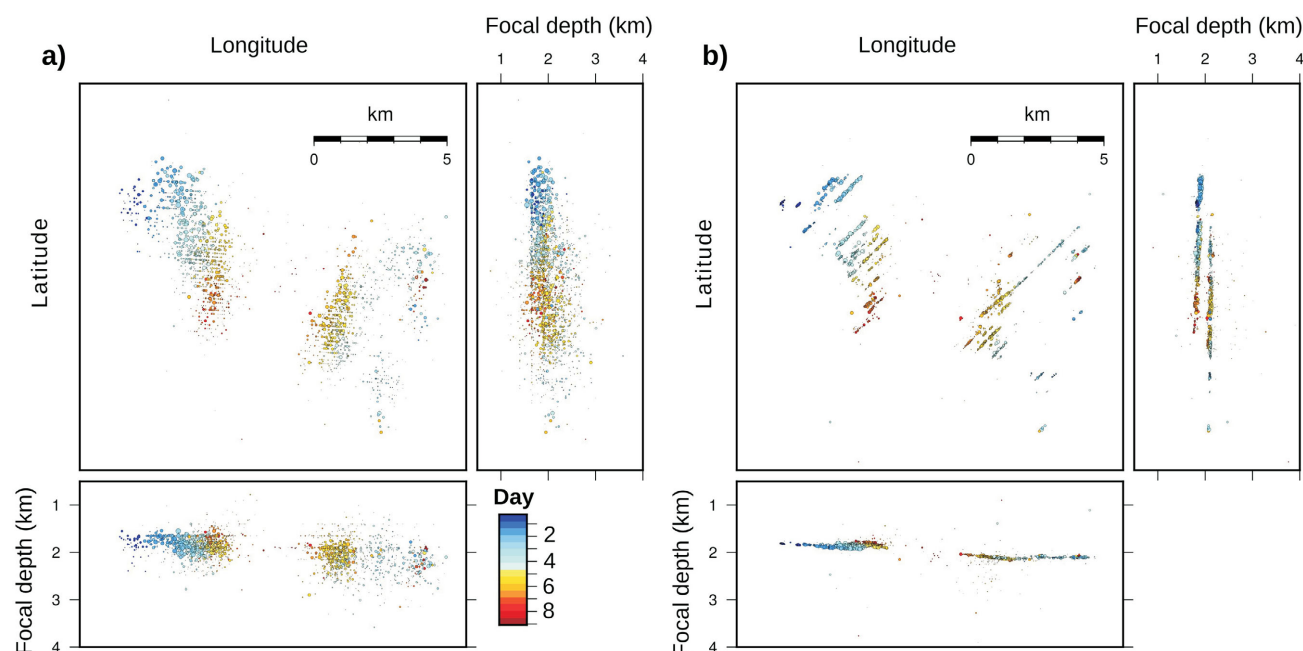
Figure 4. Spatial cluster of 2098 seismic events occurring over ~10 days at the end of March 2020 in part of the Kiskatinaw Seismic Monitoring and Mitigation Area. This example of preprocessing conducted by Nanometrics Seismic Monitoring Services shows the difference between **a)** their calculated standard locations of seismic events and **b)** their calculated high-precision locations of seismic events using a double-differencing algorithm. High-precision locations clearly denote linear features, which appear to correlate temporally with ongoing hydraulic fracturing operations in the area. Latitude and longitude values are not shown in order to preserve the location of this specific seismicity.

Overview of Recorded Seismicity

The first data from the EO network were received on January 22, 2020. At that time four stations had been installed; the remaining stations were installed in the spring. At the time of writing (October 1, 2020), a total of 7216 events had been detected in the KSMMA using the EO network and available public stations, with 7057 events reporting high-precision relocations. All events were automatically detected but have been manually verified by an expert at Nanometrics. Figure 5a (upper) shows the temporal evolution of detected seismicity from January 22 to October 1, 2020, both daily and cumulative. Distinct heightened periods of seismicity can be observed, particularly in February, March, August and September. This reflects ongoing operations in the area during these times. A clear period of quiescence is observed from April until August, representing the unprecedented situation that occurred in 2020 with the lockdown of people, businesses and cities due to the COVID-19 pandemic.

Spatially, seismicity in the KSMMA appears to occur within a band orientated to the northwest-southeast (Figures 3, 5c). Seismicity in 2020 appears to occur within a more spatially distinct region than it did in 2018 (Figure 3b versus 3a), but this may be due to the fact that there have been significantly fewer operations in 2020 due to the COVID-19 pandemic. Interestingly, the largest event in 2018 (M_L 4.50, November 30) occurred to the north of Tower Lake, away from the densest cluster of seismic events (Figure 3a). To date, the largest event of 2020 occurred on September 11 (M_L 3.41) in the southern area of the KSMMA (Figure 3b), but again away from the densest cluster of events. Assuming this seismicity is associated with ongoing hydraulic fracturing operations, this suggests that the largest magnitude events do not necessarily occur near the densest activity. Moreover, given that the largest event in 2020 did not occur in the same cluster as the largest event of 2018, it appears that the occurrence of M_L 3–4+ events is not confined to a single region.

Distinct clusters of seismicity are also seen in focal depth plots (Figure 5c), with the majority of events occurring between 1 and 2 km deep, although a number of smaller events do extend down toward the basement (which lies at an average depth of 4 km across the KSMMA). Target formations for hydraulic fracturing within the KSMMA (e.g., upper and lower Montney Formation) typically sit between 2000 and 2500 m (total vertical depth), suggesting the majority of seismicity occurs within or just above these formations. A deepening of seismicity toward the east likely indicates a deepening of the target formations or target zones in this direction.

As well as detailing the target formations at depth, the spatial evolution of seismicity allows the detailing of fault and fracture growth in near real-time (Figure 4). High-precision locations (using double-differencing techniques) reveal clear planar features associated with active hydraulic fracturing operations. Figure 4 shows a spatial cluster of 2098 seismic events occurring over ~10 days at the end of March 2020. In Figure 4a, events appear scattered spatially, although there is some degree of order to the events temporally, with the oldest events occurring to the northwest. Following relocation using double-differencing methods (Figure 4b), clear planar features are evident, which appear to 'grow' with time toward the southwest. Two distinct populations are identified, which appear to be simultaneously active. The largest planar feature in the southeast is approximately 3 km in length, allowing a better understanding of the extent of ongoing operations in the area, in lieu of having detailed injection data from individual operators.

The installation of the majority of seismic sensors in the EO network in March is clearly evident with the reduction in the minimum detected magnitude at this time (Figure 5a, lower panel). With four stations installed in January (in addition to the public sensors in the area), the minimum detected magnitude was close to M_L 0. In March 2020, this was significantly reduced, with the EO network (when combined with available public stations) now recording some events close to M_L −1. This was partly due to the installation of stations creating a denser network, but also reflects the introduction of the AI Analyst processing tool by Nanometrics, which incorporated machine-learning techniques to further refine M_L for detected events. The current estimated magnitude of completeness (Mc) is 0.074, suggesting that all events larger than this are detected (Figure 5b). This is significantly lower than the estimated Mc of 0.6 that was postulated in the funding proposal to Geoscience BC and is in part due to the optimized network design.

Seismicity directly relating to hydraulic fracturing (operationally induced seismicity) has been shown to have a higher b-value (~2; Maxwell et al., 2009; Wessels et al., 2011), indicating the dominance of many small earthquakes in comparison to large events. In comparison, b-values for natural seismicity in the northern hemisphere sit around 1 (El-Isa and Eaton, 2014). The estimated b-value for events detected in KSMMA, from the EO network and available public station data, is 1.13 (Figure 5b), which suggests that the seismicity has characteristics relating to natural fault systems. Schorlemmer et al. (2005) suggested that the b-value is greatly influenced by the tectonic stress regime, and that a value close to 1.1 is indicative of normal and strike-slip regimes. The KSMMA is strongly influenced by the Fort St. John graben complex, an asymmetrical half graben that has also undergone significant strike-slip and rotational movement upon reactivation of the basement faults in the area (Barclay et al., 1990), with a number
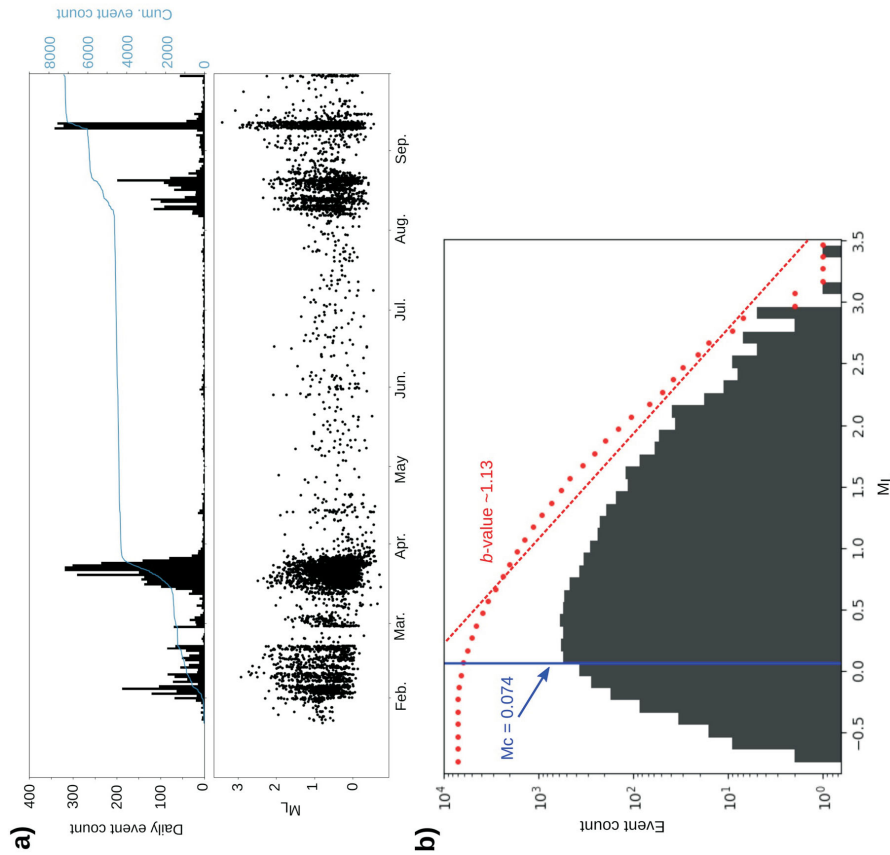
Figure 5. Evolution of seismicity detected since installation of the Earth–System Observing Network–Réseau d'Observation du Système Terrestre (EO) network within the Kiskatinaw Seismic Monitoring and Mitigation Area (KSMMA) from January 22 until October 1, 2020, 7216 events in total. **a)** Time series of events detected. Upper panel denotes event count per day and the cumulative event count through time; lower panel denotes local magnitude (M_L) of each event. Distinct temporal patterns are observed with periods of heightened seismicity in February, March, August and September. These time periods also contain events with seemingly higher magnitude events. **b)** Frequency-magnitude distribution of all events within the catalogue (n=7216). The magnitude of completeness (Mc) is estimated to be 0.074, and the estimated *b*-value is ~1.13. The largest magnitude event in the sequence is M_L 3.41. **c)** Spatial evolution of seismicity, which appears in distinct spatial clusters. The majority of seismic events have a focal depth of 1–2 km. Known normal faults within the KSMMA are shown, taken from Furlong et al., 2020. Abbreviations: Cum., cumulative; DC, Dawson Creek; FSJ, Fort St. John.

of normal faults associated with the extension of the graben falling within the KSMMA (Furlong et al., 2020; Figure 5c).

The largest magnitude event of 2020 at the time of writing (October 1, 2020) occurred on September 11 at 22:37 UTC with an estimated M_L of 3.41, following which operations in the area were shut down in accordance with the BCOGC's traffic light protocol introduced for the KSMMA (BC Oil and Gas Commission, 2018). Due to the COVID-19 pandemic in 2020, operations only restarted in the KSMMA at the beginning of August, following approximately four months of almost total quiescence (Figure 5a). The event on September 11 occurred quickly following this resurgence of activity. A total of 73 precursory events occurred over approximately four hours, with events locating within a small spatial extent (~300 by 150 m). These events are probably directly related to ongoing operations in the area based on the correlation in space and time of events and injection. Events within this precursory sequence had magnitudes between M_L 0.2 and 2.6, and were all located at depths of approximately 2.05 km. The mainshock was located at a similar depth of 2.01 km.

Ongoing Research
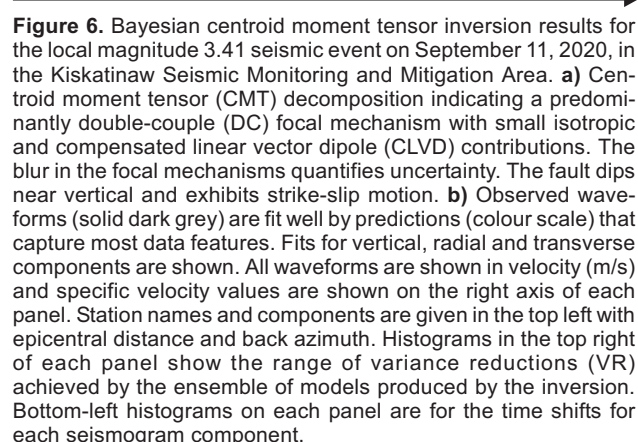
Seismic data is analyzed in near real-time by Nanometrics to provide an accurate and up-to-date catalogue of seismicity. Using this as a base, the University of Calgary, in collaboration with other institutions, is undertaking further research into the seismic sequences that are occurring within the KSMMA, in particular, the characteristics of the source of the events, spatio-temporal clustering of events, and fault and fracture dynamics at depth.

Understanding the source characteristics of an earthquake is fundamental to better discerning the physics behind source rupture processes and the kinematic behaviour of the source, and consequently understanding why seismic activity manifested in the first instance (e.g., Kanamori and Brodsky, 2004; Abercrombie, 2015). This is important for the determination of hazards in the area. Characterization of an earthquake source in terms of the deformation the rupture produces is fundamental to understand the evolving stress field and growing fracture network within a given environment (e.g., Eyre and van der Baan, 2015). One common method for calculating this is the moment tensor inversion (MTI), which aims to calculate the magnitude and orientation of fracture planes often based on body-wave polarities, amplitude ratios or waveform inversions.

A fully nonlinear Bayesian centroid moment tensor (CMT) inversion, based on the Bayesian earthquake analysis tool (BEAT; Vasyura-Bathke et al., 2020) software, was carried out for the September 11, 2020, M_L 3.41 event (Figure 6). Data from 12 stations were processed in units of velocity and a 3rd order Butterworth filter between 0.07 and 0.2 hertz

was applied after instrument-response removal. Data included waveforms from an array in the Dawson-Septimus area (Roth et al., 2020). After rotation into radial, transverse and vertical components, only components with a pulse-like waveform were retained. Green's functions were computed with QSEIS software (Wang, 1999) for a 1-D velocity model that is representative of the Western Canada Sedimentary Basin (Wang et al., 2016). The inversion applies a lune parametrization (Tape and Tape, 2015) and includes a Bayesian implementation of the cut-and-paste (CAP) algorithm (Zhao and Helmberger, 1994) to account for potential 3-D velocity structure that is not included in the 1-D velocity model. Whereas the original CAP algorithm infers optimal time shifts, the Bayesian method fully accounts for uncertainty of these time shifts within a window of ±3 s.

The CMT results show a focal mechanism dominated by a strike-slip mechanism (Figure 6a). The fault strikes at 246° with uncertainty between 245 and 249°. The auxiliary plane strikes at 86° with uncertainty between 82 and 87°. The centroid is located at 2.6 km depth with low uncertainty. The centroid epicentre is shifted 0.4 km west and 0.5 km north compared to the catalogue location. The mechanism (Figure 6a) is predominantly a double-couple solution (72.7–85.4%). However, 2.4–9.3% of the source is explained by an isotropic component and 6.4–22.4% by a compensated linear vector dipole (CLVD). Such isotropic and CLVD components are not uncommon and are typically ascribed to theory errors in the inversion. For example, the fault plane may not be perfectly planar, and Green's functions may include errors. It is also noted that CMT decomposition is intrinsically based on assumptions and it is more rigorous to consider these source trade-offs with the lune diagram (Figure 7), which illustrates the uncertainty in terms of the colour scale. The results are consistent with other studies of source mechanisms within the KSMMA, which suggest mechanisms are dominated by strike-slip faulting, with some evidence of thrust faulting (Wang et al., 2018; Babaie Mahani et al., 2020).

Figure 6. Bayesian centroid moment tensor inversion results for the local magnitude 3.41 seismic event on September 11, 2020, in the Kiskatinaw Seismic Monitoring and Mitigation Area. **a)** Centroid moment tensor (CMT) decomposition indicating a predominantly double-couple (DC) focal mechanism with small isotropic and compensated linear vector dipole (CLVD) contributions. The blur in the focal mechanisms quantifies uncertainty. The fault dips near vertical and exhibits strike-slip motion. **b)** Observed waveforms (solid dark grey) are fit well by predictions (colour scale) that capture most data features. Fits for vertical, radial and transverse components are shown. All waveforms are shown in velocity (m/s) and specific velocity values are shown on the right axis of each panel. Station names and components are given in the top left with epicentral distance and back azimuth. Histograms in the top right of each panel show the range of variance reductions (VR) achieved by the ensemble of models produced by the inversion. Bottom-left histograms on each panel are for the time shifts for each seismogram component.

a)

Full — Isotropic = Deviatoric = CLVD + DC

100.0% 2.4–9.3% 90.7–97.7% 6.4–22.4% 72.7–85.4

b)
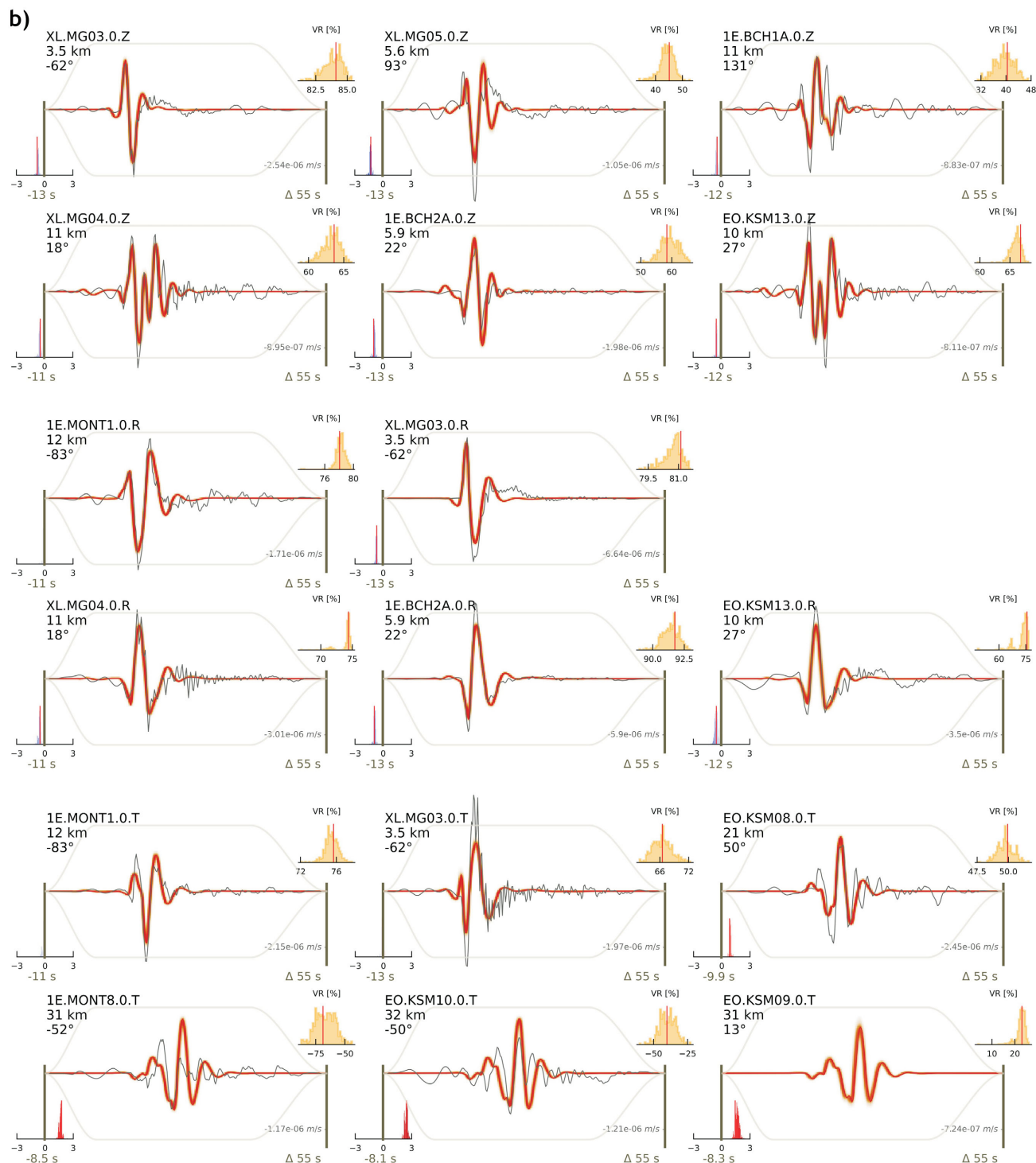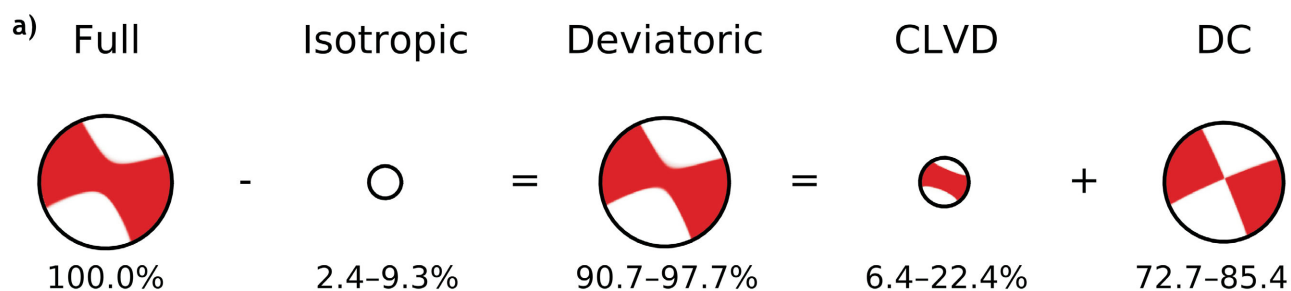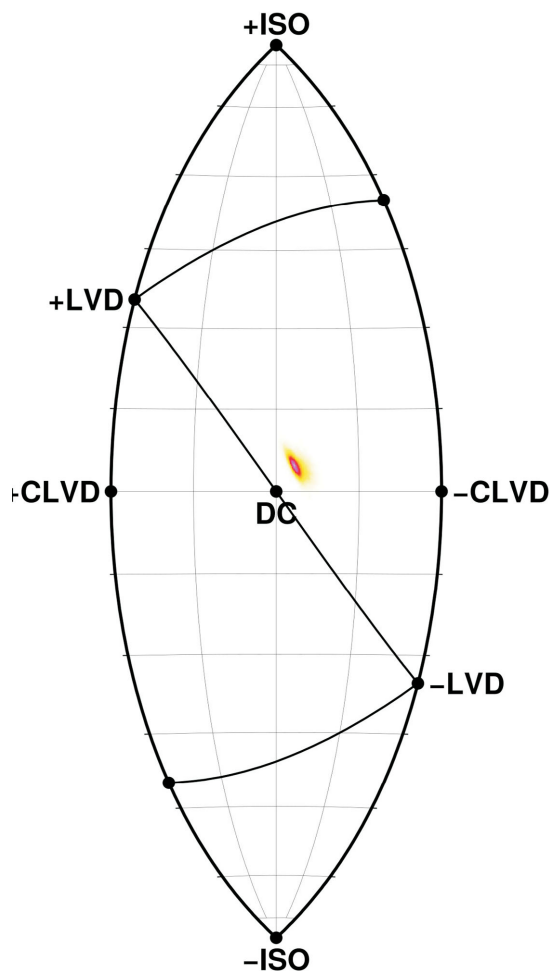
Figure 7. Bayesian centroid moment tensor (CMT) inversion results for the local magnitude 3.41 seismic event on September 11, 2020. The lune representation of the CMT more clearly shows that the event can be predominantly explained by slip on a planar fault, where the colour scale presents the probability. Lighter colours indicate low probability; darker colours indicate high probability. Abbreviations: CLVD, compensated linear vector dipole; DC, double couple; ISO, isotropic; LVD, linear vector dipole.

Observed waveforms and prediction fits, CAP time shifts and variance reduction are shown in Figure 6b. Note that agreements are excellent overall but some of the largest amplitudes are not fit well. The CAP time shifts required are negative for vertical and radial components and notably positive or neutral for the transverse component. This difference may suggest some degree of crustal anisotropy.

Since CMT estimates disagree with catalogue values, the hypocentre depth and magnitude were recalculated independently using seismic phase picks provided in the catalogue. A focal depth of ~2.75 km was calculated, which closely agrees with the centroid depth but is deeper than the hypocentre depth of ~2 km in the catalogue. Similarly, a smaller magnitude of ~M_L 3.1 (compared to M_L 3.41) was calculated. Both of these estimates agree with the CMT inversion. The discrepancy in the calculated and the original magnitude is due to the use of a different formula for calcu-

lation—a form of the Richter (1935) magnitude formula that has been modified to better reflect local attenuation characteristics of the KSMMA (Babaie Mahani and Kao, 2020) was used. In line with calculations done by NRCan, the M_L was calculated using the maximum amplitude from the vertical component, simulated on a Wood-Anderson (WA) seismometer, rather than the horizontal component, which is more common elsewhere. Plans are being made to extend the work to include events prior to this mainshock to understand the evolution of stress with time.

The year 2020 was unusual due to the COVID-19 pandemic, which caused the shutdown of many businesses and severely restricted the movement of people. A related reduction in ground motion has been accurately measured by a drop in seismic noise worldwide (e.g., Lecocq et al., 2020), which is also evidenced in the KSMMA. Over the approximately four months of quiescence, when operations within KSMMA ceased due to government regulations (April to August, Figure 5a), only 389 events were detected using the EO network and available public stations in the area. For comparison, 344 events were detected on the EO network over a single week, from February 8 to 15, when operations were in full flow. The seismicity that occurred during the quiescence is being investigated: Is it latent seismicity left over from operations in wells in the KSMMA? If so, is this from very recent operations or is it from more long-term operations? Or does it represent a natural seismicity that is now evident in the area due to changes to stress brought about by anthropogenic activity in the area? The unprecedented period of quiet allows the authors to better constrain the seismicity, since it cannot have been induced by ongoing operations in the area.

Preliminary investigations into spatio-temporal clustering of seismicity and interevent triggering within the KSMMA are being undertaken. There appears to be some evidence of interevent triggering, but correlation with injection parameters for individual wells is still required and the degree to which this influences spatio-temporal clustering remains unclear. There is also an interest in better understanding local site effects for hazard analysis, in particular, investigating spectral peaks due to resonance effects and their possible seasonal variation and amplification of seismic waves within the KSMMA. This may lead to a better understanding of why the report rate of seismic events varies spatially across the KSMMA, and why a number of residents are reporting feeling strong shaking with only very moderate magnitude events (M_L <2). Monahan et al. (2019) concluded that site amplification conditions within the KSMMA are varied, with Site Class D conditions (high amplification of seismic ground motions) being widespread. Analysis of the ambient seismic noise field, and in particular the horizontal to vertical spectral ratio (HVSR), will allow the determination of the fundamental site response frequency at different sites within KSMMA. Both of these

studies aim to better constrain the hazard from ongoing seismicity within the KSMMA, detecting 'weak' zones where seismicity is prevalent and could potentially cause alarm for the public due to amplification of the seismic wavefield.

High-precision locations of events suggest distinct planar features that develop in regions are related to ongoing hydraulic fracturing operations (e.g., Figure 4). Therefore, an analysis is being undertaken to better understand the spatio-temporal evolution of the rupture process of such planar features, using finite-fault source inversions and Bayesian analysis to better constrain the uncertainties associated with such analysis. It is hoped that this will provide a better understanding of fault nucleation, propagation and arrest, which is essential knowledge for operators and regulators.

Finally, the detailed monitoring within the KSMMA may allow the authors to better constrain a long-standing problem linked to induced seismicity: Are there diagnostic differences in the characteristics of seismicity induced by hydraulic fracturing and seismicity induced from wastewater disposal? Are the source mechanisms and rupture processes similar or different? In Canada, the majority of induced seismicity is associated with hydraulic fracturing (e.g., Rivard, 2014; Atkinson, 2016), however, in some areas of the United States seismicity is strongly associated with wastewater disposal (e.g., Ellsworth, 2013). Within the KSMMA, there are both unconventional reservoirs and wastewater disposal wells, which provides a unique opportunity to study both in detail. Currently a spatio-temporal analysis of events associated with both types of wells is being undertaken, as well as comparisons of magnitudes and source parameters, including MTI and stress changes, to better understand whether it is possible to discriminate between these two types of seismicity, and if so, learn about each of their fundamental characteristics. The objective is to gain a better understanding of the characteristic seismicity of each of these types of operations, which will enable the characterization of incoming seismicity in near real time. It will also be possible to provide insights on seismicity generation and evolution under different stress conditions to all those involved in the oil and gas industry and regulatory bodies.

Conclusions

In January 2020, the installation of a new dense seismic monitoring network began within the Kiskatinaw Seismic Monitoring and Mitigation Area (KSMMA), to better understand the relationship between ongoing hydraulic fracturing and wastewater injection operations and seismicity, in particular seismicity which is unexpected (either in terms of its location or magnitude), and seismicity that is felt by the general population. With the installation of a dense ar-

ray network, the hope is to better capture seismicity in the KSMMA at smaller magnitudes, and thereby generate a more complete catalogue of events. This catalogue will be used to better characterize the faulting and fracture mechanisms within this area, the site amplification effects and the spatial and temporal relationship between seismicity and operations, which will lead to a better understanding of the area's susceptibility to larger magnitude events. This can all aid regulatory practices and promote safer operations by the oil and gas industry within British Columbia.

The unique nature of this project means close collaboration with partners in both industry and academia to enhance the likelihood of success. By providing an evolving event catalogue (event timings, locations, magnitudes), Nanometrics Seismic Monitoring Services are significantly helping to accelerate the research within the KSMMA. To date, over 7200 events have been detected within the KSMMA using the new network and available public station networks, down to local magnitudes of –1. The installation of the new network has significantly reduced the magnitude of completeness of events detected in this area, meaning that a more complete picture of ongoing seismicity within the KSMMA has been achieved. Events appear very temporally and spatially clustered, probably related to ongoing operations in the area. Spatially, seismicity is following a similar pattern to previous years, where events cluster within a central band extending northwest to southeast. Clustering of events at depths around 2 km indicates a likely correlation between hydraulic fracturing and seismicity, as this is the average target depth of geological formations within the KSMMA. Having high-resolution locations may allow the authors to better constrain this relationship, and in particular the relationship between individual stages of operations and the temporal nature/spatial nature/magnitude of seismicity. The largest event to have occurred so far in 2020 (September 11) suggests a mechanism dominated by strike-slip movement. Using the generated seismic catalogue from the new network and available public stations, the analysis is being extended to better understand the processes at the sources of seismicity within the KSMMA and provide better constraints on faults and fractures in this area, especially their activation and development in relation to ongoing operations.

Acknowledgments

References

Abercrombie, R.E. (2015): Investigating uncertainties in empirical Green's function analysis of earthquake source parameters; Journal of Geophysical Research: Solid Earth, v. 120, issue 6, p. 4263–4277, URL <https://doi.org/10.1002/2015JB011984>.

Atkinson, G.M., Eaton, D.W., Ghofrani, H., Walker, D., Cheadle, B., Schultz, R., Shcherbakov, R., Tiampo, K., Gu, J., Harrington, R.M., Liu, Y., van der Baan, M. and Kao, H. (2016): Hydraulic fracturing and seismicity in the Western Canada Sedimentary Basin; Seismological Research Letters, v. 87, no. 3, p. 631–647, URL <https://doi.org/10.1785/0220150263>.

Babaie Mahani, A. and Kao, H. (2020): Determination of local magnitude for induced earthquakes in the Western Canada Sedimentary Basin: an update; CSEG Recorder, v. 45, no. 2, URL <https://csegrecorder.com/articles/view/determination-of-local-magnitude-for-induced-earthquakes-in-the-wcsb> [October 2020].

Babaie Mahani, A., Esfahani, F., Kao, H., Gaucher, M., Hayes, M., Visser, R. and Venables, S. (2020): A systematic study of earthquake source mechanism and regional stress field in the southern Montney unconventional play of northeast British Columbia, Canada; Seismological Research Letters, v. 91, no. 1, p. 195–206, URL <https://doi.org/10.1785/022019-0230>.

Barclay, J.E., Krause, F.F., Campbell, R.I. and Utting, J. (1990): Dynamic casting and growth faulting: Dawson Creek graben complex, Carboniferous–Permian Peace River embayment, western Canada; Bulletin of Canadian Petroleum Geology, v. 38, issue 1, p. 115–145, URL <https://pubs.geoscienceworld.org/cspg/bcpg/article/38A/1/115/582791/Dynamic-casting-and-growth-faulting-Dawson-Creek?casa_token=3fNc9UphmkkAAAAA:-16XUfhwg-2u4WaQ6JxM8unvNr7TbyR5SkyQXBMqeMtIKH8OZTboxzEQudEyey60HDIRIQ5o> [November 2020].

BC Oil and Gas Commission (2018): Order 18-90-001 (amendment #1) – Kiskatinaw Seismic Monitoring and Mitigation Area Special Project Order; BC Oil and Gas Commission, URL <https://www.bcogc.ca/files/reports/Technical-Reports/Kiskatinaw-Seismic-Monitoring-and-Mitigation-Area-KSMMA-Special-Project-Order-18-90-001-Amendment-1.pdf> [October 2020].

El-Isa, Z.H. and Eaton, D.W. (2014): Spatiotemporal variations in the *b*-value of earthquake magnitude–frequency distributions: classification and causes; Tectonophysics, v. 615, p. 1–11, URL <https://doi.org/10.1016/j.tecto.2013.12.001>.

Ellsworth, W.L. (2013): Injection-induced earthquakes; Science, v. 341, issue 6142, art. 1225942, URL <https://doi.org/10.1126/science.1225942>.

Eyre, T.S. and van der Baan, M. (2015): Overview of moment-tensor inversion of microseismic events; The Leading Edge, v. 34, no. 8, p. 882–888, URL <https://doi.org/10.1190/tle-34080882.1>.

Furlong, C.M., Gingras, M.K. and Zonneveld, J.P. (2020): High-resolution sequence stratigraphy of the Middle Triassic Sunset Prairie Formation, Western Canada Sedimentary Basin, north-eastern British Columbia; The Depositional Record, v. 6, issue 2, p. 343–408, URL <https://doi.org/10.1002/dep2.107>.

Hutton, L.K. and Boore, D.M. (1987): The ML scale in southern California; Bulletin of the Seismological Society of America, v. 77, no. 6, p. 2074–2094, URL <https://pubs.geoscienceworld.org/ssa/bssa/article/77/6/2074/119025?casa_token=PI7rujdIrZwAAAAA:-GNMZJu9tTvReL9QJWdi7EU01HkyyrRhGoRaj56aiexX2LgzEja_3CSX6hv6L5lNaixfgMw> [October 2020].

Kanamori, H. and Brodsky, E.E. (2004): The physics of earthquakes; Reports on Progress in Physics, v. 67, no. 8, p. 1429–1496, URL <https://doi.org/10.1088/0034-4885/67/8/R03>.

Lecocq, T., Hicks, S.P., Van Noten, K., van Wijk, K., Koelemeijer, P., De Plaen, R.S.M., Massin, F., Hillers, G., Anthony, R.E., Apoloner, M.-T., Arroyo-Solorzano, M., Assink, J.D., Buyukakpinar, P., Cannata, A., Cannavo, F., Carrasco, S., Caudron, C., Chaves, E.J., Cornwell, D.G., Craig, D., et al. (2020): Global quieting of high-frequency seismic noise due to COVID-19 pandemic lockdown measures; Science, v. 369, issue 6509, p. 1338–1343, URL <https://doi.org/10.1126/science.abd2438>.

Maxwell, S.C., Jones, M., Parker, R., Miong, S., Leaney, S., Dorval, D., D'Amico, D., Logel, J., Andersen, E. and Hammermaster, K. (2009): Fault activation during hydraulic fracturing; Society of Exploration Geophysicists, SEG 2009 Annual Meeting, October 25–30, 2009, Houston, Texas, Technical Program Expanded Abstracts, p. 1552–1556, URL <https://doi.org/10.1190/1.3255145>.

Monahan, P.A., Hayes, B.J., Perra, M., Mykula, Y., Clarke, J., Galamboos, B., Griffiths, D., Bayarsaikhan, O. and Oki, U. (2019): Amplification of seismic ground motion in the Fort. St. John–Dawson Creek area, northeastern British Columbia (NTS 093P, 094A); *in* Geoscience BC Summary of Activities 2019: Energy and Water, Geoscience BC, Report 2020-02, p. 1–12, URL <http://www.geosciencebc.com/i/pdf/SummaryofActivities2019/EW/Project%202018-052_EW_SOA2019.pdf> [October 2020].

Nanometrics Seismic Monitoring Services (2020): Athena web portal; Nanometrics Seismic Monitoring Services, URL <https://www.nanometrics.ca/products/software/athena> [October 2020].

Richter, C.F. (1935): An instrumental earthquake magnitude scale; Bulletin of the Seismological Society of America, v. 25, no. 1, p. 1–32, URL <https://pubs.geoscienceworld.org/ssa/bssa/article/25/1/1/115102?casa_token=Z56vuuclvy-

UAAAAA:uWJSrfF7dP-J9x-ZJiiKMKV5TY0QZy-ayaVS6QmYEkF82cNy9Y3f4tRxxX4estOSXZ1ePiM> [October 2020].

Rivard, C., Lavoie, D., Lefebvre, R., Séjourné, S., Lamontagne, C. and Duchesne, M. (2014): An overview of Canadian shale gas production and environmental concerns; International Journal of Coal Geology, v. 126, p. 64–76, URL <https://doi.org/10.1016/j.coal.2013.12.004>.

Roth, M.P., Verdecchia, A., Harrington, R.M. and Liu, Y. (2020): High-resolution imaging of hydraulic-fracturing induced earthquake clusters in the Dawson-Septimus area, northeast British Columbia, Canada; Seismological Research Letters, v. 91, no. 5, p. 2744–2756, URL <https://doi.org/10.1785/0220200086>.

Schorlemmer, D., Wiemer, S. and Wyss, M. (2005): Variations in earthquake-size distribution across different stress regimes; Nature, v. 437, p. 539–542, URL <https://doi.org/10.1038/nature04094>.

Tape, W. and Tape, C. (2015): A uniform parametrization of moment tensors; Geophysical Journal International, v. 202, issue 3, p. 2074–2081, URL <https://doi.org/10.1093/gji/ggv262>.

U.S. Geological Survey (2014): Shuttle Radar Topography Mission, digital topographic data; U.S. Geological Survey, 30 m cell, zipped hgt format, URL <http://dds.cr.usgs.gov/srtm/> [October 2020].

Vasyura-Bathke, H., Dettmer, J., Steinberg, A., Heimann, S., Isken, M.P., Zielke, O., Mai, P.M., Sudhaus, H. and Jónsson, S. (2020): The Bayesian earthquake analysis tool; Seismological Research Letters, v. 91, no. 2A, p. 1003–1018, URL <https://doi.org/10.1785/0220190075>.

Visser, R., Kao, H., Smith, B., Goerzen, C., Kontou, B., Dokht, R.M.H., Hutchinson, J., Tan, F. and Babaie Mahani, A. (2020): A comprehensive earthquake catalogue for the Fort St. John – Dawson Creek region, British Columbia, 2017-2018; Geological Survey of Canada, Open File 8718, 20 p., URL <https://doi.org/10.4095/326015>.

Wang, R. (1999): A simple orthonormalization method for stable and efficient computation of Green's functions; Bulletin of the Seismological Society of America, v. 89, no. 3, p. 733–741, URL <https://pubs.geoscience-world.org/ssa/bssa/article/89/3/733/120414?casa_token=thLuvQpSH9MAAAAA:-CAzeIbpJr9NwXs4i-LEqc1t20hNqWO1EVDad8GWCWtNCMXeqj8O2LdetI50c1_eR_523Bw8> [October 2020].

Wang, R., Gu, Y.J., Schultz, R. and Chen, Y. (2018): Faults and non-double-couple components for induced earthquakes; Geophysical Research Letters, v. 45, issue 17, p. 8966–8975, <https://doi.org/10.1029/2018GL079027>.

Wang, R., Gu, Y.J., Schultz, R., Kim, A. and Atkinson, G. (2016): Source analysis of a potential hydraulic-fracturing-induced earthquake near Fox Creek, Alberta; Geophysical Research Letters, v. 43, issue 2, p. 564–573, URL <https://doi.org/10.1002/2015GL066917>.

Wessels, S., Kratz, M. and De La Pena, A. (2011): Identifying fault activation during hydraulic stimulation in the Barnett Shale: source mechanisms, b values, and energy release analyses of microseismicity; Society of Exploration Geophysicists, SEG 2011 Annual Meeting, September 18–23, 2011, San Antonio, Texas, Technical Program Expanded Abstracts, p. 1463–1467, URL <https://doi.org/10.1190/1.3627478>.

Zhao, L.S. and Helmberger, D.V. (1994): Source estimation from broadband regional seismograms; Bulletin of the Seismological Society of America, v. 84, no. 1, p. 91–104, URL <https://pubs.geoscienceworld.org/ssa/bssa/article/84/1/91/102552?casa_token=SGrBfXFtlWQAAAAA:wc0w90lgm_hIViATij3P90ePfluK85nzL8LQQPvx0B7Gi0Y8TMXWImxaDYW3VGGDQYqfg5w> [October 2020].

Numerical Modelling and Triggering Mechanism of the Largest Hydraulic Fracturing–Induced Earthquake in Northeastern British Columbia, Canada (NTS 094B/16)

B. Wang, School of Earth and Ocean Sciences, University of Victoria, Victoria, British Columbia and Natural Resources Canada, Geological Survey of Canada–Pacific, Sidney, British Columbia

A. Verdecchia, Department of Earth and Planetary Sciences, McGill University, Montréal, Quebec

H. Kao, Natural Resources Canada, Geological Survey of Canada–Pacific, Sidney, British Columbia and School of Earth and Ocean Sciences, University of Victoria, Victoria, British Columbia, honn.kao@canada.ca

R.M. Harrington, Institute of Geology, Mineralogy and Geophysics, Ruhr University Bochum, Bochum, Germany

Y. Liu, Department of Earth and Planetary Sciences, McGill University, Montréal, Quebec

H. Yu, Geological Survey of Canada–Pacific, Sidney, British Columbia

Introduction

For the past decade, the sharply increased seismicity in the central United States has been attributed to wastewater injection through disposal wells, and the majority of events occurred deeper than the target injection layers, within the basement rocks (e.g., Ellsworth, 2013; Keranen et al., 2014). In contrast, several studies suggested that hydraulic fracturing (HF) could be responsible for the majority of induced earthquakes in the Western Canada Sedimentary Basin (Figure 1; e.g., BC Oil and Gas Commission, 2012; Atkinson et al., 2016; Mahani et al., 2017; Schultz et al., 2018; Yu et al., 2019; Roth et al., 2020). On August 17, 2015, an M_w 4.6 earthquake occurred within the southern Montney play northwest of Fort St. John in northeastern British Columbia (BC). The earthquake occurred within 500 m of an actively stimulated well and less than 7 km from two nearby wells (Figure 1). This event has been recognized as the largest HF-induced event in Canada.

A previous study (Wang et al., 2020) investigated the source characteristics of this M_w 4.6 sequence and found 1) a clear spatiotemporal relationship between the local HF operations and the observed earthquake sequence (Figure 1); 2) the static stress–drop values of the induced earthquakes fell within the typical range of tectonic events; and 3) a significant variation in the seismic response times at nearby wells, even though the injection sites are located less than 10 km apart. For example, the first recorded event occurred

five days after the onset of injection at the closest well (W1), whereas earthquakes occurred nearly simultaneously at two nearby wells (W2 and W3) within 1 day after the operation started. The locations of the three wells are shown in Figure 1c. Based on these observations, Wang et al. (2020) inferred that the M_w 4.6 earthquake occurred on a pre-existing fault with a significant amount of preloaded tectonic strain.

However, questions remain about the seismogenic behaviour of the M_w 4.6 earthquake sequence. For example, what is the most plausible triggering mechanism for the mainshock and why is the seismic response at the two nearby HF wells (W2 and W3) much faster compared to the delay of ~5 days at W1? Therefore, the objective of this study is to investigate the various aspects of seismogenesis of the M_w 4.6 earthquake and the different response times at the three nearby HF sites. This will involve 3-D poroelastic models with detailed numerical simulations of the geomechanical evolution caused by fluid injection.

Method

Focal Mechanism Determination

The gCAP method is used to determine the moment-tensor solution for the M_w 4.6 earthquake by inverting the body and surface waveforms recorded at local distances (Figure 2), and the P-wave first-motion method is used as a consistency check. First, the Green's functions are computed for a wide range of distances (50–350 km) using the frequency-wavenumber integration approach (Aki and Richards, 2002; Zhu and Rivera, 2002). This study employs the
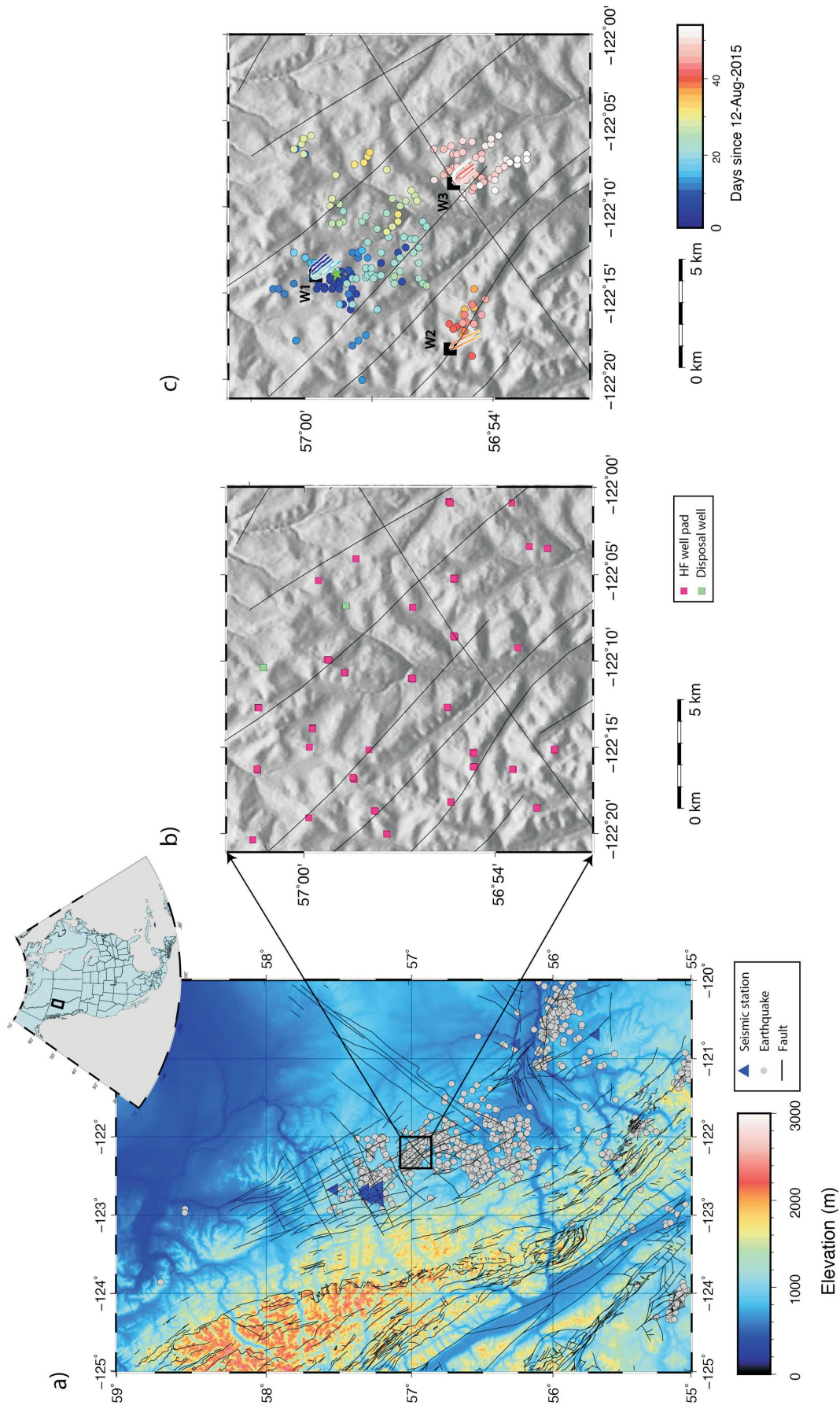
Figure 1. a) Seismicity in northeastern British Columbia from 2011 to 2020 reported by Natural Resources Canada (https://www.earthquakescanada.nrcan.gc.ca), with the black rectangle marking the study area. Thin lines mark known geological faults. **b)** Hydraulic-fracturing pads and disposal wells in the study area. **c)** Spatiotemporal distribution of the induced earthquakes from Wang et al. (2020), with the colours of the wells and earthquakes corresponding to occurrence time since August 12, 2015, the green star denoting the M_w 4.6 mainshock.

same regional 1-D velocity model used in the routine moment-tensor inversion for significant earthquakes in western Canada (Kao et al., 2012). The misfit between the synthetic and observed waveforms is then calculated to obtain the final solution. The moment-tensor inversion is repeated for each depth in the range 1–10 km, and the solution with the lowest overall misfit is found at a depth of 4 km (Figure 2), which is also comparable to the depth solution of 3.5 km from Wang et al. (2020). The present solution shows a slightly oblique thrust mechanism with northwest-southeast nodal planes (nodal plane 1: strike 131°, dip 37° and rake 42°; nodal plane 2: strike 005°, dip 66° and rake 119°). The consistency check using the available P-wave first motions shown in Figure 2c shows polarities consistent with the gCAP focal-mechanism solution except for station NBC4, which is located close to one of the nodal planes.

Poroelastic Model

Analytical and numerical models have been widely used to study stress changes caused by fluid injection and their relation to seismicity (e.g., Segall and Lu, 2015; Bao and Eaton, 2016; Deng et al., 2016; Goebel et al., 2017; Yu et al., 2019). Both increase in pore-fluid pressure and poroelastic-stress perturbation have been proposed as potential mechanisms. This study uses the COMSOL Multiphysics® software (version 5.3a) to model the distribution and evolution of pore pressure and poroelastic stress surrounding injection wells W1–W3 (Figure 1).

The solid-mechanism module and Darcy's fluid-flow module are used to simulate the poroelastic-coupling process. By assuming an isotropic and homogeneous medium, the pore pressure can be obtained by solving the coupled-diffusion equation (similar equivalent forms of the equations can be found in, for example, Wang and Kumpel [2003], Shapiro and Dinske [2009]),

$$\rho S \frac{\partial p}{\partial t} - \nabla \cdot \left(\rho \frac{\kappa}{\mu_d} \nabla p \right) = Q_m(x,t) - \rho \alpha \frac{\partial \varepsilon_{vol}}{\partial t} \tag{1}$$

$$S = \chi_f \epsilon + \chi_p (1 - \epsilon) \tag{2}$$

$$q = -\frac{\kappa}{\mu_d} \nabla p , \tag{3}$$

where S is the linearized storage parameter, p is the fluid's pressure in the pore space, ε_{vol} is the volumetric strain of the porous matrix, κ is the permeability of the block, Q_m is the volumetric flow rate for a fluid source, α is the Biot-Willis coefficient, ρ is the pore-fluid density, μ_d is its dynamic viscosity, χ_f is the compressibility of the fluid, χ_p is the compressibility of the rock, ε is strain tensor and q is the velocity variable that gives a volume flow rate per unit area of the porous material. COMSOL uses S as the default parameter in Equation 2, whereas some studies use the Biot modulus (M^{-1}), which can be calculated from Young's modulus (G)

and Poisson's ratio (ν; e.g., Rice and Cleary, 1976; Detournay and Cheng, 1993; Leake and Hsieh, 1995). The governing equations for the poroelastic model are

$$-\nabla \cdot \sigma = F_v \tag{4}$$

$$\sigma_{ij} = \frac{2Gv}{(1-2v)} \varepsilon_{kk} \delta_{ij} + 2G\varepsilon_{ij} - \alpha p \delta_{ij} \tag{5}$$

$$\varepsilon_{ij} = \frac{1}{2}((\nabla \boldsymbol{u})^T + \nabla \boldsymbol{u}) , \tag{6}$$

where σ is the stress tensor, F_v is the volume force vector, δ_{ij} is the Kronecker delta (equal to 1 when i = j and to 0 when i ≠ j) and $\boldsymbol{u}$ is the deformation vector. When gravity is the only driving force (F_v) is $(\rho_\theta + \rho_b)g$, where g is the acceleration of gravity, θ is porosity and ρ_b is bulk density.

With the stress tensor and pore-pressure change calculated by COMSOL, the following equation, adapted from Xu et al. (2010), is used to calculate the Coulomb Stress changes (ΔCFS) resolved on the fault plane as determined from the focal mechanism solution,

$$\Delta CFS = \sin \lambda \left[-\frac{1}{2} sin^2 \phi \, sin(2\tilde{\delta}) \, \sigma_{11} + \right.$$

$$\frac{1}{2} sin(2\phi) \, sin(2\tilde{\delta}) \, \sigma_{12} + sin \, \phi \, cos(2\tilde{\delta}) \, \sigma_{13} -$$

$$\frac{1}{2} cos^2 \phi \, sin(2\tilde{\delta}) \, \sigma_{22} - cos\phi \, sin(2\tilde{\delta}) \, \sigma_{23} +$$

$$\left. \frac{1}{2} sin(2\tilde{\delta}) \, \sigma_{33} \right] + cos\lambda \left[-\frac{1}{2} sin(2\phi) \, sin \, \tilde{\delta} \, \sigma_{11} + \right.$$

$$cos(2\phi) \, sin \, \tilde{\delta} \, \sigma_{12} + cos\phi cos\tilde{\delta} \sigma_{13} +$$

$$\left. \frac{1}{2} sin(2\phi) \, sin \, \tilde{\delta} \, \sigma_{22} + sin\phi cos\tilde{\delta} \sigma_{23} \right] +$$

$$\mu \left[sin^2 \phi sin^2 \tilde{\delta} \sigma_{11} - sin(2\phi) \, sin^2 \tilde{\delta} \sigma_{12} - \right.$$

$$sin \, \phi \, sin(2\tilde{\delta}) \, \sigma_{13} + cos^2 \phi sin^2 \tilde{\delta} \sigma_{22} +$$

$$\left. cos\phi \, sin(2\tilde{\delta}) \, \sigma_{23} + cos^2 \phi \sigma_{33} + \Delta P , \right] \tag{7}$$

where μ is the friction coefficient (set here as 0.6); ϕ, δ and λ are the strike, dip and rake of the receiver fault, respectively; σ_{ij} is the stress tensor, where $i, j = 1,2,3$ are the 3-D components in the Cartesian co-ordinate system; and ΔP is the pore-pressure change. It is worth noting that, since the stress tensor and pore pressure are both time dependent, ΔCFS is a property that also evolves with time.

Numerical Simulation and Results

Poroelastic Models for the M_w 4.6 Mainshock

To investigate the most plausible triggering mechanism for the M_w 4.6 earthquake, 3-D models were constructed with dimensions of 5 km in all co-ordinate directions. Each model is divided into four layers (Figure 3a) to represent the stratigraphy of the study area: the upper sedimentary
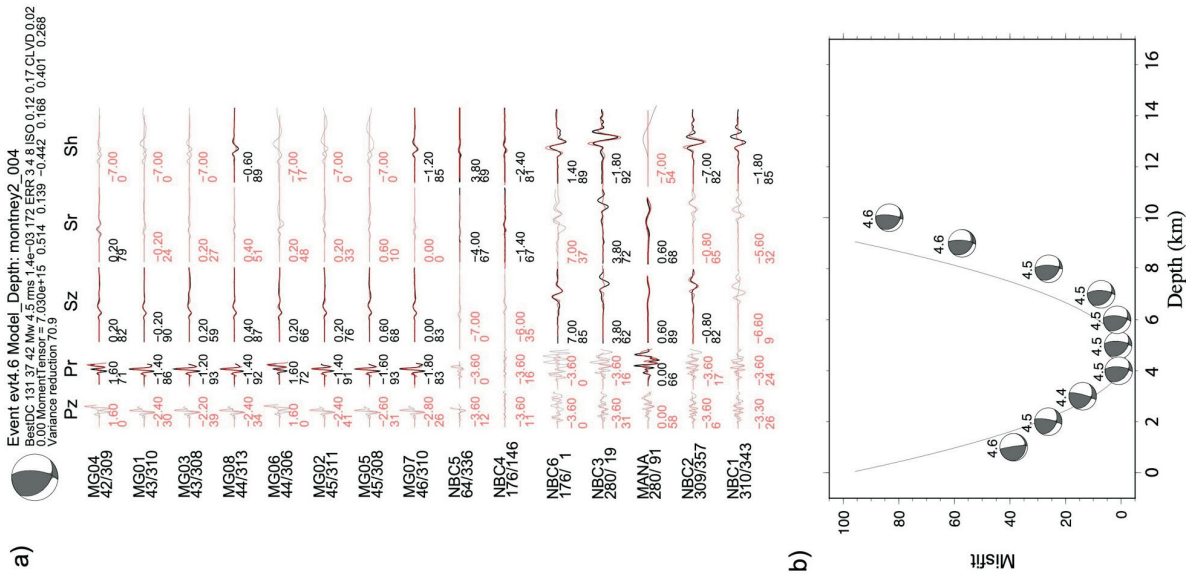
Figure 2. Focal mechanism solutions for the M_w 4.6 earthquake of August 12, 2015: **a)** synthetic and observed seismograms plotted as red and black lines, respectively; thick lines with black numbers below are the matches used in the inversion, whereas lines with red numbers below are discarded pairs; **b)** misfit error of moment-tensor inversion versus depth by gCAP method; and **c)** confidence check using P-wave polarities. Black circles in the beach–ball plot indicate stations with positive polarity (upward) and white circles indicate negative polarity (downward). Note that the polarity at station NBC4 is uncertain.
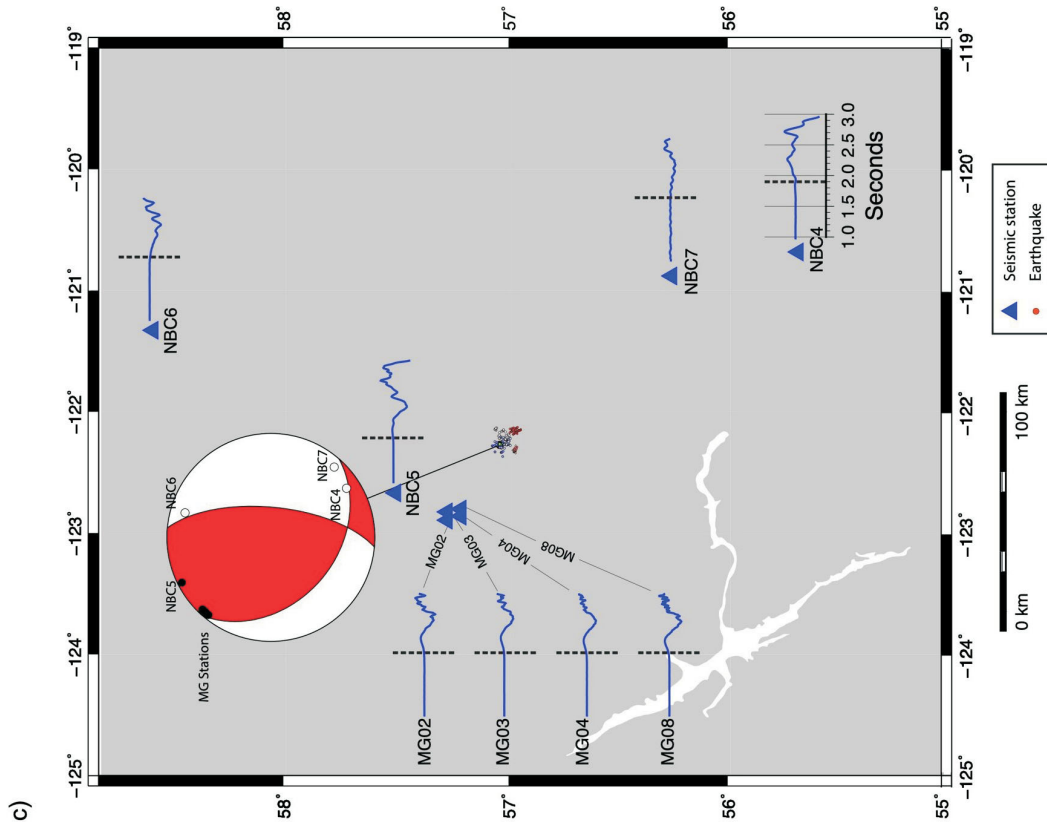
layer, the shale layer where the HF occurs, the lower sedimentary layer and the crystalline basement (e.g., Davies et al., 1997). Published data are used to set the solid and hydrogeological properties of each layer (Clauser, 1992; Neuzil, 1994; Rokosh et al., 2008, 2010; Laske et al., 2013; Dong et al., 2017; Vishkai et al., 2017; Cui and Nassichuk, 2018); the major properties used in the model are listed in Table 1. It is assumed that the fluid properties do not change with depth or time (see Table 1). Based on the corner frequency (fc) of ~3.2 Hz derived by Wang et al. (2020) for the M_w 4.6 mainshock and the assumption of a circular rupture, the radius of its rupture is estimated to be 400 m (Madariaga, 1977). Consequently, a 3 × 3 km fault patch was established to adequately encompass the entire circular rupture. Previous studies suggest that the hydrological characteristics along the fault surface could be very different from the surrounding rocks due to the fault's damage zone (e.g., Yehya et al., 2018), so it has been assumed that permeability along the fault is one order of magnitude larger than in the confining layers (Table 1).

With the basic model set up, three scenarios were designed to investigate the influence of different hydrogeological structures on the stress-field changes due to multistage injection. In Model 1 (Figure 3b), only the fluid injection was simulated for each stage without considering the effect of any potential fractures or conduits outside of the fault surface. In Model 2 (Figure 3c), besides the fluid-injection points, it was assumed that the HF operations created a fracture zone surrounding the horizontal wells, leading to an increased permeability compared to the unfractured shale formation. In Model 3 (Figure 3d), a conduit is added to connect the fracture zone and the pre-existing fault, the conduit having a permeability two orders of magnitude greater than the surrounding formations (5×10^{-12} m^2), similar to the studies of Deng et al. (2016) and Peña Castro et al. (2020). Note that the permeability of the conduit falls at the high end of the observed values for fault-damage zones (e.g., Cappa, 2009; Farrell and Taylor, 2014).

Next, the multistage fluid-injection process is simulated by assuming that fluid is injected at a single point of each stage, and the consecutive stages migrate along the horizontal wellbore. However, due to the lack of precise timing of each HF stage, it was arbitrarily assumed that the HF operations start at 8:00 a.m. local time each morning and individual stages are finished without overlapping in time.

Figure 4a and b show the evolutions of ΔCFS and pore pressure, respectively, on the mainshock fault surface for the three models (Figure 4c and d are the enlarged version). The results indicate that the ΔCFS calculated on the receiver fault in both Models 1 and 2 is small and negative, and would discourage slip on the fault surface. In contrast, the ΔCFS for Model 3 has a much higher and positive value, ~0.56 MPa, which works to encourage fault slip.

Poroelastic Models for Nearby HF Sites (W2 and W3)

Next, work focused on the differing seismogenic behaviours at the two nearby HF sites (wells W2 and W3; Figure 1), namely the 1 day seismic response as triggered at wells W2 and W3 compared to the 5 day response time at well W1 (i.e., delayed triggering). The method in the previous section was used to calculate the ΔCFS imposed on the receiver faults, by coupling progression of the elastic-stress and pore-pressure changes from the injected fluids, as described below.

Wells W2 and W3 were simulated separately, but the model setup is the same (20 × 20 × 5 km). The number of layers and the solid and hydrogeological properties are identical to the models described in the previous section. In both cases, the first earthquake in each sequence was chosen as the representative location of the receiver fault and the cumulative effects from previous injections were simulated (i.e., effects from W1 on the fault next to W2, and effects from both W1 and W2 on the fault next to W3, given the injection timing as indicated in Figure 5). Since no reliable fault-plane solutions exist for the two selected events, the

Table 1. Solid and fluid properties of each layer used in Models 1, 2 and 3 for the M_w 4.6 simulation shown in Figure 3, and for the two models for W2 and W3.

Variable	Layer 1	Layer 2	Layer 3	Layer 4
Depth	0–1.7 km	1.7–2.1 km	2.1–3 km	3–5 km
Biot-Willis	0.7	0.7	0.7	0.7
P-wave velocity	3600 m/s	4400 m/s	6300 m/s	7100 m/s
S-wave velocity	2080 m/s	2540 m/s	3630 m/s	3990 m/s
Bulk Density (r_b)	2160 kg/m^3	2460 kg/m^3	2740 kg/m^3	3000 kg/m^3
Permeability (κ)	7.5×10^{-14} m^2	0.1×10^{-16} m^2	0.5×10^{-16} m^2	0.1×10^{-16} m^2
Porosity (q)	0.1	0.05	0.05	0.08
Fluid density (r)	1000 kg/m^3	1000 kg/m^3	1000 kg/m^3	1000 kg/m^3
Fluid compressibility (χ_f)	4.5×10^{-10} Pa^{-1}	4.5×10^{-10} Pa^{-1}	4.5×10^{-10} Pa^{-1}	4.5×10^{-10} Pa^{-1}
Fluid dynamic viscosity (μ_d)	0.79×10^{-3} Pa•s	0.79×10^{-3} Pa•s	0.79×10^{-3} Pa•s	0.79×10^{-3} Pa•s
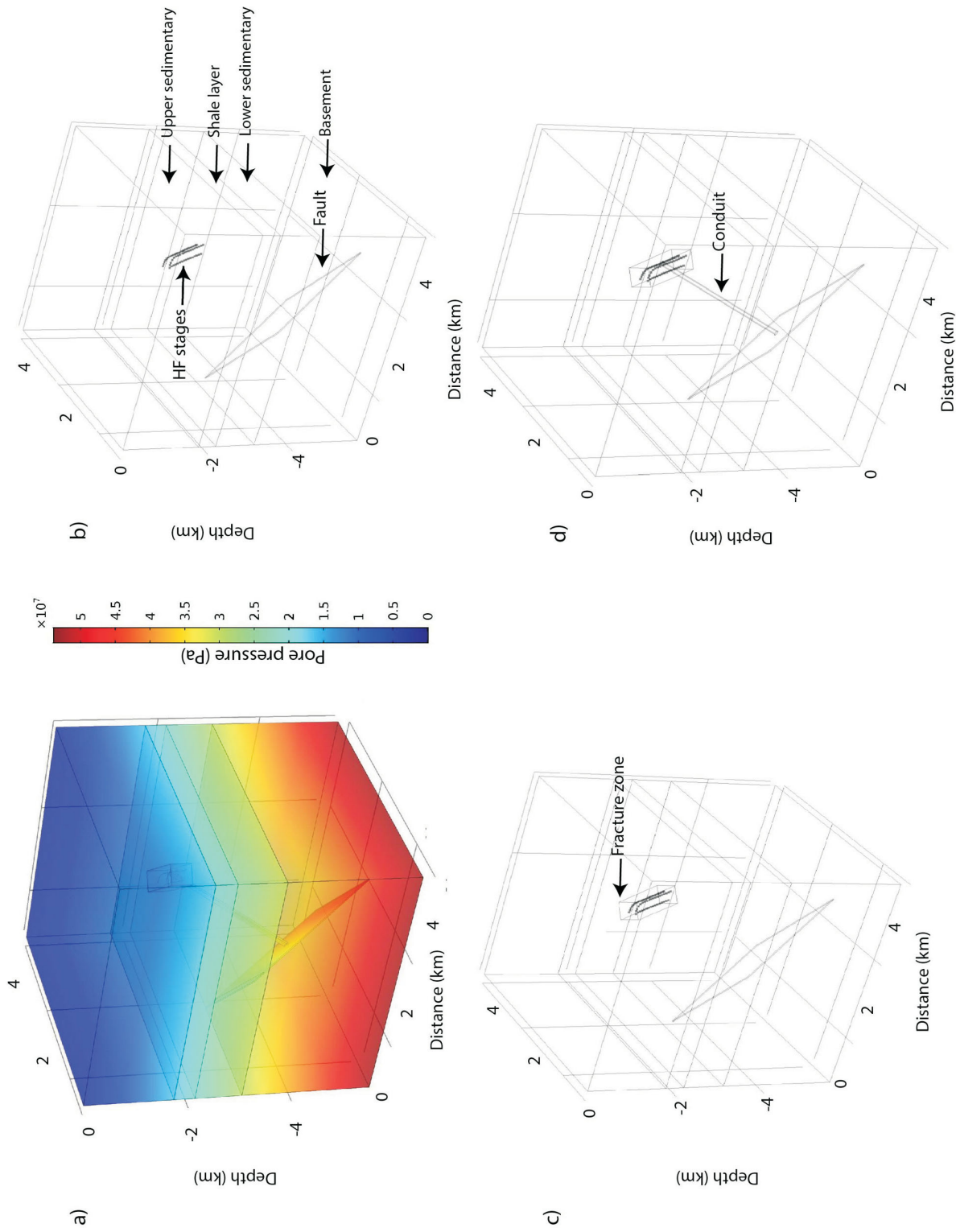
Figure 3. Four-layer model built with COMSOL to simulate the triggering mechanisms of the M$_w$ 4.6 earthquake: **a)** hydrostatic pore pressure from the transient model before HF starts, which is used as the initial value input for the following time-dependent study; **b)** Model 1, with the large square in the fourth layer denoting the fault patch and the small squares representing the injection points for each stage. **c)** Model 2, similar to Model 1 but with a high-permeability fracture zone caused by HF operation, as indicated by the cuboid in the second shale layer; and **d)** Model 3, similar to Model 2 but with a high-permeability conduit represented by the narrow cylinder.
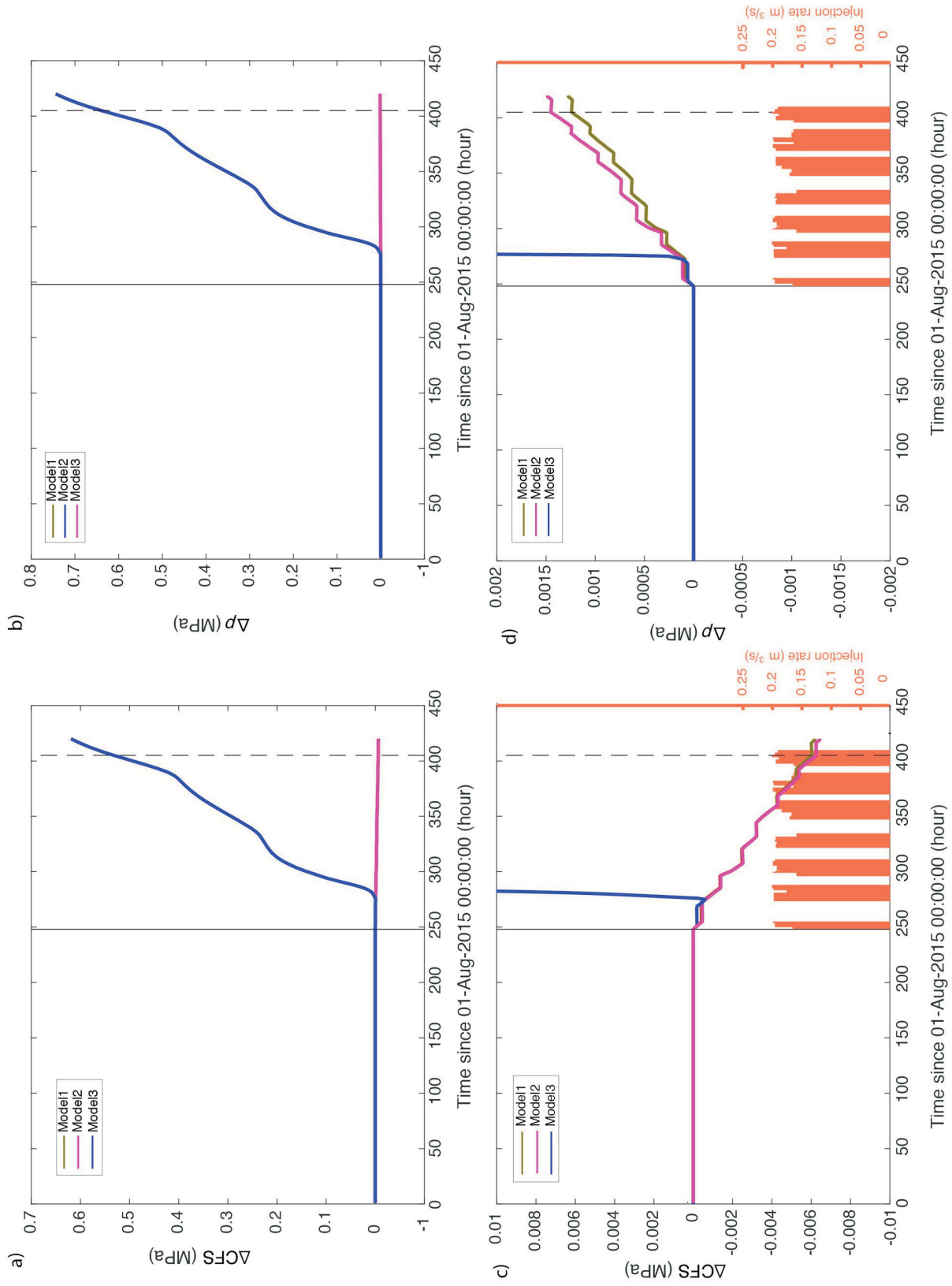
Figure 4. ΔCFS and pore-pressure change (Δ*p*) results for poroelastic Models 1, 2 and 3. Top two panels denote the results for the three models, and bottom two denote the enlarged version for Models 1 and 2. **a)** and **c)** show ΔCFS calculated using Equation 7. **b)** and **d)** show pore-pressure changes only. Solid vertical lines represent onset time of HF operations, and dashed vertical lines represent occurrence time of M_w 4.6 earthquake. Bottom bars represent fluid-injection rate and duration for individual HF stages.

two receiver faults were assumed to be optimally oriented to the local tectonic-stress field (e.g., Bell and Grasby, 2012) when the corresponding ΔCFS values were calculated using Equation 7. Unlike the three scenarios used for W1 (Figure 3b–d), only the simplest configuration was simulated (i.e., without the existence of the fracture zone around the horizontal wells or hydrological conduits, similar to Model 1). The results of the ΔCFS, pore-pressure change and poroelastic-stress change are shown in Figure 5.

There are several notable features of the temporal evolution of the ΔCFS and pore pressure calculated for the faults at W2 and W3 (Figure 5). First, the ΔCFS shows a similar monotonic increase when there is a fluid-injection operation, but the amplitude is smaller at W3 (Figure 5b) due to the negative poroelastic-stress change. Second, it is clear that the ΔCFS results calculated with the poroelastic model on the receiver faults at W2 and W3 both have positive values, suggesting that the nearby HF injections could facilitate the faulting process. However, it is acknowledged that the simulated ΔCFS is approximately one order of magnitude smaller than the static stress–triggering threshold of 0.02 MPa (e.g., Stein, 1999). Third, there are simultaneous step-like jumps of the ΔCFS and pore-pressure change in response to the HF operations.

Finally, it should be noted that the ΔCFS at W3 is smaller than at W2, even though the area near W3 is subjected to the effects of injections at both W1 and W2, whereas the W2 area is affected only by injections at W1. The difference can be explained by the relative positions of the three injection sites. Since the orientation of the fault is an important factor controlling the amplitude of ΔCFS (Equation 7), the stress changes caused by injection at W1 and W2, to a large degree, cancel at the receiver fault near W3. On the other hand, the pore-pressure change exhibits similar behaviour at W2 and W3, as it is less sensitive to the directional factor.

Discussion and Implications

Considering the ΔCFS from the three models (Figure 4), the M_w 4.6 earthquake is more likely to have been triggered by the elevated pore pressure associated with the migration of injected fluid through pathways of relatively high permeability, as suggested by Model 3. Although the conduit in Model 3 is an assumption, several factors may hint at its possible existence. First, as the ΔCFS values calculated on the receiver fault in both Models 1 and 2 are negative, the existence of a conduit is probably a necessary condition to flip the sign of ΔCFS (Figure 4). Second, previous studies have suggested that the Dawson Creek graben complex hosts several faults in the Precambrian crystalline basement that developed during the subsidence process (e.g., Berger, 1994). The extended fault system and the associated frac-ture zones can act as pathways of elevated permeability connecting the reservoir and the Precambrian crystalline basement (e.g., Kozlowska et al., 2018).

Fault orientation/geometry represents an important factor in the determination of the ΔCFS (and in the time lag) required to activate a fault (e.g., Lei et al., 2017, 2019). Thus, it is important to investigate how different fault types and strike/dip angles could influence the amplitude of the ΔCFS on the receiver fault of the M_w 4.6 earthquake. Figure 6 shows the maximum ΔCFS for all strike and dip combinations on the reverse-style receiver fault in the context of the three poroelastic models. Although the ΔCFS could vary with fault geometry caused by elastic-stress transfer alone (Figure 6a, b), the amplitudes of the maximum stress perturbation for Models 1 and 2 are negligible compared to that of Model 3 and therefore unlikely to have activated the fault. In contrast, Figure 6c suggests that, if the fluid has migrated to the fault, then the fault could be activated regardless of the orientation of the pre-existing fault (i.e., whether or not it is preferably/optimally oriented). Similarly, Cochran et al. (2020) suggested that the 2011 wastewater disposal–induced sequence in Prague, Oklahoma occurred on both optimally and unfavourably oriented faults. Thus, the estimate depicted in Figure 6 supports the inference that elevated pore pressure through high-permeability pathways, rather than elastic-stress transfer, could be the dominant factor in activating the M_w 4.6 earthquake. The results here suggest that the sole implication of the traditional traffic light protocol (TLP) for induced seismicity that has been adopted by many regulatory agencies may not be enough to assess the potential seismic hazard induced by HF operations (Kao et al., 2018), as the TLP does not consider any potential pre-existing faults or conduit-like pathways.

Given that the ΔCFS values at receiver faults in the vicinity of W2 and W3 are too small to reactivate a shear dislocation (Figure 5), the almost instantaneous seismic response to nearby HF injection suggests that additional factors not included in the poroelastic models should also be considered. First, the models do not include any conduit-like structures, but the possibility that a complex conduit system could exist on a broader scale and may facilitate the fluid-pressure migration process cannot be ruled out. For example, several regional faults, such as the Bonanza fault and the Gordondale fault, have been documented across northeastern BC and northwestern Alberta (e.g., Mossop and Shetsen, 1994). Second, the M_w 4.6 mainshock may have exerted non-negligible effects in combination with fracture openings from nearby HF operations. Third, the difference between the current level of stress on the fault and the required stress level for failure (i.e., the magnitude of stress perturbation required to activate faulting) may play an important role. In the present case, the 5 day delayed seismic response at W1 suggests that the faults at W1 were proba-
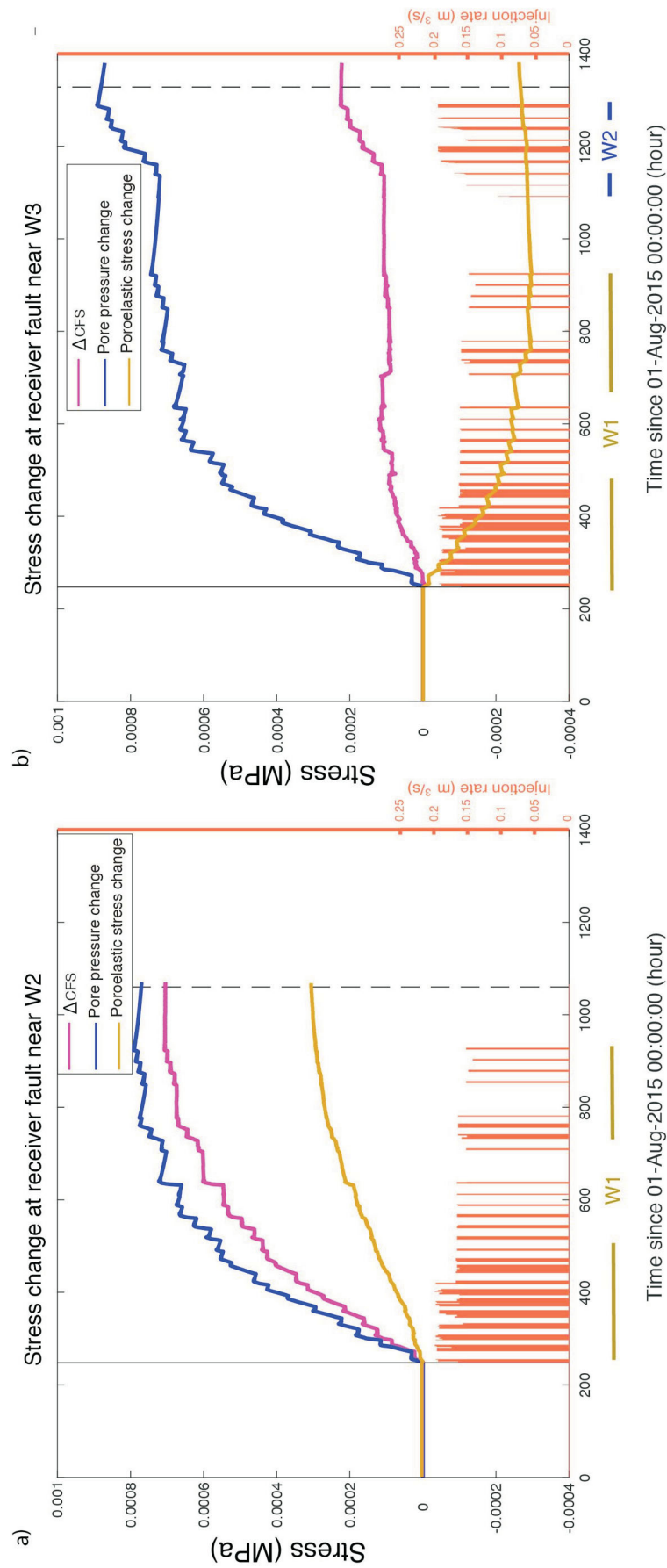
Figure 5. Stress change as a function of time for the receiver faults at injection sites near **a)** well W2, and **b)** well W3. The bottom bars represent the fluid-injection rate and duration for individual HF stages. In each graph, the solid vertical line represents the onset time of HF operations and the dashed vertical line represents the occurrence time of the first earthquakes near the injection wells.
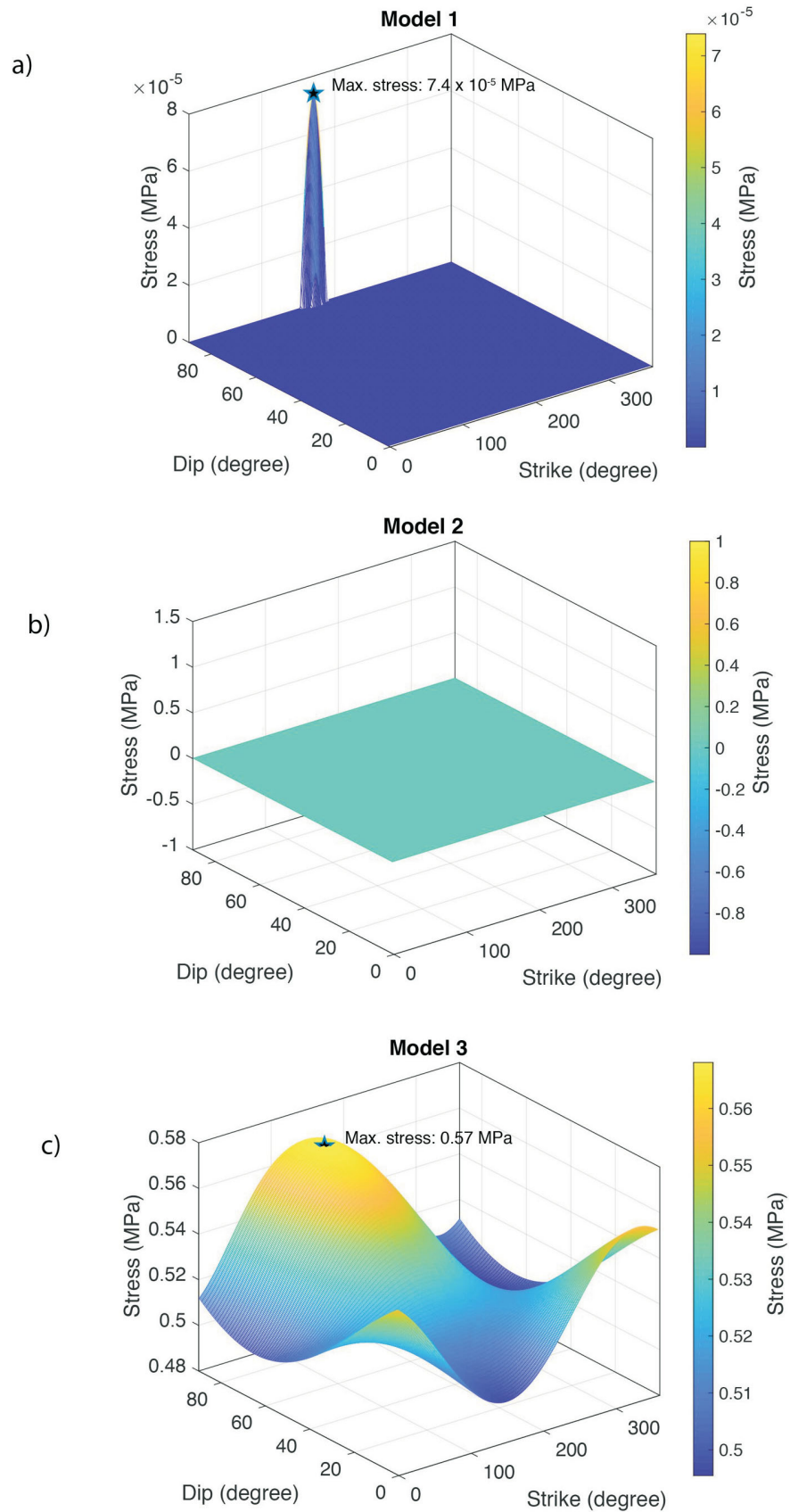
Figure 6. Maximum ∆CFS for a range of strike and dip combinations on the receiver fault during the M_w 4.6 reverse-faulting event: **a)** calculated for Model 1, where only positive ∆CFS is shown here and negative ∆CFS is shown as 0 values; and **b)** and **c)** calculated for Models 2 and 3, respectively.

bly at a relatively lower 'critically stressed' level than the faults at W2 and W3. This contrast, in terms of the value of ΔCFS when the first earthquake was induced at each well pad, became smaller with the increase of conduit permeability assumed in Model 3. Finally, the specific geological settings at W2 and W3, such as the location and orientation of local faults with respect to the HF wells, the spatial heterogeneity of the tectonic stress within such a small region (~10 km) and the permeability of the sedimentary and basement layers, could all have influenced the seismic-response time. Without further details on local structures, their effects are difficult to assess and will therefore not be discussed here.

Conclusion

Coulomb failure criteria were employed to investigate the triggering mechanism of the largest (M_w 4.6) HF-induced earthquake sequence in Canada. Numerical poroelastic simulation was used to calculate the coupled evolution of elastic stress and pore pressure caused by HF-fluid injections on the corresponding receiver faults. For the M_w 4.6 mainshock, three different scenarios were compared: the first scenario simulating the spatiotemporal effect due to HF-injection stages only; the second scenario adding a fracture zone around the HF horizontal wells; and the third scenario further adding a conduit to connect the HF well and the receiver fault.

The results suggest that a conduit-like structure can efficiently facilitate the migration of fluid pressure from the injection well (W1) to the receiver fault and increase the ΔCFS by as much as ~0.5 MPa to destabilize the fault, thus providing the best explanation of the observed 5 day delay since the start of HF injection. The sole elastic-stress perturbation (ΔCFS approx. –0.005 MPa) caused by interactions between the injected fluids and the rock matrix is too small (and negative) to trigger the fault slip, even with full consideration of the fault-orientation effect.

The immediate seismic response at the two nearby HF sites (W2 and W3) was investigated by conducting the same numerical poroelastic simulation to examine the cumulative effects from all HF stimulations. The results suggest that the poroelastic effect from W1 could have altered the local stress field at W2, whereas the poroelastic effect from W1 and W2 could have influenced the local stress field at W3 but the ΔCFS (~0.001 MPa) was not large enough to reach the static stress–triggering threshold (0.02 MPa).

These results have important implications for the energy industry and regulators when establishing effective strategies for mitigating the seismic hazard from induced earthquakes. Detailed mapping of the location and geometry of pre-existing faults in the injection area is necessary and should be required to provide the first-order evaluation of induced seismic risk. Finally, structures with high permeability can be effective conduits for fluid-pressure migration and should therefore be avoided at all stages of HF operations.

References

Aki, K. and Richards, P.G. (2002): Quantitative Seismology; University Science Books, Mill Valley, California, 704 p.

Atkinson, G.M., Eaton, D.W., Ghofrani, H., Walker, D., Cheadle, B., Schultz, R., Shcherbakov, R., Tiampo, K., Gu, J., Harrington, R.M., Liu, Y.J., van der Baan, M. and Kao, H. (2016). Hydraulic fracturing and seismicity in the Western Canada Sedimentary Basin; Seismological Research Letters, v. 87, no. 3, p. 631–647, URL <https://doi.org/10.1785/0220150263>.

Bao, X. and Eaton, D.W. (2016): Fault activation by hydraulic fracturing in western Canada; Science, v. 354, no. 6318, p. 1406–1409, URL <https://doi.org/10.1126/science.aag2583>.

BC Oil and Gas Commission (2012): Investigation of observed seismicity in the Horn River basin; Technical Report, URL <https://www.bcogc.ca/files/reports/Technical-Reports/investigation20of20observed20seismicity20in20the20horn20river20basinaug202012.pdf> [November 2020].

Bell, J. and Grasby, S. (2012): The stress regime of the Western Canadian sedimentary basin; Geofluids, v. 12, no. 2, p. 150–165, URL <https://doi.org/10.1111/j.1468-8123.2011.00349.x>.

Berger, Z. (1994): The Fort St. John Graben, western Canada; in Satellite Hydrocarbon Exploration, Springer, Berlin, Heidelberg, p. 239–248, URL <https://doi.org/10.1007/978-3-642-78587-0_13>.

Cappa, F. (2009): Modelling fluid transfer and slip in a fault zone when integrating heterogeneous hydromechanical characteristics in its internal structure; Geophysical Journal International, v. 178, no. 3, p. 1357–1362, URL <https://doi.org/10.1111/j.1365-246X.2009.04291.x>.

Clauser, C. (1992): Permeability of crystalline rocks; Eos, Transactions American Geophysical Union, v. 73, no. 21, p. 233–238, URL <https://doi.org/10.1029/91EO00190>.

Cochran, E.S., Skoumal, R.J., McPhillips, D., Ross, Z.E. and Keranen, K.M. (2020): Activation of optimally and unfavourably oriented faults in a uniform local stress field during the 2011 Prague, Oklahoma, sequence; Geophysical Journal International, v. 222, no. 1, p. 153–168, URL <https://doi.org/10.1093/gji/ggaa153>.

Cui, X. and Nassichuk, B. (2018): Permeability of the Montney Formation in the Western Canada Sedimentary Basin: insights from different laboratory measurements; Bulletin of Canadian Petroleum Geology, v. 66, no. 2, p. 394–424.

Davies, G.R., Moslow, T.F. and Sherwin, M.D. (1997): The Lower Triassic Montney Formation, west-central Alberta; Bulletin of Canadian Petroleum Geology, v. 45, no. 4, p. 474–505.

Deng, K., Liu, Y. and Harrington, R.M. (2016): Poroelastic stress triggering of the December 2013 Crooked Lake, Alberta induced seismicity sequence; Geophysical Research Letters, v. 43, p. 8482–8491, URL <https://doi.org/10.1002/2016-GL070421>.

Detournay, E. and Cheng, A.H.-D. (1993): Fundamentals of poroelasticity; Chapter 5 in Analysis and Design Methods: Principles, Practice and Projects, Elsevier, p. 113–171, URL <https://doi.org/10.1016/B978-0-08-040615-2.50011-3>.

Dong, T., Harris, N.B., Ayranci, K., Twemlow, C.E. and Nassichuk, B.R. (2017): The impact of composition on pore throat size and permeability in high maturity shales: Middle and Upper Devonian Horn River Group, northeastern British Columbia, Canada; Marine and Petroleum Geology, v. 81, p. 220–236, URL <https://doi.org/10.1016/j.marpetgeo.2017.01.011>.

Ellsworth, W.L. (2013): Injection-induced earthquakes; Science, v. 341, no. 6142, art. 1225942, URL <https://doi.org/10.1126/science.1225942>.

Farrell, N., Healy, D. and Taylor, C. (2014): Anisotropy of permeability in faulted porous sandstones; Journal of Structural Geology, v. 63, p. 50–67, URL <https://doi.org/10.1016/j.jsg.2014.02.008>.

Goebel, T., Weingarten, M., Chen, X., Haffener, J. and Brodsky, E. (2017): The 2016 M_w 5.1 Fairview, Oklahoma earthquakes: evidence for long-range poroelastic triggering at >40 km from fluid disposal wells; Earth and Planetary Science Letters, v. 472, p. 50–61, URL <https://doi.org/10.1016/j.epsl.2017.05.011>.

Kao, H., Shan, S.-J., Bent, A., Woodgold, C., Rogers, G., Cassidy, J.F. and Ristau, J. (2012): Regional centroid-moment-tensor analysis for earthquakes in Canada and adjacent regions: an update; Seismological Research Letters, v. 83, no. 3, p. 505–515, URL <https://doi.org/10.1785/gssrl.83.3.505>.

Kao, H., Visser, R., Smith, B. and Venables, S. (2018): Performance assessment of the induced seismicity traffic light protocol for northeastern British Columbia and western Alberta; The Leading Edge, v. 37, no. (2, p. 117–126, URL <https://doi.org/10.1190/tle37020117.1>.

Keranen, K., Weingarten, M., Abers, G., Bekins, B. and Ge, S. (2014): Sharp increase in central Oklahoma seismicity since 2008 induced by massive wastewater injection; Science, v. 345, no. 6195, p. 448–451, URL <https://doi.org/10.1126/science.1255802>.

Kozlowska, M., Brudzinski, M.R., Friberg, P., Skoumal, R.J., Baxter, N.D. and Currie, B.S. (2018): Maturity of nearby faults influences seismic hazard from hydraulic fracturing; Proceedings of the National Academy of Sciences of the United States of America, v. 115, no. 8, p. E1720–1729, URL <https://doi.org/10.1073/pnas.1715284115>.

Laske, G., Masters, G., Ma, Z. and Pasyanos, M. (2013): Update on CRUST 1.0 – A 1-degree global model of Earth's crust; Geophysical Research Abstracts, v. 15, Abstract EGU2013-2658, URL <https://meetingorganizer.copernicus.org/EGU2013/EGU2013-2658.pdf> [November 2020].

Leake, S. and Hsieh, P.A. (1995): Simulation of deformation of sediments from decline of ground-water levels in an aquifer underlain by a bedrock step; in U.S. Geological Survey Subsidence Interest Group Conference, Proceedings of the Technical Meeting, Las Vegas, Nevada, February 14–16, 1995, United States Geological Survey, Open File Report 97-47, p. 10-14, URL <https://pubs.usgs.gov/of/1997/ofr97-047/pdf/OFR97-47.pdf#page=15> [November 2020].

Lei, X., Huang, D., Su, J., Jiang, G., Wang, X., Wang, H., Guo, X. and Fu, H. (2017): Fault reactivation and earthquakes with magnitudes of up to Mw4.7 induced by shale-gas hydraulic fracturing in Sichuan Basin, China; Scientific Reports, v. 7, no. 1, p. 1–12, URL <https://doi.org/10.1038/s41598-017-08557-y>.

Lei, X., Wang, Z. and Su, J. (2019): The December 2018 ML 5.7 and January 2019 ML 5.3 earthquakes in south Sichuan basin induced by shale gas hydraulic fracturing; Seismological Research Letters, v. 90, no. 3, p. 1099–1110, URL <https://doi.org/10.1785/0220190029>.

Madariaga, R. (1977): Implications of stress-drop models of earthquakes for the inversion of stress drop from seismic observations; chapter in Stress in the Earth, M. Wyss (ed.) Birkhäuser, Basel, Switzerland, Contributions to Current Research in Geophysics (CCRG), p. 301–316, URL <https://doi.org/10.1007/978-3-0348-5745-1_19>.

Mahani, A.B., Schultz, R., Kao, H., Walker, D., Johnson, J. and Salas, C. (2017): Fluid injection and seismic activity in the northern Montney play, British Columbia, Canada, with special reference to the 17 August 2015 M_w 4.6 induced earthquake; Bulletin of the Seismological Society of America, v. 107, no. 2, p. 542–552, URL <https://doi.org/10.1785/0120160175>.

Mossop, G.D. and Shetsen, I. (1994): Geological Atlas of the Western Canada Sedimentary Basin; Canadian Society of Petroleum Geologists, Calgary, Alberta and Alberta Research Council, Edmonton, Alberta, 510 p.

Neuzil, C. (1994): How permeable are clays and shales? Water Resources Research, v. 30, no. 2, p. 145–150, URL <https://agupubs.onlinelibrary.wiley.com/doi/abs/10.1029/93WR02930> [November 2020].

Peña Castro, A.F., Roth, M.P., Verdecchia, A., Onwuemeka, J., Liu, Y., Harrington, R.M., Zhang, Y. and Kao, H. (2020): Stress chatter via fluid flow and fault slip in a hydraulic fracturing-induced earthquake sequence in the Montney Formation, British Columbia; Geophysical Research Letters, v. 47, no. 14, URL <https://doi.org/10.1029/2020GL087254>.

Rice, J.R. and Cleary, M.P. (1976): Some basic stress diffusion solutions for fluid-saturated elastic porous media with compressible constituents; Reviews of Geophysics, v. 14, no. 2, p. 227–241, URL <https://doi.org/10.1029/RG014i002p-00227>.

Rokosh, C.D., Anderson, S.D., Beaton, A.P., Berhane, M. and Pawlowicz, J. (2010): Geochemical and geological charac-

terization of the Duvernay and Muskwa Formation in Alberta; paper presented at the Canadian Unconventional Resources and International Petroleum Conference, abstract, URL <https://www.onepetro.org/conference-paper/SPE-137799-MS> [November 2020].

Rokosh, C., Pawlowicz, J., Berhane, H., Anderson, S. and Beaton, A. (2008): Geochemical and sedimentological investigation of Banff and Exshaw Formations for shale gas potential: initial results; Energy Resources Conservation Board, ERCB/AGS Open File Report 2008-10, 46 p., URL <https://ags.aer.ca/publication/ofr-2008-10> [November 2020].

Roth, M.P., Verdecchia, A., Harrington, R.M. and Liu, Y. (2020): High-resolution imaging of hydraulic-fracturing-induced earthquake clusters in the Dawson-Septimus area, northeast British Columbia, Canada; Seismological Research Letters, v. 91, no. 5, URL <https://doi.org/10.1785/0220200086>.

Schultz, R., Atkinson, G., Eaton, D., Gu, Y. and Kao, H. (2018): Hydraulic fracturing volume is associated with induced earthquake productivity in the Duvernay play; Science, v. 359, no. 6373, p. 304–308, URL <https://doi.org/10.1126/science.aao0159>.

Segall, P. and Lu, S. (2015): Injection-induced seismicity: poroelastic and earthquake nucleation effects; Journal of Geophysical Research: Solid Earth, v. 120, no. 7, p. 5082–5103, URL <https://doi.org/10.1002/2015JB012060>.

Shapiro, S. and Dinske, C. (2009): Fluid-induced seismicity: pressure diffusion and hydraulic fracturing; Geophysical Prospecting, v. 57, no. 2, p. 301–310, URL <https://doi.org/10.1111/j.1365-2478.2008.00770.x>.

Stein, R.S. (1999): The role of stress transfer in earthquake occurrence; Nature, v. 402, no. 6762, p. 605–609, URL <https://doi.org/10.1038/45144>.

Vishkai, M., Wang, J., Wong, R.C., Clarkson, C.R. and Gates, I.D. (2017): Modeling geomechanical properties in the Montney Formation, Alberta, Canada; International Journal of Rock Mechanics and Mining Sciences, v. 96, p. 94–105, URL <https://doi.org/10.1016/j.ijrmms.2017.04.001>.

Wang, B., Harrington, R.M. Liu, Y., Kao, H. and Yu, H. (2020): A study on the largest hydraulic-fracturing-induced earthquake in Canada: observations and static stress-drop estimation; Bulletin of the Seismological Society of America, v. 110, no. 5, p. 2283–2294, URL <https://doi.org/10.1785/0120190261>.

Wang, R. and Kümpel, H.-J. (2003): Poroelasticity: efficient modeling of strongly coupled, slow deformation processes in a multilayered half-space; Geophysics, v. 68, no. 2, p. 705–717, URL <https://doi.org/10.1190/1.1567241>.

Xu, C., Wang, J., Li, Z. and Drummond, J. (2010): Applying the Coulomb failure function with an optimally oriented plane to the 2008 M_w 7.9 Wenchuan earthquake triggering; Tectonophysics, v. 491, no. 1–4, p. 119–126, URL <https://doi.org/10.1016/j.tecto.2009.09.019>.

Yehya, A., Yang, Z. and Rice, J.R. (2018): Effect of fault architecture and permeability evolution on response to fluid injection; Journal of Geophysical Research: Solid Earth, v. 123, no. 11, p. 9982–9997, URL <https://doi.org/10.1029/2018JB016550>.

Yu, H., Harrington, R.M., Liu, Y. and Wang, B (2019): Induced seismicity driven by fluid diffusion revealed by a near-field hydraulic stimulation monitoring array in the Montney Basin, British Columbia; Journal of Geophysical Research: Solid Earth, v. 124, no. 5, URL <https://doi.org/10.1029/2018jb017039>.

Zhu, L. and Rivera, L.A. (2002): A note on the dynamic and static displacements from a point source in multilayered media; Geophysical Journal International, v. 148, no. 3, p. 619–627, URL <https://doi.org/10.1046/j.1365-246X.2002.01-610.x>.

Machine-Learning Analysis of Factors Influencing Induced Seismicity Susceptibility in the Montney Play Area, Northeastern British Columbia (NTS 093P, 094A, B, G, H)

A. Amini, Department of Earth, Ocean and Atmospheric Sciences, The University of British Columbia, Vancouver, British Columbia, aamini@eoas.ubc.ca

E. Eberhardt, Department of Earth, Ocean and Atmospheric Sciences, The University of British Columbia, Vancouver, British Columbia

Introduction

Unconventional gas resources represent an emerging low-cost, clean-burning energy source, the export of which presents both a greener transition option to replace more carbon-intensive fossil fuels like coal and a key economic opportunity for British Columbia (BC) and Canada. In northeastern BC, new discoveries and advancements in extraction technologies have led to resource estimates of 94.5 trillion m^3 (3337 tcf) of gas-in-place (BC Oil and Gas Commission, 2018), enough to support development and export operations for more than 150 years. However, with the development of these new resources comes new challenges. Amongst these are public, First Nations and regulator concerns regarding induced seismicity associated with hydraulic fracturing and wastewater injection operations. Both activities involve the injection of large volumes of fluids into deep geological formations, which serve to create localized increases in pore pressures and stress changes acting on critically stressed faults, resulting in fault slip and induced seismicity. Notable induced events in northeastern BC include one magnitude (M) 4.4 and two M 4.6 events between 2014 and 2018.

In response to these events, and other environmental concerns, the BC government appointed a scientific panel to review hydraulic fracturing practices and their impacts (Scientific Hydraulic Fracturing Review Panel, 2019). In their review, a key knowledge gap was identified in relation to induced seismicity susceptibility. In particular, the effects of different geological and operational factors on the spatial and temporal distribution of events are not well understood and vary in importance for different unconventional gas plays. Although separating geological from operational factors is a complex task, it is also recognized that a massive amount of geological, operational and seismic data are be-

ing collected from hydraulic fracturing activities for which robust analysis methods are needed. The rapid development of multivariate statistical and machine-learning techniques to analyze large datasets makes the application of these techniques to this problem especially attractive and conducive, although there is not a lot of experience yet in applying these to induced seismicity hazard assessments (i.e., likelihood, severity, etc.), especially in analyzing both operational and geological parameters together. Distinguishing between these factors is of interest as the influence of geological factors on induced seismicity susceptibility for a given formation being targeted cannot be controlled or manipulated (outside of avoidance), whereas many operational factors (i.e., well completion related) can be controlled to some extent offering a means to potentially mitigate induced seismicity hazards for a susceptible formation.

Presented in this paper are the preliminary results of research (Geoscience BC project 2019-014) investigating the development of induced seismicity susceptibility maps to aid decision makers with their planning of hydraulic fracturing activities and managing of induced seismicity hazard. To accomplish this, machine-learning techniques will be integrated with mechanistic validation using controlled laboratory experiments and three-dimensional (3-D) numerical modelling (to account for cause and effect relationships). The results presented here are from the first phase of this work, the application of different machine-learning algorithms to determine the relative importance of several geological and operational parameters (termed feature importance) in relation to the triggering of induced seismicity. This is done for data compiled for the Montney Formation in northeastern BC. The algorithms applied and compared include the decision-tree, random-forest and gradient-boost methods. In addition to testing the robustness of these algorithms through a comparative analysis, guidance is provided in the use of machine learning to identify influencing factors as a step toward developing induced seismicity susceptibility maps.

Background

A significant increase in the seismicity rate in western Canada in recent years has been associated with the development of unconventional oil and gas resources, including the related activities of hydraulic fracturing (Bao and Eaton, 2016) and wastewater disposal (Schultz et al., 2014). There are numerous operators conducting these activities, each using different operational parameters (e.g., fluid injection volumes and rates) tailored for the local geological setting and targeted formation, as well as further shaped by in-house objectives, experiences and optimization efforts. This raises the question of what are the cause and effect relationships of these parameters on induced seismicity susceptibility and magnitude distribution? The question of susceptibility addresses the likelihood that a particular well will generate induced seismicity; this can be viewed as a classification problem (seismogenic or not seismogenic). The question of magnitude distribution addresses the potential severity.

With respect to operational parameters, it has been argued that the moment release attributable to induced earthquakes is related to the net volume of the injected fluid, with empirical trends established that link an upper limit for the moment magnitude to injection volume (Hallo et al., 2014; McGarr, 2014). The data analyzed in these studies included a mix of hydraulic fracturing and wastewater disposal activities in sedimentary rocks and enhanced geothermal-development activities in crystalline rocks, combining data from Europe, the United States and Australia. Weingarten et al. (2015) carried out a similar study combining information on injection wells from public databases with available earthquake catalogues and concluded that injection rate is the most important operational parameter affecting induced seismicity. Their study focused on data from hydraulic fracturing and wastewater disposal activities in the eastern and central United States. For the Western Canada Sedimentary Basin (WCSB), where the Montney Formation is situated, different studies have shown that injection volume is associated with induced seismicity (Schultz et al., 2014; Babaie Mahani et al., 2017). Schultz et al. (2018) investigated the relationship between injection parameters and induced seismicity in the Duvernay shale play in Alberta and concluded that events are associated with completions that used larger injection volumes and that seismic productivity scales linearly with injection volume. Their analysis further showed that the wellhead injection pressure and rate have an insignificant association with seismic response, and that geological factors account for the variability in induced seismicity susceptibility observed in the region.

With respect to geological parameters, Göbel (2015) compared several fluid injection operations in California and Oklahoma and examined the temporal and spatial variations in their induced seismicity responses. His results suggest that operational parameters for fluid injection are likely of secondary importance and that the primary controls on seismicity induced by injection are the site-specific geology and geological setting. Van der Baan and Calixto (2017) compared current and historic seismicity rates in six states in the United States and three Canadian provinces to past and present oil and gas production. Their study showed that in addition to injection volumes, local- and regional-scale geology and tectonics influenced earthquake hazard susceptibility. Amini and Eberhardt (2019) similarly compared induced seismicity and well data for several key North American unconventional gas plays, with a focus on magnitude distribution relative to differences in the tectonic in situ stress regime. They found that stress regime has a significant influence on event magnitude with a thrust fault stress regime, as exists in parts of the Montney play area, being more susceptible to large magnitude events compared to a strike-slip or normal fault stress regime.

In Oklahoma, Shah and Keller (2017) combined geophysical and drillhole data to map subsurface geological features in the Precambrian crystalline basement and found that most induced seismicity events are located where the crystalline basement is likely composed of fractured intrusive or metamorphic rock; areas of extrusive rock or thick sedimentary cover (>4 km) exhibited little induced seismicity. They concluded that the differences in seismicity may be due to variations in permeability structure; within intrusive rocks, fluids can become narrowly focused in fractures and faults, causing a concentrated increase in local pore fluid pressures, whereas more distributed pore space in sedimentary and extrusive rocks may relax pore fluid pressures. Hincks et al. (2018) developed an advanced Bayesian network to model joint conditional dependencies between spatial, operational and seismicity parameters in Oklahoma. They found that injection depth relative to crystalline basement most strongly correlates with seismic moment release and that the combined effects of depth and volume are critical, as injection rate becomes more influential near the basement interface. Similar findings were reported by Skoumal et al. (2015) and Currie et al. (2018) for hydraulic fracturing operations in Ohio. The latter showed that seismicity occurred along faults below the injection interval in the crystalline basement. From seismic reflection lines, they showed that these fault systems intersected the injection interval targeted by the well, providing permeability pathways for fluid pressure increases leading to fault slip.

Specific to the geology of the WCSB, Schultz et al. (2016) found that hypocentres of induced seismicity clusters in Alberta coincided with the margins of the Devonian carbonate reefs and interpreted this spatial correspondence as the result of geographically biased activation potential, possibly as a consequence of reef nucleation preference to paleo-bathymetric highs associated with Precambrian basement

tectonics. Their work provided evidence that in some areas Paleozoic and Precambrian strata are likely to be in hydraulic communication, which points to the important role of regional- and local-scale geological factors in the nature of induced seismicity. Eaton and Schultz (2018) also suggested natural processes involving the transformation of organic material (kerogen) into hydrocarbons and cracking to produce gas can cause fluid overpressures resulting in an increased susceptibility to induced seismicity. They presented two examples from the WCSB where induced seismicity attributed to hydraulic fracturing is strongly clustered within areas characterized by high pore-pressure gradients.

The above examples highlight the importance of different operational and geological factors on induced seismicity, but do so from the perspective of studying the influence of a single factor. It is unlikely, however, that a single causative factor is solely responsible for an induced seismicity event. Instead, multiple factors can play an influencing role. Therefore, it is important to consider and understand the cause and effect relationships of different operational and geological factors on the spatial and temporal distribution of induced seismicity events. However, this is not a simple task and requires probing a wide variety of linear and non-linear associations and interaction terms between factors affecting induced seismicity without assuming a priori knowledge on the nature of the relationships between these factors.

The use of machine learning and data analytics are quickly evolving as a means to identifying hidden patterns and extracting information from large datasets. In the geosciences and rock engineering, they have been applied to predicting rockburst potential in deep mines (Ribeiro e Sousa et al., 2017; Pu et al., 2018) and squeezing behaviour in deep tunnels (Sun et al., 2018), as well as developing geological maps using remote sensing data (Cracknell and Reading, 2014) and analyzing data from rock testing (Millar and Clarici, 1994) and blasting (Liu and Liu, 2017). In the context of earthquake seismology, machine learning has been applied to a variety of problems such as laboratory earthquake identification (Rouet-Leduc et al., 2017) and forecasting (Panakkat and Adeli, 2009). Building on these studies, it is recognized that a massive amount of geological, operational and seismic data are being collected with hydraulic fracturing activities, and the size and complexity of these datasets have made traditional empirical and statistical analyses inefficient and ineffective. This has led to recent studies by Pawley et al. (2018) who combined tectonic, geomechanical and hydrological data with induced seismicity data, related to hydraulic fracturing operations in the Duvernay play in Alberta, to train a logistic regression algorithm to map and develop an induced seismicity potential map. Their results suggest that the proximity to basement, formation overpressure, minimum horizontal

stress, proximity to reef margins, lithium concentrations and natural seismicity rate are the dominant contributing factors/indicators to triggering induced seismicity within the study area. Zhang et al. (2020) used machine learning on real-time induced seismicity data to locate small events in Oklahoma by accessing seismic waveform data from a regional network. They designed a fully convolutional network (FCN), to predict a 3-D image of the earthquake location probability from a volume of input data recorded at multiple network stations. Their results showed that the designed system is capable of locating small events of local magnitude (M_L) ≥2.0 with a mean epicentre error of 4 to 6 km.

Data Compilation and Preparation

A database of 16 945 hydraulic fracturing stages from 1244 horizontal wells within the Montney Formation (from 2014 till end of 2016) was compiled and analyzed using multiple sources that reported well activities in northeastern BC (BC Oil and Gas Commission, 2018; geoLOGIC systems ltd., 2019). This was combined with a second database that included a comprehensive earthquake catalogue compiled for northeastern BC and western Alberta (Visser et al., 2017). This was produced specifically to study induced seismicity in this region and consists of 4916 events for the period of January 2014 to December 2016 with a magnitude of completeness (M_L) of 1.8.

To prepare the data for analysis using a supervised machine-learning algorithm (as discussed in the next section), it was necessary to determine the output labels. Here, induced seismicity was considered as a binary-classification problem with respect to the observed seismic activity. Wells were classified as being either 'aseismic' or 'seismic' based on spatial and temporal correlations with hydraulic fracturing operations. This was done by cross-correlating the earthquake catalogue with the well database and applying a series of spatial and temporal filters to identify the subset of earthquake events that are likely induced seismicity events related to hydraulic fracturing. The first step was to clip the data to only include earthquakes located within the boundaries of the Montney play area in northeastern BC and to filter out events spatially associated with anthropogenic activities that are not related to oil and gas activities, such as those from mining and construction (e.g., blasting). This step reduced the total number of events being considered from 4916 to 2867. Next, a spatial filter was applied to search for all event locations that were within a 5 km radius of an active hydraulic fracturing well. The 5 km radius represents the uncertainty in the event location accuracy reported for the earthquake catalogue. To this, a three-month temporal filter was applied (see Atkinson et al., 2016). Thus, if the epicentre of an earthquake event was recorded as occurring within 5 km from the surface location of an active well and within three months from the start date of the

hydraulic fracturing activity, it was considered here to be an induced seismicity event and the corresponding well was classified as being seismogenic. This resulted in a subset of 543 events identified as induced seismicity events.

The input parameters for the machine-learning analysis, referred to herein as features (using the term common to machine learning), were selected from available geological and operational data for the Montney Formation. For the geological features such as distance to basement, if data was not available for a given well, values were interpolated using the average of the three closest wells. The operational features were treated differently as only wells that had complete data throughout all features were included. This resulted in data for 11 415 stages out of 16 945 being used for the machine-learning analysis. The input features are described in Table 1.

The interpolated pore-pressure gradients ranged from 5.4 to approximately 18 kilopascals per metre (kPa/m). In addition to the reservoir pore pressure, information regarding the maximum horizontal stress (S_{Hmax}) direction was included. This was calculated for each well based on S_{Hmax} azimuths extracted from the World Stress Map database (Heidbach et al., 2018) and interpolated for each well. Two different values were investigated: 1) the difference between the local S_{Hmax} and the horizontal well azimuths; and 2) the difference between the local and regional S_{Hmax} azimuths, where N45°E was assumed to be the regional S_{Hmax} direction in the Montney play area. Injection depth (total vertical depth [TVD]) was also considered as a proxy for the magnitude of stresses in this region. Specific to the local geology, the vertical distance between the injection depth and the top of the Montney and Debolt formations were considered, together with the distance to the Precambrian crystalline basement. For these, a negative value indicates an injection depth above the formation top/basement and a positive value refers to below the formation top. It should be noted that there is a high degree of uncertainty in the interpolated values for the top of the basement due to a lack of direct borehole measurements (from vertical wells). Lastly, the two-dimensional (2-D) distance from the well to the closest mapped fault (Hayes et al., 2021) was included. This was taken as the shortest horizontal distance between the wellhead and closest fault. In this analysis, no cutoff value for distance to fault was considered.

Machine-Learning Algorithm Development

Machine learning can be undertaken using supervised or unsupervised algorithms. Supervised learning is where the input features and an output result are given, and an algorithm is used to learn the mapping function between these. The goal is to approximate the mapping function so well that for any new input data, the output can be predicted for that specific data. This contrasts with unsupervised learn-

ing where only the input data is known, and no corresponding output variables are given. The goal for unsupervised learning is to model the underlying structure or distribution in the data in order to learn more about the data. For this study, supervised learning was used for the initial data analysis to identify which wells were associated with induced seismicity and which were not. These represent the correct answers to the classification problem for training the mapping function; the corresponding data associated with each set of wells is referred to as the training data.

Three different supervised machine-learning algorithms were used that are generally considered to be robust for classification problems: decision tree, random forest and gradient boost (Hastie et al., 2017). These methods were chosen because of the ease of interpretability of their results and also because they are not sensitive to the scale of input data. The objective of the algorithm is to iteratively make predictions on the training data and to correct these until the algorithm achieves an acceptable level of performance.

Decision trees are a nonparametric supervised learning method used for classification and regression. The goal is to create a model that predicts the value of a target variable by learning simple decision rules inferred from the data features. Decision trees have two advantages: the resulting model can easily be visualized and understood by non-experts, and the algorithms are completely invariant to scaling of the data. As each feature is processed separately, and the possible splits of the data do not depend on scaling, no preprocessing of features is needed for decision-tree algorithms. The main limitation of decision trees is that they tend to over fit the data and provide poor generalization performance.

A random forest is essentially a collection of decision trees, where each tree is slightly different from the others. In a random forest each tree might do a relatively good job of predicting but will likely over fit part of the data. To reduce the amount of overfitting, many trees are built, all of which work well and over fit the data in different ways, and the results are averaged.

The gradient-boost regression tree is another ensemble method that combines multiple decision trees to create a more powerful model. This can be used for both regression and classification. In contrast to the random-forest approach, gradient boosting works by building trees in a serial manner, where each tree tries to correct the mistakes of the previous one. The main idea is to combine many simple models (known as weak learners) that can provide good predictions on parts of the data, and so more and more trees are added to iteratively improve performance.

All three machine-learning models were built using scikit-learn, a Python library for machine learning (Pedregosa et al., 2011). The data was divided into training and validation

Table 1. Input features used for machine-learning analysis of induced seismicity in the Montney play area, northeastern British Columbia.

Feature category	Feature name (units)	Abbreviation	Source	Number of available data points	Lower limit	Upper limit	Median
Geological	Pore-pressure gradient (kPa/m)	PP_grad	BC Oil and Gas Commission (2018)	2252	5	18	12
Geological	Local and regional S_{Hmax} azimuth difference (deg)	Az_diff_L_R	Heidbach et al. (2018)	601	0	12	5
Geological	Distance from injection depth to top of Montney Fm. (m)	D_Mont	BC Oil and Gas Commission (2018), geoLOGIC Systems ltd. (2019)	8232	-100	420	78
Geological	Distance from injection depth to top of Debolt Fm. (m)	D_Deb	BC Oil and Gas Commission (2018), geoLOGIC Systems ltd. (2019)	2183	-478	9	-247
Geological	Distance from injection depth to basement (m)	D_Base	BC Oil and Gas Commission (2018), geoLOGIC Systems ltd. (2019)	28	-2450	-130	-1660
Geological	Distance from wellhead to faults (m)	Dist_F	Hayes et al. (2021)	16945	2	70400	1770
Operational	Local S_{Hmax} and horizontal well azimuth difference (deg)	Az_diff_L_W	BC Oil and Gas Commission (2018), geoLOGIC Systems ltd. (2019)	16945	0	88	42
Operational	Injection depth (m)	Inj. Depth	geoLOGIC Systems ltd. (2019)	16945	1312	3416	2052
Operational	Well completion length (m)	Comp_Len	geoLOGIC Systems ltd. (2019)	16945	90	3830	1610
Operational	Maximum injection pressure (MPa)	Max_P	geoLOGIC Systems ltd. (2019)	13889	4	99	56
Operational	Average injection rate (m^3/min)	Rate	geoLOGIC Systems ltd. (2019)	15472	1	22	8
Operational	Stage injection volume (m^3)	Volume	geoLOGIC Systems ltd. (2019)	16603	1	5640	592

Abbreviations: kPa, kilopascal; Mpa, megapascal; S_{Hmax}, maximum horizontal stress

sets accounting for 75% and 25% of the full dataset, respectively. The training dataset was further divided into training and test sets, which were used to train the algorithm using 50-fold cross validations, with the training set accounting for 98% of the training dataset and the test set for 2% at each cross-validation run.

The training data was used to train and evaluate the optimum tree depths of the three algorithms using 50-fold cross validations. Figure 1 shows the results of 50-fold cross validations for each algorithm. At each run, the accuracy of the model for a specific tree depth is calculated. In these figures the orange line represents the accuracy of the training set. The blue line shows the mean cross-validation accuracy and the shaded area represents the confidence interval (±2 standard deviations) for the calculated means. For these plots, an accuracy of 1 represents 100% accuracy. This determines if the training set is over fitted, and alongside this, it determines the optimal tree depth based on the confidence interval. Based on the cross-validation results, the tree depths of 16, 12 and 8 were chosen for the decision-tree, random-forest and gradient-boost algorithms, respectively.

Machine-Learning Results

Feature Importance

The results of the cross validations using each algorithm were further analyzed to investigate the importance of each feature on the classification outcome. Figure 2 shows the feature importance calculated using each of the three classification algorithms. The bars are colour coded to differenti-
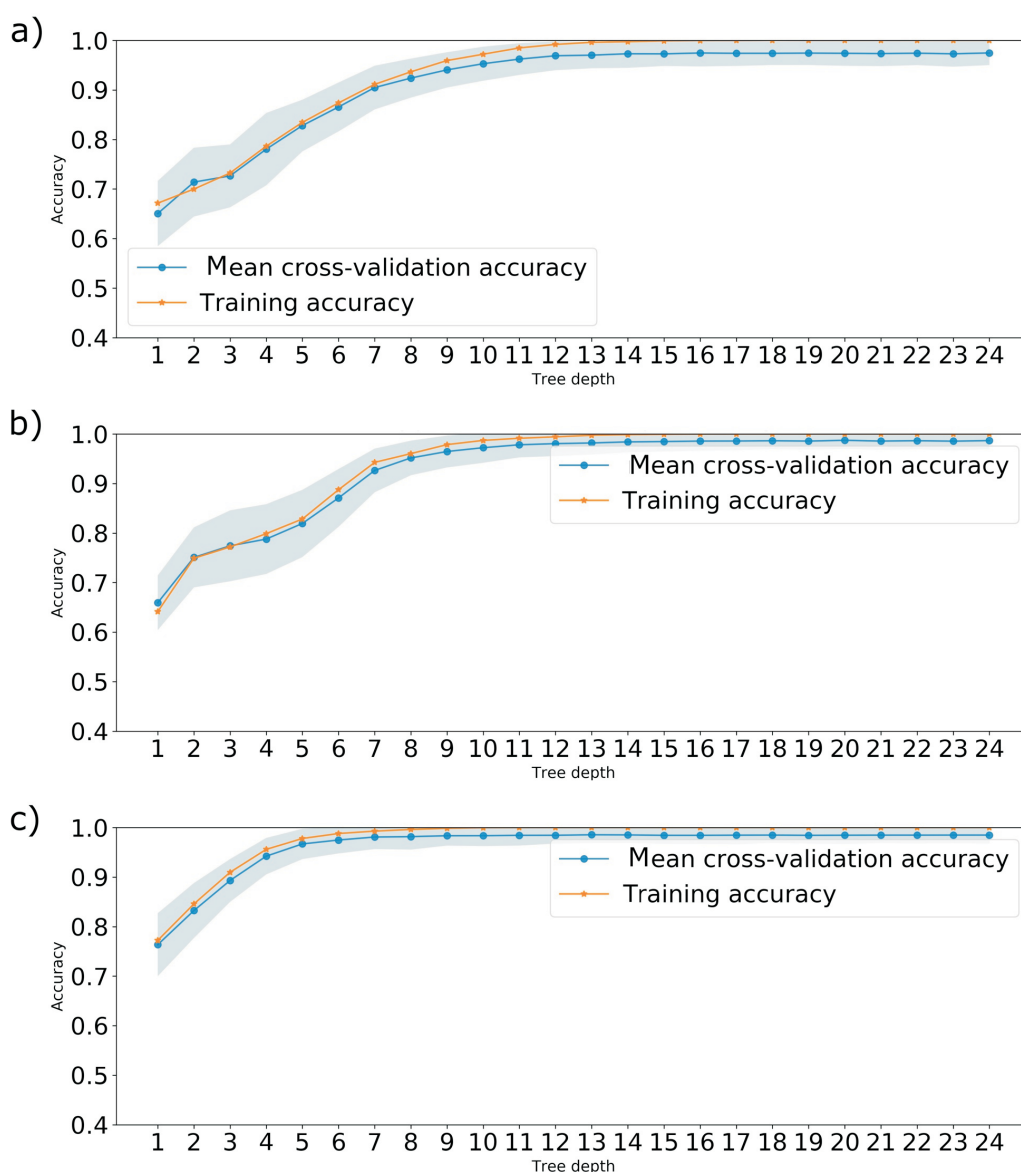
Figure 1. Results of the 50-fold cross validations to determine the optimum tree depth for each algorithm: **a)** decision tree, **b)** random forest and **c)** gradient boost. An accuracy of 1 represents 100% accuracy.

a)

b)

c)

ate features that relate to the geology from those that are operational. The importance of each feature is indicated as a coefficient; these coefficients do not have a physical meaning and are compared based on the relative values and not the absolute values.

Based on the results from the decision-tree analysis, the high importance features were determined to be pore-pressure gradient, distance to basement, well completion length, azimuth difference between the local and regional S_{Hmax} orientation and distance to faults. Four of these five features also form the top five ranked features from the random-forest analysis, although in a slightly different order and with injection depth replacing azimuth difference between the local and regional S_{Hmax} as being of higher importance. For the gradient-boost analysis, again four of these features were ranked in the top five, the exception being that this model showed a higher sensitivity to the horizontal well direction than the completion length. The gradient-boost model also showed very high sensitivity to azimuth difference between the local and regional S_{Hmax} and azimuth difference between local S_{Hmax} and horizontal well direction compared to other features.

Overall, the features consistently ranked as being highly influential by all three machine-learning algorithms were pore-pressure gradient, distance to faults and distance to basement. In all models the same groupings of operational features were observed; injection rate and maximum injection pressure were ranked lowest in importance, and injection volume ranked in the middle. This is an interesting result because injection rate and volume are often cited as operational features that have a significant influence on induced seismicity (McGarr, 2014; Schultz et al., 2018). This appears to hold partly true in the case of injection volume, but operational features such as well completion length and injection depth, which have not been thoroughly studied, appear to have a stronger correlation with induced seismicity.

Model Validation

To validate the trained algorithms, they were next applied to the test data that was set aside to evaluate each model's performance. The test data comprised 25% of the full dataset and was not previously used to train the algorithms. To evaluate the performance of each algorithm, a confusion matrix was calculated. Also known as an error matrix, the confusion matrix allows visualization of the performance of a supervised machine-learning algorithm by reporting the number of true and false positives and true and false negatives. These are based on predictions using the test data relative to the mapping functions determined from the training data. In this case, a true positive would be a correct prediction that a well is associated with induced seismicity and a true negative would be a correct prediction that the well is not. Similarly, a false positive would be the incorrect prediction of a well being associated with induced seismicity where there was none, and a false negative would be an incorrect prediction of a well not being associated with induced seismicity when it was.

The results from calculating a confusion matrix for each algorithm are shown in Figure 3. Comparing these, the random-forest and gradient-boost classifiers performed slightly better than the decision-tree classifier. However, all three models performed with a very high accuracy (97–98%).

To further interpret the results, a SHapley Additive exPlanations (SHAP) analysis was run. The SHAP is a game theory approach used to help interpret predictions from complex models, for example the output from machine-learning models. The SHAP assigns each feature an importance value for a particular prediction and shows there is a unique solution for each class of additive feature importance that adheres to desirable properties (Lundberg and Lee, 2017). The SHAP TreeExplainer tool is a subcategory of SHAP that is specifically built for interpreting tree models, such as decision trees and random forests. The SHAP value plot can show the positive and negative relationships of the predictors with the target variable. The analysis presented here is for the random-forest model as it performed slightly better than the decision-tree model.

Figure 4 presents the summary plot from the SHAP analysis, which combines feature importance with feature impact. Based on this plot, the following information can be gained. First, each feature is ordered according to its importance (starting with the most important at the top). Note that the SHAP plot is calculated for one instance of the random-forest model, whereas the ranking of feature importance in

Figure 3. Confusion matrices comparing predicted versus actual results for the **a)** decision-tree, **b)** random-forest and **c)** gradient-boost trained models. Abbreviations: IS, induced seismicity events; No-IS, no induced seismicity events.
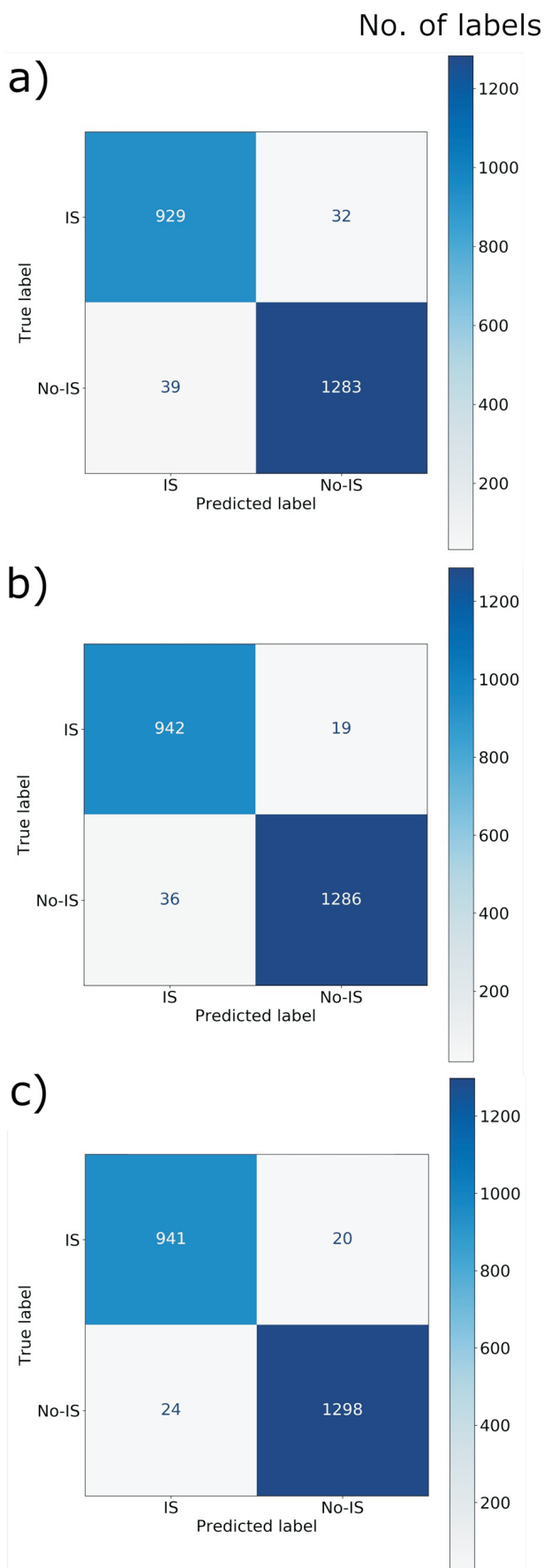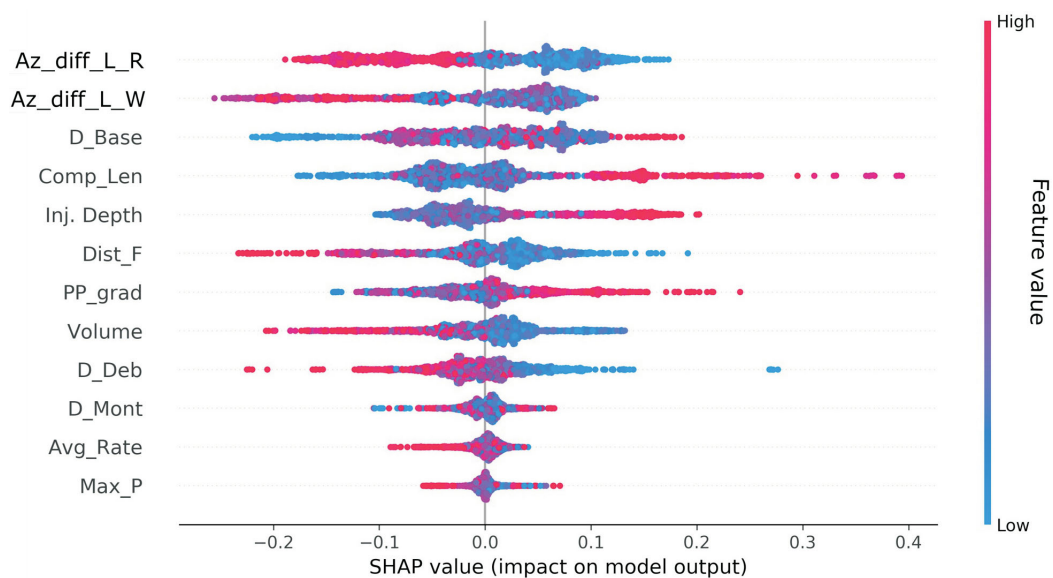
Figure 4. Results for a SHapley Additive exPlanations (SHAP) feature importance analysis using the random-forest trained model. Feature abbreviations: Az_diff_L_R, local and regional maximum horizontal stress azimuth difference; Az_diff_L_W, local maximum horizontal stress and horizontal well azimuth difference; Comp_Len, well completion length; D_Base, distance from injection depth to basement; D_Deb, distance from injection depth to top of Debolt Fm.; D_Mont, distance from injection depth to top of Montney Fm.; Dist_F, distance from wellhead to faults; Inj. Depth, injection depth; Max_P, maximum injection pressure; PP_grad, pore-pressure gradient; Rate, average injection rate; Volume, stage injection volume.

Figure 2 is based on an averaging of 50-fold cross-validation runs. Thus, the order of feature importance between the two is slightly different. Next, points are plotted to show the distribution of the SHAP values using colour to represent the feature value and stacking of overlapping points in the y-axis direction to give a sense of the distribution of the SHAP values. From this, the impact (both positive and negative) is shown through the horizontal location of stacking, which shows whether the effect of that value is associated with a higher or lower prediction. This can be compared to whether the value for that variable/observation is high (red) or low (blue). For example, it can be seen that high values of completion length have a high positive impact on the quality rating. The high values related to this feature are indicated by the red colour of the points, and the high positive impact is shown by its extent on the x-axis.

The results of the SHAP feature importance analysis of the random forest model help to validate the meaningfulness of the algorithm results. Inspecting both Figures 2 and 4, it can be seen that key influencing features such as completion length, pore-pressure gradient and injection depth have a positive correlation with induced seismicity. The influence of pore pressures in the Montney Formation has been studied by Eaton and Schultz (2018), who demonstrated a positive relationship between overpressured areas and induced seismicity. The positive correlation of completion length is also valid as higher completion lengths correspond with larger stimulated volumes and therefore a higher probability of adversely interacting with a critically stressed fault. Features such as distance from the basement or distance to a known fault have negative correlations, meaning shorter distances between the injection point and basement or fault increase the likelihood of triggering an induced seismicity event.

Discussion

Machine-learning models are highly dependent on the quality and quantity of the input data. For the analyses presented here, for a feature where data was either limited or the spatial distribution and/or coverage of the data was sparse relative to the distribution of the wells, this was compensated for by using linear interpolation. However, large distances between points can reduce the accuracy of interpolation, as can the interpolation method itself (e.g., assigning linear versus nonlinear weightings). With time, as new data becomes available, including that for features not included in this study, the induced seismicity susceptibility model can be updated to improve its predictive capabilities.

Based on the results obtained, an interesting observation is the correlation of injection volume and SHAP values. As can be seen in Figure 4, high injection volumes have a negative correlation with triggering induced seismicity. This might be interpreted as high injection volumes reduce the risk of induced seismicity, which is counter to general experience. Thus, empirical analyses and machine-learning data correlations for feature analysis do have their limitations and should be constrained by an understanding of the physics of fault slip and induced seismicity mechanisms.

When comparing the ranking of feature importance, the decision-tree and random-forest models provided similar results. In these models, high importance features included the geological parameters of pore-pressure gradient, distance to basement and distance to faults. The operational features of well completion length and injection depth were also highly ranked by the random-forest model. For the gradient-boost method, the ranking was slightly different with the stress field showing greater influence, both with respect to the geological feature of local and regional S_{Hmax} azimuth difference and related operational feature of the horizontal well and local S_{Hmax} azimuth difference. These differences in ranking are related to how each algorithm works. Gradient-boost models are based on shallow trees (high bias, low variance) and they reduce error mainly by reducing bias. Bias is the simplifying assumptions made by a model to make the target function easier to learn. In contrast, decision-tree and random-forest models use fully grown trees (low bias, high variance) and they reduce the model's error by reducing variance. Variance is the amount that the estimate of the target function will change if different training data were used. For this problem, the source of bias is the number of features that are used for classification, and by including both operational and geological features, the overall bias tends to be less than that if just considering one or the other. The variance of the data can be calculated, and as shown in Table 2, it is higher for parameters such as injection volume and distance to faults whereas it is lower for the two features related to the in situ stress. Thus, this explains the differences between the gradient-boost results and those from the decision-tree and random-forest models.

The comparison of feature importance between the geological and operational parameters show that, overall, the geological parameters generally ranked higher in importance. In all models, the operational parameters of average injection rate and maximum injection pressure consistently ranked as being the least influential. It should be noted that the maximum injection pressure data analyzed was limited to the pressure values measured at the wellheads. Another parameter that is worth investigating is the bottom hole pressure (BHP), which is more applicable to the influence of injection pressure on triggering induced seismicity. The compilation and analysis of BHP data is the subject of on-going research as part of this project. The only operational features ranked as being of high importance were the completion length and the horizontal well direction relative to the S_{Hmax} azimuth. As was shown in Figure 4, completion length had a positive correlation with seismicity and can be thought of in terms of increasing the volume of the formation being stimulated by hydraulic fracturing. The larger the stimulated volume, the higher the probability of intersecting a fault (directly or indirectly).

Conclusions

The application of machine learning was investigated for the purpose of ranking the influence of geological and operational parameters on the classification problem of induced seismicity susceptibility (i.e., distinguishing between wells that are associated with induced seismicity and those that are not). Three different algorithms, decision tree, random forest and gradient boost, were tested using data related to hydraulic fracturing activities in the Montney play area in northeastern British Columbia. All models were initially trained on a subset of 75% of the total data compiled using a 50-fold cross-validation analysis. The remaining 25% of the data was used as a validation set to test the trained models. The validation results showed a high accuracy of successful predictions (97–98%) for all three models.

The classification results were used to calculate the relative importance of all features on whether a well had or had not been associated with induced seismicity. Geological features were differentiated from operational features as the latter are of particular interest as they can be controlled or manipulated to mitigate induced seismicity hazards. However, it was the geological features that generally rated higher with respect to correlation with wells associated with induced seismicity. In all models, pore-pressure gradient (hydrostatic versus overpressured) ranked highly as having a major influence. For the decision-tree and random-forest trained models, distance to basement and distance to known faults also ranked highly, whereas for the gradient boost, the maximum horizontal stress azimuth was a key geological feature that ranked highly. For the operational features, the completion length was the feature most consistently ranked as being of high importance.

Overall, the results of these analyses agree with the current understanding of features that influence induced seismicity susceptibility, such as reservoir overpressure, stress regime and injection volume to stimulate well productivity. These point to the importance of understanding the geology of the Montney Formation including the three-dimensional seismic mapping of faults and taking in situ stress measurements. The machine-learning algorithms investigated here can be used to better understand induced seismicity by determining and ranking the factors that influence induced

Table 2. Variance of features that differ in rank based on the algorithm used. The highly important features of the gradient-boost results (where local and regional maximum horizontal stress azimuth difference [Az_diff_L_R] and local maximum horizontal stress and horizontal well azimuth difference [Az_diff_L_W] are ranked in the top five) are compared with distance to faults (Dist_F) and stage injection volume (Volume). The values of variances reported are divided by the mean for each feature in order to make them unitless for comparison.

Feature	Az_diff_L_R	Az_diff_L_W	Dist_F	Volume
Variance/mean	17	2	19110	370

seismicity susceptibility and therefore further improve industry practices and regulator oversight.

However, it is also recognized that machine-learning analyses focus exclusively on prediction, bypassing the need for explanations of causality that can add reasoning and confidence to the results. The next steps in this research program will be to add a step of refining the machine-learning output through mechanistic validation using a combination of controlled laboratory experiments and three-dimensional numerical simulations to account for known cause and effect relationships. This will help to increase the reliability of the results and deliver a more robust susceptibility map to help decision makers with their planning of hydraulic fracturing activities and induced seismicity hazard management, as well as identifying areas requiring additional focused research.

Acknowledgments

References

Amini, A. and Eberhardt, E. (2019): Influence of tectonic stress regime on the magnitude distribution of induced seismicity events related to hydraulic fracturing; Journal of Petroleum Science and Engineering, v. 182, URL <https://doi.org/10.1016/j.petrol.2019.106284>.

Atkinson, G.M., Eaton, D.W., Ghofrani, H., Walker, D., Cheadle, B., Schultz, R., Shcherbakov, R., Tiampo, K., Gu, J., Harrington, R.M., Liu, Y., Van Der Baan, M. and Kao, H. (2016): Hydraulic fracturing and seismicity in the Western Canada Sedimentary Basin; Seismological Research Letters, v. 87, no. 3, p. 631–647, URL <https://doi.org/10.1785/0220150263>.

Babaie Mahani, A., Schultz, R., Kao, H., Walker, D., Johnson, J. and Salas, C. (2017): Fluid injection and seismic activity in the northern Montney play, British Columbia, Canada, with special reference to the 17 August 2015 Mw 4.6 induced earthquake; Bulletin of the Seismological Society of America, v. 107, issue 2, p. 542–552, URL <https://doi.org/10.1785/0120160175>.

Bao, X. and Eaton, D.W. (2016): Fault activation by hydraulic fracturing in western Canada; Science, v. 354, issue 6318, p. 1406–1409.

BC Oil and Gas Commission (2018): BC Oil and Gas Commission data & reports; BC Oil and Gas Commission, URL <https://www.bcogc.ca/data-reports/> [September 2018].

BC Oil and Gas Commission (2019): British Columbia's Oil and Gas Reserves and Production Report 2018; Reservoir Engineering Department, BC Oil and Gas Commission, 29 p.,

URL <https://www.bcogc.ca/files/reports/Technical-Reports/2018-oil-and-gas-reserves-and-production-reportfinal.pdf> [November 2020].

Cracknell, M.J. and Reading, A.M. (2014): Geological mapping using remote sensing data: a comparison of five machine learning algorithms, their response to variations in the spatial distribution of training data and the use of explicit spatial information; Computers and Geosciences, v. 63, p. 22–33.

Currie, B.S., Free, J.C., Brudzinski, M.R., Leveridge, M. and Skoumal, R.J. (2018): Seismicity induced by wastewater injection in Washington County, Ohio: influence of preexisting structure, regional stress regime, and well operations; Journal of Geophysical Research: Solid Earth, v. 123, issue 5, p. 4123–4140, URL <https://doi.org/10.1002/2017JB015297>.

Eaton, D.W. and Schultz, R. (2018): Increased likelihood of induced seismicity in highly overpressured shale formations; Geophysical Journal International, v. 214, issue 1, p. 751–757.

geoLOGIC systems ltd. (2019): geoSCOUT version 8.12; geoLOGIC systems ltd., URL <https://www.geologic.com/products/geoscout/> [March 2020].

Göbel, T. (2015): A comparison of seismicity rates and fluid-injection operations in Oklahoma and California: implications for crustal stresses; The Leading Edge, v. 34, issue 6, p. 640–648, URL <https://doi.org/10.1190/tle34060640.1>.

Hallo, M., Oprsal, I., Eisner, L. and Ali, M.Y. (2014): Prediction of magnitude of the largest potentially induced seismic event; Journal of Seismology, v. 18, issue 3, p. 421–431, URL <https://doi.org/10.1007/s10950-014-9417-4>.

Hastie, T., Tibshirani, R. and Friedman, J. (2017): The Elements of Statistical Learning, Data Mining, Inference, and Prediction (2nd edition); Springer-Verlag, New York, New York, corrected 12th printing January 2017, 745 p., URL <https://web.stanford.edu/~hastie/ElemStatLearn/> [April 2020].

Hayes, B.J., Anderson, J.H., Cooper, M., McLellan, P.J., Rostron, B. and Clarke, J. (2021): Wastewater disposal in the maturing Montney play fairway, northeastern British Columbia (NTS 093P, 094A, B, G, H); in Geoscience BC Summary of Activities 2020: Energy and Water, Geoscience BC, Report 2021-02, p. 91–102, URL <http://geosciencebc.com/updates/summary-of-activities/> [January 2021].

Heidbach, O., Rajabi, M., Cui, X., Fuchs, K., Müller, B., Reinecker, J., Reiter, K., Tingay, M., Wenzel, F., Xie, F., Ziegler, M.O., Zoback, M.L. and Zoback, M. (2018): The World Stress Map database release 2016: crustal stress pattern across scales; Tectonophysics, v. 744, p. 484–498.

Hincks, T., Aspinall, W., Cooke, R. and Gernon, T. (2018): Oklahoma's induced seismicity strongly linked to wastewater injection depth; Science, v. 359, issue 6381, p. 1251–1255, URL <https://doi.org/10.1126/science.aap7911>.

Liu, K. and Liu, B. (2017): Optimization of smooth blasting parameters for mountain tunnel construction with specified control indices based on a GA and ISVR coupling algorithm; Tunnelling and Underground Space Technology, v. 70, p. 363–374, URL <https://www.sciencedirect.com/science/article/pii/S0886779817301761> [November 2020].

Lundberg, S.M. and Lee, S.-I. (2017): A unified approach to interpreting model predictions; in Advances in Neural Information Processing Systems 30 (NIPS 2017), URL <https://papers.nips.cc/paper/7062-a-unified-approach-to-interpreting-model-predictions.pdf> [April 2020].

McGarr, A. (2014): Maximum magnitude earthquakes induced by fluid injection; Journal of Geophysical Research: Solid Earth, v. 119, p. 1008–1019.

Millar, D. and Clarici, E. (1994): Investigation of back-propagation artificial neural networks in modelling the stress-strain behaviour of sandstone rock; in Proceedings of 1994 IEEE International Conference on Neural Networks (ICNN'94), June 28–July 2, 1994, Orlando, Florida, p. 3326–3331, URL <https://doi.org/10.1109/ICNN.1994.374770>.

Panakkat, A. and Adeli, H. (2009): Recurrent neural network for approximate earthquake time and location prediction using multiple seismicity indicators; Computer-Aided Civil and Infrastructure Engineering, v. 24, issue 4, p. 280–292.

Pawley, S., Schultz, R., Playter, T., Corlett, H., Shipman, T., Lyster, S. and Hauck, T. (2018): The geological susceptibility of induced earthquakes in the Duvernay play; Geophysical Research Letters, v. 45, p. 1786–1793, URL <https://agupubs.onlinelibrary.wiley.com/doi/full/10.1002/2017GL076100> [November 2020].

Pedregosa, F., Varoquaux, G., Gramfort, A., Michel, V., Thirion, B., Grisel, O., Blondel, M., Prettenhofer, P., Weiss, R., Dubourg, V., Vanderplas, J., Passos, A., Cournapeau, D., Brucher, M., Perrot, M. and Duchesnay, E. (2011): Scikit-learn: machine learning in Python; Journal of Machine Learning Research, v. 12, p. 2825–2830.

Pu, Y., Apel, D.B. and Lingga, B. (2018): Rockburst prediction in kimberlite using decision tree with incomplete data; Journal of Sustainable Mining, v. 17, issue 3, p. 158–165.

Ribeiro e Sousa, L., Miranda, T., Leal e Sousa, R. and Tinoco, J. (2017): The use of data mining techniques in rockburst risk assessment; Engineering, v. 3, issue 4, p. 552–558.

Rouet-Leduc, B., Hulbert, C., Lubbers, N., Barros, K., Humphreys, C.J. and Johnson, P.A. (2017): Machine learning predicts laboratory earthquakes; Geophysical Research Letters, v. 44, no. 18, p. 9276–9282.

Schultz, R., Atkinson, G., Eaton, D.W., Gu, Y.J. and Kao, H. (2018): Hydraulic fracturing volume is associated with induced earthquake productivity in the Duvernay play; Science, v. 359, issue 6373, p. 304–308.

Schultz, R., Corlett, H., Haug, K., Kocon, K., Maccormack, K., Stern, V. and Shipman, T. (2016): Linking fossil reefs with earthquakes: geologic insight to where induced seismicity occurs in Alberta; Geophysical Research Letters, v. 43, issue 6, p. 2534–2542, URL <https://doi.org/10.1002/2015GL067514>.

Schultz, R., Stern, V. and Gu, Y.J. (2014): An investigation of seismicity clustered near the Cordel Field, west central Alberta, and its relation to a nearby disposal well; Journal of Geophysical Research: Solid Earth, v. 119, no. 4, p. 3410–3423.

Scientific Hydraulic Fracturing Review Panel (2019): Scientific review of hydraulic fracturing in British Columbia; BC Ministry of Energy, Mines and Low Carbon Innovation, final report, 220 p., URL <https://www2.gov.bc.ca/assets/gov/farming-natural-resources-and-industry/natural-gas-oil/responsible-oil-gas-development/scientific_hydraulic_fracturing_review_panel_final_report.pdf> [May 2019].

Shah, A.K. and Keller, G.R. (2017): Geologic influence on induced seismicity: constraints from potential field data in Oklahoma; Geophysical Research Letters, v. 44, issue 1, p. 152–161, URL <https://doi.org/10.1002/2016GL071808>.

Skoumal, R.J., Brudzinski, M.R. and Currie, B.S. (2015): Earthquakes induced by hydraulic fracturing in Poland township, Ohio; Bulletin of the Seismological Society of America, v. 105, issue 1, p. 189–197, URL <https://doi.org/10.1785/0120140168>.

Sun, Y., Feng, X. and Yang, L. (2018): Predicting tunnel squeezing using multiclass support vector machines; Advances in Civil Engineering, v. 2018, art. 4543984, 12 p.

Van der Baan, M. and Calixto, F.J. (2017): Human-induced seismicity and large-scale hydrocarbon production in the USA and Canada; Geochemistry, Geophysics, Geosystems, v. 18, issue 7, p. 2467–2485, URL <https://doi.org/10.1002/2017GC006915>.

Visser, R., Smith, B., Kao, H., Babaie Mahani, A., Hutchinson, J. and McKay, J.E. (2017): A comprehensive earthquake catalogue for northeastern British Columbia and western Alberta, 2014-2016; Geological Survey of Canada, Open File 8335, 28 p., URL <https://doi.org/10.4095/306292>.

Weingarten, M., Ge, S., Godt, J.W., Bekins, B.A. and Rubinstein, J.L. (2015): High-rate injection is associated with the increase in U.S. mid-continent seismicity; Science, v. 348, issue 6241, p. 1336–1340, URL <https://doi.org/10.1126/science.aab1345>.

Zhang, X., Zhang, J., Yuan, C., Liu, S., Chen, Z. and Li, W. (2020): Locating induced earthquakes with a network of seismic stations in Oklahoma via a deep learning method; Scientific Reports, v. 10, no. 1, p. 1–12, URL <https://doi.org/10.1038/s41598-020-58908-5>.

Investigation of the Dependence of Induced Seismicity Magnitudes on Differential Stress and Pore Pressure Using Supervised Machine Learning, Northeastern British Columbia (NTS 093, 094A, B, G, H) and Globally

A. Mehrabifard[1], Department of Earth, Ocean and Atmospheric Sciences, The University of British Columbia, Vancouver, British Columbia, amehrabifard@eoas.ubc.ca

E. Eberhardt, Department of Earth, Ocean and Atmospheric Sciences, The University of British Columbia, Vancouver, British Columbia

Introduction

Observed increases in seismic activity in the Western Canada Sedimentary Basin, and in particular northeastern British Columbia (BC), have been attributed to hydraulic fracturing operations required for unconventional gas development (Atkinson et al., 2016). Several large magnitude events have been caused by fluid injection related to hydraulic fracturing completions (Babaie Mahani et al., 2017, 2019; Fox and Watson, 2019), which have raised concerns and exposed knowledge gaps related to the underlying factors that influence the likelihood of induced seismicity events exceeding acceptable magnitudes (Allen et al., 2020). Yet this issue is not specific to hydraulic fracturing. It is well established that subsurface injection of fluids may induce seismicity (Healy et al., 1968; Raleigh et al., 1976) through anthropogenic alteration of crustal stresses (Ellsworth, 2013; Segall and Lu, 2015). Induced seismicity has been observed and recorded during a wide range of subsurface fluid-injection activities including wastewater disposal (e.g., Chen et al., 2017), geothermal energy development either by hydraulic stimulation for enhanced geothermal systems (EGS; e.g., Bachmann et al., 2012) or hydrothermal fluid circulation (e.g., Hopp et al., 2020), geological carbon sequestration (GCS; e.g., Verdon, 2016) and scientific experiments (e.g., Haney et al., 2011). For these operations, fluid injection results in a localized increase in pore pressure. This increased pressure, if proximal to a critically stressed fault, will act to reduce the effective normal stresses acting on the fault, resulting in fault slip and induced seismicity.

Despite recent progress in understanding the mechanisms of induced seismicity, there remain several important questions that need to be resolved. These can benefit from a comparison of induced seismicity across different fluid-injection activities as well as a comparison to natural earthquakes. For example, do the magnitude distributions of induced seismicity events follow similar trends as those for natural earthquakes? If pore pressure plays an important role in altering the effective stresses acting on a fault, does it then have a greater influence than depth and differential stress on the seismogenic response to fluid injection? For a given fluid-injection operation, what is the probability of induced seismicity exceeding magnitude *M*? What parameters are impacting this probability? Are these parameters the same for different types of fluid-injection activities that inherently involve different geological settings (e.g., EGS operations often target stronger crystalline rock whereas hydraulic fracturing operations for unconventional gas target weaker sedimentary rocks albeit in many cases close to the crystalline basement)?

To address these questions, induced seismicity magnitude data were compiled from projects involving the different fluid-injection activities described above. These projects span multiple continents, geological settings and depths. Where earthquake catalogues were provided, magnitude distributions were analyzed directly. Although the data in these seismic catalogues were recorded using different seismic monitoring systems with different calibration methods and sensitivity, by assuming self-similarity they are comparable by a simple power-law relationship that can approximate the frequency-magnitude distribution (FMD) of these seismic events. When earthquake catalogues were not provided, results from FMD analyses that followed the same methods were used. The FMD describes the relationship between the frequency of occurrence and the seismic magnitude (Ishimoto and Iida, 1939; Gutenberg and Richter, 1944):

$$\log_{10}(N \geq M) = a - bM$$

where *N* refers to the number of earthquakes with magnitudes larger or equal than *M*. The *a*-value is the seismicity

---

rate (i.e., 10^a is the number of earthquakes whose magnitude is larger than 0 in the period during which the seismic catalogue was gathered). The b-value in this relationship describes the relative size distribution of events. To estimate the b-value, a maximum-likelihood estimation (MLE) is suggested:

$$b = \frac{\log_{10} e}{\left[\overline{M} - \left(M_c - \Delta M_{bin}/2\right)\right]}$$

where $\overline{M}$ is the mean magnitude of the sample, M_c is the magnitude of completeness, which is defined as the lowest magnitude at which 100% of the events in a space-time volume are detected, and ΔM_{bin} is the binning width of the catalogue (Aki, 1965; Bender, 1983). For consistency, this b-value was used and the maximum curvature method (MCM) was applied to calculate M_c (Wiemer and Wyss, 2000; Woessner and Wiemer, 2005). In using this relationship, a higher b-value indicates that smaller magnitude earthquakes are more dominant in the seismic catalogue and, conversely, a lower b-value indicates an increased number of larger magnitude earthquakes in the catalogue.

Spada et al. (2013) and Scholz (2015) have studied the dependence of FMDs for natural earthquakes as a function of depth and differential stress. The latter is defined as the difference between the maximum and minimum principal stresses. However, there are limitations in these studies that reduce their applicability to fluid-injection induced seismicity. For example, the hypocentre depths of natural earthquakes are generally much deeper (in the range of 5 to 20 km) than those of induced seismicity (1 to 6 km). Moreover, the number of natural earthquakes in the catalogues at depths comparable to induced seismicity (i.e., less than 6 km) is insufficient to allow reliable conclusions to be drawn; these small numbers (about 50 events per catalogue) make FMD analyses more prone to error (Nava et al., 2017). The other limitation of Scholz's (2015) study is that he was restricted to estimating the dominant stress regime and stress magnitudes based on the hypocentre depth. His focus on natural earthquakes at considerable depths meant there was no opportunity to use direct in situ stress measurement data. In this work, the focus has been on fluid-injection operations where in situ stress measurement data is more commonly available, allowing added consideration of relationships involving injection depth, differential stress and preinjection reservoir pore pressure. These parameters were investigated with respect to their influence on the FMDs and b-values. To further analyze the relationships between injection depth, differential stress, pore pressures and b-values, supervised machine learning (ML) was applied. The use of ML and data analytics are quickly evolving as a means to identifying hidden patterns and extracting information from datasets. In earthquake seismology, ML has been applied to problems ranging from the laboratory scale with the analysis of velocity tomography

(Zhao and Glaser, 2019) to the field scale with earthquake identification (Rouet-Leduc et al., 2017) and forecasting (Panakkat and Adeli, 2009). In this study, ML was used to compare the relative importance of each parameter (injection depth, differential stress and preinjection reservoir pore pressure) on the prediction of b-value to gain important insights into seismic hazard susceptibility as a means of guiding the calculation of the probability that an induced seismicity event will exceed an acceptable magnitude (e.g., see Langenbruch and Zoback, 2016).

Data Compilation

Using the published literature, empirical data was compiled of induced seismicity events recorded during different subsurface fluid-injection operations around the world. Other data extracted for each case included the injection depth and in situ stress and preinjection reservoir pore-pressure measurements. A summary of this data is listed in Table 1. For this data, the b-value data was calculated using MLE and MCM. The in situ stresses reported for each case were then used to calculate the differentials between the three principal stresses (S1, maximum; S2, intermediate; S3, minimum), specifically, the differentials between S1-S3 and S2-S3. The number of events in each of the induced seismicity catalogues was sufficiently large enough to ensure a reliable calculation of the b-value. The events recorded were also confirmed to be induced seismicity and not natural earthquakes based on their spatio-temporal correlation with the location and time of the fluid-injection operations. Moreover, it is assumed that the b-value calculated for each project field site is robust since the seismic monitoring stations at these sites were dense enough to ensure a high-quality earthquake catalogue entry.

In order to compare this study's results for induced seismicity with those of Scholz (2015) for natural earthquakes, the differential stress was calculated using the same procedure as Scholz. As previously noted, Scholz (2015) did not have access to in situ stress measurement data for the natural earthquakes in his study and therefore was required to estimate the differential stress based on the earthquake hypocentre depth. Using the same assumptions of a friction coefficient (μ) of 0.75, a rock density of 2500 kg/m^3 and hydrostatic pore pressures (see Scholz, 2015), the following vertical gradients of differential stress (S1-S3) were obtained: i) 45 MPa/km for compressional regimes dominated by thrust faulting; ii) 11.25 MPa/km for extensional regimes dominated by normal faulting; and iii) 20 MPa/km for a strike-slip–dominated region. The stress regime for each fluid-injection site was classified in the database according to Anderson's (1942) strike-slip fault stress regimes, using the in situ stresses reported in the published sources, and then, based on the hypocentre depths, the appropriate stress gradient was applied to calculate Scholz's (2015) approximation of differential stress.

Table 1. Summary of induced seismicity project data compiled from different fluid-injection sites. Abbreviations: EGS, enhanced geothermal systems; GCS, geological carbon sequestration; HF, hydraulic fracturing; Hydro. circ., hydrothermal fluid circulation; LL, lower limit; M, mean; MPa, megapascal; Pore pressure, preinjection reservoir pore pressure; S, stress; S1, maximum stress; S2, intermediate stress; S3, minimum stress; Sci. exp., scientific experiments; UL, upper limit; WD, wastewater disposal.

Type	Number of project sites	Number of earthquakes			b-value			Injection depth (km)			S1-S3 (MPa)			S2-S3 (MPa)			Pore pressure (MPa)		
		LL	M	UL	LL	M	UL	LL	M	UL	LL	M	UL	LL	M	UL	LL	M	UL
HF	14	175	4007	25116	0.64	1.19	2.67	1.60	2.70	3.50	15.90	62.00	131.20	2.80	18.00	39.40	16.00	31.10	62.00
EGS	11	96	8260	43882	0.73	1.12	2.28	2.00	4.00	6.10	33.00	60.10	130.00	20.00	36.00	70.00	6.00	46.20	77.50
WD	4	79	1757	3884	0.66	1.03	1.33	3.50	4.53	6.00	33.80	77.50	140.80	0.00	27.00	40.20	36.00	42.20	50.00
Hydro. circ.	5	130	9610	25148	0.79	1.06	1.42	2.00	3.00	4.00	16.00	40.00	91.00	1.20	16.30	31.30	15.50	25.14	38.00
GCS	2	9506	9506	9506	1.10	1.64	2.17	1.40	1.70	1.90	14.00	15.50	16.90	3.30	5.90	8.40	17.50	18.80	20.00
Sci. exp.	1	2500	2500	2500	0.78	0.78	0.78	4.00	4.00	4.00	105.00	105.00	105.00	35.00	35.00	35.00	48.60	48.60	48.60
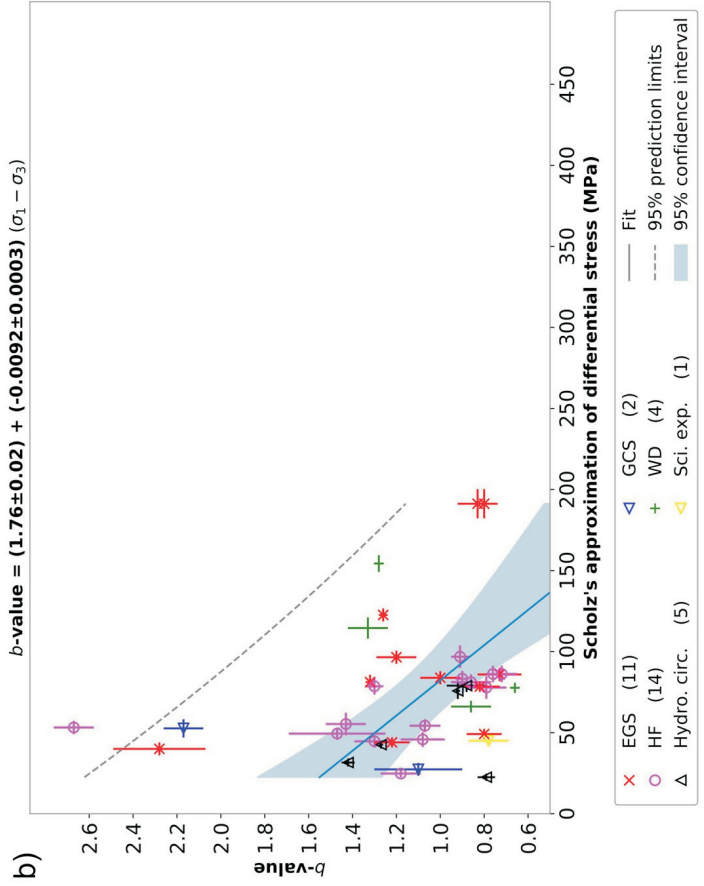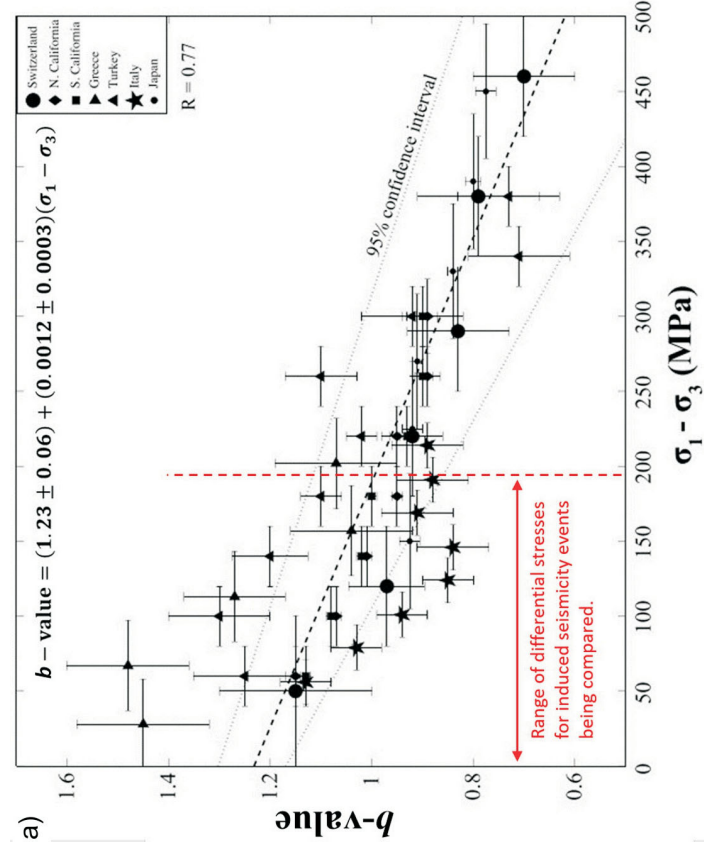
Figure 1. The dependence of b-value on Scholz's differential stress estimation for **a)** the natural earthquake dataset compiled by Scholz (2015) and **b)** the induced seismicity dataset compiled for this study (number of sites indicated in parentheses). The dashed red line in a) shows the upper limit of the calculated differential stresses in the induced seismicity dataset for direct comparison. Abbreviations: σ_1, maximum stress; σ_3, minimum stress; EGS, enhanced geothermal systems; GCS, geological carbon sequestration; HF, hydraulic fracturing; Hydro. circ., hydrothermal fluid circulation; MPa, megapascal; N, northern; S, southern; Sci. exp., scientific experiments; WD, wastewater disposal.

Results and Discussion

Figure 1 compares the dependence of *b*-value on differential stress magnitudes (S1-S3) for natural earthquakes by Scholz (2015) and that for the induced seismicity cases compiled for this study using the same differential stress calculation employed by Scholz. For this, a vertical range of 200 m was assumed for the cloud of induced seismicity hypocentres to allow error bars to be attached to the stress data. It is noteworthy to mention that when there are uncertainties with both independent (e.g., differential stress) and dependent variables (e.g., *b*-value), it is no longer possible to use ordinary least square methods to fit a line to the data. Instead, an orthogonal distance regression was used (see Boggs et al., 1992), which takes into account error bars.

The results from this analysis show that *b*-values decrease as differential stresses increase for both natural earthquakes and induced seismicity. In other words, as expected, higher differential stresses increase the likelihood of larger magnitude seismic events. However, comparing the two plots, the results also show that for the same differential stress, induced seismicity events are more likely to produce larger magnitude events than natural earthquakes. This difference is starker at higher differential stresses. For differential stresses smaller than 83 MPa, the fitted trends in Figure 1a (natural earthquakes) and 1b (induced seismicity) both predict *b*-values >1. However, for differential stresses

greater than 83 MPa, up to the maximum value in the compiled data for induced seismicity of 190 MPa, the *b*-values for the fitted line through the induced seismicity data are <1. For the same range, the *b*-values for the fitted line through the earthquake data are >1. Across this differential stress range, the rate at which the *b*-value decreases is about 7.7 times greater for the induced seismicity trend compared to the natural earthquake trend. This suggests that the anthropogenic influence of increased pore pressures arising from fluid-injection operations, and the extent of pore-pressure diffusion, works to activate larger slip areas on critically stressed faults. On the other hand, it is also noted that the *b*-value intercept of the fitted trend line is higher for induced seismicity than that for natural earthquakes. This is expected as most fluid-injection operations are not associated with large magnitude events. For instance, amongst all completed hydraulic fracturing wells in the Montney Formation in northeastern BC, only 1.3% were associated with induced seismicity events of magnitude (M) >3 (Amini, 2020). This would further influence the numerous precautions and hazard mitigation measures enacted to avoid the occurrence of large magnitude events (e.g., the use of a traffic light system to stop a hydraulic fracturing treatment when larger events are being detected; for an example see Kim et al., 2018).

Figure 2 replots the data in Figure 1b but now using the differential stresses calculated using the site specific in situ

b-value = (3.62±0.01) + (-0.0411±0.0021) $(\sigma_1 - \sigma_3)$

Figure 2. The dependence of the *b*-value on differential stress for the induced seismicity dataset compiled for this study, plotted using the in situ stress magnitudes reported in the source publications (number of sites indicated in parentheses). Abbreviations: σ_1, maximum stress; σ_3, minimum stress EGS, enhanced geothermal systems; GCS, geological carbon sequestration; HF, hydraulic fracturing; Hydro. circ., hydrothermal fluid circulation; MPa, megapascal; Sci. exp., scientific experiments; WD, wastewater disposal.

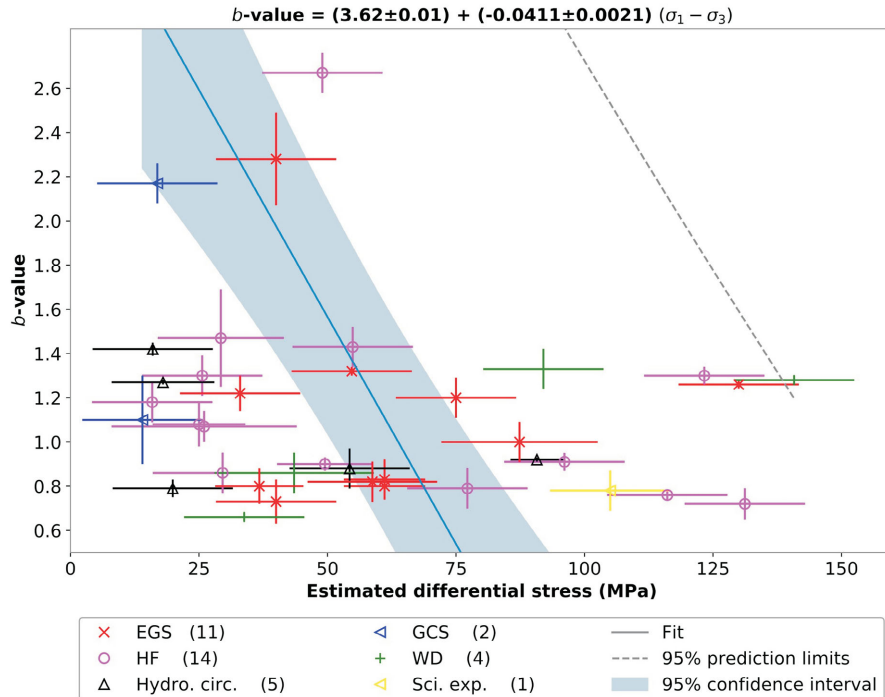stress magnitudes reported in the source publications used for this study. It should be noted that if an ordinary least square method had been used, which does not consider the error bars in the independent variable, the fitted line would be closer to horizontal. Instead, by using the orthogonal distance regression algorithm, which accounts for error bars, the resulting slope of the trend line is even steeper than in Figure 1b. This suggests that the b-value for induced seismicity is more sensitive to differential stress changes than the b-value for natural earthquakes.

To further investigate this dependency, applied machine learning was applied to test the importance of differential stress on b-value and included injection depth and preinjection reservoir pore pressure for comparison. Since the number of data points available is limited (i.e., 37), a simple machine-learning analysis was performed with the goal of comparing the relative influence of each parameter on b-value without setting data aside for a validation dataset (see Amini, 2020). The selected parameters (referred to as features in machine learning) were injection depth in kilometres, preinjection reservoir pore pressure in megapascals (MPa), and the differential stresses S1-S3 and S2-S3 in MPa. For simplicity, there was no consideration of any uncertainties associated with these features. It should be noted that all features were scaled and therefore the feature importance coefficients calculated by the different machine-learning algorithms tested are comparable. Table 2 lists the

top two performing machine-learning algorithms tested with the XGBoostRegressor algorithm outperforming all other regressor models, followed by the RandomForest-Regressor. These returned the highest R^2 scores and lowest mean absolute percentage errors (MAPE). A smaller MAPE means the regressor model predictions of b-value are closer to the actual values.

The results from the machine-learning analysis are presented in Figure 3. Both of the top two performing regressors show that preinjection reservoir pore pressure has the highest impact on b-value. To further investigate this, a linear trend line was fitted to the b-value versus pore pressure data for the induced seismicity cases, as illustrated in Figure 4. The results show that the overall b-value decreases as the preinjection reservoir pore pressure increases. In other words, fluid-injection operations targeting reservoirs with higher pore pressures are more likely to generate higher magnitude induced seismicity events. Figure 5 breaks the data down further according to whether underpressured, hydrostatic or overpressured reservoir conditions were reported at the fluid-injection sites. The number of data points through which each trend line is fitted is evenly distributed between the three scenarios with 13 sites reporting underpressured conditions, 12 reporting hydrostatic conditions and 12 reporting overpressured conditions. Comparing the best fit lines to each data subset, the trends indicate that overpressured reservoirs generally have lower b-values indicating a higher likelihood of producing larger magnitude induced seismicity events. This agrees with the findings of Eaton and Schultz (2018), who reported a correlation between large magnitude events and hydraulic fracturing operations in highly overpressured shale formations.

To further analyze the machine-learning results, a SHapley Additive exPlanations (SHAP) analysis (Lundberg and Lee, 2017) was carried out. The SHAP plots compare the

Table 2. Ranking of the top two machine-leaning algorithms tested based on their performance scores. The ranking shows the mean absolute percentage error (MAPE), which indicates how far the predicted model b-values are from their actual values.

Regressor algorithm	R^2 score (%)	MAPE (%)
XGBoostRegressor	99.90	6.96
RandomForestRegressor	88.19	10.67
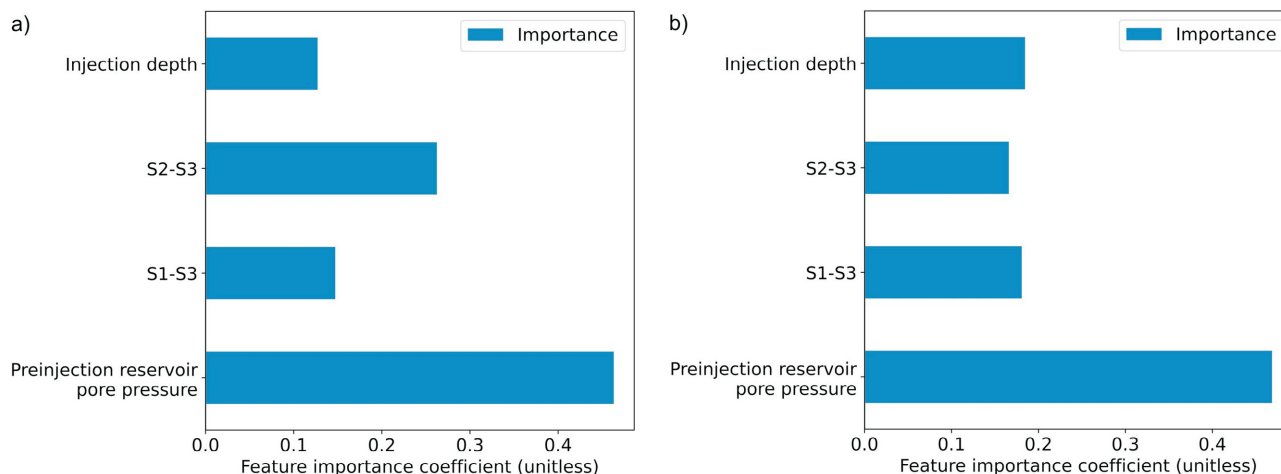
Figure 3. Results from the machine-learning regression analysis showing parameter influence on b-value calculated by the top two performing algorithms: **a)** XGBoostRegressor and **b)** RandomForestRegressor. Abbreviations: S1, maximum stress; S2, intermediate stress; S3, minimum stress.

All fields:
$b\text{-value} = (2.11\pm0.03) + (-0.0320\pm0.0008)\,(P_p)$
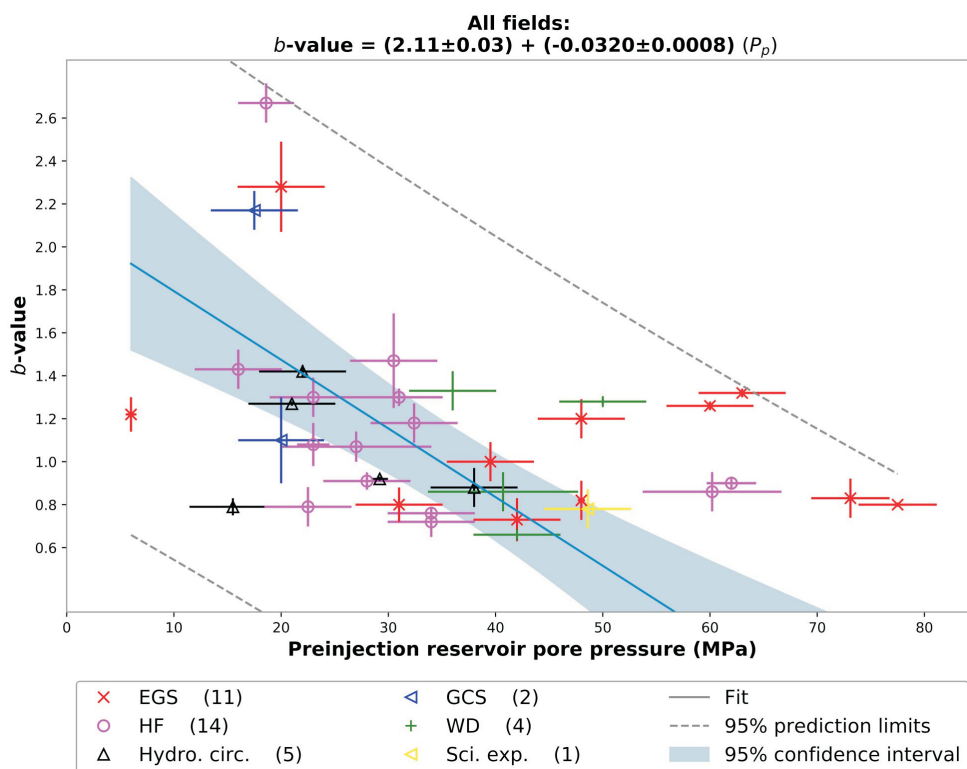
Figure 4. The dependence of b-value on preinjection reservoir pore pressures for induced seismicity based on the pore pressure values reported for each injection site in the dataset compiled for this study (number of sites indicated in parentheses). Abbreviations: P_p, preinjection reservoir pore pressure; EGS, enhanced geothermal systems; GCS, geological carbon sequestration; HF, hydraulic fracturing; Hydro. circ., hydrothermal fluid circulation; MPa, megapascal; S1, maximum stress; S2, intermediate stress; S3, minimum stress; Sci. exp., scientific experiments; WD, wastewater disposal.
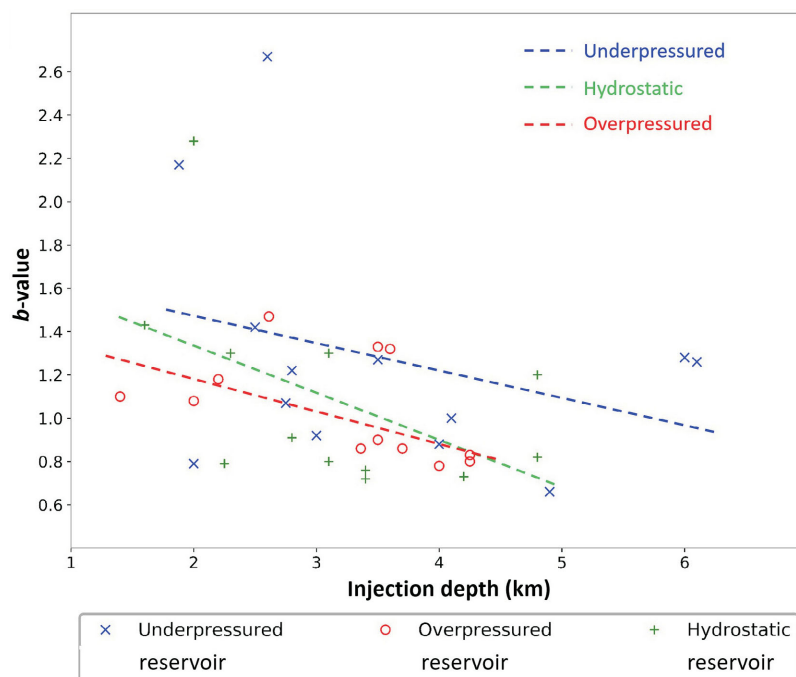
Figure 5. The dependence of b-value on injection depth for induced seismicity based on the preinjection reservoir pore pressure values reported for each injection site in the dataset compiled for this study, separating those reporting underpressured, hydrostatic or overpressured reservoir conditions.
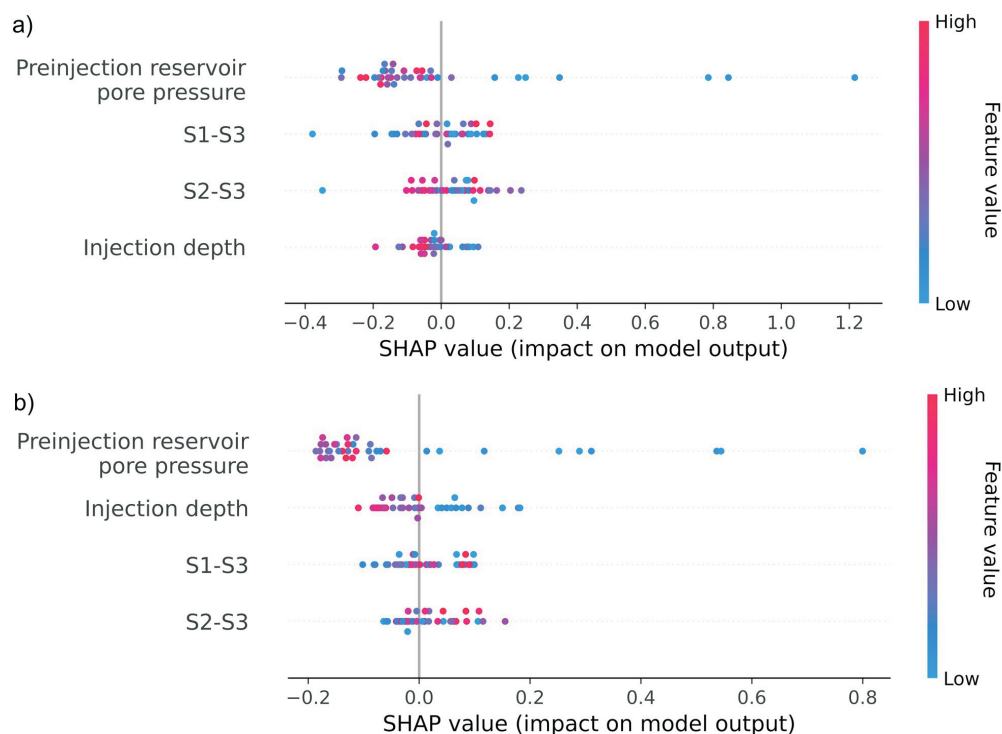
Figure 6. Results from the SHapley Additive exPlanations (SHAP) feature importance analysis showing the impact of low (blue) to high (red) values for each parameter on the *b*-value, as determined from the top two performing machine-learning algorithms: **a)** XGBoostRegressor and **b)** RandomForestRegressor. Note that a more negative SHAP value corresponds with smaller *b*-values (i.e., an increased likelihood of larger magnitude induced seismicity events). Abbreviations: S1, maximum stress; S2, intermediate stress; S3, minimum stress.

impact of the values for each feature, in this case on the *b*-value. Looking at the summary plot in Figure 6, each point represents a single fluid-injection site from the compiled induced seismicity dataset (Table 1), and is colour coded according to whether its value for the feature is low to high relative to the range of values for the other sites in the dataset. The calculated SHAP value for each point shows the impact of that feature on the calculation of the *b*-value for the site. Lower SHAP values (extending into negative numbers) indicate the model is more inclined to predicting lower *b*-values (i.e., higher magnitude induced seismicity events), and vice versa, higher SHAP values indicate a model more likely to predict higher *b*-values (i.e., lower magnitude induced seismicity events). As can be seen in Figure 6a and b, the two top performing machine-learning models both show that higher preinjection reservoir pore pressures have the strongest correlation with smaller *b*-value predictions; all points with high values (coloured red) have negative SHAP values. Again, this is well aligned with Eaton and Schultz's (2018) findings that large magnitude induced seismicity events are most likely associated with overpressured formations. It is also clear that this relationship is not monotonically linear and a significant number of points representing smaller pore pressures (coloured blue) also have negative SHAP values. These establish that lower pore pressures, for example the underpressured and

hydrostatic cases in Figure 5, are associated with both low and high *b*-values.

Both machine-learning models are also in agreement that deeper injections (coloured red) result in lower *b*-values. This is well aligned with Scholz's (2015) findings since the differential stress is calculated based on depth and therefore *b*-value is similarly dependent on depth. However, this is not as clear when looking at the differential stress SHAP values, whether S1-S3 or S2-S3. For S1-S3, the SHAP values show a mix of predictions for both low and high *b*-values, although high values of S1-S3 mostly correspond with low *b*-values, which agrees with findings by Mehrabifard et al. (2019). For S2-S3, the SHAP values calculated for the XGBoostRegressor model predict lower values *b*-values for medium to high values of S2-S3, whereas this correlation is not as clear in the SHAP values for the RandomForestRegressor model. Further investigations are required to draw a firm conclusion on the dependence of *b*-value on S1-S3 and S2-S3, recognizing that the influence of pore pressure is acting in parallel to the differential stresses.

Conclusions

A dataset of induced seismicity magnitude distributions was compiled for a wide range of fluid-injection operations, and *b*-values were calculated for each site. The influ-

ence of differential stress on b-values for induced seismicity events was investigated and compared with trends published for natural earthquakes. It was found that in both cases b-values decrease with increasing differential stresses (maximum stress minus minimum stress), but that the rate of this decrease for induced seismicity is 7.7 times greater than that for natural earthquakes for the same range of depths (1 to 6 km). This suggests that for a given differential stress, the distribution of magnitudes for induced seismicity events is more likely to include higher magnitude events than the distribution for natural earthquakes. This is believed to be due to the influence of induced pore pressures resulting from fluid injection.

The influence of pore pressures on the magnitude distribution of induced seismicity events was further confirmed using machine learning. Results testing feature importance, comparing injection depth, differential stress and preinjection reservoir pore pressure, showed that the seismogenic response was most strongly influenced by the preinjection reservoir pore pressure. This was also seen in the results of a SHAP analysis performed on the machine-learning results. This is interpreted to mean that susceptible faults in reservoirs with higher pore pressures, especially those that are overpressured, are in a more critical state and require only a very small pore pressure disturbance to slip. Thus, given that fluid-injection operations typically involve a large volume of fluid that perturbs the native pore pressure in an extensive zone surrounding the injection well, the likelihood of inducing slip over a larger area of the critically stressed fault is more possible resulting in a larger magnitude event.

In general, injection depth was also seen to have a high correlation with lower b-values. However, the results of the SHAP analysis for injection depth and differential stress were not as clear as those for pore pressure, perhaps because the reservoir conditions at each fluid injection site in the dataset encompasses a mix of underpressured and overpressured reservoir conditions, which again, have a more dominant influence on the correlation with b-value. To isolate the influence of differential stresses, the continuation of this work will explore the use of more sophisticated machine-learning techniques to build on the simpler linear analyses performed here.

Together, these results and the continuation of this research will provide important insights and constraints on 1) the distribution of the magnitudes of induced seismic events and 2) the probability than an event will exceed an acceptable magnitude. This will support the analyses of induced seismicity hazards.

Acknowledgments

References

Aki, K. (1965): Maximum likelihood estimate of b in the formula logN=a-bM and its confidence limits; Bulletin of the Earthquake Research Institute, v. 43, p. 237–239.

Allen, T.I., Griffin, J.D., Leonard, M., Clark, D.J. and Ghasemi, H. (2020): The 2018 national seismic hazard assessment of Australia: quantifying hazard changes and model uncertainties; Earthquake Spectra, v. 36, no. S1, p. 5–43, URL <https://doi.org/10.1177/8755293019900777>.

Amini, A. (2020): Investigation of induced seismicity mechanisms and magnitude distributions under different stress regimes, geomechanical factors, and fluid injection parameters; Ph.D. thesis, University of British Columbia, 155 p., URL <https://open.library.ubc.ca/collections/ubctheses/24/items/1.0394963> [November 2020].

Anderson, E.M. (1942): The dynamics of faulting and dyke formation: with applications to Britain; Nature, v. 149, p. 651–652, URL <https://www.nature.com/articles/149651b0> [November 2020].

Atkinson, G.M., Eaton, D.W., Ghofrani, H., Walker, D., Cheadle, B., Schultz, R., Shcherbakov, R., Tiampo, K., Gu, J., Harrington, R.M., Liu, Y., Van Der Baan, M. and Kao, H. (2016): Hydraulic fracturing and seismicity in the Western Canada Sedimentary Basin; Seismological Research Letters, v. 87, no. 3, p. 631–647, URL <https://doi.org/10.1785/0220150263>.

Babaie Mahani, A., Kao, H., Atkinson, G.M., Assatourians, K., Addo, K. and Liu, Y. (2019): Ground-motion characteristics of the 30 November 2018 injection-induced earthquake sequence in northeast British Columbia, Canada; Seismological Research Letters, v. 90, no. 4, p. 1457–1467, URL <https://doi.org/10.1785/0220190040>.

Babaie Mahani, A., Schultz, R., Kao, H., Walker, D., Johnson, J. and Salas, C. (2017): Fluid injection and seismic activity in the northern Montney play, British Columbia, Canada, with special reference to the 17 August 2015 Mw 4.6 induced earthquake; Bulletin of the Seismological Society of America, v. 107, issue 2, p. 542–552, URL <https://doi.org/10.1785/0120160175>.

Bachmann, C.E., Wiemer, S., Goertz-Allmann, B.P. and Woessner, J. (2012): Influence of pore-pressure on the event-size distribution of induced earthquakes; Geophysical Research Letters, v. 39, issue 9, p. 1–7, URL <https://doi.org/10.1029/2012GL051480>.

Bender, B. (1983): Maximum likelihood estimation of b values for magnitude grouped data; Bulletin of the Seismological Society of America, v. 73, no. 3, p. 831–851, URL <https://pubs.geoscienceworld.org/ssa/bssa/article/73/3/831/118402/maximum-likelihood-estimation-of-b-values-for> [November 2020].

Boggs, P.T., Byrd, R.H., Rogers, J.E. and Schnabel, R.B. (1992): User's reference guide for ODRPACK version 2.01 software for weighted orthogonal distance regression; U.S. Department of Commerce, National Institute of Standards and Technology, NISTIR 4834, 99 p., URL <https://docs.scipy.org/doc/external/odrpack_guide.pdf> [November 2020].

Chen, X., Nakata, N., Pennington, C., Haffener, J., Chang, J.C., He, X., Zhan, Z., Ni, S. and Walter, J.I. (2017): The Pawnee

earthquake as a result of the interplay among injection, faults and foreshocks; Scientific Reports, v. 7, art. 4945, URL <https://doi.org/10.1038/s41598-017-04992-z>.

Eaton, D.W. and Schultz, R. (2018): Increased likelihood of induced seismicity in highly overpressured shale formations; Geophysical Journal International, v. 214, issue 1, p. 751–757, URL <https://doi.org/10.1093/gji/ggy167>.

Ellsworth, W.L. (2013): Injection-induced earthquakes; Science, v. 341, issue 6142, art. 1225942, URL <https://doi.org/10.1126/science.1225942>.

Fox, A.D. and Watson, N.D. (2019): Induced seismicity study in the Kiskatinaw Seismic Monitoring and Mitigation Area, British Columbia; report prepared for the BC Oil and Gas Commission, 51 p., URL <https://www.bcogc.ca/data-reports/reports/?year=2019> [November 2020].

Gutenberg, B. and Richter, C.F. (1944): Frequency of earthquakes in California; Bulletin of the Seismological Society of America, v. 34, no. 4, p. 185–188, URL <http://pubs.geoscienceworld.org/ssa/bssa/article-pdf/34/4/185/2690674/BSSA0340040185.pdf> [November 2020].

Haney, F., Kummerow, J., Langenbruch, C., Dinske, C., Shapiro, S.A. and Scherbaum, F. (2011): Magnitude estimation for microseismicity induced during the KTB 2004/2005 injection experiment; Geophysics, v. 76, no. 6, p. WC47–WC53, URL <https://doi.org/10.1190/geo2011-0020.1>.

Healy, J., Rubey, W., Griggs, D. and Raleigh, C.B. (1968): The Denver earthquakes; Science, v. 161, no. 3848, p. 1301–1310, URL <https://earthquake.usgs.gov/static/lfs/research/induced/Healy-et-al-1968-Science-(New-York-NY).pdf> [November 2020].

Hopp, C., Sewell, S., Mroczek, S., Savage, M. and Townend, J. (2020): Seismic response to evolving injection at the Rotokawa geothermal field, New Zealand; Geothermics, v. 85, art. 101750, URL <https://doi.org/10.1016/j.geothermics.2019.101750>.

Ishimoto, M. and Iida, I. (1939): Observations of earthquakes registered with the microseismograph constructed recently; Bulletin of the Earthquake Research Institute, v. 17, p. 443–478.

Kim, K.-I., Min, K.-B., Kim, K.-Y., Choi, J.W., Yoon, K.-S., Yoon, W.S., Yoon, B., Lee, T.J. and Song, Y. (2018): Protocol for induced microseismicity in the first enhanced geothermal systems project in Pohang, Korea; Renewable and Sustainable Energy Reviews, v. 91, p. 1182–1191, URL <https://doi.org/10.1016/j.rser.2018.04.062>.

Langenbruch, C. and Zoback, M.D. (2016): How will induced seismicity in Oklahoma respond to decreased saltwater injection rates?; Science Advances, v. 2, no. 11, art. e1601542, URL <https://doi.org/10.1126/sciadv.1601542>.

Lundberg, S. and Lee, S. (2017): A unified approach to interpreting model predictions; in Advances in Neural Information Processing Systems 30 (NIPS 2017), p. 4765–4774, URL <http://papers.nips.cc/paper/7062-a-unified-approach-to-interpreting-model-predicti> [November 2020].

Mehrabifard, A., Eberhardt, E. and Damjanac, B. (2019): Empirical and numerical investigation of the effects of in situ stress regime on induced seismicity magnitude distribution; Canadian Society of Petroleum Geologists–Canadian Society of Exploration Geophysicists–Canadian Well Logging Society, Joint Annual Convention (GeoConvention 2019), May 13–17, 2019, Calgary, Alberta, conference paper, 6 p., URL <https://www.researchgate.net/publication/333787173_Empirical_and_numerical_investigation_of_the_effects_of_in_situ_stress_regime_on_induced_seismicity_magnitude_distribution> [November 2020].

Nava, F.A., Márquez-Ramírez, V.H., Zúñiga, F.R., Ávila-Barrientos, L. and Quinteros, C.B. (2017): Gutenberg-Richter b-value maximum likelihood estimation and sample size; Journal of Seismology, v. 21, p. 127–135, URL <https://doi.org/10.1007/s10950-016-9589-1>.

Panakkat, A. and Adeli, H. (2009): Recurrent neural network for approximate earthquake time and location prediction using multiple seismicity indicators; Computer-Aided Civil and Infrastructure Engineering, v. 24, issue 4, p. 280–292, URL <https://doi.org/10.1111/j.1467-8667.2009.00595.x>.

Raleigh, C.B., Healy, J.H. and Bredehoeft, J.D. (1976): An experiment in earthquake control at Rangely, Colorado; Science, v. 191, issue 4233, p. 1230–1237, URL <https://doi.org/10.1126/science.191.4233.1230>.

Rouet-Leduc, B., Hulbert, C., Lubbers, N., Barros, K., Humphreys, C.J. and Johnson, P.A. (2017): Machine learning predicts laboratory earthquakes; Geophysical Research Letters, v. 44, issue 18, p. 9276–9282, URL <https://doi.org/10.1002/2017GL074677>.

Scholz, C.H. (2015): On the stress dependence of the earthquake b value; Geophysical Research Letters, v. 42, issue 5, p. 1399–1402, URL <https://doi.org/10.1002/2014GL062863>.

Segall, P. and Lu, S. (2015): Injection-induced seismicity: poroelastic and earthquake nucleation effects; Journal of Geophysical Research: Solid Earth, v. 120, issue 7, p. 5082–5103, URL <https://doi.org/10.1002/2015JB012060>.

Spada, M., Tormann, T., Wiemer, S. and Enescu, B. (2013): Generic dependence of the frequency-size distribution of earthquakes on depth and its relation to the strength profile of the crust; Geophysical Research Letters, v. 40, issue 4, p. 709–714, URL <https://doi.org/10.1029/2012GL054198>.

Verdon, J.P. (2016): Using microseismic data recorded at the Weyburn CCS-EOR site to assess the likelihood of induced seismic activity; International Journal of Greenhouse Gas Control, v. 54, p. 421–428, URL <https://doi.org/10.1016/j.ijggc.2016.03.018>.

Wiemer, S. and Wyss, M. (2000): Minimum magnitude of completeness in earthquake catalogs: examples from Alaska, the Western United States, and Japan; Bulletin of the Seismological Society of America, v. 90, no. 4, p. 859–869, URL <https://doi.org/10.1785/0119990114>.

Woessner, J. and Wiemer, S. (2005): Assessing the quality of earthquake catalogues: estimating the magnitude of completeness and its uncertainty; Bulletin of the Seismological Society of America, v. 95, no. 2, p. 684–698, URL <https://doi.org/10.1785/0120040007>.

Zhao, Q. and Glaser, S.D. (2019): Relocating acoustic emission in rocks with unknown velocity structure with machine learning; Rock Mechanics and Rock Engineering, v. 53, p. 2053–2061, URL <https://doi.org/10.1007/s00603-019-02028-8>.

Preliminary Results of Source Parameter Inversion of Earthquake Sequences Induced by Hydraulic Fracturing in the Kiskatinaw Area, Northeastern British Columbia (Parts of NTS 093P, 094A)

M.P. Roth[1], Ruhr University Bochum, Bochum, Germany, marco.roth@rub.de

K.B. Kemna, Ruhr University Bochum, Bochum, Germany

R.M. Harrington, Ruhr University Bochum, Bochum, Germany

Y. Liu, McGill University, Montréal, Quebec

Introduction

The occurrence of earthquakes in relation to hydraulic fracturing (HF) during hydrocarbon production is of considerable scientific interest on a global scale (Foulger et al., 2018). Especially in historically seismically quiescent regions, HF-induced events can increase the natural seismic hazard in the time period of anthropogenic interference. The significance of increased seismic hazard associated with HF operations was illustrated by several damaging induced events, including an M_L 5.7 earthquake in the Sichuan Basin on December 16, 2018 (Lei et al., 2019). Nevertheless, to ensure the energy needs of the general public, research is needed on the interaction between energy production and earthquakes induced by fluid injection (McGarr et al., 2015). As an example, the Western Canada Sedimentary Basin (WCSB) has experienced an increasing number of M3+ events in the last decade, which correlates with an increase in oil and gas production (Atkinson et al., 2016). Particularly the Montney Formation, a major shale-gas play in northeastern British Columbia (BC) and northwestern Alberta, is capable of hosting events of magnitude 4+, such as an M_W 4.6 on August 17, 2015 near Fort St. John (Babaie Mahani et al., 2017; Wang et al., 2020) and an M_W 4.2 (M_L 4.5) on November 30, 2018 near Dawson Creek (Babaie Mahani et al., 2019; Peña Castro et al., 2020).

Recently, Roth et al. (2020) found a high temporal and spatial correlation between HF operations and the occurrence of earthquakes in the Kiskatinaw area (Figure 1), a region extending between Fort St. John and Dawson Creek that covers parts of the Montney Formation (Figure 1, purple area on inset map). The linear features evident in the spatial distribution of induced earthquakes align primarily at low angles to S_H, the orientation of maximum horizontal compressive stress. The alignment is interpreted as a fault orientation and is therefore consistent with strike-slip faulting on optimally oriented slip surfaces. Further estimations of focal-mechanism solutions (FMSs) of moderate-sized events in the study area suggest the occurrence of strike-slip, as well as thrust-faulting, events (Onwuemeka et al., 2019; Babaie Mahani et al., 2020; Peña Castro et al., 2020). This paper focuses on the inversion of earthquake-source parameters (i.e., FMS, seismic moment and stress drop) to evaluate possible activated fault planes and to investigate the scaling relations for repeating induced events in the study area.

Earthquake Catalogue

The earthquakes considered in this study are based on an automated earthquake catalogue by Roth et al. (2020) extending to the time period from July 12, 2017 to July 31, 2020. The catalogue contains a total of 8302 events (circles in Figure 1) detected with a short-term average/long-term average (STA/LTA) trigger that includes a 3–20 Hz, 4th order Butterworth bandpass filter, an STA duration of 0.2 s, an LTA duration of 10 s, a triggering threshold of 2.5 and a detriggering threshold of 1.5 for P-wave first arrivals, as well as a 3–12 Hz, 3rd order Butterworth bandpass filter and an Akaike information-criterion algorithm for S-wave first arrivals. All phase arrivals are reviewed by an analyst. This study uses a total of 25 stations (triangles in Figure 1) operated by Ruhr University Bochum (RUB), McGill University (MGU) and Natural Resources Canada (NRCan), although several stations were not operating from the starting time of the catalogue (Table 1).

Focal-Mechanism Inversion

This study uses the probabilistic earthquake-source inversion framework 'Grond' (Dahm et al., 2018) to estimate the

---

FMS for 11 representative earthquakes with a magnitude of M_L 2.7+ in the earthquake catalogue. The FMS is computed for a variety of earthquake sequences based on the waveform-similarity clustering in Roth et al. (2020). Grond inverts for the optimal hypocentral location and moment tensor by applying a bootstrap technique on a dataset of fully inverted waveforms that are compared to a synthetic dataset modelled from Green's functions. These were previously calculated by 'Qseis' (Wang, 1999) and 'Fomosto' (Heimann et al., 2017) using the same velocity model as in Roth et al. (2020; this velocity model is used throughout

this study). The optimal FMS is calculated based on the time and frequency domains, as well as the waveform envelopes. The initial Green's functions are modelled up to 10 Hz, which allows fitting of the full waveforms in a low-frequency band up to 5 Hz, the Nyquist frequency. For each event, several inversions are run in varying frequency bands to compute an FMS with a minimum mean bootstrap misfit of at least <0.65 to be considered for this study, a value dependent on the individual dataset determined by empirical testing. In general, the comparison of modelled versus observed waveforms is the crucial factor in judging
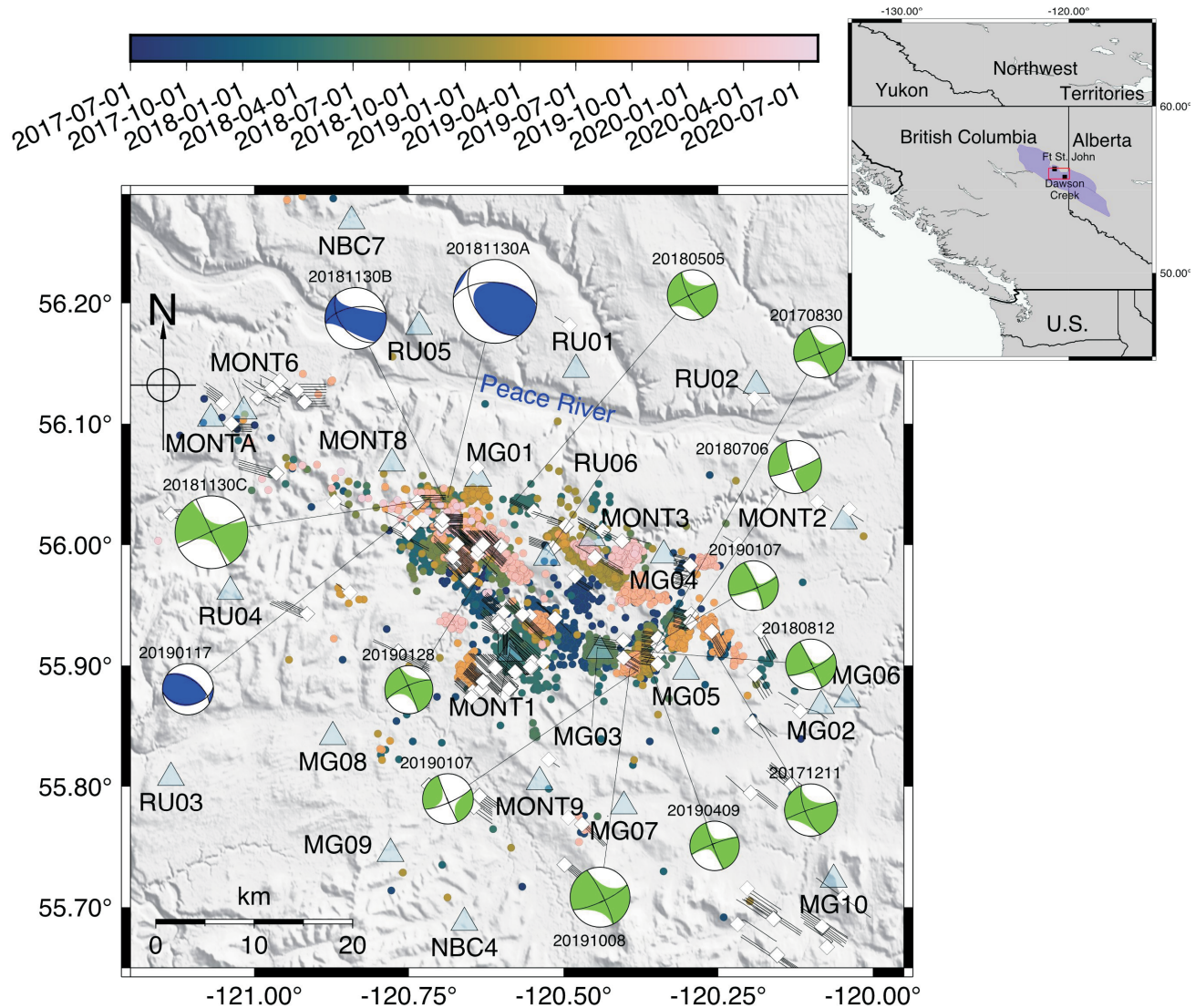
Figure 1. Overview of the Kiskatinaw area in northeastern British Columbia, indicated by the red box on the inset map. The purple-highlighted area on the inset map denotes the shape of the Montney Formation, as reported by the BC Oil and Gas Commission (BCOGC; last accessed October 2018), and the Alberta Energy Regulator (AER; last accessed May 2020). Blue triangles denote stations. Stations starting with RU are operated by Ruhr University Bochum (RUB), those starting with MG are operated by McGill University (MGU) and those starting with MONT and NBC are operated by Natural Resources Canada (NRCan). Circles show the epicentre of earthquake locations, colour coded by origin time. Focal-mechanism plots illustrate the fault type of some representative events in the catalogue, labelled by their respective origin date (YYYYMMDD; blue for dominantly thrust faulting, green for dominantly strike-slip faulting). White diamonds represent HF wells operating in the catalogue's time period, with black lines indicating the trajectories of the horizontal wells (injection data are provided by the BC Oil and Gas Commission; last accessed August 13, 2020). Additional wells might be updated by the respective operators.

Table 1. Overview of all stations, with their locations, used in this study. Stations with network code XL are operated by MGU and RUB, and those with network code 1E and CN by NRCan. The start time shows the beginning of data collection, while the end date gives the supposed date of removal. Station information is archived on the Incorporated Research Institutions for Seismology (IRIS) Data Management Center (www.iris.edu; last accessed October 2020).

Network	Station name	Latitude	Longitude	Start date	End date
XL	MG01	56.05484	-120.637993	2017-Jun-19	2020-Dec-31
XL	MG02	55.866791	-120.083992	2017-Jun-14	2020-Dec-31
XL	MG03	55.912151	-120.44136	2017-Jun-16	2020-Dec-31
XL	MG04	55.99136	-120.338043	2017-Jun-17	2020-Dec-31
XL	MG05	55.895142	-120.301949	2017-Jun-15	2020-Dec-31
XL	MG06	55.87212	-120.041481	2018-Jun-22	2020-Dec-31
XL	MG07	55.783562	-120.40242	2017-Aug-02	2020-Dec-31
XL	MG08	55.84116	-120.87307	2017-Jun-14	2020-Dec-31
XL	MG09	55.74419	-120.779617	2017-Jun-18	2020-Dec-31
XL	MG10	55.722851	-120.063347	2019-Oct-01	2020-Dec-31
XL	MG11	55.86168	-120.11468	2020-Sep-01	2022-Jun-30
XL	RU01	56.145069	-120.480042	2019-Jul-30	2020-Dec-31
XL	RU02	56.131989	-120.188187	2019-Jul-30	2020-Dec-31
XL	RU03	55.807442	-121.134506	2019-Sep-26	2020-Dec-31
XL	RU04	55.961369	-121.038788	2019-Oct-03	2020-Dec-31
XL	RU05	56.180611	-120.733391	2019-Oct-04	2020-Dec-31
XL	RU06	55.98959	-120.526909	2019-Sep-29	2020-Dec-31
1E	MONT1	55.910149	-120.58654	2018-Oct-01	2021-Oct-01
1E	MONT2	56.019718	-120.046967	2018-Oct-01	2021-Oct-01
1E	MONT3	56.005779	-120.45388	2018-Oct-01	2021-Oct-01
1E	MONT6	56.110291	-121.016991	2018-Oct-03	2021-Oct-01
1E	MONT8	56.06731	-120.777428	2019-Jul-15	2021-Oct-01
1E	MONT9	55.803902	-120.538757	2019-Oct-07	2021-Oct-01
1E	MONTA	56.104321	-121.070038	2019-Oct-05	2021-Oct-01
CN	NBC4	55.687279	-120.66024	2013-Mar-01	2599-Dec-31
CN	NBC7	56.267792	-120.842621	2014-Aug-10	2599-Dec-31

the quality of the calculated FMS. In addition to the 11 FMSs calculated in this study, three have been included from Peña Castro et al. (2020).

Spectral Analysis

Spectral-source parameters of 8302 earthquakes were estimated based on their waveforms. The source parameter inversion to determine long-period spectral amplitude and corner frequency is based on two methods, the single spectrum and the spectral-ratio calculation, both of which are described below. As the S-waves typically have a higher signal-to-noise ratio (SNR), only they are used for this study. To estimate a time window covering the complete S-wave signal, an initial theoretical corner frequency ($f_{c,initial}$) was estimated based on the local magnitude reported in the catalogue, the relation of Ross et al. (2016) to estimate a moment magnitude, a lower-bound stress drop of 0.1 MPa, and the constant $k = 0.26$ for a singular crack expanding radially at a rupture speed of 90% of the shear-wave velocity (after recent analyses by Kaneko and Shearer, 2014).

Therefore, $t = 2/f_{c,initial}$ is used as the window length. The choice of 0.1 MPa as a stress-drop value will lead to a lower boundary for the corner-frequency estimation and, due to the inverse relation to t, the time window will therefore be long enough to guarantee coverage of the complete phase. Although longer time windows are reported (e.g., Ross and Ben-Zion, 2016), this study will continue with twice the inverse of the estimated corner frequency, as this relation will lead to $t \approx 1$ s for M_L 2.5 events at the typical depth of 2 km (Roth et al., 2020). For smaller events reported in the catalogue where the time window would be even shorter, a one-second time window is used to keep enough data points in the waveform.

Single-Spectrum Method

This study employs the waveforms for each available pick beginning at 25% of the window length before the phase arrival, and a corresponding noise window with the same length, one-time window before the P-arrival. If no P-arrival is detected, 5 s before the origin time is used. In the

next step, the single spectra of individual components are calculated using a multitaper approach (Prieto et al., 2009). To enhance the signal, the vector sum of both horizontal components, if two components were available due to the absence of data gaps, and a dynamically calculated time window are used. To avoid potential bias of the following curve fit toward higher frequencies, each spectrum is resampled using an equally spaced logarithmical sampling-size interval. Next, a numerical fit is estimated for the corner frequencies and the long-period spectral amplitude using the Boatwright source model (Boatwright, 1978),

$$\Omega(f) = \Omega_0 \frac{e^{-\left(\frac{\pi f t}{Q}\right)}}{\left(1+\left(f/f_c\right)^{\gamma n}\right)^{1/\gamma}} \, , \tag{1}$$

with the long-period spectral amplitude Ω_0 fixed to the maximum amplitude of the respective single spectrum, frequency f, the source-receiver travel time t as reported by the catalogue, the corner frequency f_c to be fitted, the high-frequency falloff rate n, the seismic attenuation Q (where Q and n will be fixed to one value, although recent studies point out lower uncertainties for a clustered-Q approach; Ko et al., 2012; Yu et al., 2020; see 'Estimation of optimal parameter settings for Q and n' below), and a factor γ that controls the shape of the corner and is fixed at $\gamma = 2$ for the Boatwright source model. One single spectrum is considered to be fitted if its SNR exceeds a threshold of 3 for 1–30 Hz ($M_L<3$), 1–20 Hz ($3<M_L<4$) or 1–15 Hz ($M_L>4$), as the instrument response function is flat between 0.1 Hz and 45 Hz, with a sampling rate of 100 Hz. One example of the fitted spectrum and the corresponding waveforms is plotted in Figure 2.

Spectral-Ratio Method

A second method for calculating source parameters is the spectral-ratio method, which can be applied if two events of similar waveforms are located within approximately one source dimension defined by the larger event (Abercrombie, 2015), and recorded at the same station; the larger event of this pair is called the 'target' event and the smaller one the 'empirical Green's function' (EGF; Hartzell, 1978). Dividing the two single spectra (Equation 1) to calculate the spectral ratio,

$$\Omega(f) = \frac{\Omega_0^{target}}{\Omega_0^{EGF}} \left[\frac{1+\left(f/f_c^{EGF}\right)^{\gamma n}}{1+\left(f/f_c^{target}\right)^{\gamma n}} \right]^{1/\gamma} \, , \tag{2}$$

cancels out instrument- and non-source–related effects, such as site effects, and leaves the source differences of the target and the EGF events. In this study, all events with a magnitude difference of at least 0.5 relative to the target event, a maximum distance of 5 km to the target event and a cross-correlation coefficient (CCC) of 0.8 or higher on one

channel of the closest station were considered as potential EGF. Although the relative magnitude difference between target event and EGF is sometimes reported to be at least 1.0 to ensure the amplitude ratio is high enough to differentiate the two corner frequencies (e.g., Hartzell, 1978), the lower difference is applied in order to avoid pre-emptively removing a large number of event pairs that may be viable, a practice that has already yielded significant results globally (Kwiatek et al., 2014; Harrington et al., 2015) and in the WCSB (Holmgren et al., 2019). The benefit of the smaller magnitude difference is a higher number of EGFs connected to the target event, which will be manually reviewed in a later stage of the analysis and ensures an adequate number of possible EGFs for the predominant small-magnitude events in the WCSB (Holmgren et al., 2019).

For calculating the CCC, a window length is chosen that covers the P- and S-wave arrival, as well as the coda, by starting 0.5 s before the P-wave onset and ending $1.8(t_S–t_P)$ after the P-wave onset, where $t_S–t_P$ describes the difference in S and P arrival times. Calculating the CCC of full wave forms ensures that the overall waveform is similar, which requires a similar FMS for both events (Harrington et al., 2015; Ruscic et al., 2019). The additional CCC criterion, to link targets with EGFs, is a further argument for only linking similar events with each other. In the preliminary processing steps for the beginning of the catalogue, where fewer stations were operating simultaneously, more successful combined target-EGF pairs were found using a rather high CCC on the closest station only, presumably because the CCC will decrease for larger distances due to attenuating effects and a lower SNR. Besides, if the CCC is high on the closest station, it suggests a similar focal mechanism (Got et al., 1994). Furthermore, the minimum magnitude for target events was limited to M_L 2, and the individual SNRs must exceed the same threshold of 3 for 1–30 Hz to guarantee a high portion of S-wave signal in the processed time window. Otherwise, the desired corner frequency might be covered by seismic noise in the same frequency band. In this study, the corner frequency can be resolved at least up to 10–15 Hz (Abercrombie, 2014), and Abercrombie et al. (2017) and Ruhl et al. (2017) reported an even higher cut-off criterion (i.e., half to two-thirds of the upper frequency for SNR resolution, in the present case 15–20 Hz). The window length of both waveforms is equal to the estimated window length for the target event. To ensure a high quality of the spectral-ratio fits, a graphical user interface (GUI) was designed to visually inspect all spectral-ratio pairs and, if needed, manually adjust some fitting parameters.

Estimation of Optimal Parameter Settings for Q and n

To guarantee a fit according to Equation 1, which will only fit the corner frequency f_c and discharges potential numeri-
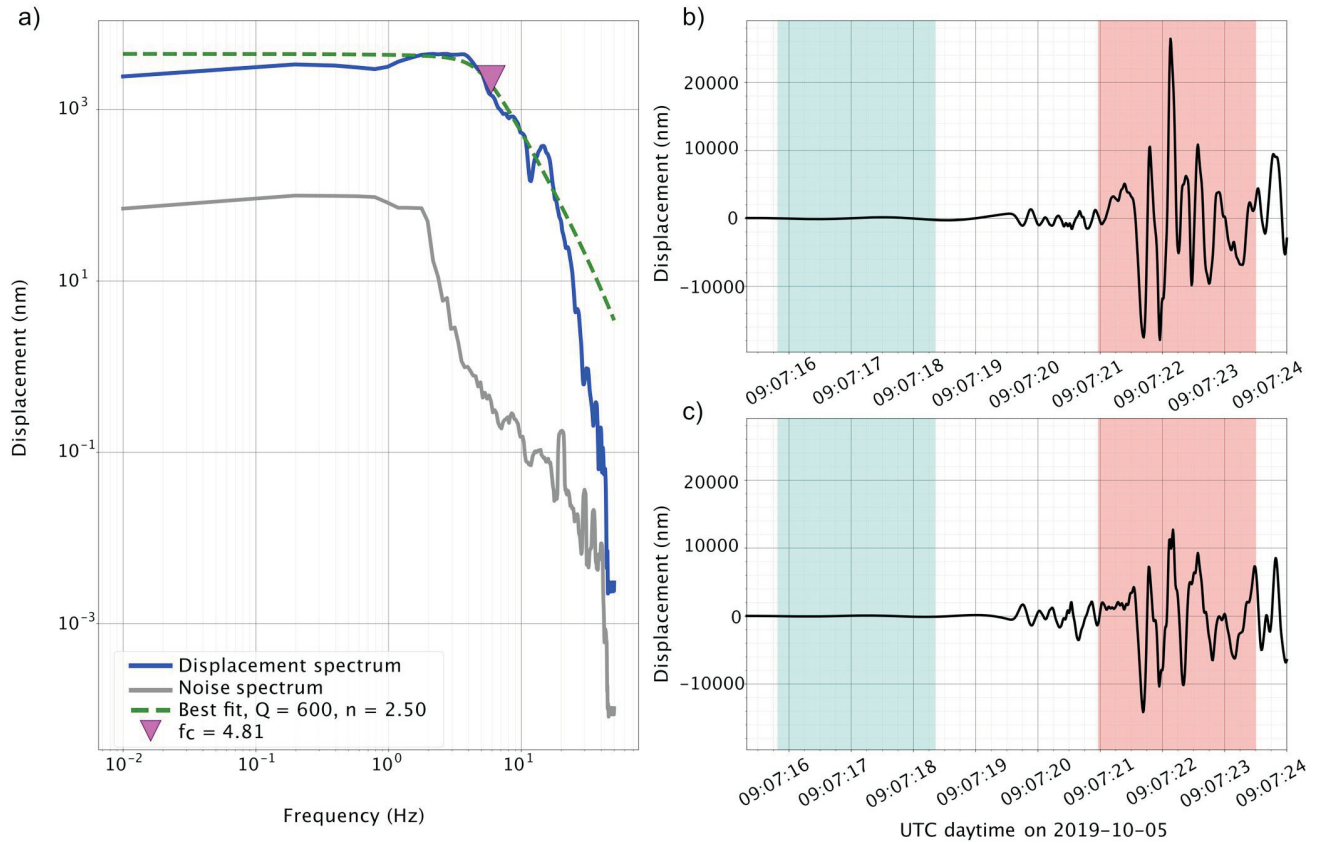
Figure 2. Example plot of one fitted single spectrum on station RU06 from an event with a magnitude of M_L 3.4 that occurred southeast of the study area on October 5, 2019: **a)** displacement spectrum (blue) of the signal (pink shading in parts b and c) and a fit using Equation 1 (green dashed line); grey line displays the noise level (blue shading in parts b and c) directly before the event happened; **b)** and **c)** displacement waveform on the north and east components of RU06, respectively.

cal trade-off effects between f_c, Q and n, constant values were chosen for Q and n. As Q describes the seismic attenuation, it is defined by rock properties. This study is limited to one region with rather uniform mechanical behaviour, as well as widespread HF operations affecting larger parts of the area. Furthermore, the high-frequency fall-off rate n is affected by rupture processes (i.e., duration time and fraction of stress drop; Brune, 1970), which are similar in this study area due to a high number of repetitive waveforms (Roth et al., 2020). Therefore, it was decided to keep both values constant. The values of the (Q, n) pair were calculated with the smallest overall misfit by a grid-search approach based on 2 066 064 individual fits for 13 n-values between 1.75 and 3.25 in a spacing of 0.125, and 56 Q-values between 250 and 3000 and a spacing of 50 for 2838 event-station pairs (Figure 3). The chosen events are a subset of 239 target events, where spectral ratios with multiple EGFs could be calculated in the later analysis step. The χ^2-misfit was first calculated for each of the desired fits. As the misfit itself is not comparable to the misfit on other stations, it is necessary to norm the individual misfit to a reference misfit, which in this study is the Q-n pair of 1000 and 2, as used in previous spectral-analysis studies for the WCSB (Clerc et al., 2016; Holmgren et al., 2019; Wang et al.

2020), and afterwards calculate the mean misfit for all event-station pairs. The warm colours in Figure 3 show a relative decrease in misfit (i.e., an improvement of the model settings, which results in the chosen values for Q and n being 600 and 2.5, respectively). A study by Yu et al. (2020) had already showed a successful application for constant Q values according to the spatial distribution of induced events in the WCSB, where the authors calculated an apparent Q, representing the ray path in a layered Q structure.

Seismic Moment and Corner Frequency

The following steps describe how the source parameters are estimated from the previously fitted single spectra and spectral ratios. First, the seismic moment can be estimated for each of the events at each of the stations that exceeded the SNR of 3 by extracting the long-period spectral amplitude of the respective single spectra. Following the Brune (1970) relation, the seismic moment is defined by

$$M_0 = \frac{4\pi\rho\beta^3\Omega_0 R}{U_{\Phi\Theta}}, \tag{3}$$

with the shear-wave velocity β, the rock density ρ (where the value is between 2.46 and 2.86 g/cm³, depending on the
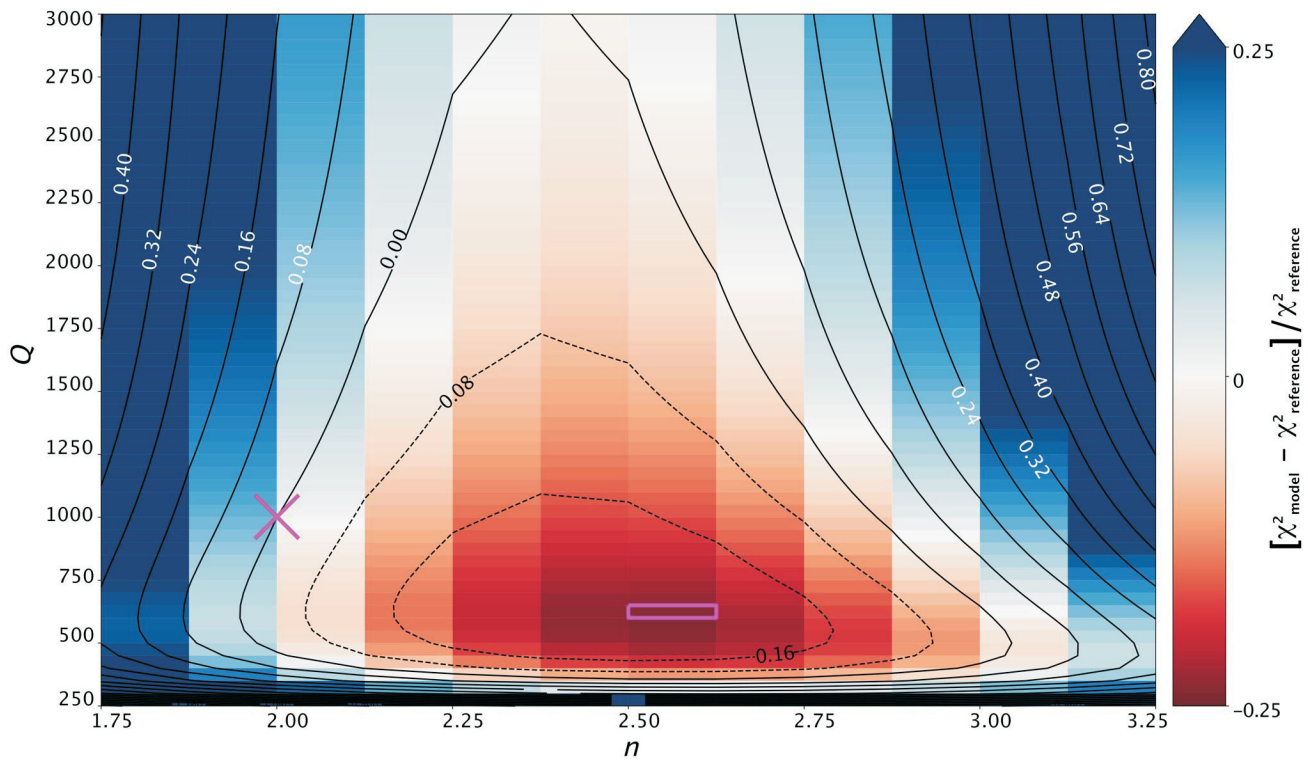
Figure 3. Relative χ^2 misfit variations of single spectra with different Q-n pairs for 239 chosen events on all possible stations, normalized on $Q = 1000$ and n = 2.0 (magenta cross). Warm colours denote a decrease in relative misfit (improvement of the fit) and cool colours an increase in relative misfit (worsening of the fit). Solid and dashed isolines show interpolations for the models with 8% increases and decreases, respectively, in relative misfit. The model used in this study is highlighted as a magenta box.

hypocentral depth), the source-receiver distance R, and the radiation pattern for S waves of $U_{\Phi\Theta} = 0.63$ (Aki and Richards, 2002). In this study, all events with a minimum of five successful fits (i.e., estimates of seismic moment and corner frequency on five stations) were considered. To calculate one seismic moment for the event, the jackknife mean, including the confidence level, is calculated from all station values of all estimates for Ω_0 (Prieto et al., 2007), where one estimate of Ω_0 is the maximum value of the respective single spectrum. The seismic moment is derived only from single-spectrum estimates, as Equation 2 does not contain a spectral amplitude isolated for the events.

To minimize the variables that need to be fitted into Equation 2, the low frequency level was set to the maximum of the observed spectral ratio, and n = 2.5. A target-EGF pair was considered if at least five spectral ratios were calculated. Next, all potential target-EGF pairs were stacked and evaluated by a newly developed GUI (Figure 4), which allows the analyst to add or remove single stations to or from the fit, and adapt the frequency band in which the fit should be calculated. For spectral ratios, where both fitted corner frequencies are close to each other and where the amplitude ratio between the lower- and upper-frequency portions is low, f_c^{target} is not distinct. To ensure that the second corner frequency f_c^{EGF} is not misinterpreted as the first corner frequency f_c^{target} by the numerical fit, the analyst can add a

source spectrum (Brune, 1970), which is Equation 1 reduced by the attenuation term (i.e., the exponential term involving Q). If the fit of the target-EGF pair has an adequate shape, and f_c^{target} is resolvable, the analyst can decide to save or withdraw the pair. Figure 4 shows one example of a well-resolved spectral ratio. This study is limited to estimations of f_c^{target} only, as the magnitude range in the catalogue does not allow large differences between target and EGF magnitude, and f_c^{EGF} will probably exceed the frequency bandwidth-limitation of 10–15 Hz.

Stress-Drop Calculation

In the next step, the prior estimated corner frequency is used to calculate the stress drop of the specific event. While the seismic moment and the corner frequency describe the fault of an earthquake, the stress drop can give insights into the rupture process (i.e., stress relief due to the event). To derive the stress drop $\Delta\sigma$ from one single spectrum and spectral ratios, a model for a circular crack is used (Eshelby, 1957), specifically

$$\Delta\sigma = \frac{7}{16}\frac{M_0}{r^3}, \tag{4}$$

where r describes the fault radius for a circular crack, calculated from the radiated S-wave spectrum (Brune, 1970, 1971)
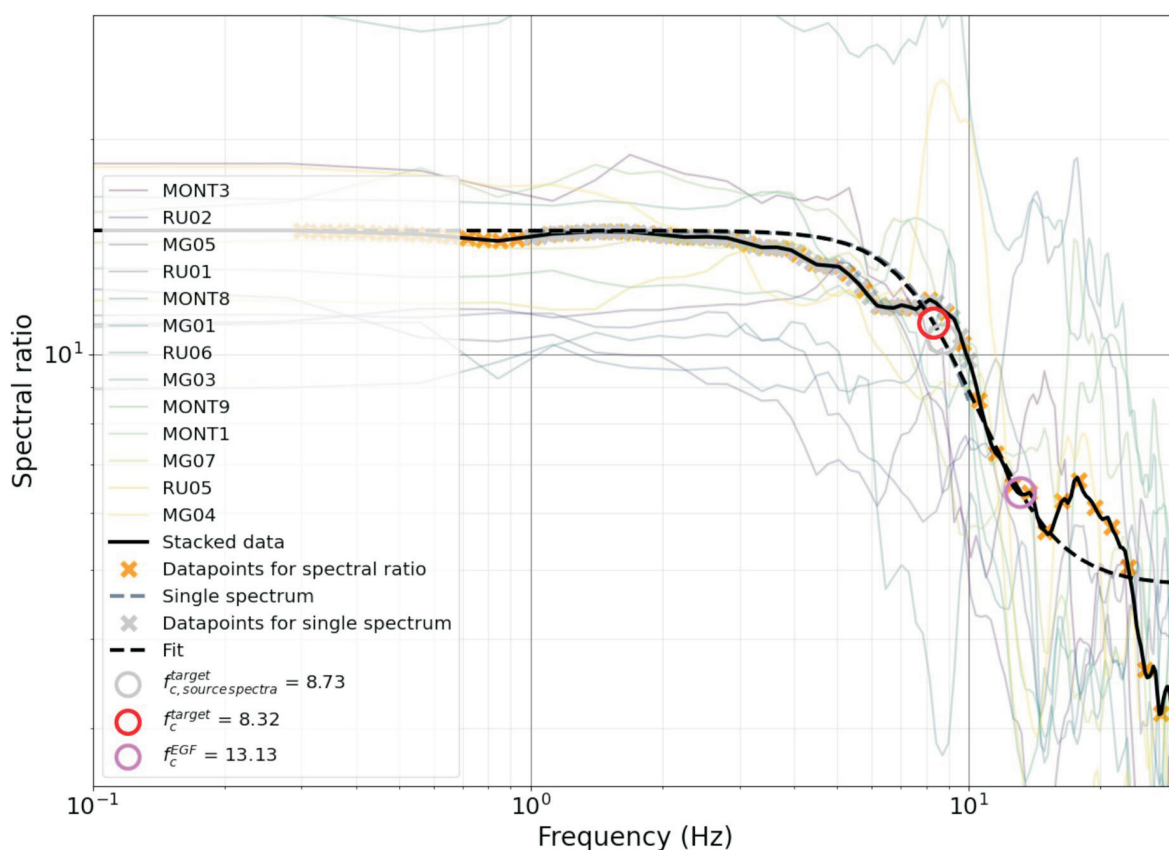
Figure 4. a) Menu bar of the GUI for one spectral-ratio pair of one M_L 3.1 target event (work ID 'bug2020ctot') and one M_L 2.0 EGF (bug2020dptv). The user can individually plot all spectral ratios ('Create Plots'), add the stack of all visible spectral ratios ('Stack Single Ratios') and add the fit, using Equation 2 ('Add Fit') for specific frequency bands. The x and y axes can be limited using the 'x lim' and 'y lim' windows, respectively. Deactivating individual checker boxes next to the stations starting with RU, MG or MONT can remove individual stations to be considered. The individual locations of the stations are provided in Figure 1 and Table 1. 'show Event info' can display the origins and magnitudes of the events. When the analyst confirms the quality of the fit, then the figure and the corner frequency for the target and for the EGF can be saved. **b)** Example plot of one fitted spectral-ratio pair. The coloured lines show individual spectral ratios on one station. The solid black line is the stack of all spectral ratios, while the dashed black line shows the determined best fit. Orange and grey crosses show the data points of the stack, which are considered for the fit using the spectral ratio (Equation 2) and the source spectrum, respectively. The red and purple circles highlight the corner frequencies for target and EGF, respectively, using Equation 2, while the grey circle can confirm the first corner frequency using the source spectrum.

$$r = \frac{k\beta}{f_c} .$$
(5)

As the previous analytical steps may yield multiple values for f_c (due to multiple single spectra on various stations, or to multiple EGFs used for one target event), the mean value is always used. In the same way that corner frequencies were calculated individually using two methods (using the single spectra and the spectral ratios), individual stress-drop values can also be calculated with both methods. However, the seismic moment is calculated using only the single-spectrum approach.

Results

Figure 1 shows 14 focal-mechanism plots, three of which are from Peña Castro et al. (2020). The majority of events are dominated by a left-lateral, strike-slip faulting mechanism (11 out of 14), and the remaining events are dominated by a thrust-faulting mechanism. While the thrust-faulting events with magnitudes between M_L 4.5 and M_L 2.7 can only be observed close to Fort St. John in the northwestern part of the Kiskatinaw area, there is no clear trend for the distribution of strike-slip events, which have magnitudes between M_L 3.4 and M_L 2.8.

In total, 1772 of the 8002 events passed the quality-control criteria for deriving source parameters by fitting the single spectra, while 303 events could be used for the spectral-ratio method. Figure 5 shows a summary of the spectral-analysis results for both single spectra (blue and grey circles) and spectral ratios (green diamonds). Comparing the single-spectra results for the events for which spectral ratios could be calculated (blue circles) with the events for which the single-spectrum method was used (grey circles) shows the same scaling, but for different magnitude ranges, due to the fact that there are fewer EGFs and smaller SNRs for smaller magnitude target events. Figure 5a shows the scaling for stress drop versus seismic moment (or moment magnitude), where single spectra suggest an increase of stress drop with increasing seismic moment between roughly 10^{-1} MPa (M_w ~1.5) and 3×10^1 MPa (M_w ~4.2). Contrary to the single spectra, the spectral ratios highlight a scattering between 10^0 and 10^2 MPa, with no clear trend apparent. Furthermore, a higher number of events seem to be underestimated, as they are above the resolvable frequency content of the instrument (grey shading on Figure 5), while only a few events are higher than 13 Hz, the instrumental resolution limit that is dictated by the SNR threshold of 30 Hz.

Plotting the seismic moment (or moment magnitude) against the corner frequency (Figure 5b) shows a steep decrease of seismic moment with corner frequency. In addition, the stress drop scatters between 10^{-1} MPa and 10^1 MPa. Results from the spectral ratios do highlight a rather slight decrease of seismic moment with increasing

corner frequency, implying a constant stress drop between 10^0 MPa and 10^2 MPa, optimally at 10^1 MPa.

Discussion and Conclusion

The estimated focal mechanism of this study agrees with the general trend of focal mechanisms from previous studies (Onwuemeka et al., 2019; Babaie Mahani et al., 2020; Peña Castro et al., 2020). In addition, the left-lateral strike-slip faults from the focal-mechanism plots are consistent with the fault orientations at roughly 30° to S_H in Roth et al. (2020). The fact that no EGF fulfills the defined quality-control criteria for the M_L 4.5 suggests an isolated hypocentre for this particular mainshock, as suggested in Peña Castro et al. (2020). Two focal-mechanism solutions are observed in the northwestern part of the study area, close to the Peace River (Figure 1) and to the Fort St. John graben (e.g., Barclay et al., 1990; Davies, 1997; Eaton et al., 1999), suggesting thrust-faulting events and strike-slip events, whereas the southeastern part of the area hosts exclusively strike-slip events. The reason for this could be that the area close to the Fort St. John graben may host normal faults formed by graben building and basin infill, which can be reactivated as thrust faults in the current stress regime. In contrast, the southeastern part of the study area hosts solely shallow strike-slip events, perhaps due to the absence of potential deep receiver faults. A second natural source for existing thrust faults would be the thrust-faulting belt in the Rocky Mountain foreland (Paná and van der Pluijm, 2015), formed during the Laramide orogeny.

Another factor supporting the observation of two types of FMS in the same region may take into account the stress constraints from borehole data and focal-mechanism inversions in Fox Creek, Alberta (Shen et al., 2019): S_v could be larger than S_h for the shallower depths in the WCSB, resulting in strike-slip events, while S_h could be larger than S_v at greater depth, the optimal stress regime for thrust-faulting events. According to Shen et al. (2019), the stress-regime transition occurs between 3.4 and 10.4 km, with the optimal depth at 5.9 km. In addition, the mixture of FMSs might imply the existence of Riedel-shear structures. The presence of Riedel-shear structures, the embryonic stage of strike-slip fault formation (Riedel, 1929), might imply the influence of large-volume fluid injection in the seismotectonic setting. Following the initiation and development of pull-apart basins with Riedel-shear mechanism in laboratory experiments (Atmaoui et al., 2006), the slip surfaces of the strike-slip faults are expected to be on structures at an early stage of development, although potential slip surfaces or zones of weakness must not be newly created.

Use of the GUI allows the analyst to refine the corner frequency from the default fit (Figure 4). In the example shown, the spectral ratio of station RU06 is conspicuously high, MG04 shows an anomaly at 7–10 Hz, and RU01 and
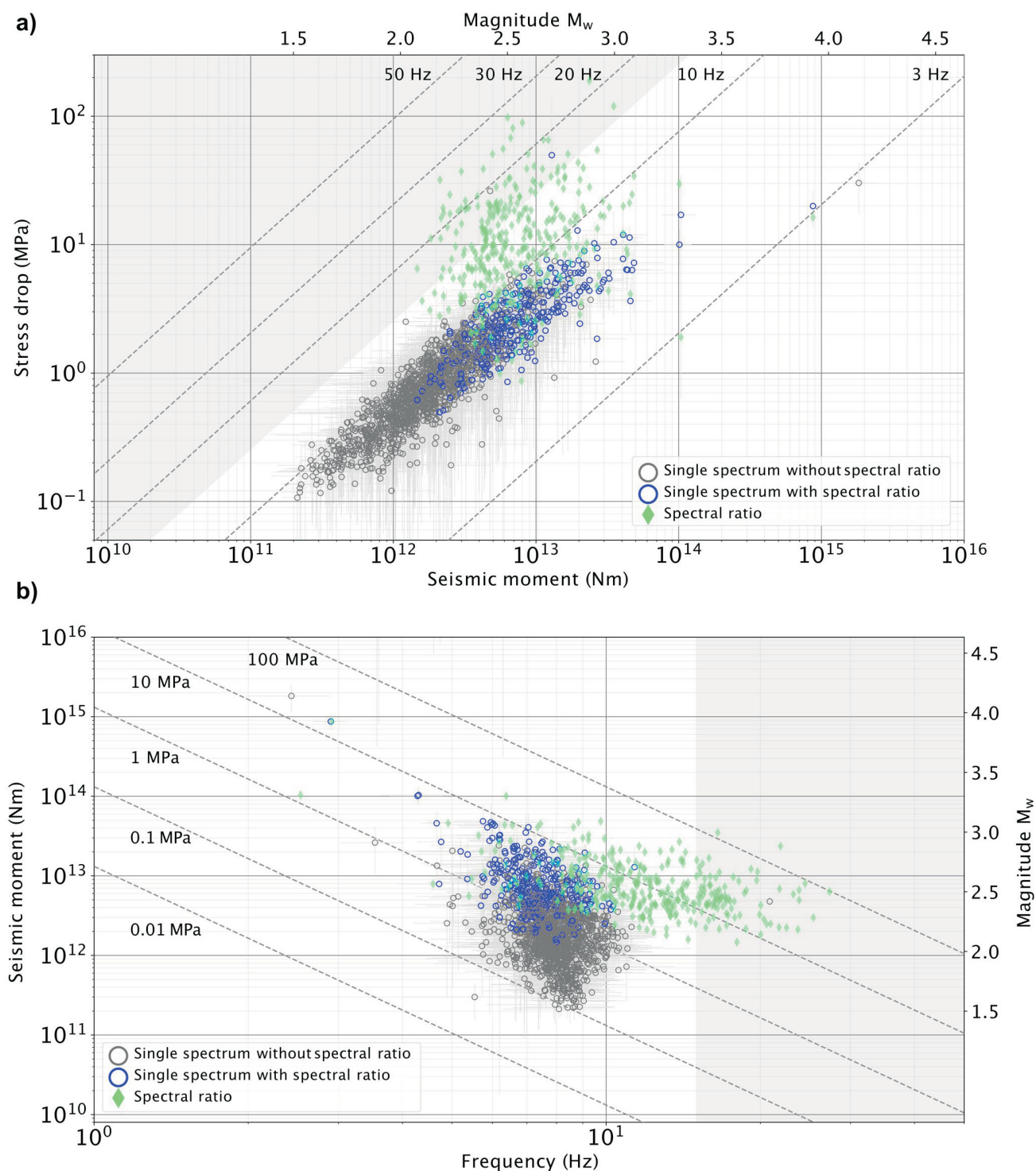
Figure 5. Scaling of stress drop versus seismic moment **(a)** and seismic moment versus corner frequency **(b)**. In both plots, circles denote solutions from single spectra, the blue circles being those events for which the spectral-ratio method was applied, whereas grey circles do not have a spectral-ratio solution. The green diamonds are the results from spectral ratios. Isolines in part a show constant corner frequencies, whereas isolines in part b highlight the levels of constant stress drops. The grey shading above 15 Hz indicates the area where the corner frequency might not be resolved correctly.

MONT1 are biasing the stacked spectral ratio between 10 and 20 Hz. By removing the individual stations before the fitting process, the corner frequency decreases from 8.32 to 7.63 Hz. Thus, using the GUI enables the processing of a dataset with higher precision compared to automatically determined corner frequencies. In the present case, by inspecting all individual spectral ratios, the analyst is able to investigate in-site effects beneath individual stations (Yang et al., 2009), as the stations are close to the clusters and the HF wells (Figure 1). Variations of individual spectral ratios from the stacked spectral ratio might indicate, for example, the influence of fluid injections.

Comparing the results from single-spectra estimates versus spectral-ratio estimates shows a strong scaling for single-spectra results and a wide range of values for spectral-ratio results, especially for lower-moment magnitudes (i.e., $\sim M_w$ 2.3). A possible reason for this might be the limited frequency band of the dataset (i.e., sampling rate of 100 Hz) and the fact that only surface stations are used, which limits the maximum resolvable corner frequency because the attenuation for higher frequencies is higher (Abercrombie, 1995; Viegas et al., 2010). The same breakdown in constant stress drop is reported from other studies that estimate source parameters with single-spectrum approaches (e.g., Onwuemeka et al., 2018; Kemna et al., 2020). The methods seem to generate the same results when considering events with M_W greater than 3, although the observation is based on few data points. However, a number of studies suggest that spectral ratios provide more reliable estimates of source parameters, particularly for smaller earthquakes, and that they should be preferred over single-spectrum estimates for interpreting scaling with size (e.g., Ide and Beroza, 2001; Ide et al., 2003). Taking the limitation of the magnitude range into account, the stress drop of the induced events in the WCSB may be constant with respect to magnitude, which agrees with the scaling laws for similar events (Aki, 1967) and the repetitive character of induced events in general (Skoumal et al., 2015), which is also observed in the WCSB (Schultz et al., 2015; Roth et al., 2020). This study can be integrated with earlier studies on stress-drop values for induced events in the Montney Formation, specifically 1) results from Yu et al. (2020) that suggest a lower stress drop for events proximal to HF wells (0.1–1 MPa), whereas events distal from HF wells have a higher stress drop (1–10 MPa); and 2) results from Wang (2020) that suggest stress-drop values between 1 and 35 MPa, in the typical range of tectonic earthquakes (0.1–100 MPa; Hanks, 1977). In a broader context, values from this study agree with the average stress drop for small- to moderate-size events in the WCSB, which is 7.5 ±0.5 MPa (Holmgren et al., 2019).

References

Abercrombie, R.E. (1995): Earthquake source scaling relationships from −1 to 5 M_L using seismograms recorded at 2.5 km depth; Journal of Geophysical Research: Solid Earth, v. 100, no. B12, p. 24015–24036, URL <https://agupubs.onlinelibrary.wiley.com/doi/abs/10.1029/95JB02397> [August 2020].

Abercrombie, R.E. (2014): Stress drops of repeating earthquakes on the San Andreas Fault at Parkfield; Geophysical Research Letters, v. 41, no. 24, p. 8784–8791, URL <https://agupubs.onlinelibrary.wiley.com/doi/full/10.1002/2014GL062079> [August 2020].

Abercrombie, R.E. (2015): Investigating uncertainties in empirical Green's function analysis of earthquake source parameters; Journal of Geophysical Research: Solid Earth, v. 120, no. 6, p. 4263–4277, URL <https://agupubs.onlinelibrary.wiley.com/doi/full/10.1002/2015JB011984> [August 2020].

Abercrombie, R.E., Poli, P. and Bannister, S. (2017): Earthquake directivity, orientation, and stress drop within the subducting plate at the Hikurangi Margin, New Zealand; Journal of Geophysical Research: Solid Earth, v. 122, no. 12, p. 10176–10188, URL <https://agupubs.onlinelibrary.wiley.com/doi/full/10.1002/2017JB014935> [August 2020].

Aki, K. (1967): Scaling law of seismic spectrum; Journal of Geophysical Research, v. 72, no. 4, p. 1217–1231, URL <https://agupubs.onlinelibrary.wiley.com/doi/abs/10.1029/JZ072i004p01217> [April 2017].

Aki, K. and Richards, P.G. (2002): Elastic waves from a point dislocation source; Chapter 4 in Quantitative Seismology (2nd edition), University Science Books, Sausalito, California, p. 63–117.

Atkinson, G.M., Eaton, D.W., Ghofrani, H., Walker, D., Cheadle, B., Schultz, R., Shcherbakov, R., Tiampo, K., Gu, J., Harrington, R.M., Liu, Y., van der Baan, M. and Kao, H. (2016): Hydraulic fracturing and seismicity in the Western Canada Sedimentary Basin; Seismological Research Letters, v. 87,

no. 3, p. 631–647, URL <https://pubs.geoscienceworld.org/ssa/srl/article/87/3/631/315665> [August 2017].

Atmaoui, N., Kukowski, N., Stöckhert, B. and König, D. (2006): Initiation and development of pull-apart basins with Riedel shear mechanism: insights from scaled clay experiments; International Journal of Earth Sciences, v. 95, no. 2, p. 225–238, URL <https://link.springer.com/article/10.1007/s00531-005-0030-1> [October 2020].

Babaie Mahani, A., Esfahani, F., Kao, H., Gaucher, M., Hayes, M., Visser, R. and Venables, S. (2020): A systematic study of earthquake source mechanism and regional stress field in the southern Montney unconventional play of northeast British Columbia, Canada; Seismological Research Letters, v. 91, no. 1, p. 195–206, URL <https://pubs.geoscienceworld.org/ssa/srl/article/91/1/195/579422> [January 2020].

Babaie Mahani, A., Kao, H., Atkinson, G.M., Assatourians, K., Addo, K. and Liu, Y. (2019): Ground-motion characteristics of the 30 November 2018 injection-induced earthquake sequence in northeast British Columbia, Canada; Seismological Research Letters, v. 90, no. 4, p. 1457–1467, URL <https://pubs.geoscienceworld.org/ssa/srl/article/90/4/1457/571681/Ground-Motion-Characteristics-of-the-30-November> [July 2019].

Babaie Mahani, A., Schultz, R., Kao, H., Walker, D., Johnson, J. and Salas, C. (2017): Fluid injection and seismic activity in the northern Montney play, British Columbia, Canada, with special reference to the 17 August 2015 Mw 4.6 induced earthquake; Bulletin of the Seismological Society of America, v. 107, no. 2, p. 542–552, URL <https://pubs.geoscienceworld.org/ssa/bssa/article/107/2/542/354161> [November 2018].

Barclay, J., Krause, F., Campbell, R. and Utting, J. (1990): Dynamic casting and growth faulting: Dawson Creek graben complex, Carboniferous–Permian Peace River embayment, western Canada; Bulletin of Canadian Petroleum Geology, v. 38, no. 1, p. 115–145, URL <https://pubs.geoscienceworld.org/cspg/bcpg/article/38A/1/115/582791/Dynamic-casting-and-growth-faulting-Dawson-Creek> [August 2019].

Boatwright, J. (1978): Detailed spectral analysis of two small New York State earthquakes; Bulletin of the Seismological Society of America, v. 68, no. 4, p. 1117–1131, URL <https://pubs.geoscienceworld.org/ssa/bssa/article/68/4/1117/117843> [November 2019].

Brune, J.N. (1970): Tectonic stress and the spectra of seismic shear waves from earthquakes; Journal of Geophysical Research, v. 75, no. 26, p. 4997–5009, URL <https://agupubs.onlinelibrary.wiley.com/doi/abs/10.1029/jb075i026p04997> [November 2019].

Brune, J.N. (1971): Correction to tectonic stress and the spectra of seismic shear waves from earthquakes; Journal of Geophysical Research, v. 76, no. 20, p. 5002, URL https://agupubs.onlinelibrary.wiley.com/doi/abs/10.1029/JB076i020p05002 [November 2019].

Clerc, F., Harrington, R.M., Liu, Y. and Gu, Y. (2016): Stress drop estimates and hypocenter relocations of induced seismicity near Crooked Lake, Alberta; Geophysical Research Letters, v. 43, no. 13, p. 6942–6951, URL <https://agupubs.onlinelibrary.wiley.com/doi/full/10.1002/2016GL069800> [August 2020].

Dahm, T., Heimann, S., Funke, S., Wendt, S., Rappsilber, I., Bindi, D., Plenefisch, T. and Cotton, F. (2018): Seismicity in the block mountains between Halle and Leipzig, central Germany: centroid moment tensors, ground motion simulation, and felt intensities of two M~ 3 earthquakes in 2015 and 2017; Journal of Seismology, v. 22, no. 4, p. 985–1003, URL <https://link.springer.com/article/10.1007/s10950-018-9746-9> [September 2020].

Davies, G.R. (1997): The Triassic of the Western Canada Sedimentary Basin: tectonic and stratigraphic framework, paleogeography, paleoclimate and biota; Bulletin of Canadian Petroleum Geology, v. 45, no. 4, p. 434–460, URL <https://pubs.geoscienceworld.org/cspg/bcpg/article/45/4/434/54206> [August 2019].

Eaton, D.W., Ross, G.M. and Hope, J. (1999): The rise and fall of a cratonic arch: a regional seismic perspective on the Peace River Arch, Alberta; Bulletin of Canadian Petroleum Geology, v. 47, no. 4, p. 346–361, URL <https://pubs.geoscienceworld.org/cspg/bcpg/article/47/4/346/57760> [August 2019].

Eshelby, J.D. (1957): The determination of the elastic field of an ellipsoidal inclusion, and related problems; Mathematical and Physical Sciences, v. 241, no. 1226, p. 376–396, URL <https://royalsocietypublishing.org/doi/10.1098/rspa.1957.0133> [November 2019].

Foulger, G.R., Wilson, M.P., Gluyas, J.G., Julian, B.R. and Davies, R.J. (2018): Global review of human-induced earthquakes; Earth-Science Reviews, v. 178, p. 438–514, URL <https://www.sciencedirect.com/science/article/pii/S001282-521730003X> [August 2020].

Got, J.L., Fréchet, J. and Klein, F.W. (1994): Deep fault plane geometry inferred from multiplet relative relocation beneath the south flank of Kilauea; Journal of Geophysical Research: Solid Earth, v. 99, no. B8, p. 15375–15386, URL <https://agupubs.onlinelibrary.wiley.com/doi/abs/10.1029/94JB00577> [August 2017].

Hanks, T.C. (1977): Earthquake stress drops, ambient tectonic stresses and stresses that drive plate motions; *in* Stress in the Earth, M. Wyss (ed.), Brinkhäuser, Basel, Contributions to Current Research in Geophysics (CCRG), p. 441–458, URL <https://link.springer.com/chapter/10.1007/978-3-0348-5745-1_28> [September 2020].

Harrington, R.M., Kwiatek, G. and Moran, S.C. (2015): Self-similar rupture implied by scaling properties of volcanic earthquakes occurring during the 2004-2008 eruption of Mount St. Helens, Washington; Journal of Geophysical Research: Solid Earth, v. 120, no. 7, p. 4966–4982, URL <https://agupubs.onlinelibrary.wiley.com/doi/full/10.1002/2014JB011744> [October 2020].

Hartzell, S.H. (1978): Earthquake aftershocks as Green's functions; Geophysical Research Letters, v. 5, no. 1, p. 1–4, URL <https://agupubs.onlinelibrary.wiley.com/doi/abs/10.1029/GL005i001p00001@10.1002/(ISSN)1944-8007.GRL40> [August 2020].

Heimann, S., Kriegerowski, M., Isken, M., Cesca, S., Daout, S., Grigoli, F., Juretzek, C., Megies, T., Nooshiri, N., Steinberg, A., Sudhaus, H., Vasyura-Bathke, H., Willey, T. and Dahm, T. (2017): Pyrocko – an open-source seismology toolbox and library; GFZ Data Services, URL <https://dataservices.gfz-potsdam.de/panmetaworks/showshort.php?id=escidoc:2144891> [November 2019].

Holmgren, J.M., Atkinson, G.M. and Ghofrani, H. (2019): Stress drops and directivity of induced earthquakes in the Western Canada Sedimentary Basin; Bulletin of the Seismological Society of America, v. 109, no. 5, p. 1635–1652, URL <https://pubs.geoscienceworld.org/ssa/bssa/article/109/5/

1635/573126/Stress-Drops-and-Directivity-of-Induced> [June 2020].

Ide, S. and Beroza, G.C. (2001): Does apparent stress vary with earthquake size?; Geophysical Research Letters, v. 28, no. 17, p. 3349–3352, URL <https://agupubs.online-library.wiley.com/doi/abs/10.1029/2001GL013106> [October 2020].

Ide, S., Beroza, G.C., Prejean S.G. and Ellsworth W.L. (2003): Apparent break in earthquake scaling due to path effects on deep borehole recordings; Journal of Geophysical Research: Solid Earth, v. 108, no. B5, URL <https://agupubs.online-library.wiley.com/doi/full/10.1029/2001JB001617> [October 2020].

Kaneko, Y. and Shearer, P.M. (2014): Seismic source spectra and estimated stress drop derived from cohesive-zone models of circular subshear rupture; Geophysical Journal International, v. 197, no. 2, p. 1002–1015, URL <https://academic.oup.com/gji/article/197/2/1002/617325> [August 2020].

Kemna, K.B., Peña Castro, A.F, Harrington, R.M. and Cochran, E.S. (2020): Using a large-n seismic array to explore the robustness of spectral estimations; Geophysical Research Letters, v. 47, no. 21, URL <https://doi.org/10.1029/2020GL089342>.

Ko, Y.T., Kuo, B.Y. and Hung, S.H. (2012): Robust determination of earthquake source parameters and mantle attenuation; Journal of Geophysical Research: Solid Earth, v. 117, no. B4, URL <https://agupubs.onlinelibrary.wiley.com/doi/full/10.1029/2011JB008759> [October 2020].

Kwiatek, G., Bulut, F., Bohnhoff, M. and Dresen, G. (2014): High-resolution analysis of seismicity induced at Berlín geothermal field, El Salvador; Geothermics, v. 52, p. 98–111, URL <https://www.sciencedirect.com/science/article/pii/S0375650513000825> [October 2020].

Lei, X., Wang, Z. and Su, J. (2019): The December 2018 ML 5.7 and January 2019 ML 5.3 earthquakes in South Sichuan basin induced by shale gas hydraulic fracturing; Seismological Research Letters, v. 90, no. 3, p. 1099–1110, URL <https://pubs.geoscienceworld.org/ssa/srl/article/90/3/1099/569798/The-December-2018-ML-5-7-and-January-2019-ML-5-3> [September 2019].

McGarr, A., Bekins, B., Burkardt, N., Dewey, J., Earle, P., Ellsworth, W., Ge, S., Hickman, S., Holland, A., Majer, E. and Rubinstein, J. (2015): Coping with earthquakes induced by fluid injection; Science, v. 347, no. 6224, p. 830–831, URL <https://science.sciencemag.org/content/347/6224/830.summary> [August 2018].

Onwuemeka, J., Harrington, R.M., Liu, Y. and Kao, H. (2019): Source properties of earthquakes around hydraulic-fracturing sites near Dawson Creek, northeastern British Columbia; in Geoscience BC Summary of Activities 2018: Energy and Water, Geoscience BC, Report 2019-02, p. 63–66, URL <http://cdn.geosciencebc.com/pdf/SummaryofActivities2018/EW/Schol_SoA2018_EW_Onwuemeka.pdf> [September 2019].

Onwuemeka, J., Liu, Y. and Harrington, R.M. (2018): Earthquake stress drop in the Charlevoix seismic zone, eastern Canada; Geophysical Research Letters, v. 45, no. 22, p. 12226–12235, URL <https://agupubs.onlinelibrary.wiley.com/doi/full/10.1029/2018GL079382> [August 2020].

Panã, D.I. and van der Pluijm, B.A. (2015): Orogenic pulses in the Alberta Rocky Mountains: radiometric dating of major faults and comparison with the regional tectono-strati-graphic record; Geological Society of America Bulletin, v. 127, no. 3/4, p. 480–502, URL <https://pubs.geoscience-world.org/gsa/gsabulletin/article/127/3-4/480/126124> [August 2019].

Peña Castro, A.F., Roth, M.P., Verdecchia, A., Onwuemeka, J., Liu, Y., Harrington, R.M., Zhang, Y. and Kao, H. (2020): Stress chatter via fluid flow and fault slip in a hydraulic fracturing–induced earthquake sequence in the Montney formation, British Columbia; Geophysical Research Letters, v. 47, no. 14, URL <https://agupubs.onlinelibrary.wiley.com/doi/full/10.1029/2020GL087254> [July 2020].

Prieto, G.A., Parker, R.L. and Vernon III, F.L. (2009): A Fortran 90 library for multitaper spectrum analysis; Computers & Geosciences, v. 35, no. 8, p. 1701–1710, URL <https://www.sciencedirect.com/science/article/pii/S0098300-409000077> [August 2020].

Prieto, G.A., Thomson, D.J., Vernon, F.L., Shearer, P.M. and Parker, R.L. (2007): Confidence intervals for earthquake source parameters; Geophysical Journal International, v. 168, no. 3, p. 1227–1234, URL <https://academic.oup.com/gji/article/168/3/1227/931413> [August 2020].

Riedel, W. (1929): Zur Mechanik geologischer Bruchscherungen ein Beitrag zum Problem der Fiederspatten; Zentralblatt Mineral. Geol. Paläont., p. 354–368.

Ross, Z.E. and Ben-Zion, Y. (2016): Toward reliable automated estimates of earthquake source properties from body wave spectra; Journal of Geophysical Research: Solid Earth, v. 121, no. 6, p. 4390–4407, URL <https://agupubs.online-library.wiley.com/doi/full/10.1002/2016JB013003> [August 2020].

Ross, Z.E., Ben-Zion, Y., White, M.C. and Vernon, F.L. (2016): Analysis of earthquake body wave spectra for potency and magnitude values: implications for magnitude scaling relations; Geophysical Journal International, v. 207, no. 2, p. 1158–1164, URL <https://academic.oup.com/gji/article/207/2/1158/2583777> [May 2019].

Roth, M.P., Verdecchia, A., Harrington, R.M. and Liu, Y. (2020): High-resolution imaging of hydraulic-fracturing-induced earthquake clusters in the Dawson-Septimus area, northeast British Columbia, Canada; Seismological Research Letters, v. 91, no. 5, p. 2744–2756, URL <https://pubs.geoscience-world.org/ssa/srl/article/91/5/2744/588077/High-Resolu-tion-Imaging-of-Hydraulic-Fracturing> [July 2020].

Ruhl, C.J., Abercrombie, R.E. and Smith, K.D. (2017): Spatiotemporal variation of stress drop during the 2008 Mogul, Nevada, earthquake; Journal of Geophysical Research: Solid Earth, v. 122, no. 10, p. 8163–8180, URL <https://agupubs.onlinelibrary.wiley.com/doi/full/10.1002/2017-JB014601> [August 2020].

Ruscic, M., Bocchini, G.M., Becker, D., Meier, T. and van Keken, P.E. (2019): Variable spatio-temporal clustering of microseismicity in the Hellenic subduction zone as possible indicator for fluid migration; Lithos, v. 346, p. 105154, URL <https://www.sciencedirect.com/science/article/abs/pii/S0024493719303056> [August 2019].

Schultz, R., Stern, V., Novakovic, M., Atkinson, G. and Gu, Y.J. (2015): Hydraulic fracturing and the Crooked Lake sequences: insights gleaned from regional seismic networks; Geophysical Research Letters, v. 42, no. 8, p. 2750–2758, URL <https://agupubs.onlinelibrary.wiley.com/doi/full/10.1002/2015GL063455> [April 2020].

Shen, L.W., Schmitt, D.R. and Haug, K. (2019): Quantitative constraints to the complete state of stress from the combined borehole and focal mechanism inversions: Fox Creek, Alberta; Tectonophysics, v. 764, p. 110–123, URL <https://www.sciencedirect.com/science/article/abs/pii/S0040195119301477> [May 2020].

Skoumal, R. J., Brudzinski, M.R. and Currie, B.S. (2015): Distinguishing induced seismicity from natural seismicity in Ohio: demonstrating the utility of waveform template matching; Journal of Geophysical Research, v. 120, no. 9, p. 6284–6296, URL <https://agupubs.onlinelibrary.wiley.com/doi/full/10.1002/2015JB012265%4010.1002/%28ISSN%291944-8007.FRACKING> [April 2020].

Viegas, G., Abercrombie, R.E. and Kim, W.Y. (2010): The 2002 M5 Au Sable Forks, NY, earthquake sequence: source scaling relationships and energy budget; Journal of Geophysical Research, v. 115, no. B7, URL <https://agupubs.onlinelibrary.wiley.com/doi/full/10.1029/2009JB006799> [August 2020].

Wang, B., Harrington, R.M., Liu, Y., Kao, H. and Yu, H. (2020): A study on the largest hydraulic-fracturing-induced earthquake in Canada: observations and static stress-drop estimation; Bulletin of the Seismological Society of America, URL <https://pubs.geoscienceworld.org/ssa/bssa/article/110/5/2283/587916/A-Study-on-the-Largest-Hydraulic-Fracturing> [July 2020].

Wang, R. (1999): A simple orthonormalization method for stable and efficient computation of Green's functions; Bulletin of the Seismological Society of America, v. 89, no. 3, p. 733–741, URL <https://pubs.geoscienceworld.org/ssa/bssa/article/89/3/733/120414> [September 2020].

Yang, W., Peng, Z. and Ben-Zion, Y. (2009): Variations of strain-drops of aftershocks of the 1999 İzmit and Düzce earthquakes around the Karadere-Düzce branch of the North Anatolian Fault; Geophysical Journal International, v. 177, no. 1, p. 235–246, URL <https://academic.oup.com/gji/article/177/1/235/729018> [September 2020].

Yu, H., Harrington, R.M., Kao, H., Liu, Y., Abercrombie, R.E. and Wang, B. (2020): Well proximity governing stress drop variation and seismic attenuation associated with hydraulic fracturing induced earthquakes; Journal of Geophysical Research: Solid Earth, v. 125, no. 9, URL <https://agupubs.onlinelibrary.wiley.com/doi/full/10.1029/2020JB020103> [September 2020].

Analysis of the Seismogenic Activation Potential in the Montney Formation, Northeastern British Columbia and Northwestern Alberta (Parts of NTS 083, 084, 093, 094)

P. Wozniakowska[1], Department of Geoscience, University of Calgary, Calgary, Alberta, paulina.wozniakowska@ucalgary.ca

D.W. Eaton, Department of Geoscience, University of Calgary, Calgary, Alberta

Introduction

Hydraulic fracturing is used in unconventional resource development to enhance the fluid migration in low-permeability reservoirs. It involves the creation of complex fracture systems during injection of fluids at pressures exceeding in situ breakdown pressures (Smith and Shlyapobersky, 2000). In recent years, hydraulic-fracturing technology has been associated with earthquakes reaching moment magnitudes (M_W) of 5.2 (Lei et al., 2019). Although the basic requirements for generating induced seismicity are well understood (e.g., Ellsworth, 2013; Eaton, 2018), current physical models fail to explain all the fundamental characteristics. One of the extensively studied features is the spatially clustered distribution of induced earthquakes (Skoumal et al., 2015), which has commonly been observed in the Montney Formation (Atkinson et al., 2016; Schultz et al., 2017; Eaton and Schultz, 2018) as well as in other unconventional plays in Canada (Bao and Eaton, 2016; Schultz and Wang, 2020), the United States (Skoumal et al., 2019) and China (Dengfa et al., 2019). Spatial clustering implies a similar underlying distribution of the geological susceptibility to fault activation by hydraulic fracturing.

To date, multiple models have been proposed that seek to explain the physical basis for this apparent variability of geological susceptibility to induced seismicity (Schultz et al., 2016; Shah and Keller, 2017; Pawley et al., 2018). In this study, a machine-learning approach is used to investigate the spatial distribution of the seismogenic activation potential (SAP) in the Montney Formation in British Columbia (BC) and Alberta, where industrial activities have triggered earthquakes of magnitudes as high as M_W 4.6 (Babaie Mahani et al., 2017). The SAP is a probabilistic measure of geological susceptibility to induced earthquake during hydraulic-fracturing operations.

Machine learning has proven to be a helpful tool in many geoscientific areas, including seismic-data processing (Chen et al., 2019), earthquake detection (Perol et al., 2018) and structural interpretation (Huang et al., 2017; Wrona et al.; 2018). Due to its ability to analyze patterns in multidimensional datasets, it can be effectively used to investigate complex relationships and provide additional insights into the mechanisms controlling the occurrence of seismicity induced by hydraulic fracturing (Pawley et al, 2018).

The goal of this study is to reveal underlying mechanisms for seismicity occurring on critically stressed faults in response to elevated pore-fluid pressure. This work is a continuation of the analysis presented in Wozniakowska and Eaton (2020), which investigated the primary factors controlling induced seismicity in the Montney using tree-based algorithms. In the current study, an alternative machine-learning approach (logistic regression) is introduced, the input data and seismicity catalogue are enhanced, and a preliminary seismogenic activation potential map is created for the Montney play.

The project database consisted of 6466 hydraulically fractured horizontal wells and related geological, geomechanical and tectonic characteristics. Each well was classified as seismogenic or nonseismogenic using spatiotemporal association criteria related to seismicity induced by hydraulic fracturing. The next step involved training a supervised machine-learning model to determine the factors controlling the induced seismicity potential in the Montney. In addition, probabilities of seismogenic class determined for each sample were used to estimate the SAP distribution for the whole formation. Based on the results, it appears that seismogenic potential is primarily influenced by the distance to the Cordilleran foreland thrust-and-fold belt and the depth of fractioning-fluid injection. A logistic-regression model predicted the highest occurrence of SAP in the
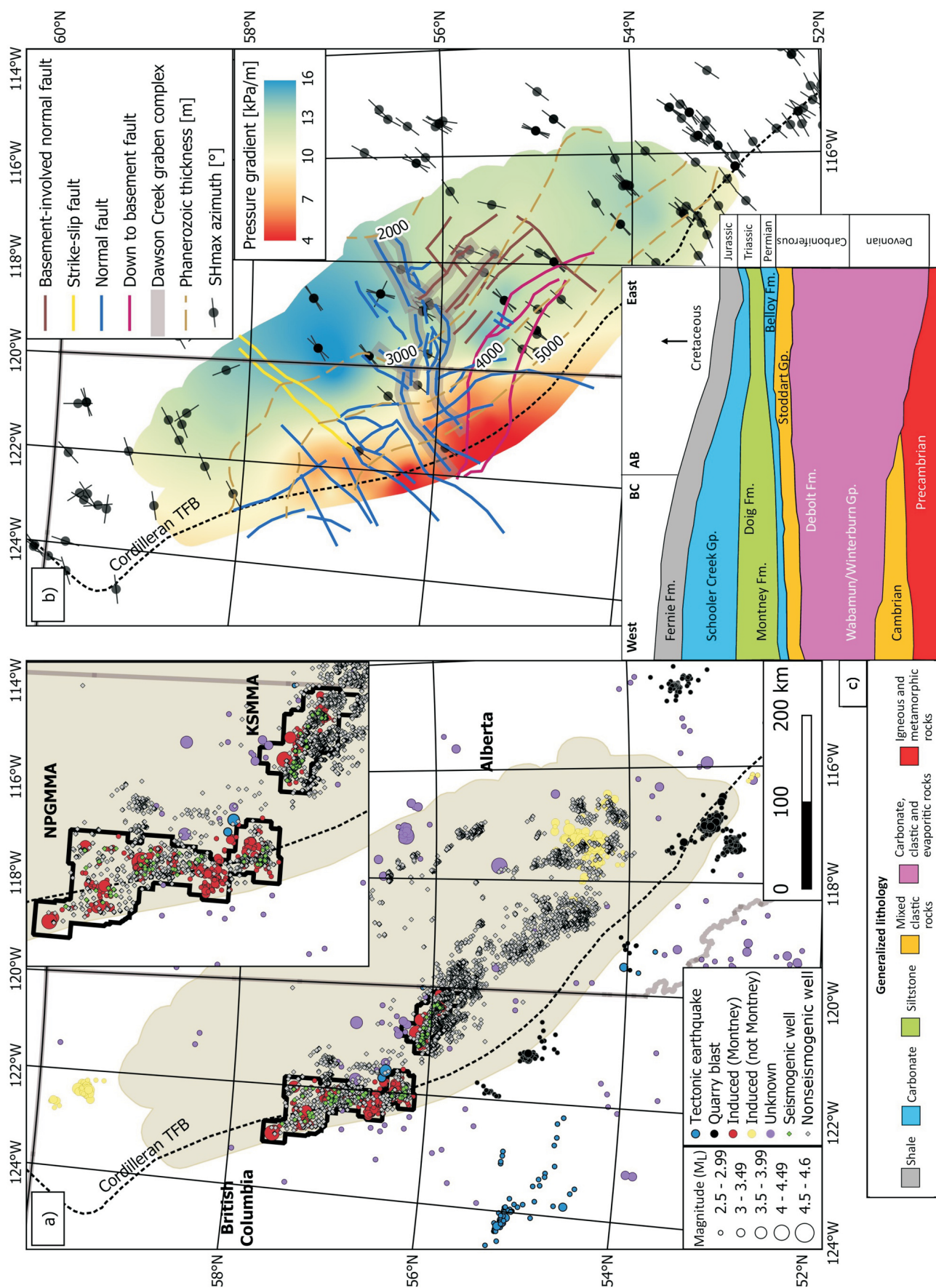
Figure 1. The Montney unconventional play (shaded area), showing **a)** seismic magnitude (coloured circles) by category for the period of March 22, 2006 to January 21, 2020, seismogenic (green dots) and nonseismogenic (grey dots) hydraulically fractured horizontal wells drilled into the Montney Formation, the western edge of the Cordilleran foreland thrust-and-fold belt (TFB; dashed line), as well as the North Peace Ground Motion Monitoring Area (NPGMMA) and Kiskatinaw Seismic Monitoring and Mitigation Area (KSMMA) outlined in black (BC Oil and Gas Commission, 2017; Fox and Watson, 2019); **b)** examples of input data used in the study, including maximum horizontal stress (S_{Hmax}) azimuths (Heidbach et al., 2018), Phanerozoic thickness isolines, and known faults influencing the middle and lower units of the Montney (coloured lines) according to type (after Furlong et al., 2020) within the Dawson Creek graben complex; **c)** schematic cross-section through northeastern BC and western Alberta (at about 56°N) of the generalized lithology and age (modified from Liseroudi et al., 2020). Abbreviations: Fm., Formation; Gp., Group.

northwestern part of the Montney, which is consistent with observed seismicity patterns in BC and Alberta (Figure 1a).

Methodology

Input Parameters Description

One of the biggest challenges of machine-learning analysis is data compilation and preprocessing. Incomplete or incorrect information will result in biased predictions. It is important to include all potentially relevant features, as well as potentially insignificant and less obvious characteristics, as the significance (or lack thereof) of each characteristic will be manifested in the feature importance analysis.

The selection of features for this study was dependent on availability of data that could assist in examining current hypotheses concerning the factors influencing SAP distribution in the Montney Formation. As no direct measurements were available for some of the features, proxies were used that were assumed to have a similar correlation with induced seismicity. Interpolated values were used in the case of those features for which no point data were available (see below). Input parameters used in this study and the reasons for their inclusion are presented in Table 1.

Seismicity Data Compilation

Seismicity data (Figure 1a) were compiled from publicly available catalogues provided by Natural Resources Canada (Visser et al., 2017; Huang et al., 2020; Visser et al., 2020), Alberta Energy Regulator (https://ags-aer.maps.arcgis.com) and Canadian Induced Seismicity Collaboration (Cui et al., 2015). The final catalogue included the events from the period between January 1, 2006 and January 21, 2020. The spatial and temporal variability of the magnitude of completeness was investigated to determine the threshold of the seismicity that would guarantee unbiased classification of hydraulically fractured wells. Magnitude of completeness for the 2006–2013 period ranged from local magnitude (M_L) = 2.0 for southwestern Alberta to M_L 3.0 in the northeastern corner of Alberta

(Stern et al., 2013; Schultz et al., 2015; Cui and Atkinson, 2016). More recent catalogues (2014–2016) are estimated to have a magnitude of completeness of M_L = 1.8 (northeastern BC and western Alberta), whereas the rest of the Western Canada Sedimentary Basin was estimated at M_L~2.3. Considering the detectability thresholds throughout the entire period, only earthquakes above M_L 2.5 were considered for this analysis; the threshold was based on the local magnitude (M_L), which was the primary magnitude scale used for the compiled seismic catalogues. Natural earthquakes and seismicity associated with industrial activities other than hydraulic fracturing in the Montney were removed from the analysis. Data removed included quarry blasts (Dokht et al., 2020), saltwater disposal wells and hydraulic fracturing in other unconventional plays, including the Duvernay Formation (Schultz et al., 2017; Eaton and Schultz, 2018), and drilling activity in the Horn River Basin (BC Oil and Gas Commission, 2012; Farahbod et al., 2015).

Well Labels

A spatiotemporal association filter was implemented to label wells as seismogenic or nonseismogenic. Following previously published studies that investigated induced seismicity in western Canada (e.g., Atkinson et al., 2016), wells were identified as seismogenic if one (or more) induced earthquakes above M_L 2.5 had occurred after the start of hydraulic-fracturing operations (to establish potential causality) and within three months after operations were completed (the maximum estimated lag time). To address the uncertainty of earthquake location, a spatial constraint was applied specifying that the event epicentre had to be located within 5 km of the horizontal wellbore.

Data Preprocessing and Model Development

Feature Interpolation

The compilation of features for machine-learning analysis required interpolation of irregularly sampled input data. Data-point values, such as formation tops, pressure and maximum horizontal-stress values, were interpolated to determine the values corresponding to each of the wells, which were then inspected to ensure that valid interpolated values had been obtained. For example, data were analyzed to ensure correct stratigraphic association (Montney Formation – Debolt Formation – Precambrian basement), depth of the hydraulic-fracturing operation (approximated by the true vertical depth of the well) within the Montney Formation, as well as depth-index values (correct values are indicated by depth index ranging between 0 and 1; Table 1). Erroneous wells were excluded from further analysis. Only horizontal wells were considered, as production had ended at nearly all Montney vertical wells before the start of this analysis. The final dataset consisted of 6466 hydraulically fractured wells spread over a significant area of

Table 1. Description of the input parameters used in the analysis of the seismogenic activation potential in the Montney Formation.

Characteristic	Background
Distance to the Cordilleran deformation front	Distance from the deformation front is used here as a proxy for tectonic strain (Kao et al., 2018).
Injection depth	Injection depth is used here as a proxy for the target-formation depth, documented to strongly correlate with probability of induced seismicity (Ries et al., 2020).
Vertical distance to top of Precambrian basement	Previous studies suggest higher susceptibility in the vicinity of crystalline basement (Hincks et al., 2018; Kozłowska et al., 2018; Skoumal et al., 2018).
Pore-pressure gradient	A correlation between induced seismicity and formation overpressure has been identified by Eaton and Schultz (2018) and Ries et al. (2020).
Difference between local and regional average S_{Hmax} direction	Rotation of maximum horizontal-stress direction (S_{Hmax}) may be indicative of nearby critically stressed fault (McLellan et al., 2014; Zhang et al., 2019).
Vertical distance to Debolt Formation	This massive carbonate unit is documented to host larger magnitude induced seismicity (Riazi et al., 2020).
Depth index (fractional depth from top to base of Montney)	Completions in the lower and middle units of the Montney appear to be more prone to induce seismicity compared to those in the upper and middle units (BC Oil and Gas Commission, 2014).
Distance to the closest (known) fault	Virtually all currently existing models for seismicity induced by hydraulic fracturing assume that slip occurs on a pre-existing fault (Eaton, 2018).

the study region (Figure 1a). Part of the machine-learning process involved randomly splitting the total number of wells into a training set (including labeled samples, used to determine the model coefficients) and a testing set (including unlabeled samples, used to evaluate the performance of the model; James et al., 2013). Implementing a standard train-test split ratio (75:25) resulted in 4849 samples being assigned to the training set and 1617 samples to the testing set.

Logistic Regression

Logistic regression is a type of supervised machine learning (James et al., 2013); for an n-dimensional problem the classification probability p is given by

$$p = 1 / \left(1 + e^{-\left[\beta_0 + \beta_1 * x_1 + \dots + \beta_n * x_n \right]} \right) \qquad (1)$$

where x_i, $i = 1,\dots 7$, are the normalized input-data values at each well location and the parameter weights β_i are calculated during the training phase. Probabilities calculated for each well and coefficients of the model were obtained by averaging individual realizations over 1000 bootstrap samples. Wells with $p > 0.5$ are labelled as seismogenic, whereas samples with lower probabilities correspond to nonseismogenic wells.

Results

Feature Importance Analysis

Feature importance was investigated using the weights extracted from the trained logistic-regression model. The al-

gorithm was developed using scikit-learn, a Python library for machine learning. Ultimate feature weights correspond to average weights of the normalized input parameters from the multiple bootstrap realizations (Equation 1). The values of the model coefficients are indicative of the relative influence of each parameter on the classification results (Molnar, 2019). Based on this analysis, distance to the Cordilleran foreland thrust-and-fold belt and depth of the hydraulic-fracturing operation are the two most important characteristics controlling the SAP. The vertical distance to the top of the Precambrian basement, the difference between local and regional S_{Hmax} and the pore-pressure gradient are moderately important. Remaining parameters (i.e., vertical distance to the Debolt Formation, depth index and distance to known faults) have no influence on SAP distribution (Figure 2a).

SAP Distribution Map

A map of the SAP distribution was created based on the probability of the seismogenic class for each hydraulically fractured well; probabilities were interpolated using a radial-basis function (Lazzaro and Montefusco, 2002). The extrapolation outside the location of the wells over the regular grid yielded values beyond the [0,1] range; therefore, normalization was done to obtain the values matching the realistic probability values (Figure 3). Virtually all higher magnitude ($M_L = 2.5$) earthquakes induced by hydraulic fracturing occurred within the Kiskatinaw Seismic Monitoring and Mitigation Area (KSMMA) and the North Peace Ground Motion Monitoring Area (NPGMMA); both seis-
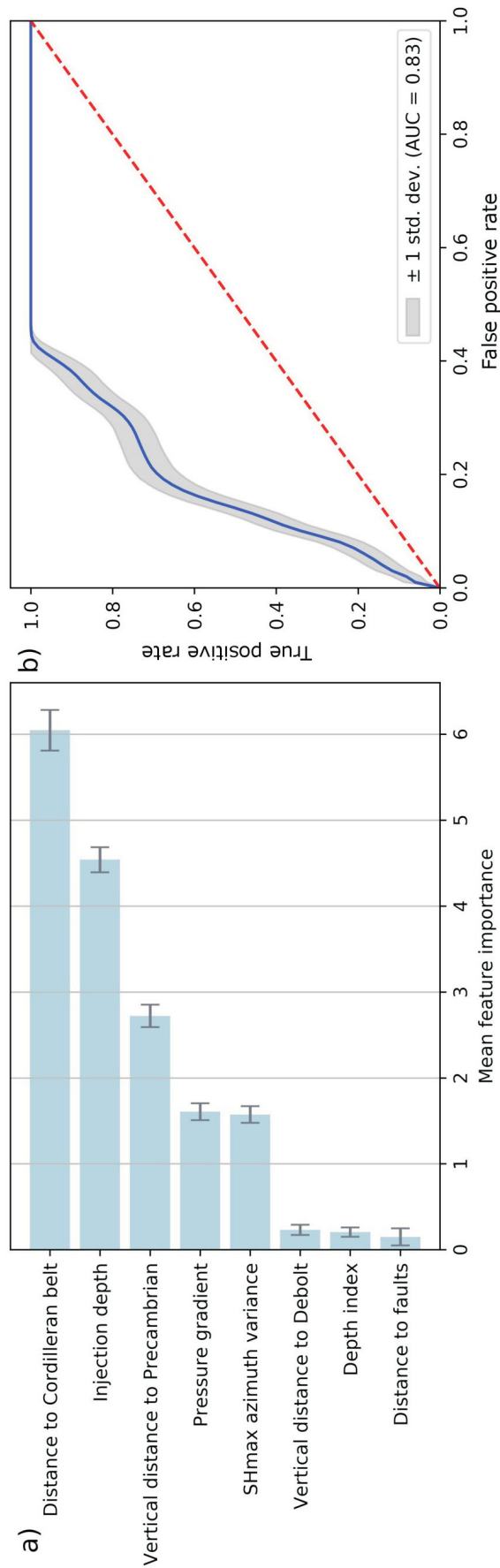
Figure 2. a) Logistic-regression model coefficients. **b)** Average receiver operating characteristic (ROC) curve calculated using 1000 stratified random shuffles (shaded area represents one standard deviation). Abbreviations: AUC, area under the ROC curve; Debolt, Debolt Formation; std. dev., standard deviation.
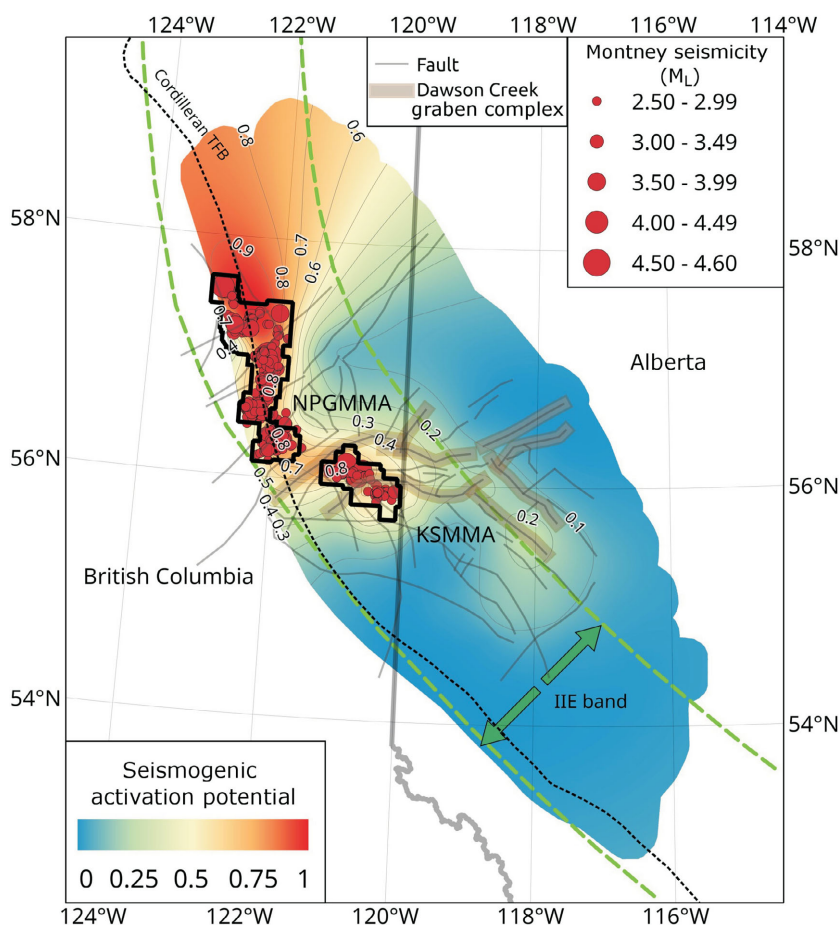
Figure 3. Seismogenic activation potential (SAP) in the Montney Formation. The red circles indicate local magnitude (M_L) =2.5 seismic events associated with hydraulic fracturing in the Montney Formation. Black outlines correspond to seismicity monitoring areas. Approximate range of the injection-induced earthquake (IIE) band is marked by the green dashed lines (after Kao et al., 2018). Cordilleran foreland thrust-and-fold belt (TFB; black dashed line), known faults and Dawson Creek graben complex are also shown. Abbreviations: KSMMA, Kiskatinaw Seismic Monitoring and Mitigation Area; NPGMMA, North Peace Ground Motion Monitoring Area.

micity monitoring areas correspond to areas of higher seismogenic potential (SAP > 0.5; Figure 3).

The highest SAP values (>0.8) are located north of the NPGMMA in BC, whereas the KSMMA region is characterized by a slightly lower SAP, reaching ~0.8 only in its western part. Within Alberta, the SAP of the Montney does not exceed 0.5, excluding a small portion in its northern part, where no hydraulic fracturing operations have yet taken place.

Performance Evaluation

Performance of the machine-learning algorithm was evaluated using the receiver operating characteristics (ROC) curve, which plots the true positive rate versus the false positive rate (Figure 2b) for the validation dataset (Davis and Goadrich, 2006). The area under the ROC curve of the logistic-regression model achieved a score of 0.83, as com-

pared to a value of 0.5 corresponding to the accuracy of random guesses. However, this study is an example of unbalanced classification, characterized by an unequal ratio between samples in one of the specific classes (majority of wells are nonseismogenic). Therefore, metrics other than the ROC may be more suitable to evaluate the performance of the predictive model (Saito and Rehmsmeier, 2015). Hence, the 'recall' score was computed, as it may be better suited to induced-seismicity classification since it quantifies the correct positive class predictions (correctly predicted seismogenic wells) relative to the all positive predictions (both correctly and incorrectly predicted seismogenic wells). 'Recall' is defined as

Recall = true positives/(true positives + false negatives)

The study model achieved a recall score of 77.92%, which provides a good indication that the approach was successful.

Discussion

The results of this study can be compared with those of recent studies that investigated the seismogenic potential in other unconventional plays. It is important to note that choice of input parameters strictly depends on the availability of data and the geological setting of the specific region. Despite the differences in the input features, individual trends can be used to determine the major parameters influencing the induced-seismicity potential in each of the unconventional plays.

For example, Pawley et al. (2018) used a similar machine-learning technique to investigate the SAP distribution in the Duvernay Formation. Their analysis revealed that seismogenic potential in the Duvernay play is influenced by the vertical proximity to the crystalline basement, formation overpressure and minimum horizontal-stress value. In the model developed for this study, distance to the Precambrian basement was shown to be less important than the distance to the Cordilleran foreland thrust-and-fold belt and the depth of hydraulic-fracturing operations.

In contrast to the commonly established mechanisms regarding induced seismicity on pre-existing faults (Eaton, 2018), influence of the known fault structures is not supported by any of these models. Specifically, the distance to known faults both in the Montney and the Duvernay formations was indicated as one of the least important features. Information about the location, type and stress state of the faults in the area is inferred to likely be incomplete. Other geological proxies can be used to infer the potential location of unmapped faults. For example, the presence of lithium-rich brines can be indicative of the faults acting as hydrogeological pathways connecting upper sedimentary layers with the Precambrian basement (Pawley at al., 2018). Further work is needed to obtain lithium-concentration data throughout the Montney play.

As noted above, distance to the western edge of the Cordillera emerges as the most important factor controlling the distribution of SAP in the Montney. This appears to be consistent, at least in part, with the hypothesis of Kao et al. (2018) regarding the correlation of SAP with areas showing an elevated rate of tectonic strain. However, this association does not explain the apparent difference in seismicity levels for Montney wells located at an equivalent distance from the deformation front in BC and Alberta.

Conclusions and Future Work

In this study, a machine-learning approach was used to investigate the spatial variability of induced seismicity in the Montney Formation during hydraulic-fracturing operations. Areas with higher values of the calculated SAP are congruent with the observed pattern of induced seismicity. The map (Figure 3) indicates lower SAP values for the

Montney in Alberta, which is consistent with seismicity observations. Multiple hypotheses were tested regarding the factors controlling the potential of fault-slip activation during hydraulic fracturing. The model shows that SAP in the Montney play is primarily controlled by proximity to the Cordilleran deformation front and the depth of fluid injection during hydraulic-fracturing operations. The area of highest SAP (>80%) occurs in the northwestern part of the subsurface extent of the Montney Formation, which is outside both the KSMMA and NPGMMA seismic monitoring regions. Planned future research will include incorporation of new input parameters and enhancement of key sources of data currently being used. More complete information about the distribution and stress state of the faults in the area, the influence of operational parameters and the distinctions between events triggered by completions performed in the upper, middle and lower units of the Montney present some of the current limitations that need to be addressed to better understand the complex mechanisms driving seismicity induced by hydraulic fracturing in the Montney Formation.

Acknowledgments

References

Atkinson, G.M., Eaton, D.W., Ghofrani, H., Walker, D., Cheadle, B., Schultz, R., Shcherbakov, R., Tiampo, K., Gu, J., Harrington, R.M. and Liu, Y. (2016): Hydraulic fracturing and seismicity in the Western Canada Sedimentary Basin; Seismological Research Letters, v. 87, no. 3, p. 631–647, URL <https://www.inducedseismicity.ca/wp-content/uploads/2015/01/r16_Atkinson-et-al_Hydraulic-Fracturing-and-Seismicity-in-the-Western-Canada-Sedimentary-Basin.pdf> [March 2016].

Babaie Mahani, A., Schultz, R., Kao, H., Walker, D., Johnson, J. and Salas, C. (2017): Fluid injection and seismic activity in the northern Montney play, British Columbia, Canada, with special reference to the 17 August 2015 M$_W$ 4.6 induced earthquake; Bulletin of the Seismological Society of America, v. 107, no. 2, p. 542–552, URL <https://www.ernstversusencana.ca/wp-content/uploads/2017-April-Mahani-et-al-Fluid-injection-seismic-Activity-in-N-Monteney-Play-BC-w-special-ref-to-Aug-17-2005-4.6M-induced-earthquake.pdf> [February 2017].

Bao, X. and Eaton, D.W. (2016): Fault activation by hydraulic fracturing in western Canada; Science, v. 354, no. 6318, p. 1406–1409, URL <https://science.sciencemag.org/content/354/6318/1406> [December 2016].

BC Oil and Gas Commission (2012): Investigation of observed seismicity in the Horn River Basin; BC Oil and Gas Commission, Technical Report, 29 p., URL <http://www.bcogc.ca/node/8046/download> [August 2012].

BC Oil and Gas Commission (2014): Investigation of observed seismicity in the Montney Trend; BC Oil and Gas Commission, Technical Report, 32 p., URL <https://www.bcogc.ca/files/reports/Technical-Reports/investigation-observed-seismicity-montney-trend.pdf> [December 2014].

BC Oil and Gas Commission (2017): Guidance for ground motion monitoring and submission; BC Oil and Gas Commission, 2 p., URL <https://www.bcogc.ca/files/operations-documentation/Induced-Seismicity-Data-and-Submission/ground-motion-guidance-document-december-20-release-2017.pdf> [December 2017].

Chen, Y., Zhang, M., Bai, M. and Chen, W. (2019): Improving the signal-to-noise ratio of seismological datasets by unsupervised machine learning; Seismological Research Letters, v. 90, no. 4, p. 1552–1564, URL <https://www.seismosoc.org/wp-content/uploads/2019/07/SRL-90.3-Machine-Learning.pdf> [July 2019].

Cui, L. and Atkinson, G.M. (2016): Spatiotemporal variations in the completeness magnitude of the Composite Alberta Seismicity Catalog (CASC); Seismological Research Letters, v. 87, no. 4, p. 853–863, URL <https://doi.org/10.1785/0220150268>.

Cui, L., Fereidoni, A. and Atkinson, G.M. (2015): Compilation of Composite Alberta Seismicity Catalog (CASC) for earthquake hazard from induced seismicity in Alberta; American Geophysical Union–Geological Association of Canada–Mineralogical Association of Canada–Canadian Geophysical Union, Joint Assembly, May 3–7, 2015, Montréal, Québec, poster presentation, URL <https://www.inducedseismicity.ca/wp-content/uploads/2015/01/AlbertaCompCat2020-01-1.zip> [November 2015].

Davis, J. and Goadrich, M. (2006): The relationship between Precision-Recall and ROC curves; *in* Proceedings of the 23rd International Conference on Machine Learning, W. Cohen and A. Moore (ed.), June 25–29, 2006, Pittsburgh, Pennsylvania, p. 233–240, URL <https://doi.org/10.1145/1143844.1143874>.

Dengfa, H.E., Renqi, L.U., Huang, H., Xiaoshan, W., Jiang, H. and Zhang, W. (2019): Tectonic and geological setting of the earthquake hazards in the Changning shale gas development zone, Sichuan Basin, SW China; Petroleum Exploration and Development, v. 46, no. 5, p. 1051–1064, URL <https://www.sciencedirect.com/science/article/pii/S1876380419602624?via%3Dihub> [October 2019].

Dokht, R.M., Smith, B., Kao, H., Visser, R. and Hutchinson, J. (2020): Reactivation of an intraplate fault by mine-blasting events: implications to regional seismic hazard in Western Canada; Journal of Geophysical Research: Solid Earth, v. 125, no. 6, art. e2020JB019933, URL <https://doi.org/10.1029/2020JB019933>.

Eaton, D.W. (2018): Passive seismic monitoring of induced seismicity: fundamental principles and application to energy technologies; Cambridge University Press, Cambridge, United Kingdom, 360 p.

Eaton, D.W. and Schultz, R. (2018): Increased likelihood of induced seismicity in highly overpressured shale formations; Geophysical Journal International, v. 214, no. 1, p. 751–757, URL <https://www.inducedseismicity.ca/wp-content/uploads/2015/01/r18_Eaton-and-Schultz_Increased-likelihood-of-IS-in-highly-overpressured-shale-formations.pdf> [July 2018].

Ellsworth, W.L. (2013): Injection-induced earthquakes; Science, v. 341, no. 6142, 7 p., URL <https://science.sciencemag.org/content/341/6142/1225942> [July 2013].

Farahbod, A.M., Kao, H., Walker, D.M. and Cassidy, J.F. (2015): Investigation of regional seismicity before and after hydraulic fracturing in the Horn River Basin, northeast British Columbia; Canadian Journal of Earth Sciences, v. 52, no. 2, p. 112–122, URL <https://doi.org/10.1139/cjes-2014-0162>.

Fox, A.D. and Watson, N.D. (2019): Induced seismicity study in the Kiskatinaw Seismic Monitoring and Mitigation Area, British Columbia; report prepared by Enlighten Geoscience Ltd. for the BC Oil and Gas Commission, 51 p., URL <https://www.bcogc.ca/files/reports/Technical-Reports/final-report-enlighten-geoscience-kssma-phase-1-study-2019w-appendices-links.pdf> [June 2019].

Furlong, C.M., Gingras, M.K. and Zonneveld, J.P. (2020): High-resolution sequence stratigraphy of the Middle Triassic Sunset Prairie Formation, Western Canada Sedimentary Basin, north-eastern British Columbia; The Depositional Record, v. 6, no. 2, p. 383–408, URL <https://doi.org/10.1002/dep2.107>.

Heidbach, O., Rajabi, M., Cui, X., Fuchs, K., Müller, B., Reinecker, J., Reiter, K., Tingay, M., Wenzel, F., Xie, F., Ziegler, M.O., Zoback, M.-L. and Zoback, M. (2018): The World Stress Map database release 2016: crustal stress pattern across scales; Tectonophysics, v. 744, p. 484–498, URL <https://doi.org/10.1016/j.tecto.2018.07.007>.

Hincks, T., Aspinall, W., Cooke, R. and Gernon, T. (2018): Oklahoma's induced seismicity strongly linked to wastewater injection depth; Science, v. 359, no. 6381, p. 1251–1255, URL <https://science.sciencemag.org/content/359/6381/1251.full> [March 2018].

Huang, L., Dong, X. and Clee, T.E. (2017): A scalable deep learning platform for identifying geologic features from seismic attributes; The Leading Edge, v. 36, no. 3, p. 249–256, URL <https://doi.org/10.1190/tle36030249.1>.

Huang, G.D., Kao, H. and Gu, Y.J. (2020): A comprehensive earthquake catalogue for southwestern Alberta, between 2004 and 2015; Geological Survey of Canada, Open File 8705, 49 p., URL <https://doi.org/10.4095/321826>.

James, G., Witten, D., Hastie, T. and Tibshirani, R. (2013): An introduction to statistical learning – with applications in R; Springer-Verlag, New York, New York, 426 p., URL <https://doi.org/10.1007/978-1-4614-7138-7>.

Kao, H., Hyndman, R., Jiang, Y., Visser, R., Smith, B., Babaie Mahani, A., Leonard, L., Ghofrani, H. and He, J. (2018): Induced seismicity in western Canada linked to tectonic strain rate: implications for regional seismic hazard; Geophysical Research Letters, v. 45, no. 20, p. 11 104–11 115, URL <https://doi.org/10.1029/2018GL079288>.

Kozłowska, M., Brudzinski, M.R., Friberg, P., Skoumal, R.J., Baxter, N.D. and Currie, B.S. (2018): Maturity of nearby faults influences seismic hazard from hydraulic fracturing; Proceedings of the National Academy of Sciences, v. 115, no. 8, p. E1720–E1729, URL <https://www.pnas.org/content/115/8/E1720> [February 2018].

Lazzaro, D. and Montefusco, L.B. (2002): Radial basis functions for the multivariate interpolation of large scattered data sets; Journal of Computational and Applied Mathematics, v. 140, no. 1–2, p. 521–536, URL <https://core.ac.uk/download/pdf/82502771.pdf> [September 2000].

Lei, X., Wang, Z. and Su, J. (2019): The December 2018 M_L 5.7 and January 2019 M_L 5.3 earthquakes in South Sichuan Basin induced by shale gas hydraulic fracturing; Seismological Research Letters, v. 90, no. 3, p. 1099–1110, URL <https://pubs.geoscienceworld.org/ssa/srl/article-abstract/90/3/1099/569798/The-December-2018-ML-5-7-and-January-2019-ML-5-3?redirectedFrom=fulltext> [April 2019].

Liseroudi, M.H., Ardakani, O.H., Sanei, H., Pedersen, P.K., Stern, R.A. and Wood, J.M. (2020): Origin of sulfate-rich fluids in the Early Triassic Montney Formation, Western Canadian Sedimentary Basin; Marine and Petroleum Geology, v. 114, art. 104236, URL <https://doi.org/10.1016/j.marpetgeo.2020.104236>.

McLellan, P., Anderson, I., Wong, J. and Mostafavi, V. (2014): Geomechanical characterization of the Farrell Creek Montney reservoir, northeast British Columbia; GeoConvention 2014, Canadian Society of Petroleum Geologists-Canadian Society of Exploration Geophysicists-Canadian Well Logging Society, Joint Annual Convention, May 12–16, 2014, Calgary, Alberta, extended abstract, 2 p., URL <https://www.researchgate.net/publication/3138-79972_Geomechanical_Characterization_of_the_Farrell_Creek_Montney_Reservoir_Northeast_British_Columbia> [May 2014].

Molnar, C. (2019): Interpretable machine learning – a guide for making black box models explainable; Lulu, 318 p., URL <https://christophm.github.io/interpretable-ml-book/> [November 2020].

Pawley, S., Schultz, R., Playter, T., Corlett, H., Shipman, T., Lyster, S. and Hauck, T. (2018): The geological susceptibility of induced earthquakes in the Duvernay play; Geophysical Research Letters, v. 45, no. 4, p. 1786–1793, URL <https://doi.org/10.1002/2017GL076100>.

Perol, T., Gharbi, M. and Denolle, M. (2018): Convolutional neural network for earthquake detection and location; Science Advances, v. 4, no. 2, art. e1700578, URL <https://doi.org/10.1126/sciadv.1700578>.

Riazi, N., Eaton, D.W., Aklilu, A. and Poulin, A. (2020): Application of focal-time analysis for improved induced seismicity depth control: a case study from the Montney Formation, British Columbia, Canada; Geophysics, v. 85, no. 6, p. 1–70, URL <https://prism.ucalgary.ca/handle/1880/112701> [October 2020].

Ries, R., Brudzinski, M.R., Skoumal, R.J. and Currie, B.S. (2020): Factors influencing the probability of hydraulic fracturing-induced seismicity in Oklahoma; Bulletin of the Seismological Society of America, v. 110, no. 5, p. 2272–2282, URL <https://doi.org/10.1785/0120200105>.

Saito, T. and Rehmsmeier, M. (2015): The precision-recall plot is more informative than the ROC plot when evaluating binary classifiers on imbalanced datasets; PloS ONE, v. 10, no. 3, 21 p., URL <https://doi.org/10.1371/journal.pone.0118432>.

Schultz, R. and Wang, R. (2020): Newly emerging cases of hydraulic fracturing induced seismicity in the Duvernay East Shale Basin; Tectonophysics, v. 779, art. 228393, URL <https://doi.org/10.1016/j.tecto.2020.228393>.

Schultz, R., Corlett, H., Haug, K., Kocon, K., MacCormack, K., Stern, V. and Shipman, T. (2016): Linking fossil reefs with earthquakes: geologic insight to where induced seismicity occurs in Alberta; Geophysical Research Letters, v. 43, no. 6, p. 2534–2542, URL <https://doi.org/10.1002/2015GL067514>.

Schultz, R., Stern, V., Gu, Y.J. and Eaton, D. (2015): Detection threshold and location resolution of the Alberta Geological Survey earthquake catalogue; Seismological Research Letters, v. 86, no. 2A, p. 385–397, URL <https://pdfs.semanticscholar.org/c58e/0f16df77818121d-11a9c1128b79e99dd38aa.pdf> [September 2020].

Schultz, R., Wang, R., Gu, Y.J., Haug, K. and Atkinson, G.M. (2017): A seismological overview of the induced earthquakes in the Duvernay play near Fox Creek, Alberta; Journal of Geophysical Research: Solid Earth, v. 122, no. 1, p. 492–505, URL <https://doi.org/10.1002/2016JB-013570>.

Shah, A.K. and Keller, G.R. (2017): Geologic influence on induced seismicity: constraints from potential field data in Oklahoma; Geophysical Research Letters, v. 44, no. 1, p. 152–161, URL <https://doi.org/10.1002/2016GL07-1808>.

Skoumal, R.J., Brudzinski, M.R. and Currie, B.S. (2015): Distinguishing induced seismicity from natural seismicity in Ohio: demonstrating the utility of waveform template matching; Journal of Geophysical Research: Solid Earth, v. 120, no. 9, p. 6284–6296, URL <https://doi.org/10.1002/2015JB012265>.

Skoumal, R.J., Brudzinski, M.R. and Currie, B.S. (2018): Proximity of Precambrian basement affects the likelihood of induced seismicity in the Appalachian, Illinois, and Williston Basins, central and eastern United States; Geosphere, v. 14, no. 3, p. 1365–1379, URL <https://pubs.geoscienceworld.org/gsa/geosphere/article/14/3/1365/530435/Proximity-of-Precambrian-basement-affects-the> [April 2018].

Skoumal, R.J., Kaven, J.O. and Walter, J.I. (2019): Characterizing seismogenic fault structures in Oklahoma using a relocated template matched catalog; Seismological Research Letters, v. 90, no. 4, p. 1535-1543, URL <https://pubs.geoscienceworld.org/ssa/srl/article-abstract/90/4/1535/570858> [May 2019].

Smith, M.B. and Shlyapobersky, J.W. (2000): Basics of hydraulic fracturing; chapter *in* Reservoir Stimulation (3rd edition), M.J. Economides and K.G. Nolte (ed.), John Wiley and Sons, New York, New York, 856 p.

Stern, V.H., Schultz, R.J., Shen, L., Gu, Y.J. and Eaton, D.W. (2013). Alberta earthquake catalogue, version 1.0: September 2006 through December 2010; Alberta Energy Regulator, AER/AGS Open File Report 2013-15, p. 29, URL <https://ags.aer.ca/publication/ofr-2013-15> [September 2013].

Visser, R., Kao, H., Smith, B., Goerzen, C., Kontou, B., Dokht, R.M.H., Hutchinson, J., Tan, F. and Babaie Mahani, A. (2020): A comprehensive earthquake catalogue for the Fort St. John–Dawson Creek region, British Columbia, 2017–2018; Geological Survey of Canada, Open File 8718, 28 p., URL <https://doi.org/10.4095/326015>.

Visser, R., Smith, B., Kao, H., Babaie Mahani, A., Hutchinson, J. and McKay, J. (2017): A comprehensive earthquake catalogue for northeastern British Columbia and western Alberta, 2014–2016; Geological Survey of Canada, Open File, 8335, 28 p., URL <https://doi.org/10.4095/306292>.

Wozniakowska, P. and Eaton, D.W. (2020): Determination of factors controlling geological susceptibility to induced seismicity in the Montney Formation, northeastern British Columbia and northwestern Alberta, based on a machine-learning approach; *in* Geoscience BC Summary of Activities 2019: Energy and Water, Geoscience BC, Report 2020-

02, p. 19–26, URL <http://www.geosciencebc.com/i/pdf/SummaryofActivities2019/EW/Sch_PW_EW_SOA-2019.pdf> [February 2020].

Wrona, T., Pan, I., Gawthorpe, R.L. and Fossen, H. (2018): Seismic facies analysis using machine learning; Geophysics, v. 83, no. 5, p. O83-O95, URL <https://doi.org/10.1190/geo2017-0595.1>.

Zhang, H., Eaton, D., Rodriguez, G., and Jia, S.Q. (2019): Source-mechanism analysis and stress inversion for hydraulic-fracturing-induced event sequences near Fox Creek, Alberta; Bulletin of the Seismological Society of America, v. 109, no. 2, p. 636–651, URL <https://pubs.geoscienceworld.org/ssa/bssa/article-abstract/109/2/636/569194/Source-Mechanism-Analysis-and-Stress-Inversion-for?redirectedFrom=fulltext> [March 2019].

Wastewater Disposal in the Maturing Montney Play Fairway, Northeastern British Columbia (NTS 093P, 094A, B, G, H)

B.J. Hayes, Petrel Robertson Consulting Ltd., Calgary, Alberta, bhayes@petrelrob.com

J.H. Anderson, Reservoir Engineering Consultant, Calgary, Alberta

M. Cooper, Sherwood Geological Consulting, Calgary, Alberta

P.J. McLellan, McLellan Energy Advisors Inc., Calgary, Alberta

B. Rostron, University of Alberta, Edmonton, Alberta

J. Clarke, Petrel Robertson Consulting Ltd., Calgary, Alberta

Introduction

In 2019, British Columbia's Scientific Hydraulic Fracturing Review Panel (2019) identified knowledge gaps in the understanding of water disposal in deep saline aquifers in the Montney play fairway in northeastern British Columbia (BC). The Petrel Robertson Consulting Ltd. (PRCL) team has undertaken a project for Geoscience BC to address these knowledge gaps, consistent with Geoscience BC's strategic objective to support development of the Montney play through technical studies that aid safe oil and gas production and waste fluid disposal.

Study Methodology

Wastewater disposal is a complex issue, and presents varying challenges across the huge Montney play fairway (Figure 1). Recognizing the scope of these challenges, the workplan for this project builds on the experience of Montney play operators, service companies and the British Columbia Oil and Gas Commission (BCOGC), and includes the following elements:

1) consult with operators, service companies and BCOGC staff to best understand disposal requirements and operational experiences;
2) interpret performance of existing disposal wells, paying particular attention to information around regulator-imposed restrictions or shutdowns;
3) build on existing aquifer characterization work to complete updated maps on disposal aquifer distribution, quality and fluid composition;
4) map and assess structural elements across the Montney play fairway to identify discontinuities related to containment risks, and to help understand disposal reservoir geomechanical settings;
5) integrate well test, production and reservoir pressure data with geomechanical data to characterize in situ stresses and rock properties, which can influence disposal aquifer compartmentalization and containment risks;
6) undertake targeted laboratory work to address critical data gaps; and
7) develop practical conclusions and recommendations to guide operators and BCOGC in decisions around development and regulation of disposal capacity and containment across the entire Montney play fairway.

Consultation Findings

Seventeen companies, including wastewater disposal firms, operating in the BC Montney play fairway were consulted. Key points resulting from these consultations include

- many operators manage their own water resources, some in co-operation with other operators in order to maximize recycling and disposal efficiencies;
- recycling is a very important strategy to minimize disposal needs but most companies must dispose of wastewater at least periodically;
- most disposal is into regional aquifers; few companies target depleted oil and gas reservoirs, although some are looking at the option;
- limited disposal reservoir capacity in close proximity to operations is an important issue for many operators;
- seismicity induced by wastewater injection is uncommon but has resulted in curtailment or modification of operations in at least 11 wells to date;
- fluid compatibilities and rock-fluid interactions are critically important in minimizing degradation of injection zone quality; they are managed primarily by careful
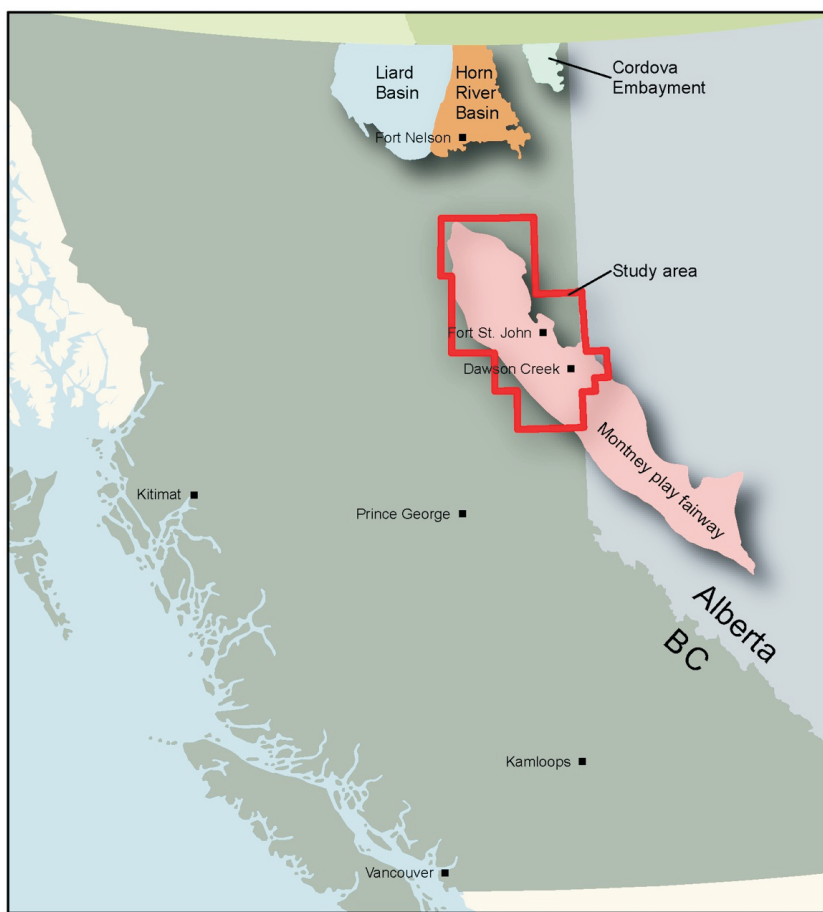
Figure 1. Location of study area within the Montney play fairway of northeastern British Columbia and northwestern Alberta.

monitoring of the water chemistries in fluid batches to be disposed;

- wellbore integrity is not a major issue but operators generally avoid re-entering older wellbores, or those with suspected integrity issues, for disposal purposes.

Consultation with staff at the BCOGC was very productive in understanding their strategies in regulating disposal wells, and in accessing online databases and matters related to induced seismicity.

Review of Existing Disposal Wells

A total of 162 active, suspended and abandoned wastewater disposal wells were found in the study area by inspecting well data files hosted by geoSCOUT (geoLOGIC systems ltd., 2020) and the BCOGC, including 139 in BC and 23 in Alberta (Figure 2). Acid gas disposal wells were not included, nor were water injection wells that provide pressure support in oil fields. Twenty wells tested and/or injected into two disposal zones, and one well tested and/or injected into three disposal zones.

Each disposal zone was assigned to the appropriate stratigraphic interval(s), and relevant data were tabulated to sup-

port the analysis of each aquifer interval across the study area.

Disposal Aquifer Mapping and Characterization

The BCOGC regulations dictate that deep disposal aquifers must lie below the base of usable groundwater, which is defined as between 300 and 600 m below ground surface, and below the Base of Fish Scales stratigraphic marker (BC Oil and Gas Commission, 2020d). Eight formations were identified that offer widespread disposal capacity and have been used as disposal zones in the Montney play area: Peace River (Paddy/Cadotte members), Bluesky, Cadomin, Buick Creek sandstone/Nikanassin, Baldonnel, Halfway, Belloy and Debolt (Figure 3). A small number of wells have disposed of fluids into the Charlie Lake and Spirit River formations, but these wells are very isolated, and regional characterization of the formations would not have been useful in defining additional potential.

Each disposal formation has been mapped and characterized regionally, building on studies in the public domain (e.g., Petrel Robertson Consulting Ltd., 2011, 2015), pro-
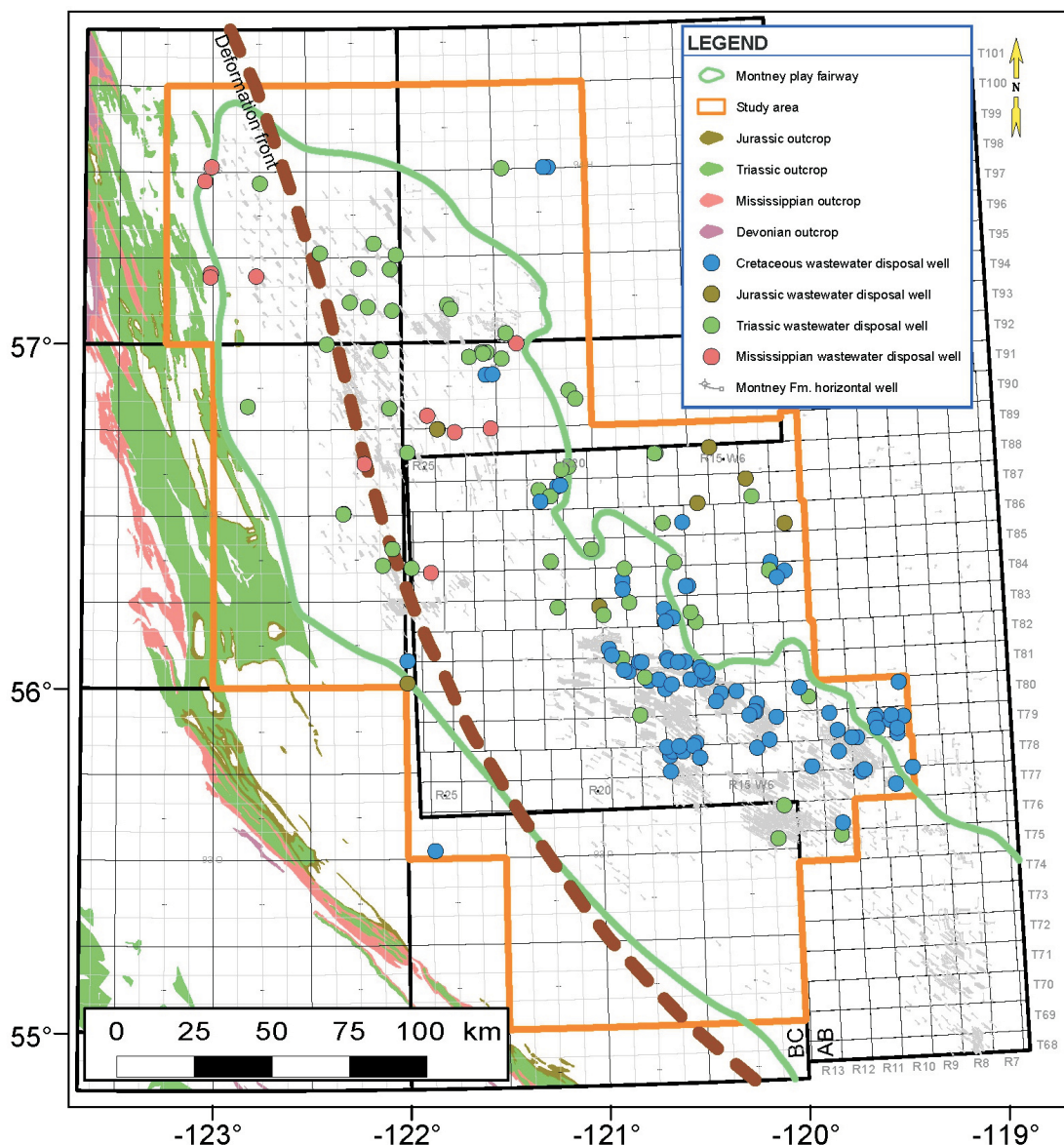
Figure 2. Distribution of existing wastewater disposal wells in the study area, northeastern British Columbia and northwestern Alberta (well data from British Columbia Oil and Gas Commission and geoLOGIC Systems ltd., 2020). Background shows Devonian–Jurassic bedrock outcrops (modified from Cui et al., 2017).

prietary PRCL studies, and new work. Gross thickness, net porous reservoir thickness and depth-to-top formation maps have been prepared as warranted by available data. Most disposal formations exhibit depositional and/or erosional limits that sharply define their distribution and utility.

Figure 4 shows the gross thickness of the Cadomin Formation, one of the major disposal aquifers. The Fox Creek Escarpment defines a sharp northern depositional limit, confining Cadomin Formation disposal zone potential to the southern part of the Montney play fairway. Depth to top of the formation and net porous reservoir mapping (not shown here) demonstrate that the disposal potential of the Cadomin Formation is best in shallower updip areas in the

east, which feature better reservoir quality and most of the Cadomin Formation disposal wells.

Structural Geology Review

To provide a structural framework for the study, data from various sources were compiled on a summary map of structural elements (Figure 5). It is particularly striking that the extrapolation of the Hay River shear zone (HRSZ) southwestwards into the Rocky Mountain fold-and-thrust belt (FTB; yellow chevrons on Figure 5), coincides with significant shifts to the southwest in the eastern limits of the outcrop edge of the FTB, the subsurface eastern limit of the FTB and the eastern limit of the subsurface inversion. To the north of the HRSZ, the edge of the deformed belt is

AQUIFER STRATIGRAPHY
S. REGION NEBC PLAINS

WAPITI

PUSKWASKAU

BAD HEART
MUSKIKI

CARDIUM

SMOKY

KASKAPAU

HOWARD CREEK SS
POUCE COUPE SS
DOE CREEK SS

DUNVEGAN

SHAFTESBURY

FORT ST. JOHN

Base of Fish Scales

Disposal zones must lie below the base of usable groundwater (600 m below ground surface and the Base of Fish Scales marker)

PEACE RIVER

PEACE RIVER — PADDY / CADOTTE / HARMON / NOTIKEWIN

SPIRIT RIVER — FALHER / WILRICH

BLUESKY — BLUESKY

CADOMIN

GETHING

CADOMIN — BUICK CREEK SS — **BUICK CREEK SS**

BULLHEAD

NIKANASSIN

DUNLEVY

NIKANASSIN — NIKANASSIN

FERNIE

PASSAGE BEDS

POKER CHIP SHALE

NORDEGG

PARDONET

SCHOOLER CREEK

BALDONNEL — **BALDONNEL**

CHARLIE LAKE

HALFWAY — **HALFWAY**

DOIG

DAIBER

MONTNEY

ISHBEL

BELLOY — **BELLOY**

STODDART

TAYLOR FLAT

STODDART

KISKATINAW

GOLATA

RUNDLE

DEBOLT — **DEBOLT**

SHUNDA

PEKISKO

BANFF

EXSHAW

Figure 3. Stratigraphic column for northeastern British Columbia (NEBC), highlighting disposal zone aquifers addressed in this paper (modified from BC Ministry of Energy, Mines and Low Carbon Innovation, 2011). Abbreviations: S., south; SS, sandstone.

Belloy thick. There is also an eastward shift in the eastern limit of overpressure in the Montney Formation south of the HRSZ.

A series of seven regional cross-sections is being constructed; the Cameron cross-section is shown in Figure 6. The cross-sections have been constructed using surficial geology, well data within a ±5 km corridor of each section (usually 150–250 wells per section) and limited seismic data. Formation tops for the wells were obtained from the BCOGC website (BC Oil and Gas Commission, 2020b) and validated against formation tops picked by PRCL. Where available, well deviation surveys and dip data have been included. The location of structural highs and lows, stratigraphic erosional and depositional edges, structural and overpressure limits and the HRSZ are shown on the Cameron section (Figure 5). In addition, the locations of oil and gas pools based on the BCOGC shapefiles of pools are also indicated. The cross-section shows a combination of thick- and thin-skinned compressional deformation at the western end of the section with a notable detachment within the Besa River Formation shales. Close to the outcrop edge of the FTB, a major inverted extensional fault creates a broad anticline at Cameron River. Further east there are some low amplitude thin-skinned compressional structures and deeper rooted extensional faults that influence stratigraphic thickness changes from the Devonian to Early Cretaceous and also act as triggers for thin-skinned structures to develop, for example at the Blueberry field (Figure 6).

Reservoir Engineering

The goals of the reservoir engineering work are to evaluate injection efficiency (injectivity index and reservoir storage capacity), as well as comparing and contrasting disposal performance of horizontal with vertical wells, the different disposal formations and their variations across the basin, and deterioration or enhancement of disposal performance with time and injection volumes. The terms injection and disposal are used interchangeably and refer only to wastewater disposal, not to waterflooding or pressure maintenance operations.

The relevant data, including disposal rates versus time, injection wellhead pressures and reservoir pressures, were gathered. The first two types of data are in the production/injection databases (geoLOGIC systems ltd., 2020), but reservoir pressures are more difficult to determine and are found in a variety of sources.

Firstly, the injectivity index, defined as injection rate per pressure gradient from sandface to reservoir (units of bbl/day/psi or m³/day/kilopascal), was estimated. To do this, sandface pressure was estimated using recorded surface pressure plus vertical pressure head to the mid-point of perforations minus frictional pressure losses, using a friction factor derived from commonly used pipeflow correla-

much more diffuse, forming a broad zone extending east of the outcrop edge of the FTB. South of the HRSZ, the surface and subsurface eastern limits of the FTB are essentially coincident. The southwest extension of the HRSZ into the FTB also appears to coincide with the western limit of the Fort St. John graben and the northern edge of the Peace River Arch and with three structural lows: the Hudson Hope low, the Hudson Hope Embayment and the

Figure 4. Gross thickness of Cadomin Formation in the study area. Well data accessed through geoSCOUT (geo-LOGIC systems ltd., 2020).

tions. For reservoir pressure, data recorded by the well operator was used, which included drill-stem test results, static gradients, buildups, falloffs and diagnostic fracture injection test (DFIT) results, judiciously examining the conditions and shut-in times of the tests, and discarding any data that were erroneous or not deemed reasonable. Wellbore pressure calculations were carefully made using data from the same month as the reservoir pressures were taken. Injectivity index estimates were not normalized to formation thickness, although this will be reviewed for the final report.

An injectivity index was obtained for shortly after the start of injection for 86 wells (13 of which were horizontal), for near the end of injection (or present day) for 101 wells (14

horizontal wells), and for both early and late times for 75 wells (13 horizontal wells). Pressure measurement timing varied with operator practice, and so time intervals could not be standardized for these calculations. Obvious anomalies are being evaluated in a handful of wells, but early results indicate that about 30% of the wells showed improved injectivity over time, about 10% stayed the same, and about 60% lost injectivity over time. Not all wells are on the same time scale or have received the same injection. Focusing on the Cadomin Formation as an example, where there are 25 vertical and 6 horizontal disposal wells, the horizontal wells on average showed approximately four times the injectivity index of the vertical wells, and deteriorated less with time: 6% versus 23% (Figure 7).
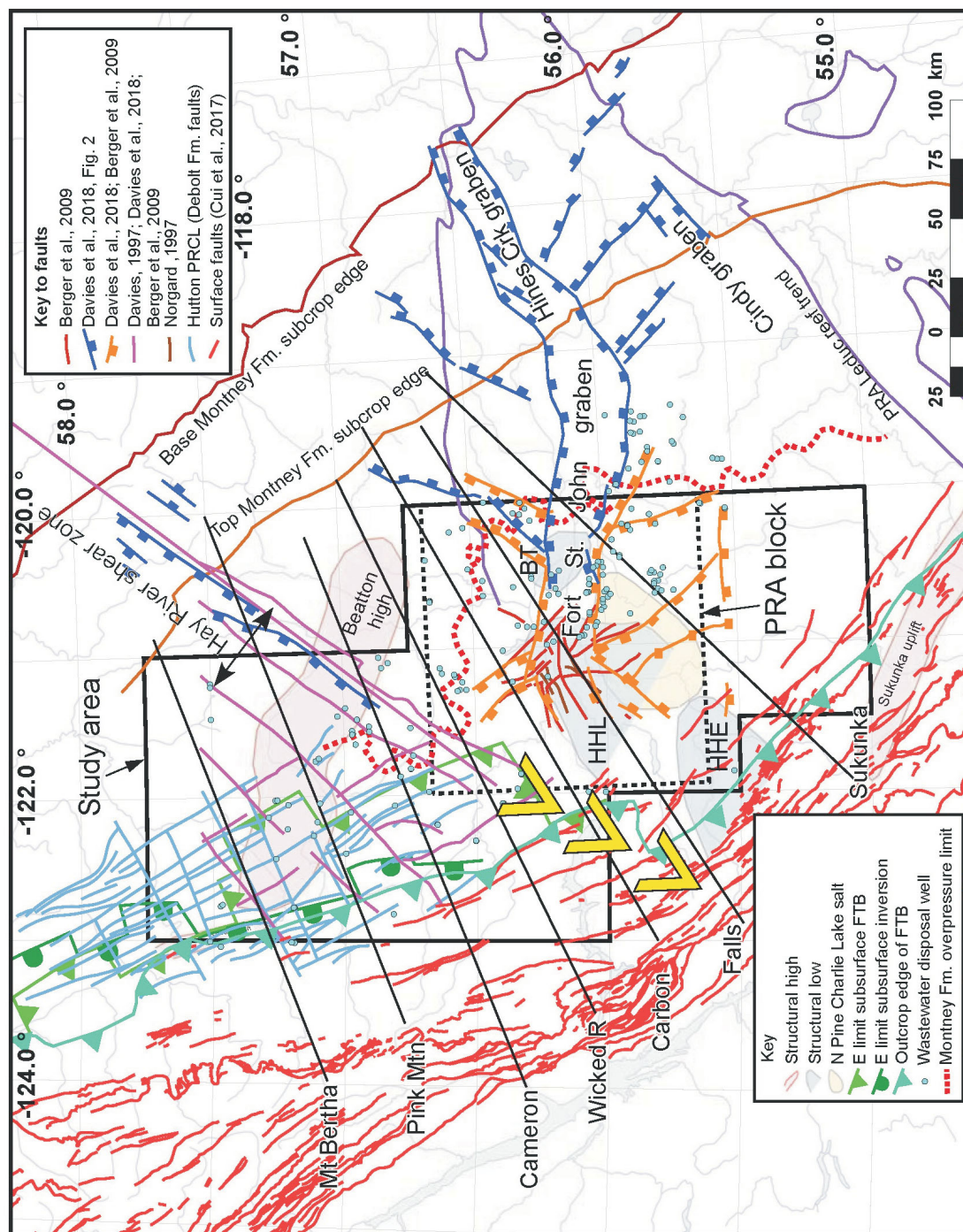
Figure 5. Summary map of structural elements in the study area. Locations of structural highs and lows, top and base of the Montney Formation subcrop edge, eastern limit of Montney Formation overpressure and Leduc reef trend of the Peace River Arch (PRA) are from Davies (1997) and Davies et al. (2018). Outcrop edge of the fold-and-thrust belt (FTB) is based on BC Geological Survey digital bedrock geology (Cui et al., 2017). Subsurface limits of the FTB and inversion have been interpreted based on BC Oil and Gas Commission pool (BC Oil and Gas Commission, 2020c) and well data (BC Oil and Gas Commission, 2020e). The yellow chevrons show the inferred location of the Hay River shear zone projected into the FTB. The North Pine Charlie Lake Formation salt basin is from Davies et al. (2018). Enlighten Geoscience Ltd. kindly provided some of the data as shapefiles (Fox and Watson, 2019). Lines of seven structural cross-sections (thin black lines) are named; the Cameron cross-section is shown in Figure 6. Abbreviations: BT, Belloy thick; E, east; HHE, Hudson Hope Embayment; HHL, Hudson Hope low; N, north.
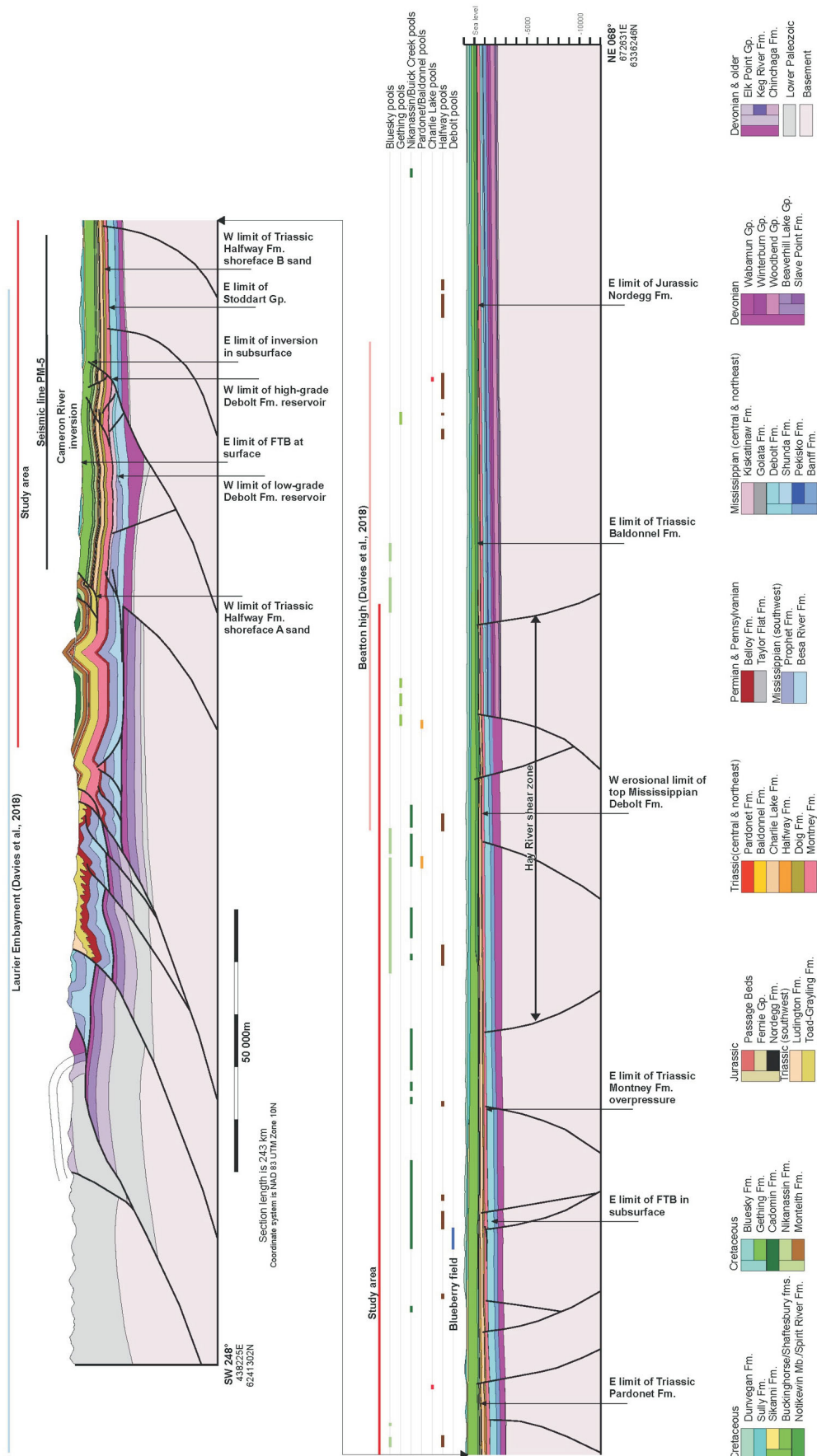
Figure 6. A simplified version of the Cameron structural cross-section showing the structural configuration from the Front Ranges in the southwest to the foreland basin beyond the northeastern edge of the Hay River shear zone (HRSZ). Location of the section is shown on Figure 5. Well data used to construct the section are omitted for clarity but all of the faults and edges shown on Figure 5 are indicated as are all oil and gas pools arranged by the stratigraphic age of the reservoir. Abbreviations: E, east; FTB, fold-and-thrust belt; N, north; S, south; W, west.
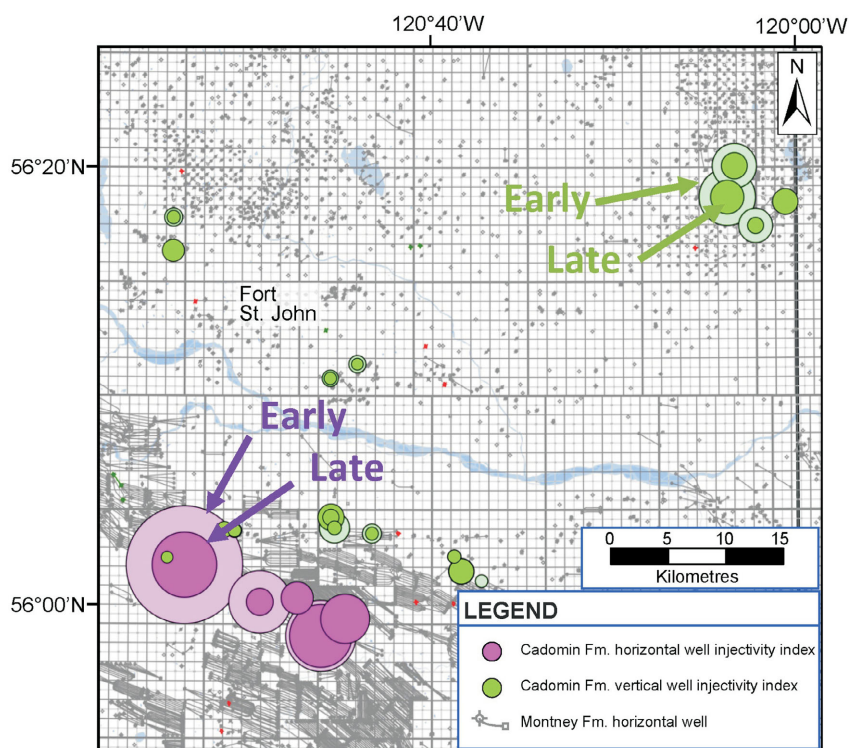
Figure 7. A bubble map showing early and late injectivity indices for Cadomin Formation horizontal and vertical disposal wells in the Fort St. John area. Size of the bubbles is proportional to the injectivity index. Horizontal wells (in magenta) generally show higher injectivity indices than vertical wells, and many of the wells show decreased injectivity over time. Well data accessed through geoSCOUT (geoLOGIC systems ltd., 2020).

Reservoir pressure change was tabulated as a function of water injected over the life of the well. This was intended as a proxy for material balance, a difficult problem because original reservoir saturations prior to injection have not been quantified consistently. One would expect reservoir pressures to rise with continued injection, and the authors expected to compare pressure increases with volumes injected to get a proxy for reservoir size. However, of the 92 wells in this dataset, 15 wells showed a pressure *decrease* with injection, and several more showed no change at all. Some of the wells exhibiting a negative pressure response had been converted from production in the same zone, so it is possible that continued production from offset wells has contributed to this anomaly. Other possibilities include inconsistent pressure measurement procedures or formation fracturing; more work is needed in this aspect of the study. The horizontal wells, with only one exception, behaved as expected, with pressures rising as injection progressed.

Geomechanical Analysis

Basic geomechanical data on horizontal in situ stress orientations and in situ stress magnitudes in wastewater disposal reservoirs are being compiled, analyzed and interpreted. These data are needed for assessing maximum injection pressures to preclude hydraulic fracturing in vertical and horizontal wells, and to conduct risk assessments for fault

reactivation due to high pressure injection. In situ stress investigations for application to wastewater disposal wells have not previously been presented or published, except for an examination of injection potential in the Debolt and Belloy formations in northeastern BC, prepared by Canadian Discovery Ltd. (2015). Considerably more in situ stress data exists for producing oil and gas reservoirs in northeastern BC, such as the Montney play (e.g., McLellan, 2016); however, the scope for stress magnitudes in this project has been limited to data from the disposal formations only.

Orientations of maximum and minimum horizontal stresses (S_{Hmax} and S_{Hmin}) in this part of the Western Canada Sedimentary Basin have typically been determined from borehole breakouts, which are elongations of a drilled borehole cross-section parallel to S_{Hmin} and perpendicular to S_{Hmax}. Elongation of the borehole is usually due to shear failure occurring at the highest concentration of stress around the borehole, which extends for some distance into the borehole wall, and creates a 'breakout angle' on opposite sides of the borehole wall. Weaker rocks like shale host most breakouts, with breakouts being less common in hard stiff carbonate and clastic rocks.

The S_{Hmax} legacy data for northeastern BC were compiled in the in situ stress chapter of the Geological Atlas of Western Canada (Bell et al., 1994). These same data are also shown for the project study area on the World Stress Map (Heidbach et al., 2016), along with more recent horizontal stress determinations using other techniques such as earthquake focal mechanism inversion, sonic log anisotropy and drilling-induced fractures. Haug and Bell (2016) also published a digital file with some additional horizontal stress determinations for Alberta and northeastern BC. The most recent publicly available datasets for horizontal in situ stresses will be compiled on a map and in rose diagrams to be included in the final report for this project. A limited number of new stress determinations have been made for this project.

The S_{Hmax} determinations from earthquake focal mechanism inversion have received attention lately, especially in the Septimus region of northeastern BC, where a magnitude 4.6 earthquake in November 2018 was caused by hydraulic fracturing (Babaie Mahani, 2020). Interestingly, there appears to be a systematic difference between S_{Hmax}

determinations from focal mechanism inversion in this region, compared to the orientation of local borehole breakouts. Possible reasons for this will be offered in the final report.

Of high interest in disposal reservoirs of the study area is the original S_{Hmin} magnitude, which is confidently measured only with a small volume mini-fracture test, often called a Diagnostic Fracture Injection Test (DFIT). However, in the review of disposal well files in the study area it was found that the term DFIT was used loosely by some operators and service companies to describe a variety of injection tests, some of which did not require the creation of a small hydraulic fracture. Only DFITs where a hydraulic fracture was created and an instantaneous shut-in pressure (ISIP) and a fracture closure pressure (FCP) were recorded were used in this geomechanical analysis. Reservoir falloff pressure tests, typically performed to determine reservoir pressure and permeability, are being analyzed in the reservoir engineering part of the project.

Step rate tests (SRT) have been performed by operators in a few disposal wells, but they are surprisingly uncommon. In an SRT, surface injection pressure and rate are increased in a series of steps, designed to find a breakpoint or 'parting pressure' where a hydraulic fracture is created, thereby increasing the injectivity. Subsequent injection pressures are then maintained below the parting pressure. The surface pressure from this crude test is related to the minimum horizontal in situ stress, S_{Hmin}, which must be overcome to initiate a hydraulic fracture. High injection rates and accompanying uncertain pipe and perforation friction losses render SRTs less accurate for stress determinations than DFITs.

As shown in Table 1, DFIT and SRT data have been compiled for the study area from a total of 10 well licenses, which represented 12 formation intervals and one co-mingled disposal interval with two formations. The availability of ISIP, FCP, reservoir pressure (P_r), permeability to water (k_w) and SRT data are noted. The DFITs were performed in two horizontal disposal wells; the rest were in vertical wells. In a few cases, data from a small propped hydraulic fracture treatment in what is now a disposal well were noted in the well records, and ISIP and 15-minute shut in pressure (SIP) data have also been extracted. The final

Table 1. Diagnostic fracture injection test (DFIT) and step rate test (SRT) data for the part of the study area in northeastern British Columbia, from British Columbia Oil and Gas Commission files.

Month and year tested	Well license	Field, operator	Tested formation	ISIP	FCP	P_r	k_w	SRT	Other
Jan 2017	15702	Doe, Arc Resources Ltd.	Bluesky	X	X	X	X		Stimulation fracture
Aug–Sep 2017	20155	Tower, Catapult Water Midstream	Bluesky	X	X	X	X	X	Stimulation fracture
Jan 2017	24350	Doe, Arc Resources Ltd.	Cadomin	X	X	X	X	X	Stimulation fracture
Jan 2015	26920	Dawson, SECURE Energy Services Inc.	Paddy Mb.	X	?	X	X	X	
Feb 2017	27473	Altares, Pacific Canbriam Energy	Baldonnel	X	X	X	X		
Sep 2014	30410	Tower, Tervita Corporation	Cadomin					?	
Oct 2014	30428	Tower, Tervita Corporation	Cadomin					?	
Jan 2019	31016	Altares, Pacific Canbriam Energy	Baldonnel	X	X	X	X		Horizontal well
Sep 2019	31916	Altares, Pacific Canbriam Energy	Charlie Lake	X	X	X	X		Horizontal well
			Baldonnel	X	X	X	X		Horizontal well
			Charlie Lake/ Baldonnel					X	Horizontal well
Dec 2017	35043	Sunrise, Aqua Terra Water Management	Cadomin	X	X	X	X		
			Nikanassin	X	X	X	X		

Abbreviations: FCP, fracture closure pressure (estimated minimun horizontal in situ stress; ISIP, instantaneous shut-in pressure; k_w, permeability to water; P_r, reservoir pressure

report will include an appendix showing all the DFIT, SRT and stimulation-fracture-treatment–derived data, along with other useful calculated metrics and comments on the analyses that were undertaken by service companies, operators and engineering consulting firms.

Trends in the FCP (a proxy for the S_{Hmin} magnitude) and the reservoir pressure will be analyzed for different parts of the study area, and in different formations, especially where they relate to a well's production and injection history. Given the relatively small number of quality FCP tests obtainable from DFITs and SRTs, it is not possible to prepare maps to show spatial trends by geological unit. The DFIT-derived reservoir pressures for disposal wells represent a small subset of the reservoir pressure tests examined in the reservoir engineering part of this study.

Vertical stress gradients have not yet been calculated for the top of any of the key disposal reservoirs at the time of writing. This is usually a straightforward calculation, based on integrating corrected bulk density logs to determine the weight of the overburden to a depth of interest. For the final report, the plan is to produce one illustrative example map of the vertical stress gradient at the top of one disposal unit, likely the Cadomin Formation.

An open-hole completion would be required to obtain an S_{Hmax} determination from a sequence of small hydraulic fractures pumped into a short interval, isolated with packers, or below a bridge plug. No such data were obtained by any operator, according to the records examined. Typically other methods are used to calculate a S_{Hmax} magnitude value using a DFIT-derived S_{Hmin} and assumptions regarding the creation of borehole breakouts or fault reactivation using the stress polygon method (Zoback, 2010). Such estimates were not performed for this project, largely because of the lack of quality data, and the focus on in situ measurements.

Similarly, datasets of high quality laboratory-derived static or dynamic elastic or strength property tests for water disposal units were not found. In a few cases compressional and shear sonic log data were identified in some disposal wells, which could be used to make first order predictions of the dynamic elastic properties. This was not considered a priority task for this project.

On the other hand, a petrophysical property called pore volume compressibility (PVC) is used in some well test analyses and reservoir simulation. It can be a particularly sensitive parameter in stiff systems where water fills the pore space, such as wastewater disposal operations. The authors are currently considering a laboratory program with one of the project partners to evaluate the range of stress-dependent PVC values typical of one of the most common disposal formations in this project.

Incidents of wastewater injection–induced seismicity in the study area have been compiled by the BCOGC. The common learnings from these cases, based on the injection metrics, geological and geomechanical setting, including the proximity to major faults, will be examined. The BC Oil and Gas Commission (2020a) cited 11 wells known to have produced high levels of seismicity that resulted in their operations being curtailed or modified by the BCOGC. Only 3 of these 11 wells had DFITs where FCP (i.e., S_{Hmin}) data were obtained. As such it was not deemed a priority in this study to undertake fault reactivation predictions, given the paucity of quality in situ stress magnitude and rock mechanical property data.

Future Work

Two components of the project are in the early stages: regional assessment of aquifer fluid properties and pressure regimes, and supplemental lab work to address data gaps regarding geomechanical properties. The authors are currently engaged in both areas, guided by the progress to date in consistently defining distribution and characteristics of disposal aquifers and the relevant datasets.

Work will conclude with compilation of information from all the study components, assessment and comparison of the performance of each major disposal aquifer, and discussion of future disposal potential in the context of maximizing efficiency and minimizing containment risks.

Acknowledgments

References

Babaie Mahani, A. (2020): Systematic study of earthquake source mechanism and regional stress field in the southern Montney unconventional play of northeastern British Columbia (NTS 093P/09, 10, 15, 16, 094A/01, 02, 07, 08); *in* Geoscience BC Summary of Activities 2019: Energy and Water, Geoscience BC, Report 2020-02, p. 13–18, URL <http://www.geosciencebc.com/i/pdf/SummaryofActivities2019/EW/Project%202012-SEIS01_EW_SOA-2019.pdf> [October 2020].

BC Ministry of Energy, Mines and Low Carbon Innovation (2011): Stratigraphic correlation chart northeastern British Columbia and adjacent parts of Alberta, Yukon and Northwest Territories; BC Ministry of Energy, Mines and Low Carbon Innovation, URL <https://www2.gov.bc.ca/gov/content/industry/natural-gas-oil/petroleum-geoscience/sedimentary-basins-of-bc/northeastern-bc-basin> [November 2020].

BC Oil and Gas Commission (2020a): Approvals; BC Oil and Gas Commission, URL <https://www.bcogc.ca/data-reports/reservoir-management/reservoir-approvals/> [October 2020].

BC Oil and Gas Commission (2020b): Drilling data for all wells in BC [BCOGC 41984]; BC Oil and Gas Commission, Data Centre, URL <https://www.bcogc.ca/data-reports/data-centre/>.

BC Oil and Gas Commission (2020c): Pool contours; BC Oil and Gas Commission, open data portal, URL <https://data-bcogc.opendata.arcgis.com/datasets/c9c7ebb8c12041-ddab4c93685269ddec_0>.

BC Oil and Gas Commission (2020d): Technical guidance for determine the "base of usable groundwater"; in Oil & Gas Operations Manual, Appendix E, p. 200–201, URL <https://www.bcogc.ca/files/operations-documentation/Oil-and-Gas-Operations-Manual/ogaom-appendix-e.pdf> [October 2020].

BC Oil and Gas Commission (2020e): Well surface hole locations (permitted); BC Oil and Gas Commission, open data portal, URL <https://data-bcogc.opendata.arcgis.com/datasets/9149cb556e694617970a5774621af8be_0>.

Bell, J.S., Price, P.R. and McLellan, P.J. (1994): In-situ stress in the Western Canada Sedimentary Basin; in Geological Atlas of the Western Canada Sedimentary Basin, G.D. Mossop and I. Shetsen (comp.), Canadian Society of Petroleum Geologists, Calgary, Alberta, and Alberta Research Council, Edmonton, Alberta, URL <https://ags.aer.ca/reports/chapter-29-situ-stress> [October 2020].

Berger, Z., Boast, M. and Mushayandebvu, M. (2009): The contribution of integrated HRAM studies to exploration and exploitation of unconventional plays in North America, Part 2, basement structures control on the development of the Peace River Arch's Montney/Doig resource plays; Canadian Society of Petroleum Geologists, Reservoir, v. 36, p. 40–45.

Canadian Discovery Ltd. (2015): Characterization of Belloy and Debolt water disposal zones in the Montney play fairway, NEBC; Geoscience BC Report 2015-14, 30 p., URL <http://cdn.geosciencebc.com/project_data/GBC_Report2015-14/GBCReport2015-14_report.pdf> [November 2020].

Cooper, M.A. (2000): Structural style variations in the BC Foothills; Geological Association of Canada–Mineralogical Association, Joint Annual Meeting (GeoCanada 2000), May 29–June 2, 2000, Calgary, Alberta, Program with Abstracts, v. 25, conference CD, abstract 466, 4 p.

Cui, Y., Miller, D., Schiarizza, P. and Diakow, L.J. (2017): British Columbia digital geology; BC Ministry of Energy, Mines and Low Carbon Innovation, BC Geological Survey, Open File 2017-8, 9 p., data version 2019-12-19, URL <https://www2.gov.bc.ca/gov/content/industry/mineral-exploration-mining/british-columbia-geological-survey/geology/bcdigitalgeology> [February 2020].

Davies, G.R. (1997): The Triassic of the Western Canada Sedimentary Basin: tectonic and stratigraphic framework, paleogeography, paleo-climate and biota; Bulletin of Canadian Petroleum Geology, v. 45, p. 434–460.

Davies, G., Watson, N., Moslow, T. and MacEachern, J. (2018): Regional subdivisions, sequences, correlations and facies relationships of the Lower Triassic Montney Formation, west-central Alberta to northeastern British Columbia, Canada — with emphasis on role of paleostructure; Bulletin of Canadian Petroleum Geology, v. 66, no. 1, p. 23–92.

geoLOGIC systems ltd. (2020): geoSCOUT version 8.12; geoLOGIC systems ltd., URL <https://www.geologic.com/products/geoscout/>.

Fox, A.D. and Watson, N.D. (2019): Induced Seismicity Study in the Kiskatinaw Seismic Monitoring and Mitigation Area, British Columbia; report prepared for the BC Oil and Gas Commission, 51 p., URL <https://www.bcogc.ca/data-reports/reports/?year=2019> [November 2020].

Haug, K. and Bell, J.S. (2016): Compilation of in-situ stress data from Alberta and northeastern British Columbia; Alberta Energy Regulator, AER/AGS Digital Data 2016-0040.

Heidbach, O., Rajabi, M., Reiter, K. and Ziegler, M. (2016): World stress map 2016; GFZ Data Services, URL <https://doi.org/10.5880/WSM.2016.002>.

McLellan, P.J. (2016): Geomechanical characterization of the Farrell Creek Montney reservoir, northeast British Colombia; SPE Workshop: The Montney Play, Society of Petroleum Engineers, October 18, 2016, Calgary, Alberta, workshop presentation.

Norgard, G.T. (1997): Structural inversion of the Middle Triassic Halfway Formation, Monias Field, northeast British Columbia; Bulletin of Canadian Petroleum Geology, v. 45, p. 614–623.

Petrel Robertson Consulting Ltd. (2011): Deep subsurface aquifer characterization in support of Montney tight gas development: geological report; Geoscience BC, Report 2011-11, 386 p., URL <http://www.geosciencebc.com/reports/gbcr-2011-11/> [October 2020].

Petrel Robertson Consulting Ltd. (2015): Characterization of Belloy and Debolt water disposal zones in the Montney play fairway, NEBC; Geoscience BC, Report 2015-03, 43 p., URL <http://cdn.geosciencebc.com/project_data/GBC_Report2015-03/GBCReport2015-03_report.pdf> [October 2020].

Scientific Hydraulic Fracturing Review Panel (2019): Scientific review of hydraulic fracturing in British Columbia; BC Ministry of Energy, Mines and Low Carbon Innovation, final report, 220 p., URL <https://www2.gov.bc.ca/assets/gov/farming-natural-resources-and-industry/natural-gas-oil/responsible-oil-gas-development/scientific_hydraulic_fracturing_review_panel_final_report.pdf> [February 2019].

Zoback, M. (2010): Reservoir Geomechanics; Cambridge University Press, Cambridge, United Kingdom, 452 p., URL <https://doi.org/10.1017/CBO9780511586477> [October 2020].

Isotopic Fingerprinting of Sulphur Sources for the Hydrogen Sulphide Gas in the Montney Formation, Northeastern British Columbia (NTS 093O, P, 094A, B, G–J, N–P)

G.R.L. Chalmers, The University of the Sunshine Coast, Sippy Downs, Australia, gchalmers@usc.edu.au

R.M. Bustin, The University of British Columbia, Vancouver, British Columbia

A.A. Bustin, The University of British Columbia, Vancouver, British Columbia

Introduction

The Triassic Montney Formation in northern British Columbia (BC) and Alberta is a significant unconventional gas producer and is calculated to have contributed 34% to the total 2017 natural gas production of Canada (National Energy Board, 2018). The distribution and concentration of hydrogen sulphide in the Montney Formation in BC is complex, with no clear trends across the regional hydrocarbon play or even within the local scale of multiwell pads (Chalmers et al., 2019). This uncertainty can be problematic for operators when planning and designing operations and production, as unexpected souring increases production costs due to special infrastructure required for handling sour gas. Understanding the sour gas risk informs operators and increases lead times for acquiring bulk sour gas service infrastructure, thereby reducing costs.

Hydrogen sulphide in petroleum systems can generate from a variety of processes, which include 1) thermal sulphate reduction; 2) bacterial sulphate reduction; 3) kerogen cracking; and 4) sulphide oxidation and/or decomposition of surfactants used for well completions. The authors are investigating the sources of sulphur that contribute to the formation of hydrogen sulphide in the Montney Formation, in order to decrease the uncertainty of encountering hydrogen sulphide during operations and production. The isotopic ratio of sulphur within the hydrogen sulphide gas can be used to identify the sources of the sulphur, as the isotopic ratio of sulphur sources varies according to formation processes and the geological period of sulphur source development (i.e., Triassic versus Devonian sulphates). The authors are using this variation in sulphur isotopic ratios to determine the sources of the hydrogen sulphide in the Montney Formation in BC. These data are used to develop a model for hydrogen sulphide formation, which can provide

recommendations to future well planning in the Montney Formation.

Methods

To determine the source(s) of sulphur that contributes to the formation of hydrogen sulphide in the Montney Formation, the authors have sampled drill cuttings from the 100/01-29-082-19W6/02 well (geoLOGIC systems ltd., 2019; Figure 1). Samples were collected from the Charlie Lake, Halfway, Doig, Montney and Belloy formations. Mineralogy of the samples were identified by X-ray diffraction (XRD). Crushed samples (to particle size <250 μm) were mixed with ethanol, hand-ground in a mortar and pestle and then smear mounted on glass slides for XRD analysis (Munson et al., 2016). A normal-focus cobalt X-ray tube was used on a Siemens Diffraktometer D5000 at 40 kilivolts (kV) and 40 milliamperes (mA). The mineral composition was quantified by Rietveld analysis (Rietveld, 1967) using Bruker AXS TOPAS v.3.0 software.

The hydrogen sulphide sampling was performed by Stratum Reservoir, LLC (Calgary, Alberta). The separation technique by Seal et al. (2000) was used to isolate sulphur (sulphate) from the anhydrite mineral fraction in bulk samples. Between 20 and 30 g of sample were then cleaned by refluxing the organic solvent, toluene, within a soxhlet apparatus for a minimum of three days. Samples were dried at 110°C for 24 hours and then ground to –250 μm. Samples were then placed in a 100 mL solution of Na_2CO_3 (5% by mass) and magnetically stirred for two hours. This procedure converts the sulphate from a solid to aqueous phase. The mixture is filtered through a Büchner funnel and the solution is acidified to a pH of <4 using 20% HCl. To precipitate sulphate as a solid, 100 mL of $BaCl_2.H_2O$ (20% by mass) is added to the filtered solution and the sulphate precipitates as pure barium sulphate (baryte). The baryte is filtered and dried in the oven at 110°C overnight. All baryte samples were sent to the Ján Veizer Stable Isotope Laboratory (Ottawa, Ontario) to measure both the sulphur and oxygen isotopic ratios.
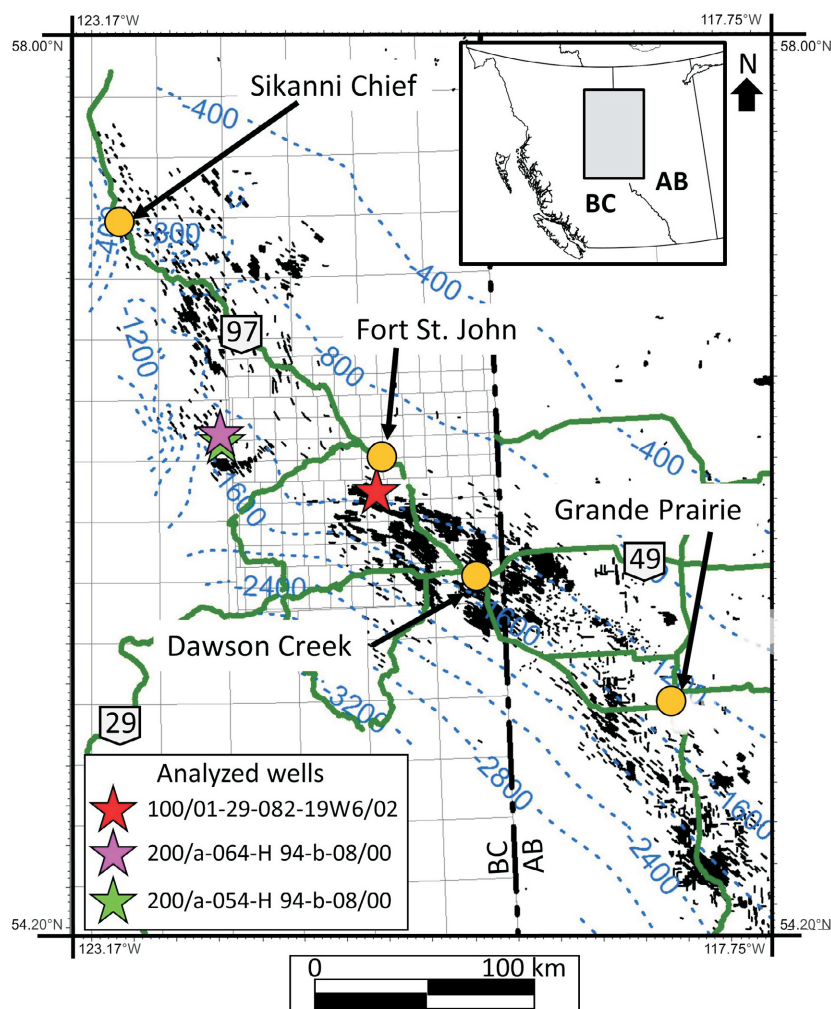
Figure 1. Location of the three wells analyzed in this study, northeastern British Columbia and northwestern Alberta. The depth contours (blue dashed lines) are to the top of the Montney Formation and are measured in subsea true vertical depth (SSTVD; metres). Orange circles represent major population centres in the region and the green lines are the primary roads. Well data (black dots) from geoLOGIC systems ltd. (2019).

Results

The mineralogy of the Charlie Lake, Halfway, Doig, Montney and Belloy formations in well 100/01-29-082-19W6/02 is shown in Table 1. The Charlie Lake Formation has the highest anhydrite content (18.6–42.6%) and the Montney Formation contains between 0.6 and 1.0%. The Halfway, Doig and Belloy formations contain between 0.3 and 0.7%.

The sulphur and oxygen isotopic ratios for anhydrite and hydrogen sulphide gas are shown for wells 200/a-054-H 094-b-08/00, 200/a-064-H 094-b-08/00 and 100/01-29-082-19W6/02 (geoLOGIC systems ltd., 2019) in Table 2 and Figure 2. The δ^{34}S sulphur isotopic ratios for the anhydrite in the Charlie Lake Formation range between 14.2 and 15.0‰. The δ^{18}O oxygen isotopic ratios for the anhydrite in the Charlie Lake Formation range between 7.69 and 8.86‰. The δ^{34}S sulphur isotopic ratios for the anhydrite in the Montney Formation range between 13.3 and 14.5‰. The δ^{18}O oxygen isotopic ratios for the anhydrite in the Montney Formation range between –1.0 and 0.2‰. The δ^{34}S sulphur isotopic ratios for hydrogen sulphide range between 12.4 and 20.9‰. Claypool et al. (1980) and Machel (1985) collected Devonian anhydrite samples across the Western Canada Sedimentary Basin. Their analyses showed that the δ^{34}S sulphur isotopic ratios range between 19.4 and 31.6‰, whereas the δ^{18}O oxygen isotopic ratios range between 12.9 and 28.3‰ (Figure 2).

Discussion

In well 100/01-29-082-19W6/02, the Charlie Lake Formation contains the highest anhydrite content (18.6–42.6%) whereas the Halfway, Doig, Montney and Belloy formations show minor anhydrite contents ranging between 0.3

Table 1. Mineralogy of the Charlie Lake, Halfway, Doig, Montney and Belloy formations in well 100/01-29-082-19W6/02 (geoLOGIC systems ltd., 2019).

Sample ID	Formation	Depth (TVD; m)	Anhydrite	Gypsum	Pyrite	Quartz	Feldspars	Clays	Carbonates	Fluorapatite
PBN-1	Charlie Lake	1392.5	42.6	0.3	0	9.1	7.5	4.1	38.1	0
PBN-2	Charlie Lake	1430	19.9	0.1	0	11.5	10.9	6.8	54.7	0
PBN-3	Charlie Lake	1467.5	21.7	0	0	14.6	12.4	9.3	43.4	0
PBN-4	Charlie Lake	1542.5	18.6	0	0	13.1	10.3	16.2	49.2	0
PBN-5	Halfway	1592.5	0.4	0.1	0.8	65.5	9.2	5.4	22.3	0
PBN-6	Doig	1642.5	0.4	0	1.2	31.5	8.5	31.2	50.1	7
PBN-7	Doig	1722.5	0.7	0	1.5	21.5	20.7	27.2	40.4	5.9
PBN-8	Doig	1757.5	0.3	0	2.4	19.7	14.3	36.8	52.4	7.3
PBN-9	Montney	1770	0.9	0	1.7	33.9	25.7	18	32.2	2.5
PBN-10	Montney	1790	1.0	0	2.2	26.7	38.4	11.2	26.8	0.3
PBN-11	Montney	1820	0.9	0	1.8	27.8	40.5	9.2	22	0
PBN-12	Montney	1857.5	0.6	0	2.4	30.9	33.4	12.8	24.7	0
PBN-13	Montney	1972.5	0.6	0	2.6	25.8	38.7	13.6	22.6	0
PBN-14	Belloy	2073.5	0.6	1.7	0.5	9.4	1.7	3.3	85.7	0

Abbreviation: TVD, total vertical depth
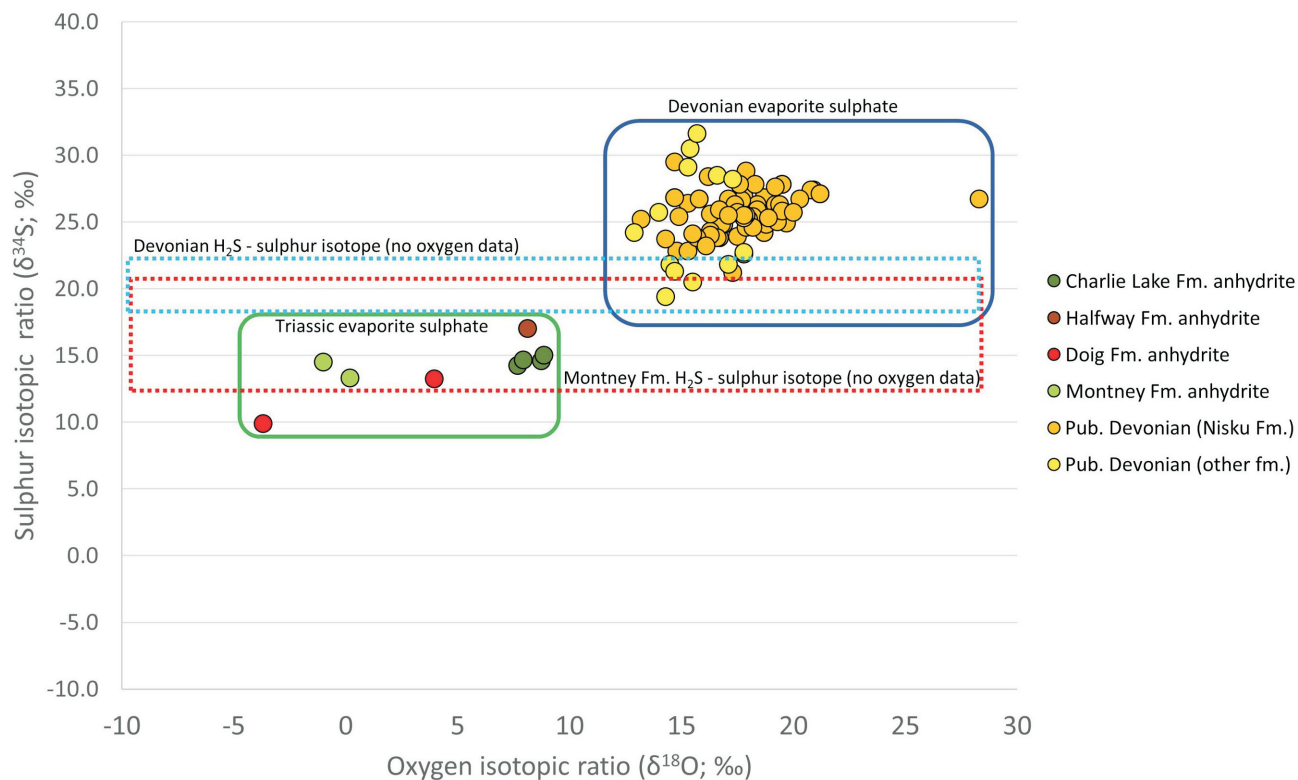
Figure 2. The sulphur and oxygen isotopic data from mineral separation of sulphate (anhydrite) from the Triassic Charlie Lake, Halfway, Doig and Montney formations in well 100/07-30-082-19W6M/00 (geoLOGIC systems ltd., 2019) and from the Devonian strata in the Western Canada Sedimentary Basin. Sulphur isotopic ratios for hydrogen sulphide are shown as dashed boxes for Montney Formation (red dashed box) and for Devonian reservoirs (blue dashed box; Krouse et al., 1988). Published (Pub.) sulphur and oxygen isotopic data for anhydrite from the Devonian strata are from Machel (1985) and Claypool et al. (1980). Sulphur isotopic ratios for hydrogen sulphide in the Montney Formation were obtained from wells 100/01-29-082-19W6/02, 200/a-064-H 094-b-08/00 and 200/a-054-H 094-b-08/00 (geoLOGIC systems ltd., 2019).

Table 2. The sulphur and oxygen isotopic ratios for anhydrite in the Charlie Lake, Halfway, Doig and Montney formations. Sulphur isotopic ratios for hydrogen sulphide gas are shown for three Montney Formation producing wells (200/a-054-H 094-b-08/00, 200/a-064-H 094-b-08/00, 100/01-29-082-19W6/02; geoLOGIC systems ltd., 2019). Anhydrite was collected from well 100/01-29-082-19W6/02. Note, isotopic analyses were not conducted on sulphate minerals from wells 200/a-054-H 094-b-08/00 and 200/a-064-H 094-b-08/00.

Sample ID	Formation	Depth (TVD; m)	δ^{34}S of anhydrite (‰ VCDT)	δ^{18}O of anhydrite (‰ VSMOW)	δ^{34}S of H$_2$S gas (‰ VCDT)
PBN - 1	Charlie Lake	1392.5	14.2	7.69	-
PBN - 2	Charlie Lake	1430.0	14.6	8.75	-
PBN - 3	Charlie Lake	1467.5	14.7	7.94	-
PBN - 4	Charlie Lake	1542.5	15.0	8.86	-
PBN - 5	Halfway	1592.5	17.0	8.14	-
PBN - 6	Doig	1642.5	13.2	3.96	-
PBN - 7	Doig	1722.5	9.9	-3.69	-
PBN - 10	Montney	1790.0	14.5	-1.0	-
PBN - 13	Montney	1972.5	13.3	0.2	-
100/01-29-082-19W6/02	Montney	1794.5	-	-	16.9
200/a-064-H 094-b-08/00	Montney	2127.6	-	-	12.4
200/a-054-H 094-b-08/00	Montney	2336.0	-	-	20.9

Abbreviations: TVD, total vertical depth; VCDT, Vienna Canyon Diablo Troilite; VSMOW, Vienna Standard Mean Ocean Water

and 1.0%. In the same well, sulphur and oxygen isotopic analyses results for the anhydrite are similar in range for all samples with δ^{34}S sulphur isotopic ratios ranging between 9.9 and 17.0‰ and δ^{18}O oxygen isotopic ratios ranging between –3.69 and 8.86‰. These values differ markedly from the published sulphur and oxygen isotopic ratios for anhydrite in Devonian rocks. The δ^{34}S sulphur isotopic ratios for Devonian anhydrite range between 19.4 and 31.6‰ and the δ^{18}O oxygen isotopic ratios range between 12.9 and 28.3‰ (Claypool et al., 1980; Machel, 1985; Figure 2). The difference between the Triassic and Devonian anhydrite isotopic ratios is used by the authors to identify the sources of the hydrogen sulphide gas within the Montney Formation in BC. The δ^{34}S sulphur isotopic ratios for hydrogen sulphide gas in the three Montney Formation producing wells range between 12.4 and 20.9‰ (Table 2, Figure 2) and indicate the sulphur source for the hydrogen sulphide is either from Triassic anhydrite or a mixture of Triassic and Devonian anhydrite. Results show that the sulphur is not only from a Devonian source as is commonly believed by some Montney play operators. Previous studies show that anhydrite in the Montney Formation has been sourced from the Charlie Lake Formation within BC (Sharma, 1969) and in Alberta (Desrocher, 1997). The Montney Formation is at risk of souring, as many drilling locations are shown to have sour reservoirs both above and below the reservoir (Chalmers et al., 2019). The recommendation to operators who would like to assess the risk of souring, is that they map sour reservoirs above and below the Montney reservoir on their acreage, as well as map structures to determine location of potential conduits for anhydrite or hydrogen sulphide gas to enter the Montney Formation.

Future Work

Additional analyses on the formation of anhydrite within the Montney Formation will be carried out to determine textural relationships between the anhydrite minerals and the other mineral grains. Thick sections of a select sample set will be analyzed using a scanning electron microscope (SEM) to determine whether anhydrite was formed syndepositionally or postdepositionally.

Conclusions

Mineralogical and geochemical analyses of the Triassic Charlie Lake, Halfway, Doig, Montney and Belloy formations indicate that the hydrogen sulphide gas in the three wells 100/01-29-082-19W6/02, 200/a-064-H 094-b-08/00 and 200/a-054-H 094-B-08/00 are from the sulphate of the Triassic anhydrite or a mixture of Triassic and Devonian anhydrite and not purely from the anhydrite within the Devonian rocks. The scanning electron microscope textural analyses will determine if the anhydrite in the Montney Formation formed during deposition or postdeposition, which will further strengthen the geological model.

Acknowledgments

References

Chalmers, G., Bustin, R.M. and Bustin, A. (2019): Hydrogen sulphide within the Triassic Montney Formation, northeastern British Columbia and northwestern Alberta; *in* Geoscience BC Summary of Activities 2018: Energy and Water, Geoscience BC, Report 2019-02, p. 41–52, URL <http://www.geosciencebc.com/summary-of-activities-2018-energy-and-water/> [April 2019].

Claypool, G., Holser, W., Kaplan, I., Sakai, H. and Zak, I. (1980): The age curves of sulfur and oxygen isotopes in marine sulfate and their mutual interpretation; Chemical Geology, v. 28, p. 199–260, URL <https://doi.org/10.1016/0009-2541(80)90047-9>.

Desrocher, S. (1997): Isotopic and compositional characterization of natural gases in the Lower and Middle Triassic Montney, Halfway, and Doig formations, Alberta Basin; M.Sc. thesis, University of Calgary.

geoLOGIC systems ltd. (2019): geoSCOUT version 8.8; geoLOGIC systems ltd., URL <https://www.geologic.com/products/geoscout/> [August 2020].

Krouse, H., Viau, C., Eliuk, L., Ueda, A. and Halas, S. (1988): Chemical and isotopic evidence of thermochemical sulphate reduction by light hydrocarbon gases in deep carbonate reservoirs; Nature, v. 333, p. 415–418.

Machel, H.G. (1985): Facies and diagenesis of the Upper Devonian Nisku Formation in the subsurface of central Alberta; Ph.D. thesis, McGill University, 392 p.

Munson, E.O., Chalmers, G.R.L., Bustin, R.M. and Li, K. (2016): Utilizing smear mounts for X-ray diffraction as a fully quantitative approach in rapidly characterizing the mineralogy of shale gas reservoirs; Journal of Unconventional Oil and Gas Resources, v. 14, p. 22–31, URL <https://doi.org/10.1016/j.juogr.2016.01.001>.

National Energy Board (2018): Canada's energy future 2018 supplement: natural gas production; National Energy Board, 12 p.

Rietveld, H.M. (1967): Line profiles of neutron powder-diffraction peaks for structure refinement; Acta Crystallographica, v. 22, p. 151, URL <https://doi.org/10.1107/S0365110-X67000234>.

Seal, R.R., II, Alpers, C.N. and Rye, R.O. (2000): Stable isotope systematics of sulfate minerals; Reviews in Mineralogy and Geochemistry, v. 40, p. 541–602.

Sharma, G. (1969): Paragenetic evolution in Peejay field, British Columbia, Canada; Mineral Deposita, v. 4, issue 4, p. 346–354.

Hydrogen Sulphide within the Triassic Doig Formation, Northeastern British Columbia and Northwestern Alberta (Parts of NTS 083, 084, 093, 094)

P.L. Silva, **The University of British Columbia, Vancouver, British Columbia, pablols@alumni.ubc.ca**

R.M. Bustin, **The University of British Columbia, Vancouver, British Columbia**

Introduction

The Lower to Middle Triassic Doig Formation of the Western Canada Sedimentary Basin (WCSB) extends continuously across northeastern British Columbia (BC) and northwestern Alberta. With the industry shifting the focus of development to unconventional reservoirs, the Doig Formation has been recognized as an important resource of gas and natural-gas liquids (Schenk et al., 2019). The Gas Technology Institute (Faraj et al., 2002) estimated the total gas-in-place in the Doig Formation at 4 trillion m^3 (140 tcf), whereas Walsh et al. (2006) estimated the total gas-in-place as ranging between 1.1 and 5.7 trillion m^3 (40–200 tcf). A more recent study by the U.S. Energy Information Administration (2015) estimated 2.8 trillion m^3 (100 tcf) of gas-in-place for the Doig phosphate zone alone. The presence of hydrogen sulphide (H_2S) associated with hydrocarbons poses a problem due to potential corrosion of downhole and surface equipment; environmental, health and safety risks; and reduction of calorific and market value of the gas. Even in trace concentrations, larger than 4 ppm for pipeline transmission and larger than 10 ppm for personnel protection (Moore and Spitler, 2003), H_2S represents a risk for personal and facilities safety.

The amount of H_2S associated with the gas produced from the Doig Formation varies greatly across the basin, and the distribution of sour zones is very complex and challenging to predict. Hydrogen sulphide in petroleum systems may be generated through various chemical-reaction pathways and from multiple sources of sulphur, such as organosulfur compounds associated with the kerogen and hydrocarbons, metal sulphide minerals and dissolved sulphates in connate or injected water (Marriott et al., 2016). At shallow depths, where temperatures are lower than 80 °C, microbial activity can result in reservoir souring by sulphate-reducing bacteria (Shen and Buick, 2004; Amrani, 2014), so long as enough sulphate is supplied. Sulphate is provided through dissolved ions in connate water, introduction of well-stim-

ulation fluid or mineral-fluid interactions. At higher temperatures, thermal sulphate-reduction reactions occur at the expense of reservoir hydrocarbons (Worden et al., 2000; Marriott et al., 2007), producing H_2S, CH_4 and CO_2, part of which is precipitated as carbonate minerals (Worden et al., 2000; Kelemen et al., 2008; King et al., 2014). Thermal sulphate reduction is initiated and catalyzed by reduced or low-oxidation–state sulphur and, owing to its slow reaction kinetics, is highly dependant on temperature. In shales, souring is commonly attributed to microbial activity due to surface-water injection during stimulation (Marriott et al., 2016); an extra layer of complexity is added to understanding the distribution of H_2S in the Doig, due to thermal sulphate reduction from the evaporitic sections of the overlying Charlie Lake and Halfway formations or the underlying Devonian section possibly generating H_2S in the Doig. Shale wells may produce H_2S-free initially, with delayed souring (Weiland and Hatcher, 2012) due to sulphate production through the introduction of oxygenated waters and bacteria that colonize the reservoir and begin feeding on mineral or completion-additive sulphate. Reducing the uncertainty related to the production of sour gas from the Doig Formation involves mapping the distribution of H_2S, as well as understanding the source of the sulphur and the processes of H_2S generation.

Methods

Approximately 700 gas analyses of a public database of drill-stem tests and production tests from over 300 wells distributed throughout the entire extension of the Doig Formation subcrop in BC and Alberta were used to map the lateral distribution of H_2S (Figure 1). The data was screened to remove analyses showing drilling-mud contamination or consisting mostly of air by reviewing analysis remarks. Where multiple analyses existed for the same well, an arithmetic average was used. Additional analyses were removed due to inconsistent alkane profiles or regional disagreement, creating mapping artifacts such as bull's eyes and butterfly wings. Data was interpolated using ordinary kriging with a spherical-type experimental semivariogram and smoothed by two iterations of minimum-curvature interpolation.
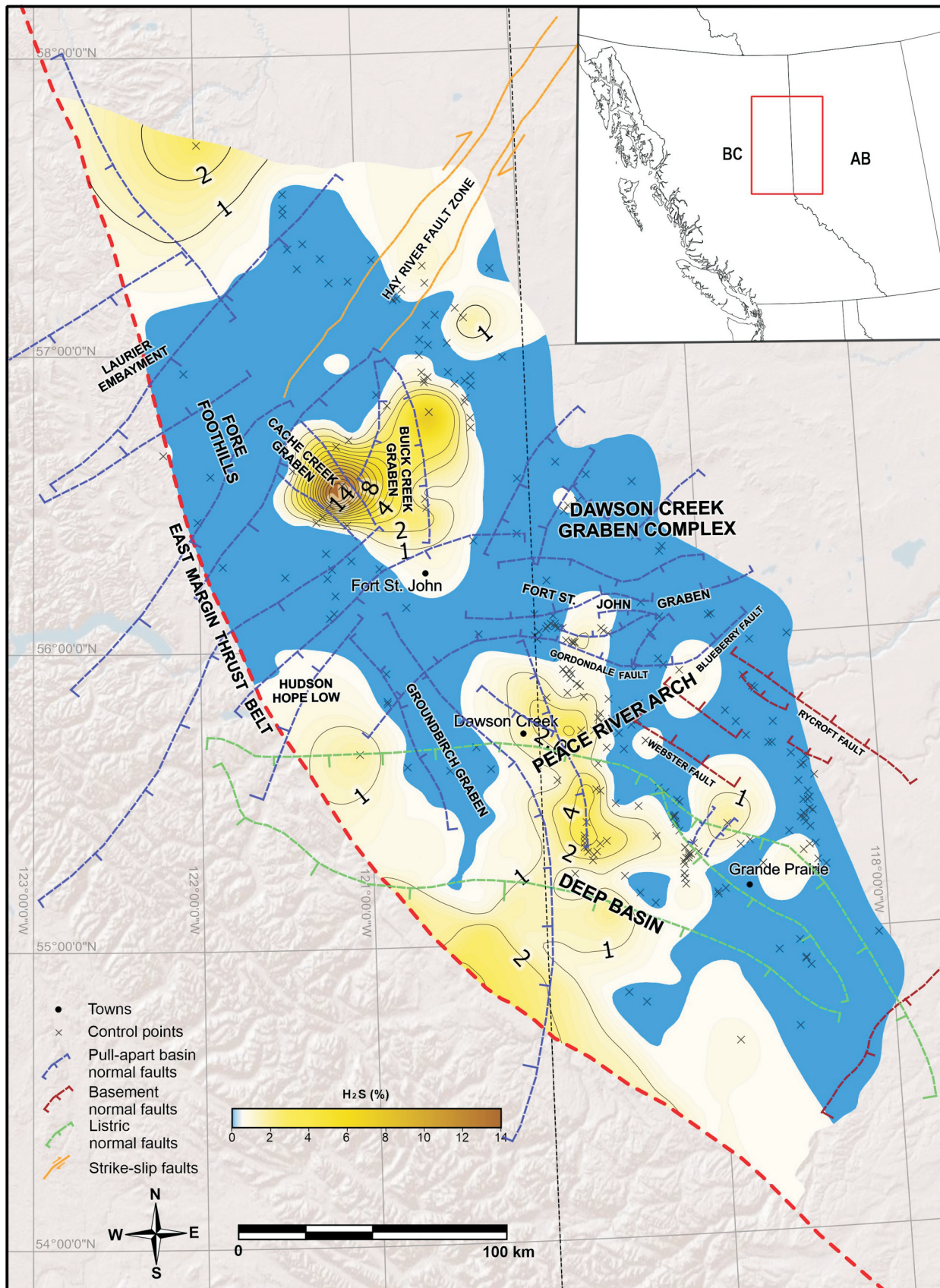
Figure 1. Distribution of H_2S from the Doig Formation based on gas samples and main faults that influence Triassic strata (after Berger et al., 2008) against a shaded-relief backdrop map, in northeastern British Columbia and adjacent area.

Geoscience BC

Preliminary Results

A total of 122 wells, representing 40% of the wells with available gas analyses, have had sour gas identified in either a drill-stem test or production test sample. The H_2S concentrations vary widely from 33 ppm to 28 000 ppm (28%), with 9% of the wells with sour gas containing 100 ppm or less and 10% of the wells containing 4000 ppm or more. The two areas with the highest concentrations of H_2S are the areas northwest of Fort St. John in BC and the area straddling the provincial border with Alberta, between Dawson Creek and Grande Prairie (Figure 1). These results confirm that there is a strong overlap between sour-gas analyses from both the Montney and the Doig formations, which had been previously noticed by Chalmers et al. (2020). These regions also largely overlap with the extent of the Charlie Lake Formation anhydrite mapped by Edwards et al. (1994), which suggests that sour gas within both the Montney and the Doig may be at least partly derived from migration of sulphate from overlying Triassic strata through fault and fracture pathways or through the contact of permeable strata created by the Coplin or sub-Manville unconformity, in addition to possible deeper Devonian sources.

Future Work

The H_2S distribution map generated by this study contributes to the mitigation of safety and health hazards and risks posed by drilling and hydrocarbon production in sour-gas zones. Additional work required to confirm the origin of the H_2S and generate predictive models includes isotopic analyses of the sulphur in the H_2S produced from the Doig and of oxygen and sulphur from Charlie Lake Formation anhydrite samples, as well as sulphur isotopes from anhydrite, pyrite and kerogen organosulfur compounds from the Doig Formation. Mapping of structures that could have potentially served as migration conduits of sulphate from the anhydrite-rich overlying Triassic strata to the Doig Formation would also be extremely valuable in explaining the origin of the sulphate; however, the lack of a public seismic database and the difficulty in accessing proprietary data pose a significant challenge to further research into this topic.

Acknowledgments

References

Amrani, A. (2014): Organosulfur compounds: molecular and isotopic evolution from biota to oil and gas; Annual Review of Earth and Planetary Sciences, v. 42, p. 733–768, URL <https://doi.org/10.1146/annurev-earth-050212-124126>.

Berger, Z., Boast, M. and Mushayandebvu, M. (2008): The contribution of integrated HRAM studies to exploration and exploitation of unconventional plays in North America. Part 1: The Peace River Arch; Reservoir, v. 35, no. 10, p. 42–47.

Chalmers, G.R.L., Bustin, R.M. and Bustin, A.A. (2020): Hydrogen sulphide within the Triassic Montney Formation, northeastern British Columbia and northwestern Alberta (NTS 083K–N, 084C–F, 093I, J, O, P, 094A, B, G, H); in Geoscience BC Summary of Activities 2019: Energy and Water, Geoscience BC, Report 2020-02, p. 41–52, URL <http://www.geosciencebc.com/i/pdf/Summaryof-Activities2019/EW/Project%202017-004_EW_SOA-2019.pdf> [November 2020].

Edwards, D.E., Barclay, J.E., Gibson, D.W., Kvill, G.E. and Halton, E. (1994): Triassic strata of the Western Canada Sedimentary Basin; Chapter 16 in Geological Atlas of the Western Canada Sedimentary Basin, G.D. Mossop and I. Shetsen (comp.), Canadian Society of Petroleum Geologists, Calgary, Alberta, and Alberta Research Council, Edmonton, Alberta, p. 257–275.

Faraj, B., Harold, W., Addison, G., McKinstry, B., Donaleshen, R., Sloan, G., Lee, J., Anderson, T., Leal, R., Anderson, C., Lafleur, C. and Ahlstrom, A. (2002): Shale gas potential of selected Upper Cretaceous, Jurassic, Triassic and Devonian shale formations in the WCSB of Western Canada: implications for shale gas production; report prepared for the Gas Technology Institute, Report GRI-02/0233, 285 p.

Kelemen, S.R., Walters, C.C., Kwiatek, P.J., Afeworki, M., Sansone, M., Freund, H., Pottorf, R.J., Machel, H.G., Zhang, T., Ellis, G.S., Tang, Y. and Peters, K.E. (2008): Distinguishing solid bitumens formed by thermochemical sulfate reduction and thermal chemical alteration; Organic Geochemistry, v. 39, no. 8, p. 1137–1143, URL <https://doi.org/10.1016/j.orggeochem.2008.04.007>.

King, H.E., Walters, C.C., Horn, W.C., Zimmer, M., Heines, M.M., Lamberti, W.A., Kliewer, C., Pottorf, R.J. and Macleod, G. (2014): Sulfur isotope analysis of bitumen and pyrite associated with thermal sulfate reduction in reservoir carbonates at the Big Piney–La Barge production complex; Geochimica et Cosmochimica Acta, v. 134, p. 210–220, URL <https://doi.org/10.1016/j.gca.2013.11.005>.

Marriott, R.A., Davis, P.M. and Clark, P.D. (2007): Estimation of sulfur deposition during the production of lean sour gas; in Proceedings of the 3rd International Conference on Sour Oil and Gas Advanced Technology, April 2007, Abu Dhabi, United Arab Emirates, p. 121–140.

Marriott, R.A., Pirzadeh, P., Marrugo-Hernandez, J.J. and Raval, S. (2016): Hydrogen sulfide formation in oil and gas; Canadian Journal of Chemistry, v. 94, no. 4, p. 406–413, URL <https://doi.org/10.1139/cjc-2015-0425>.

Moore, P.J. and Spitler, R.W. (2003): Hydrogen sulfide measurement and detection; in 2003 Proceedings, American School of Gas Measurement Technology, p. 118–123.

Schenk, C.J., Mercier, T.J., Tennyson, M.E., Finn, T.M., Woodall, C.A., Phuong, A.L., Brownfield, M.E., Marra, K.R. and Leathers-Miller, H.M. (2019): Assessment of continuous gas resources in the Montney and Doig Formations, Alberta Basin Province, Canada, 2018; U.S. Geological Survey, fact sheet 2081-3071, 2 p.

Shen, Y. and Buick, R. (2004): The antiquity of microbial sulfate reduction; Earth-Science Reviews, v. 64, no. 3–4, p. 243–272, URL <https://doi.org/10.1016/S0012-8252(03)00054-0>.

U.S. Energy Administration Information (2015): Technically recoverable shale oil and shale gas resources: Canada; U.S. Department of Energy, 58 p.

Walsh, W., Adams, C., Kerr, B. and Korol, J. (2006): Regional "shale gas" potential of the Triassic Doig and Montney formations, northeastern British Columbia; BC Ministry of Energy, Mines and Low Carbon Innovation, Oil and Gas Division, Resource Development and Geoscience Branch, Petroleum Geology Open File 2006-02, 19 p.

Weiland, R.H. and Hatcher, N.A. (2012): Overcome challenges in treating shale gases; Hydrocarbon Processing, special report, p. 45–48, URL <https://www.ogtrt.com/files/publications/69/Web_Version.pdf> [November 2020].

Worden, R.H., Smalley, P.C. and Cross, M.M. (2000): The influence of rock fabric and mineralogy on thermochemical sulfate reduction: Khuff Formation, Abu Dhabi; Journal of Sedimentary Research, v. 70, no. 5, p. 1210–1221, URL <https://doi.org/10.1306/110499701210>.

Example of Fluid Migration and Distribution Modelling in Unconventional Reservoirs from the Montney Formation, Northeastern British Columbia (NTS 093P, 094A)

V. Chevrot[1], Department of Earth and Atmospheric Sciences, University of Alberta, Edmonton, Alberta, chevrot@ualberta.ca

S. Hernandez, Department of Earth and Atmospheric Sciences, University of Alberta, Edmonton, Alberta

N.B. Harris, Department of Earth and Atmospheric Sciences, University of Alberta, Edmonton, Alberta

Introduction

Unconventional reservoirs are characterized by low permeability and generally require special well-completion methods to obtain economic flow rates. One striking feature that is common to unconventional reservoirs is the unusual fluid distribution. Conventional reservoirs typically exhibit lower density fluids overlying higher density fluids (Figure 1a), but fluid distribution can be unpredictable in unconventional reservoirs (Figure 1b). Fine-grained mixtures of silicate and carbonate minerals and organic matter generate complexities in pore systems and petrophysical properties (e.g., pore size, pore-throat size and wettability). Controls exerted by fluid properties and petrophysical properties on fluid distribution are poorly understood; consequently, saturation and flow rates are difficult to predict with confidence in unconventional reservoirs simply based on position within a geological structure. Therefore, it is critical to develop reliable petrophysical models to predict fluid distribution, improve productivity and reduce risks associated with the exploitation of unconventional plays.

Some oil and gas fields of the Montney Formation, in northeastern British Columbia (BC), present unusual fluid distributions, with gas pools either overlain by water-saturated layers (Wood, 2013) or, the major focus of this study, with gas pools overlain by oil pools. By applying numerical models to hydrocarbon migration in an oil and gas field of the Montney Formation, it is possible to test the roles of the fluid properties and petrophysical properties in controlling the fluid distribution within the reservoir.

The Montney Formation is one of the most important plays in North America (Seifert et al., 2015; Proverbs et al.,

2018), hosting the most important unconventional reservoirs of the Western Canada Sedimentary Basin (Owen et al., 2020), as well as one of the most important siltstone reservoirs in the world (Vaisblat, 2020), with estimated reserves of 12 719 billion m^3 (449 tcf) of gas, 2308 million m^3 (14 521 mmbbl) of natural-gas liquids and 179 million m^3 (1125 mmbbl) of oil (National Energy Board et al., 2013). The migration of hydrocarbons into and out of the reservoirs is simulated for a dataset from the Septimus field of the Montney Formation; located in the overpressured part of the Montney play, the Septimus field is characterized by the accumulations of oil updip of gas (Figure 1b).

Hydrocarbon Migration and Capillary Pressure

When two immiscible fluids like water and oil or gas are present in the same pore, interfacial tensions exist at the interface between the two fluids. The pressure difference at this interface describes the capillary pressure (Schowalter, 1979). The capillary pressure P_c is given by the following equation:

$$P_c = \frac{2\sigma \cos\theta}{r} \tag{1}$$

where σ is the interfacial tension, θ the contact angle, and r the pore-throat radius. An inverse relationship exists between capillary pressure and pore-throat radius. Therefore, capillary pressure is also directly related to the rock fabric and its petrophysical properties. During hydrocarbon migration, buoyancy is the driving or upward-directed force and is resisted by capillary forces (Figure 2; Schowalter, 1979; Carruthers, 2003), resulting in capillary pressure being one of the main constraints to oil migration (Carruthers and Ringrose, 1998; Carruthers, 2003). For hydrocarbon migration to occur, the buoyancy forces need to exceed the capillary forces (Carruthers, 2003).
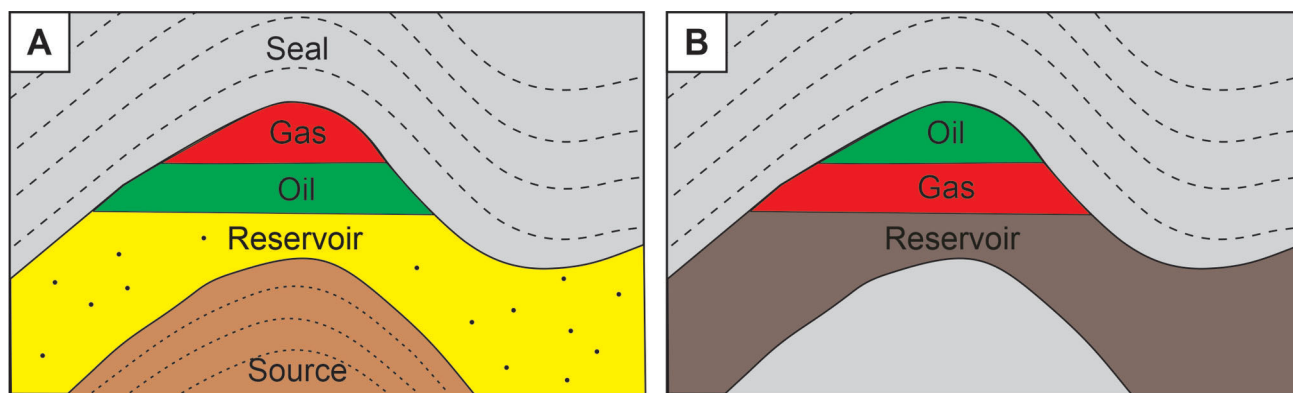
Figure 1. Fluid distribution in **a)** a conventional reservoir, with gas overlying oil, and **b)** an unconventional reservoir, with higher density fluids overlying lower density fluids, as seen in the Montney Formation of northeastern British Columbia.

Geological Setting

The Lower Triassic Montney Formation forms a west-dipping clastic wedge deposited on the northwestern margin of the supercontinent Pangea (Proverbs et al., 2018; Zonneveld and Moslow, 2018; Vaisblat 2020). The formation covers an area of 130 000 km^2 in southwestern Alberta and northeastern BC (Figure 3; Vaisblat, 2020); it can reach a thickness of up to 350 m in BC and becomes thinner to the east (Rohais et al., 2018; Wood et al., 2018). The lithology of the Montney is dominated by dolomitic siltstone, locally with very fine-grained sandstone (Zonneveld and Moslow, 2018; Owen et al, 2020). The formation was deposited on a shallow clastic ramp in an arid coastal-margin setting, with ephemeral rivers and deltas contributing to the main sediment influx (Proverbs et al., 2018; Zonneveld and Moslow, 2018). Depositional environments range from shallow marine to submarine fans (Zonneveld and Moslow, 2018; Vaisblat, 2020). The Montney is subdivided into Lower (Griesbachian–Dienerian), Middle (Smithian) and Upper (Spathian) members (Zonneveld and Moslow, 2018).

Dataset

Gamma-ray, neutron porosity and density logs from 15 wells of the Septimus field (Figure 4) were used to conduct a probabilistic cluster analysis with the GAMLS (Geologic Analysis via Maximum Likelihood System) software (Eslinger and Everett, 2012) to identify four modes (or electrofacies) that correspond to rock-type end members. Samples from the different modes were subjected to a suite of mineralogical, geochemical and petrophysical analyses (Hernandez et al., 2020). Each mode is characterized by its distinct and different mineralogical composition, organic carbon content, rock fabric and petrophysical properties that include pore-throat size and capillarity entry pressure.

Methods

The petrophysical and fluid properties are both accounted for in the modelling of hydrocarbon migration. Modelling
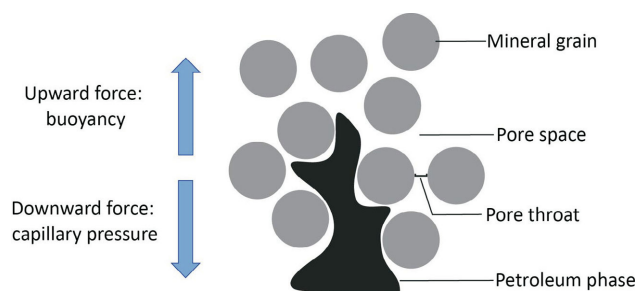
Figure 2. Illustration of opposing forces involved during the migration of hydrocarbons; this example depicts a water-wet rock.
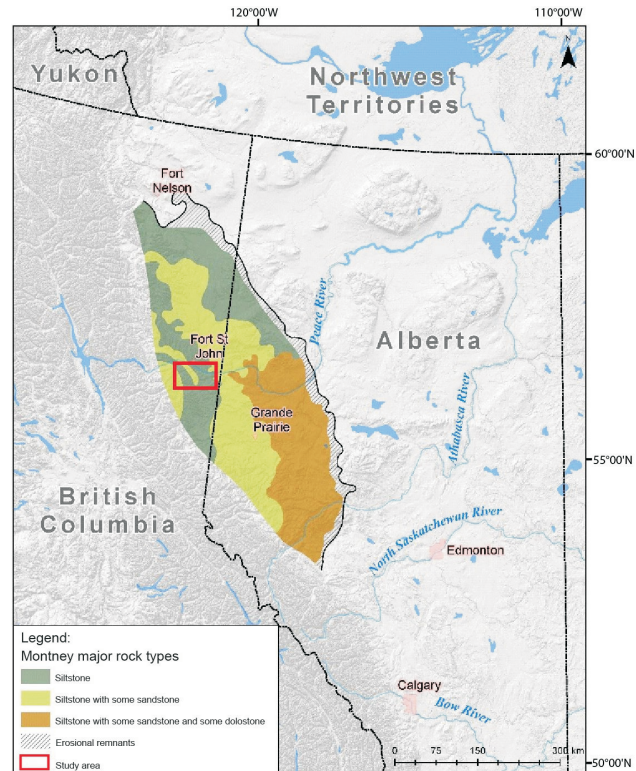
Figure 3. Geology of the Montney Formation, northeastern British Columbia (after National Energy Board et al., 2013). The location of the study area is outlined in red.
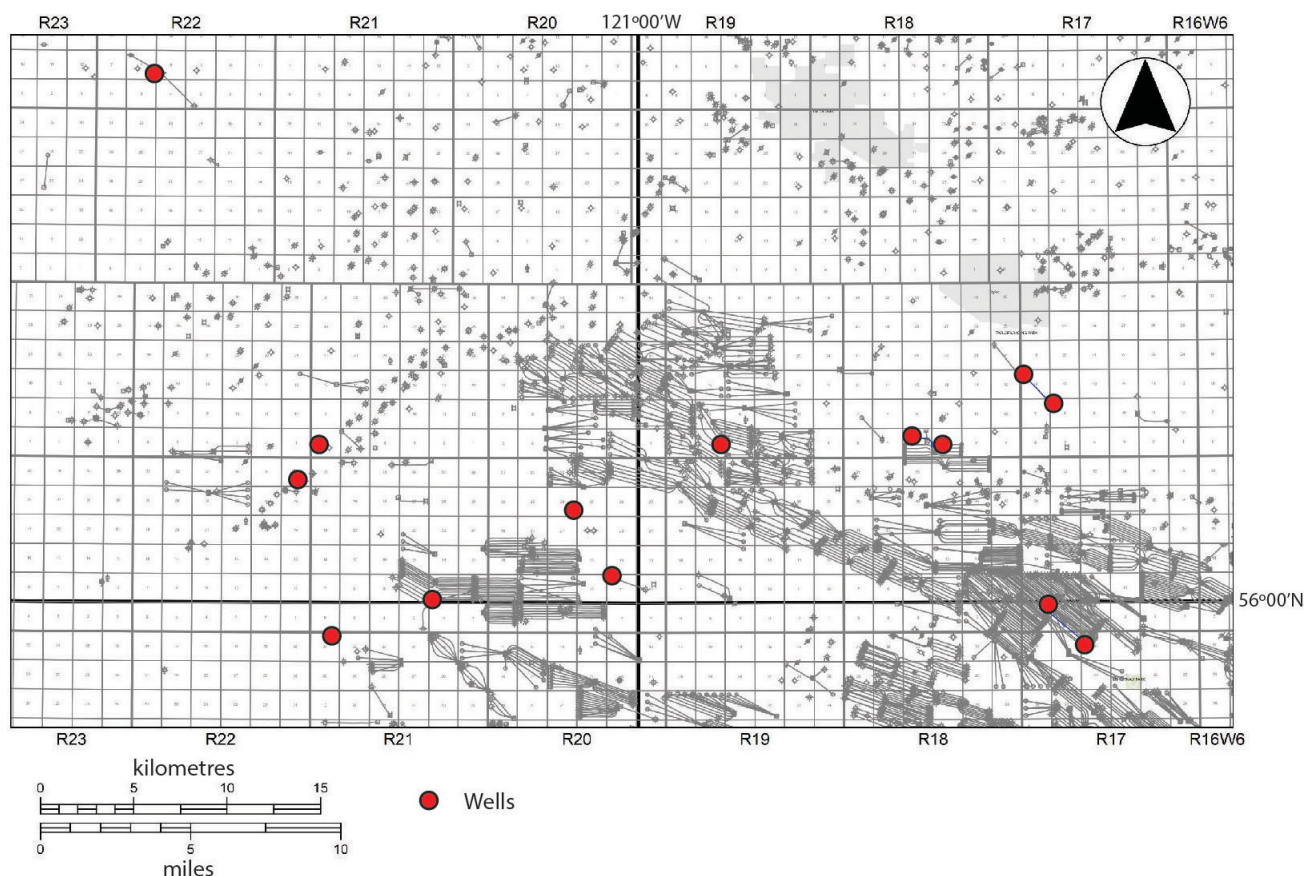
Figure 4. Septimus field of the Montney Formation, northeastern British Columbia, and location of the wells used in this study.

is accomplished using Permedia® software, a petroleum-system modelling toolkit developed by Halliburton that applies the invasion-percolation theory (Carruthers, 2003) to the simulation of complex fluid-migration processes under the influence of both capillary and buoyancy forces. The advantages of invasion-percolation theory are its low computational demand and the capability of representing small-scale heterogeneities in the reservoir (Trevisan et al., 2017).

Current Research Directions

A suite of flow simulations to test the role of petrophysical and fluid properties in controlling fluid distributions in the Septimus field is being developed, applying petrophysical data acquired by Hernandez et al. (2020) in a spatial array that mimics the Septimus-field structure.

Hernandez et al. (2020) determined specific capillary entry pressure for each of four selected rock types. In this study, only two of those rock types were used in the initial models: the ones with the lowest and highest capillary entry pressures. Using the same wells as in Hernandez et al. (2020), a reservoir mesh (Figure 5) was created incorporating only these two end-member rock types.

In model 1 (Figure 5a), the reservoir is composed of one layer consisting of two different rock types: the deepest part of the reservoir has a lower capillary entry pressure compared to the shallowest part of the reservoir. In model 2 (Figure 5b), the deepest part of the reservoir is composed of the rock type with the low capillary entry pressure, whereas the shallowest part of the reservoir consists of a layer of that same rock type with low capillary entry pressure overlain and underlain by the other rock type with a higher capillary entry pressure.

For each simulation, the reservoir is considered to be initially saturated with water. In the simulations, the reservoir will first be charged with oil and subsequently charged with gas to observe the effect of the capillary pressure on the fluid distribution. The simulation with oil is expected to invade both rock types (Figure 5c, d), based on the relatively low interfacial tension between oil and water (Schowalter, 1979). However, the interfacial tension between gas and water is higher and, as a result, the displacement pressure for water-gas is greater than the one for water-oil (Equation 1). This means that for the same rock type, a higher displacement pressure will be required for gas to enter compared to that required for oil. After injection of gas, a segregation of the fluids is expected, with gas entering only the rock type of low capillary pressure (Figure 5e, f).
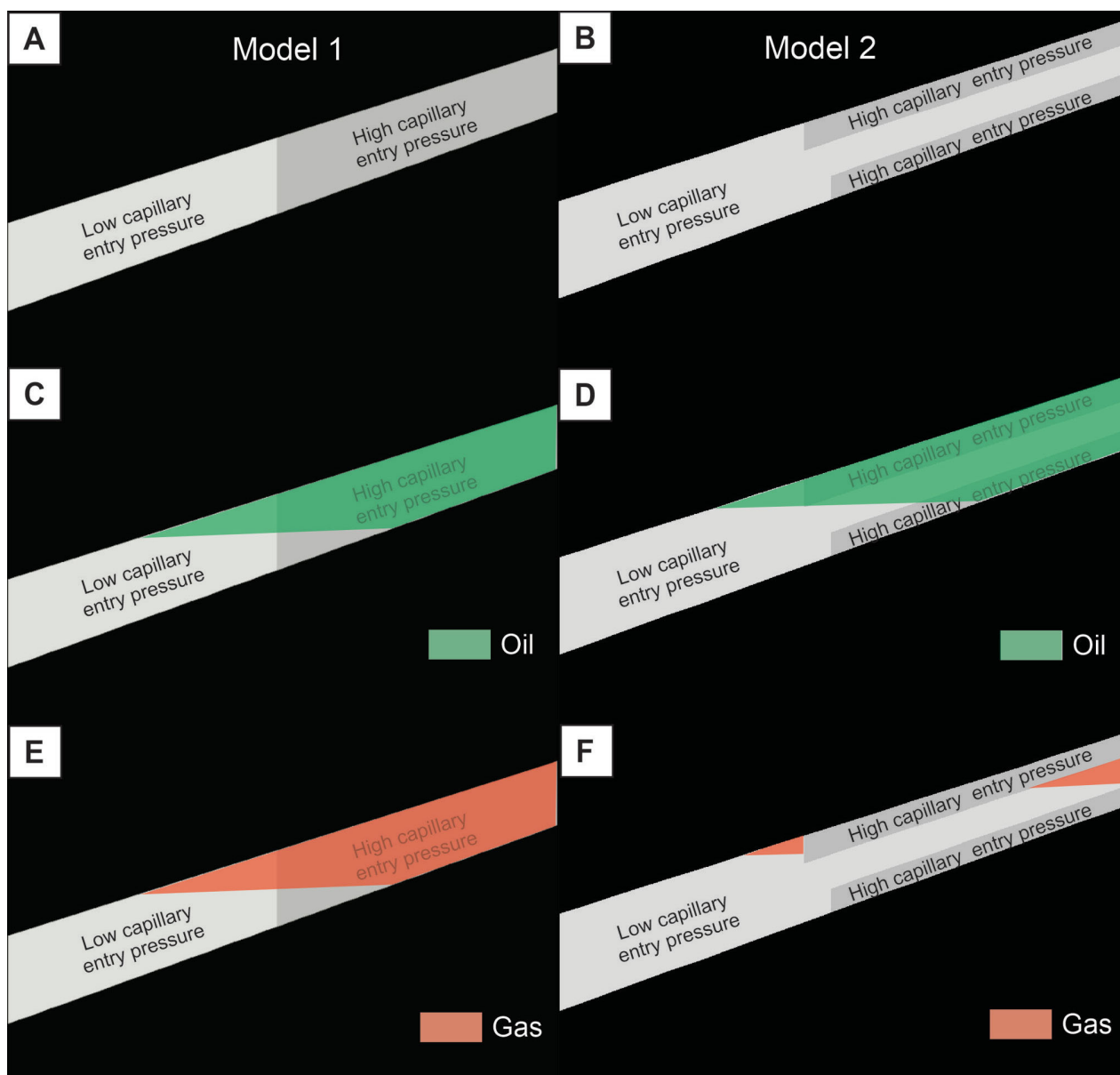
Figure 5. Models 1 and 2 of reservoirs showing in **a, b)** low and high capillary-entry–pressure rocks; **c, d)** after the injection of oil into the reservoir, oil is expected to enter both rock types; and **e, f)** after the injection of gas, only the rock type of low capillary-entry pressure is expected to be filled with gas.

Once the initial set of models is tested and results confirm that rock facies and capillary pressure control segregation of the fluids in the reservoir, new simulations will be run, integrating more wells to extend the reservoir mesh to field scale. As the work progresses and models improve, more data will be added to the model to reflect the heterogeneity and complexity of the Montney Formation. Different scenarios will be tested, some of which will apply parameters based on data collected in the Septimus field, including variable timing of charging events and different compositions and properties of fluids entering the reservoir. Some parameters will be varied outside the limits of Septimus-field data to explore factors that differentiate conventional from unconventional reservoirs.

Conclusions

The project, in an early phase of development, will apply a combination of field data, petrophysical data and numerical modelling to develop constraints on factors controlling fluid segregation in the Montney Formation.

This project will lead to the development of new models for hydrocarbon migration and distribution in unconventional reservoirs. This work is potentially of great economic significance; these models could help in predicting the type of hydrocarbons present in unconventional plays, as well as saturation values and producibility within unconventional petroleum systems and, therefore, could contribute to re-

ducing the risks and costs associated with the exploitation of these resources. The insights gained on this project may be useful not only for the Montney Formation but also for other reservoirs, such as the Lower Cretaceous sandstones in the Deep Basin of the Western Canada Sedimentary Basin or the Upper Cretaceous Rocky Mountain tight-gas-sand accumulations in the United States.

Acknowledgments

References

Carruthers, D.J. (2003): Modeling of secondary petroleum migration using invasion percolation techniques; Chapter 3 *in* Multidimensional basin modeling, S. Düppenbecker and R Marzi (ed.), American Association of Petroleum Geologists, Discovery Series, no. 7, p. 21–37, URL <https://www.petroleumengineers.ru/sites/default/files/modelling_of_secondary_petroleum_migration_using_invasion_percolation_techniques.pdf> [October 2020]

Carruthers, D.J. and Ringrose, P. (1998): Secondary oil migration: oil-rock contact volumes, flow behaviour and rates; *in* Dating and Duration of Fluid Flow and Fluid-Rock Interaction, J. Parnell (ed.), Geological Society of London, Special Publications, v. 144, p. 205–220.

Eslinger, E. and Everett, R.V. (2012): Petrophysics in gas shales; *in* Shale Reservoirs–Giant Resources for the 21st Century, J.A. Breyer (ed.), American Association of Petroleum Geologists, Memoir 97, p. 419–451, URL <https://doi.org/10.1306/13321485M971616>.

Hernandez S., Vaisblat N. and Harris N.B. (2020): Utilizing well logs to define and characterize rock types (flow units) in the Montney Formation, Western Canada; GeoConvention Partnership, GeoConvention 2020, May 11–13, 2020, Calgary, Alberta, extended abstract, 5 p.

National Energy Board, BC Oil and Gas Commission, Alberta Energy Regulator and BC Ministry of Natural Gas Development (2013): Energy briefing note: the ultimate potential for unconventional petroleum from the Montney Formation of British Columbia and Alberta; National Energy Board, BC Oil and Gas Commission, Alberta Energy Regulator and BC Ministry of Natural Gas Development, briefing note, 23 p., URL <https://www.cer-rec.gc.ca/en/data-analysis/energy-commodities/natural-gas/report/ultimate-potential-montney-formation/the-ultimate-potential-unconven-tional-petroleum-from-montney-formation-british-columbia-alberta-energy-briefing-note.html> [October 2020].

Owen, J., Bustin, R.M. and Bustin, A.M.M. (2020): Insights from mixing calculations and geochemical modeling of Montney Formation post hydraulic fracturing flowback water chemistry; Journal of Petroleum Science and Engineering, v. 195, 67 p., URL <https://doi.org/10.1016/j.petrol.2020.107589>.

Proverbs, I.P., Bann, K.L., Fratton, C.M., Frostad, C.J. and Juska, A. (2018): Facies architecture and sequence stratigraphy of the Lower Triassic Montney Formation, NE British Columbia: fundamental controls on the distribution of 'sweet spots' in a world-class unconventional reservoir; Bulletin of Canadian Petroleum Geology, v. 66, no. 1, p. 237–258.

Rohais, S., Crombez, V., Euzen, T. and Zonneveld, J.-P. (2018): Subsidence dynamics of the Montney Formation (Early Triassic, Western Canada Sedimentary Basin): insights for its geodynamic setting and wider implications; Bulletin of Canadian Petroleum Geology, v. 66, no. 1, p. 128–160.

Schowalter, T.T. (1979): Mechanics of secondary hydrocarbon migration and entrapment; American Association of Petroleum Geologists Bulletin, v. 63, p. 723–760.

Seifert M., Lenko M. and Lee J. (2015): Optimizing completions within the Montney resource play; Unconventional Resources Technology Conference, 20–22 July 2015, San Antonio, Texas, URTeC-2139640, 14 p, URL <https://doi.org/10.15530/urtec-2015-2139640>.

Trevisan L., Krishnamurthy P.G. and Meckel T.A. (2017): Impact of 3D capillary heterogeneity and bedform architecture at the sub-meter scale on CO_2 saturation for buoyant flow in clastic aquifers; International Journal of Greenhouse Gas Control, v. 56, p. 237–249, URL <http://dx.doi.org/10.1016/j.ijggc.2016.12.001>.

Vaisblat N. (2020): Controls on reservoir quality on the Lower Triassic Montney Formation; Ph.D. thesis, University of Alberta, Calgary, Alberta, 303 p., URL <https://doi.org/10.7939/r3-ja6f-6545>.

Wood, J.M. (2013): Water distribution in the Montney tight gas play of the Western Canadian Sedimentary Basin: significance for resource evaluation; Society of Petroleum Engineers, SPE Reservoir Evaluation and Engineering, v. 16, no. 3, p. 290–302.

Wood J. M., Sanei H., Haeri-Ardakani, O., Curtis M.E., Akai T. and Currie C. (2018): Solid bitumen in the Montney Formation: diagnostic petrographic characteristics and significance for hydrocarbon migration; International Journal of Coal Geology, v. 198, p. 48–62, URL <https://doi.org/10.1016/j.coal.2018.09.004>.

Zonneveld, J.P. and Moslow T.F. (2018): Palaeogeographic setting, lithostratigraphy, and sedimentary framework of the Lower Triassic Montney Formation of western Alberta and northeastern British Columbia; Bulletin of Canadian Petroleum Geology, v. 66, no. 1, p. 93–127.

Geothermal Resource Potential of the Garibaldi Volcanic Belt, Southwestern British Columbia (Part of NTS 092J)

S.E. Grasby, Natural Resources Canada, Geological Survey of Canada–Calgary, Calgary, Alberta, steve.grasby@canada.ca

S.M. Ansari, Natural Resources Canada, Geological Survey of Canada–Central, Ottawa, Ontario

A. Calahorrano-Di Patre, Simon Fraser University, Burnaby, British Columbia

Z. Chen, Natural Resources Canada, Geological Survey of Canada–Calgary, Calgary, Alberta

J.A. Craven, Natural Resources Canada, Geological Survey of Canada–Central, Ottawa, Ontario

J. Dettmer, University of Calgary, Calgary, Alberta

H. Gilbert, University of Calgary, Calgary, Alberta

C. Hanneson, University of Alberta, Edmonton, Alberta

M. Harris, The University of British Columbia, Vancouver, British Columbia

J. Liu, Natural Resources Canada, Geological Survey of Canada–Calgary, Calgary, Alberta

M. Muhammad, Simon Fraser University, Burnaby, British Columbia

K. Russell, The University of British Columbia, Vancouver, British Columbia

R.O. Salvage, University of Calgary, Calgary, Alberta

G. Savard, University of Calgary, Calgary, Alberta

V. Tschirhart, Natural Resources Canada, Geological Survey of Canada–Central, Ottawa, Ontario

M.J. Unsworth, University of Alberta, Edmonton, Alberta

N. Vigouroux-Caillibot, Douglas College, New Westminster, British Columbia

G. Williams-Jones, Simon Fraser University, Burnaby, British Columbia

Introduction

Geothermal energy holds promise to provide a source of clean and renewable energy that can support the transition to an economy with net-zero CO_2 emissions. Compared to other renewables, geothermal energy has the key advantage of providing dispatchable power supply, with one of the highest capacity factors of any energy resource. As such, geothermal can provide baseload power to the grid without need of storage solutions. In addition, geothermal energy can provide a source of low-cost heat to support the dominant energy demand in Canada.

This publication is also available, free of charge, as colour digital files in Adobe Acrobat® PDF format from the Geoscience BC website: http://geosciencebc.com/updates/summary-of-activities/.

The benefits of geothermal energy are countered, however, by a much higher exploration risk. It is much easier to determine where it is windy and sunny than it is to find a permeable reservoir of hot fluids at a depth of several kilometres. The Garibaldi volcanic belt (GVB) of southwestern British Columbia (BC) is a case in point. The Geothermal Energy Program (1975–1985) of Natural Resources Canada (NRCan), along with BC Hydro, conducted geothermal exploration in the GVB, on the southern flank of Mount Meager. The results, along with subsequent industry drilling, defined high-temperature geothermal resources (Jessop, 2008; Witter, 2019). Although a world-class thermal resource was discovered, the technical success of the exploration program at Mount Meager was limited by the ability to define a high-permeability reservoir.

To address this issue, the Garibaldi Volcanic Belt geothermal energy project focused on reducing exploration risk in volcanic belts of western Canada, was launched in 2019 by NRCan's Geological Survey of Canada (GSC), in partnership with Simon Fraser University (SFU), The University of British Columbia (UBC), Douglas College (DC), University of Calgary (U of C) and University of Alberta (U of A). A multidisciplinary geoscience field program was initiated in 2019, with a focus on developing novel tools to image zones of high permeability in the subsurface (Grasby et al., 2020). Due to Covid-19 restrictions, a more limited field program was conducted in the summer of 2020, largely focused on the north flank of Mount Meager. This paper reports on the nature of the 2020 field program and the data collected.

Garibaldi Project

The Garibaldi volcanic belt is a chain of volcanoes less than 11 000 years old in southwestern BC. Historical drilling was focused on Mount Meager, as the area experienced the most recent volcanic activity, hosts numerous hot springs that suggest the presence active hydrothermal systems, and has a high heat flow. Drilling defined high-temperature geothermal resources (>250°C). While these temperatures were sufficient to produce electricity, the fluid-production rate was not sufficient to justify the cost of the 60 km of new transmission lines required to reach the site (power generation is a function of both temperature of the fluid and the rate at which the fluid can be produced to surface). Thus, although a world-class thermal resource was found, the geological conditions required to exploit it were not economical. The lack of geoscience information regarding the regional controls on permeability pose a significant drilling risk to subsequent industry exploration in the region (Witter, 2019).

The Garibaldi project seeks to develop a multidisciplinary approach to reduce exploration risk through an integrated geological and geophysical field campaign. Project funding was provided through NRCan (Renewable and Electrical Energy Division and GSC), together with Geoscience BC. The project incorporates a range of geoscience tools, including remote sensing, bedrock mapping, fracture measurements, geochemistry, and magnetotelluric (MT), gravity and passive-seismic surveys. The ultimate project goal is to extrapolate new knowledge gained from Mount Meager to the overall Garibaldi volcanic belt, thereby developing new predictive tools for finding permeable aquifers at depth. Results will also aid development of new geothermal-resource models, creating greater certainty in geothermal-resource assessments and supporting development of effective regulatory environments.

Mount Meager 2020 Field Program

Given issues related to Covid-19, a significantly revised field program was planned in order to limit potential exposure during fieldwork. To this end, no large field camp was established and, instead, daily helicopter flights from Whistler were conducted. Although less efficient, this allowed individual field crews to be placed in the field during the day, then return to town were they stayed in individual hotel rooms. This also allowed thorough cleaning of the helicopter between use by different research groups. The field program did include establishment of remote two-person field camps. The science focus of the 2020 field season was to fill in data gaps along the north flank of Mount Meager, including MT (U of A) and gravity (SFU) surveys (Figure 1). This work was supplemented with new geological mapping (UBC and SFU). An installed fibre-optic distributed-sensing cable deployed on the flank of Mount Meager in 2019 was also retrieved. A new network of temperature loggers was deployed along the south flank of Mount Meager to record variations in ground temperature during the winter. These instruments will be collected and data downloaded during the summer 2021 season.

The spatial gravity measurements, in conjunction with other geophysical methods, are being used to map the magmatic and hydrothermal subsurface features of volcanoes. During the summer of 2020, the gravity team from SFU surveyed 41 new gravity sites with a LaCoste & Romberg spring gravity meter along the north flank of the Mount Meager Volcanic Complex (Figure 1). Of these, 15 sites were located in the Upper Lillooet Regional Park (in the northwestern quadrant of Figure 1) and the remainder in adjacent areas in order to improve on the 2019 coverage of the spatial mapping of the Mount Meager Volcanic Complex. The gravity data will aid investigation of the deep magmatic structures (depth >10 km) by comparing data from distal stations with data from the proximal dense network of stations. The measured Bouguer gravity anomalies will be analyzed via an informed inverse-modelling approach, which combines information from geological and structural mapping, and MT and seismic measurements. This will restrict the number of possible solutions for the inversion and ensure that the results best reflect plausible subsurface geological features.

Collection of magnetotelluric (MT) data was also aimed at expanding the 2019 coverage around the north flank of Mount Meager. When combined with recently developed 3-D inversion techniques, a fully 3-D subsurface resistivity model will be developed from the combined data. In total, 12 new MT measurements were taken by the University of Alberta MT group, who are conducting a deeper focused MT survey designed to image pathways that carry fluids to the geothermal reservoir and the fumaroles on Job Glacier.
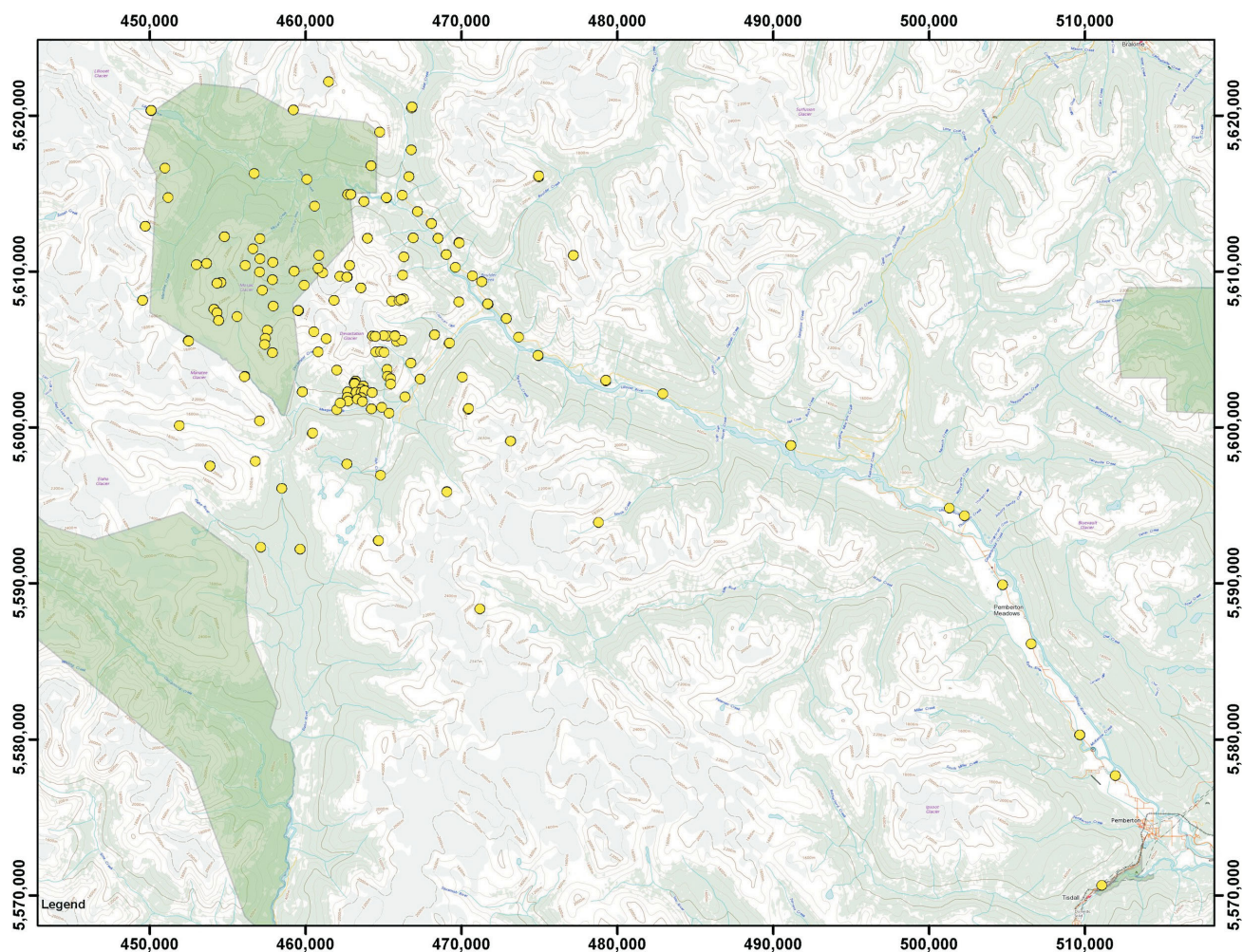
Figure 1. Location of geophysical measurements taken during the 2019 and 2020 field seasons of the Mount Meager field program. Base map from Natural Resources Canada.

These deep MT measurements will also define the size and content of any magma bodies beneath the volcano.

Detailed bedrock mapping was conducted to enhance understanding of the nature of the spatial distribution of volcanic rocks that form the Mount Meager Volcanic Complex. Field mapping included recording rock-property observations, with a particular focus on rock types with enhanced reservoir properties (Figure 2). The resultant geological maps and observations will support the development of hydrogeological models for bulk-rock permeability to better characterize potential fluid flow at depth.

In order to test potential preferential heat flow associated with fracture systems, a series of temperature-data recorders was also deployed in a grid along the south flank of Mount Meager. Each of these includes one sensor on the ground surface and one buried at a depth of ~15 cm. It is hoped that the data recorded through the winter beneath snow cover will reveal localized areas of higher heat flux.

Figure 2. Field researcher A. Calahorrano-Di Patre conducting gravity measurements on Mount Meager

Conclusions

Despite the challenges and limitations imposed by Covid-19, the summer 2020 field program was still a success. Key science goals of retrieving instruments deployed in 2019

and filling in data gaps along the north flank of Mount Meager were achieved. These data are still being processed and will be incorporated into projects of three postdoctoral fellows, six Ph.D. students and one M.Sc. student. Final results will be integrated into a new 3-D model of the geothermal and volcanic plumbing of the Mount Meager complex. Results will provide novel new methods to help predict the occurrence of permeability at depth and greatly reduce the risk associated with drilling for geothermal reservoirs in volcanic systems of British Columbia.

Acknowledgments

References

Grasby, S.E., Ansari, S.M., Calahorrano-Di Patre, A., Chen, Z., Craven, J.A., Dettmer, J., Gilbert, H., Hanneson, C., Harris, M., Liu, J., Muhammad, M., Russell, K., Salvage, R.O., Savard, G., Tschirhart, V., Unsworth, M.J., Vigouroux-Caillibot, N. and Williams-Jones, G. (2020): Geothermal resource potential of the Garibaldi volcanic belt, southwestern British Columbia (part of NTS 092J); *in* Geoscience BC Summary of Activities 2019: Energy and Water, Geoscience BC, Report 2020-02, p. 103–108, URL <http://www.geosciencebc.com/i/pdf/SummaryofActivities2019/EW/Project%202018-004_EW_SOA2019.pdf> [November 2020].

Jessop, A. (2008): Review of National Geothermal Energy Program, Phase 2 – geothermal potential of the Cordillera; Geological Survey of Canada, Open File 5906, 86 p., URL <https://doi.org/10.4095/225917>.

Witter, J. (2019): South Meager geothermal project – new perspectives from recently unearthed data; Geoscience BC, Report 2019-07, 5 p., URL <http://www.geosciencebc.com/i/pdf/Report-2019-07-Innovate-Geothermal.pdf> [November 2020].

Geoscience BC

Installation of a Purpose-Built Groundwater Monitoring Well Network to Characterize Groundwater Methane in the Peace Region, Northeastern British Columbia (NTS 093P/09–16, 094A/01–08): Activity Report 2019–2020

A. Allen, Simon Fraser University, Burnaby, British Columbia

A.M. Goetz, Energy and Environment Research Initiative, The University of British Columbia, Vancouver, British Columbia

P.S. Gonzalez, The Lyell Centre, Heriot-Watt University, Edinburgh, Scotland

B. Ladd, Energy and Environment Research Initiative, The University of British Columbia, Vancouver, British Columbia

A.G. Cahill, The Lyell Centre, Heriot-Watt University, Edinburgh, Scotland

L. Welch, British Columbia Oil and Gas Commission, Kelowna, British Columbia

B. Mayer, University of Calgary, Calgary, Alberta

C. van Geloven, British Columbia Ministry of Forests, Lands, Natural Resources Operations and Rural Development, Prince George, British Columbia

D. Kirste, Simon Fraser University, Burnaby, British Columbia

R.D. Beckie, Energy and Environment Research Initiative, The University of British Columbia, Vancouver, British Columbia, rbeckie@eoas.ubc.ca

Introduction

Northeastern British Columbia (BC) hosts some of the world's largest unconventional gas reservoirs and while the natural gas in these reservoirs has and continues to be developed, some of the effects of this development on the environment are not well understood. Of the possible effects on the environment, a 2014 report by the Council of Canadian Academies (2014) identified the effects of fugitive natural gas as the most uncertain among energy development activities. Fugitive natural gas poses three principal risks: degradation of near-surface water quality, potential for explosions, and greenhouse gas emissions, if the fugitive gas reaches the atmosphere (Cahill et al., 2017).

The overarching objective of The University of British Columbia's Energy and Environment Research Initiative (EERI) is to provide a knowledge base to support decision making around unconventional gas resources in northeastern BC. A key component of the research initiative is the Monitoring Well Installation Project (MWIP), which in-

This publication is also available, free of charge, as colour digital files in Adobe Acrobat® PDF format from the Geoscience BC website: http://geosciencebc.com/updates/summary-of-activities/.

cluded the installation of and subsequent sampling of groundwater and sediments from 29 bespoke monitoring wells in northeastern BC. The principal objectives of the MWIP are to better understand near-surface (approximately less than 100 m deep) background groundwater conditions in northeastern BC, to determine the distribution of natural gas in near-surface groundwater, and to determine if natural gas in the near surface is related to energy-development activities. By using bespoke wells in specifically chosen locations, there is a reduction in biases and sampling artifacts that can be introduced when only existing domestic wells are used to characterize groundwater conditions. After the MWIP is complete, the monitoring wells will remain and can be used to provide long-term datasets to systematically characterize groundwater conditions through time.

The MWIP project is a collaboration among The University of British Columbia (UBC), Simon Fraser University (SFU), Heriot-Watt University, the University of Calgary, and colleagues at the BC Oil and Gas Commission (BCOGC) and the BC Ministry of Forests, Lands, Natural Resource Operations and Rural Development (MFLNRORD). This project builds upon other efforts, including a program led by MFLNRORD and SFU to sample

and characterize groundwater chemistry from domestic water wells.

The MWIP commenced in spring 2018 and is still being implemented principally by M.Sc. students A. Allen (SFU) and M. Goetz (UBC). The drilling program, site selection criteria, monitoring well locations and an introduction to fugitive-gas concepts can be found in Ladd et al. (2020). Installation of the well network is complete and locations of the monitoring wells are shown in Figure 1. This paper provides an update on the status of the well network and sampling campaigns. In addition, there is a description of four affiliated substudies by A. Allen, M. Goetz and P. Gonzalez who are using samples and data collected in the context of the MWIP.

Status of Monitoring Well Network and Sampling Campaigns

Table 1 shows the sampling dates across four separate sampling campaigns for each of the 29 EERI well locations

drilled between 2018 and 2019. A total of 73 sample sets have been obtained over the past two years, the most recent of which were collected between July 16 and 28, 2020. All wells have now been sampled two or more times, except for EERI-27, which has a static water level beyond the reach of the Grundfos MP1 submersible pump used for most wells. In addition to the submersible pump, other equipment used during the most recent sampling campaign included Waterra Pumps Limited D-25 inertial foot valves for EERI-4 and -8; a Westbay® Instruments (Westbay) MOSDAX sampler probe for the Westbay installations in EERI-11 and -18B; and a Geotech Environmental Equipment, Inc. geo-pump peristaltic pump in combination with a specialized sampling rod for the Sub-Frost Artesian packer from RST Instruments Ltd. installed in EERI-1.

The most recent sampling campaign in July 2020 also afforded the opportunity to collect accurate GPS data for each EERI well location using a Leica Geosystems Viva CS10 field controller in the UTM10 co-ordinate system (Zone 10N). Postprocessing of GPS data was completed by
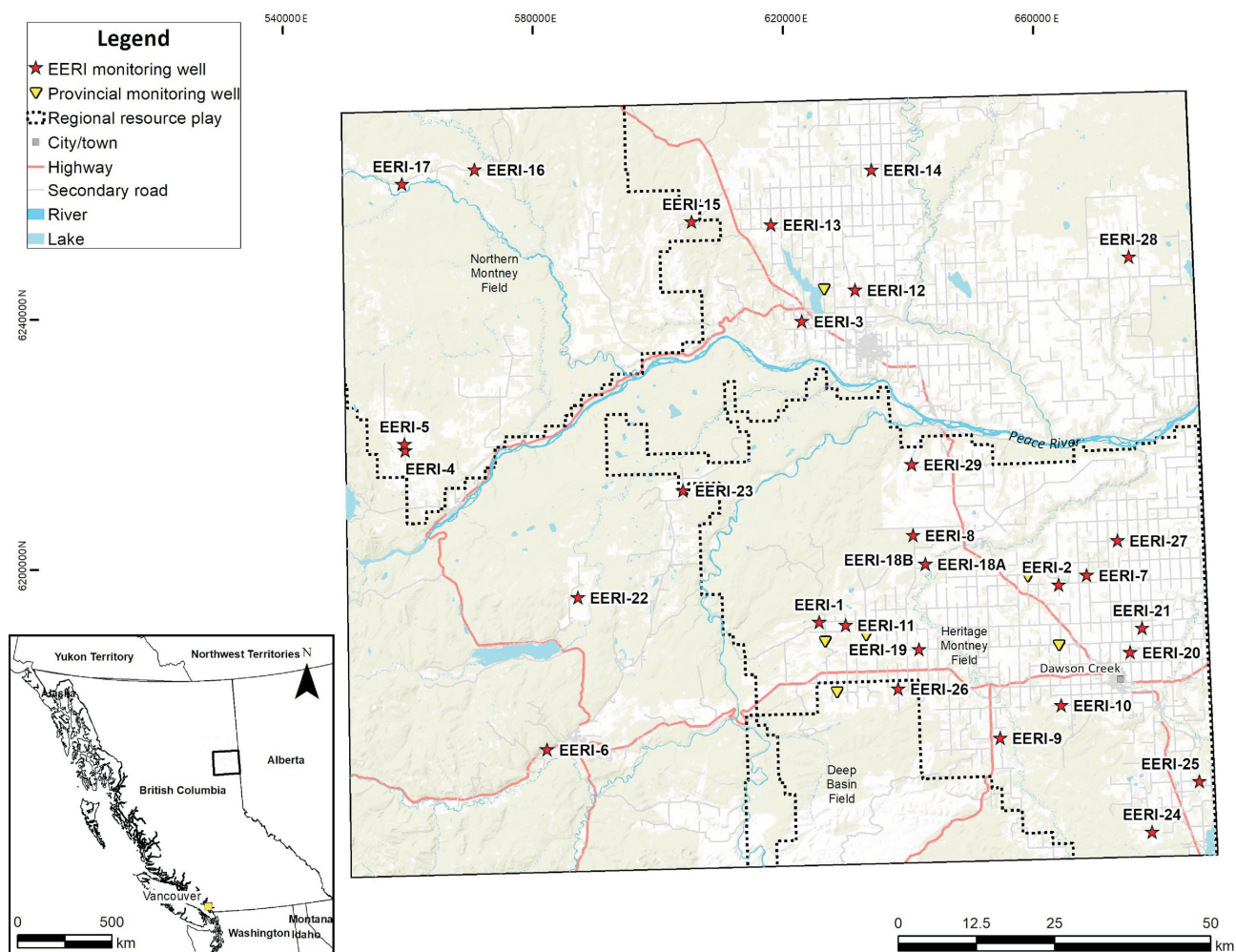
Figure 1. The Monitoring Well Installation Project area with Energy and Environment Research Initiative (EERI) monitoring well locations and regional oil and gas field boundaries, northeastern British Columbia. Background digital elevation model (DEM) from Esri Canada (2019). UTM Zone 10N, NAD 83.

Table 1. Summary of samples and dates of collection from the 29 Energy and Environment Research Initiative (EERI) Monitoring Well Installation Project (MWIP) well locations. Four separate sampling campaigns were undertaken between December 2018 and July 2020 throughout the Peace Region of northeastern British Columbia. Sample collection IDs are based on the well number and order of sampling date (e.g., first sampling date of EERI-1 is denoted as 1-1, second sampling date is 1-2, and so on). No samples were collected from EERI-27 because the depth of the water table was greater than the reach of the pump.

Well name	Winter 2018		Summer 2019		Fall 2019		Summer 2020	
	Date	Sample ID	Date	Sample ID	Date	Sample ID	Date	Sample ID
EERI-1	Dec. 4	1-1	Jun. 28	1-2	Sep. 27	1-3	Jul. 20	1-4
EERI-2	Dec. 4	2-1	Jun. 26	2-2	Oct. 1	2-3	Jul. 17	2-4
EERI-3			Jun. 28	3-1	Oct. 7	3-2	Jul. 24	3-3
EERI-4	Dec. 5	4-1			Oct. 5	4-2	Jul. 26	4-3
EERI-5			Jul. 7	5-1	Oct. 5	5-2	Jul. 26	5-3
EERI-6			Jun. 27	6-1	Oct. 4	6-2	Jul. 25	6-3
EERI-7			Jun. 26	7-1	Oct. 1	7-2	Jul. 17	7-3
EERI-8			Jul. 8	8-1	Sep. 30	8-2	Jul. 19	8-3
EERI-9			Jul. 10	9-1	Oct. 3	9-2	Jul. 18	9-3
EERI-10			Jul. 8	10-1	Oct. 3	10-2	Jul. 18	10-3
EERI-11					Sep. 26	11-1	Jul. 22	11-2
EERI-12			Jul. 8	12-1	Sep. 29	12-2	Jul. 19	12-3
EERI-13			Jul. 8	13-1	Oct. 6	13-2	Jul. 23	13-3
EERI-14			Jul. 12	14-1	Oct. 6	14-2	Jul. 23	14-3
EERI-15					Oct. 6	15-1	Jul. 24	15-2
EERI-16					Oct. 7	16-1	Jul. 28	16-2
EERI-17					Oct. 7	17-1	Jul. 28	17-2
EERI-18A					Sep. 30	18A-1	Jul. 19	18A-2
EERI-18B					Sep. 25	18B-1	Jul. 21	18B-2
EERI-19					Oct. 3	19-1	Jul. 18	19-2
EERI-20					Oct. 2	20-1	Jul. 16	20-2
EERI-21					Oct. 1	21-1	Jul. 17	21-2
EERI-22					Oct. 5	22-1	Jul. 26	22-2
EERI-23					Oct. 5	23-1	Jul. 25	23-2
EERI-24					Oct. 2	24-1	Jul. 16	24-2
EERI-25					Oct. 2	25-1	Jul. 16	25-2
EERI-26					Oct. 3	26-1	Jul. 18	26-2
EERI-27								
EERI-28					Sep. 29	28-1	Jul. 23	28-2
EERI-29					Sep. 30	29-1	Jul. 19	29-2

MFLNRORD staff using Leica Geo Office 8.4. In addition to GPS data, static water level data were downloaded from each Van Essen Instruments Micro-Diver data logger installed in 24 of the 29 well locations (EERI-1, -8, -11, -16 and -27 do not have data loggers installed). Each pressure transducer collects data at four-hour intervals; the datasets covering the longest time period are from EERI-4, -5 and -6, which were installed in February of 2019. Data loggers were installed in the other wells in July and October 2019. The combination of the GPS referenced elevations and pressure transducer datasets will provide static water levels relative to sea level, with data from some wells covering a time period of more than one year.

Descriptions of planned analyses for water samples collected from EERI wells were outlined in detail by Ladd et al. (2020). One alteration to that analysis method is the lo-

cation and equipment intended to be used for inductively coupled plasma–mass spectrometry (ICP-MS) measurements. These analyses have since been completed using an Agilent Technologies 8800 triple quadrupole ICP-MS at the Water Quality Centre (WQC) at Trent University (Peterborough, Ontario). Table 2 shows the recent status of the separate analysis categories: metals, cations and rare-earth elements by ICP-MS, anion concentrations (includes oxygen-deuterium stable isotopes), inorganic carbon and carbon isotopes, tritium enrichment, and dissolved gas concentrations. To date, all anion measurements and metal, cation and rare-earth-element measurements (ICP-MS) are complete for all 73 sample sets, and 33 inorganic carbon and carbon isotopes samples have been analyzed. No tritium enrichment results have been obtained yet. All of the sample sets submitted for dissolved gas compositions have been analyzed.

Table 2. Summary table showing the status of the analyses for each of the 73 sample sets collected from Energy and Environment Research Initiative (EERI) Monitoring Well Installation Project wells. To date, all anion, inductively coupled plasma–mass spectrometry (ICP-MS) and dissolved gas analyses are complete, and inorganic carbon (and carbon isotopes) analyses are partially complete; tritium analyses have not been completed. Some analyses do not include all 73 sample sets due to incompatible pumping methods (e.g., pumping using Waterra tubing does not allow for carbon isotope sample collection) and preservation issues after sample collection. Sample collection IDs are based on the well number and order of sampling date (e.g., first sampling date of EERI-1 is denoted as 1-1, second sampling date is 1-2, and so on). Table 1 indicates the month and year of sample collection.

Well name	ICP-MS Complete	Anions Complete	Inorganic carbon Complete	Inorganic carbon In progress	Tritium In progress	Dissolved gas Complete
EERI-1	1-1, 1-2, 1-3, 1-4	1-1, 1-2, 1-3, 1-4	1-1, 1-2, 1-3	1-4	1-2, 1-3, 1-4	1-2, 1-3, 1-4
EERI-2	2-1, 2-2, 2-3, 2-4	2-1, 2-2, 2-3, 2-4	2-1, 2-3	2-4	2-2, 2-3, 2-4	2-2, 2-3, 2-4
EERI-3	3-1, 3-2, 3-3	3-1, 3-2, 3-3	3-1, 3-2	3-3	3-1, 3-2, 3-3	3-1, 3-2, 3-3
EERI-4	4-1, 4-2, 4-3	4-1, 4-2, 4-3	4-1			
EERI-5	5-1, 5-2, 5-3	5-1, 5-2, 5-3	5-1, 5-2	5-3	5-1, 5-2, 5-3	5-1, 5-2, 5-3
EERI-6	6-1, 6-2, 6-3	6-1, 6-2, 6-3	6-1, 6-2	6-3	6-1, 6-2, 6-3	6-1, 6-2, 6-3
EERI-7	7-1, 7-2, 7-3	7-1, 7-2, 7-3	7-1, 7-2	7-3	7-1, 7-2, 7-3	7-1, 7-2, 7-3
EERI-8	8-1, 8-2, 8-3	8-1, 8-2, 8-3				
EERI-9	9-1, 9-2, 9-3	9-1, 9-2, 9-3	9-1, 9-2	9-3	9-1, 9-2, 9-3	9-1, 9-2, 9-3
EERI-10	10-1, 10-2, 10-3	10-1, 10-2, 10-3	10-1, 10-2	10-3	10-1, 10-2, 10-3	10-1, 10-2, 10-3
EERI-11	11-1, 11-2	11-1, 11-2				11-1, 11-2
EERI-12	12-1, 12-2, 12-3	12-1, 12-2, 12-3	12-1, 12-2	12-3	12-1, 12-2, 12-3	12-1, 12-2, 12-3
EERI-13	13-1, 13-2, 13-3	13-1, 3-2, 13-3	13-1, 13-2	13-3	13-1, 13-2, 13-3	13-1, 13-2, 13-3
EERI-14	14-1, 14-2, 14-3	14-1, 14-2, 14-3	14-1, 14-2	14-3	14-1, 14-2, 14-3	14-1, 14-2, 14-3
EERI-15	15-1, 15-2	15-1, 15-2	15-1	15-2	15-1, 15-2	15-1, 15-2
EERI-16	16-1, 16-2	16-1, 16-2		16-2	16-1, 16-2	16-1, 16-2
EERI-17	17-1, 17-2	17-1, 17-2	17-1	17-2	17-1,17-2	17-1, 17-2
EERI-18A	18A-1, 18A-2	18A-1, 18A-2	18A-1	18A-2	18A-1, 18A-2	18A-1, 18A-2
EERI-18B	18B-1, 18B-2	18B-1, 18B-2				18B-1, 18B-2
EERI-19	19-1, 19-2	19-1, 19-2	19-1	19-2	19-1, 19-2	19-1, 19-2
EERI-20	20-1, 20-2	20-1, 20-2		20-2	20-1, 20-2	20-1, 20-2
EERI-21	21-1, 21-2	21-1, 21-2	21-1	21-2	21-1, 21-2	21-1, 21-2
EERI-22	22-1, 22-2	22-1, 22-2	22-1	22-2	22-1, 22-2	22-1, 22-2
EERI-23	23-1, 23-2	23-1, 23-2		23-2	23-2	23-1, 23-2
EERI-24	24-1, 24-2	24-1, 24-2		24-2	24-1, 24-2	24-1, 24-2
EERI-25	25-1, 25-2	25-1, 25-2	25-1	25-2	25-1, 25-2	25-1, 25-2
EERI-26	26-1, 26-2	26-1, 26-2	26-1	26-2	26-2	26-1, 26-2
EERI-27						
EERI-28	28-1, 28-2	28-1, 28-2	28-1	28-2	28-1, 28-2	28-1, 28-2
EERI-29	29-1, 29-2	29-1, 29-2		29-2	29-2	29-1, 29-2

As stated previously, no samples have been obtained from EERI-27. Additionally, some sample sets could not be analyzed for all aspects of the analysis suite planned. Samples from EERI-11 and -18B were not analyzed for carbon isotope or tritium, as the Westbay sampling method does not yield sufficient volumes of water for these analyses. Samples from EERI-4 and -8 were not analyzed for carbon, tritium or dissolved gas due to limitations in the sampling methods.

Occurrence and Origin of Groundwater Methane in the District of Hudson's Hope Potential Water Supply

The District of Hudson's Hope is a small town located within the Peace River valley in northeastern BC, near the Rocky Mountain Foothills (Figure 1). The Peace River valley mimics the shape of an ancient buried valley, paleovalley, of the same name (Hickin and Fournier, 2011). The geology of the study area is broadly an alluvial sand/gravel plain underlain by confining clay and/or till, a thick gravel aquifer in a buried valley, and fractured Cretaceous shale bedrock (Hartman and Clague, 2008).

The construction of the Site C dam, located downstream on the Peace River near Fort St. John, required the District of Hudson's Hope to change its water supply from its current Peace River source (currently extracting a maximum of 829 661 m^3 annually), to groundwater from the buried-valley aquifer. This change in town water supply is required due to the anticipated deterioration of the Peace River water quality and because part of the water supply system will be made inoperable by the flooding caused by the dam installation (Gardiner et al., 2020). To facilitate the change, the District hired a hydrogeology consulting firm, Western Water Associates Ltd. (WWAL), to evaluate the feasibility of the transition via a test well drilling program in 2018–2019, culminating in the drilling and installation of two production wells in the fall of 2019.

Dissolved gas samples collected by the consultants during the feasibility study showed high concentrations (tens of mg/L) of dissolved methane, which prompted the District to contact the EERI group for collaboration. This presented an opportunity to gather additional data to further MWIP's objectives, while collaborating with the District and WWAL. In November 2019, the EERI group collected groundwater geochemistry and dissolved gas samples during pumping tests for one of the production wells. Using the same sampling methodology outlined in Ladd et al. (2020), groundwater discharge was sampled during a four-hour step pumping test (ranging from 12.6 to 37.9 L/s [200 to 600 gal/min]) and during a 72-hour 31.5 L/s (500 gal/min) constant-rate pumping test (Figure 2). The dissolved gas sampling methodology used by EERI differed from that used by WWAL: EERI used evacuated 250 mL containers

whereas WWAL used an air/gas separator in conjunction with Tedlar® bags. Dissolved gas concentration and isotopic results from these two methods will be compared, as both have their advantages and disadvantages (Hirsche and Mayer, 2009; Evans, 2017). In addition to the sampling of one well during the production well pumping tests in fall 2019, both production wells and a newly installed monitoring well (screened in the same aquifer) were sampled in the summer of 2020. Results from dissolved gas analyses corroborate WWAL's high dissolved methane concentrations; aqueous geochemistry data analysis is in progress.

Using these data, a substudy was undertaken to investigate the occurrence and source of groundwater methane in the buried-valley gravel aquifer beneath Hudson's Hope. There are concerns over both coal-bed methane (CBM) and fugitive gas in the study area, as an abundance of coal-bearing formations outcrop to the west, and there is unconventional natural gas activity to the north (Altares Field in the Montney Formation; Ryan et al., 2005). A coal-bearing formation of interest to this study is the Gething Formation, which commonly outcrops throughout the Rocky Mountain Foothills in northeastern BC (Gentzis et al., 2006). This unit is 400 m thick on average, varying between 100 and 1100 m, thinning toward the Alberta border. The average cumulative coal thickness in the study area is 6 m with a range of 5–20 m (Ryan et al., 2005). The coal ranks between high-volatile A bituminous and semi-anthracite, which are medium and high ranks of coal in terms of maturity, respectively (Ryan et al., 2005; Ryan and Lane, 2006).

The source of the high concentrations of hydrocarbon will be distinguished using carbon/hydrogen isotopic signatures in methane, ethane and carbon dioxide, and wetness parameter (ratio of methane to higher chain alkanes) from dissolved gas sampling. Whether the methane is from naturally occurring biogenic sources, immature thermogenic

Figure 2. Sampling setup at one of the production wells during a constant-rate pumping test in November 2019, near Hudson's Hope, northeastern British Columbia.

coal or deep formations through anthropogenic migration, it is important to characterize the source of these high concentrations (well above hazard level, typically stated as 10 mg/L) to understand potential legacy contamination, and establish baselines prior to potential future CBM or unconventional gas development near the aquifer chosen for the town's water supply.

Groundwater Recharge in a Confined Paleovalley Setting

While the monitoring well network will allow for a broad assessment of groundwater in the Peace Region, a more focused site study is better suited to quantify processes on the individual aquifer or flow system scale. The hydraulic characteristics of major aquifers of the Peace Region have been the subject of increasing interest over the last decade (Brown et al., 2011; Baye et al., 2016; Morgan et al., 2019; Chao et al., 2020). Even though groundwater is not the main source of drinking water for the over 60 000 residents of the Peace Region, as most large communities source their water supply from major rivers, understanding sustainable yield of groundwater is important for domestic, industrial, agricultural and environmental purposes (Bredehoeft, 2002; Baye et al., 2016; Statistics Canada, 2017). Most groundwater wells in northeastern BC are constructed with a well screen installed in weathered/fractured bedrock, with fewer having the screen installed in buried-valley sand/gravel aquifers (Baye et al., 2016). Buried-valley, or paleovalley, aquifers commonly host significant sources of groundwater in those areas where they are thick and laterally continuous (Hickin et al., 2008). In particular, a buried-valley aquifer located in the Peace River paleovalley near Hudson's Hope was shown to yield 31.5 L/s (600 gal/min) during a 72-hour constant-rate pumping test (Gardiner et al., 2020).

The objective of this study is to determine dominant recharge pathways through low-permeability confining layers to both weathered bedrock and buried-valley aquifers (see Goetz and Beckie, 2020, for more details). The spatial distribution of recharge values, residence times of aquifers and the quantification of the steady-state water balance of this archetypal groundwater flow system of the Peace Region will be determined. Over much of the study area, these aquifers are confined by low-permeability tills, which limit recharge rates but also isolate the aquifers from surficial processes such as drought and surficial contamination (Cummings et al., 2012). Since recharge is a major component of the groundwater budget, the interpreted model results will help inform sustainable extraction of this finite groundwater supply and help quantify the groundwater flow velocity and therefore the advective transport of dissolved fugitive gas potentially released from compromised energy wells (Bredehoeft, 2002; Cahill et al., 2019; Chao et al., 2020). As the study area is in an area of unconventional

gas development, it is important to understand typical regional-scale groundwater flow patterns that control the movement of dissolved gases.

There are no specific modelling studies with a primary focus on groundwater recharge of buried-valley settings in northeastern BC. This region is distinct from those described in most other Western Canada Sedimentary Basin (WCSB) studies due to the undulating terrain near the Rocky Mountain Foothills and the lack of features common to the Prairie Pothole Region, which are hypothesized to be the dominant recharge mechanism found in many WCSB buried-valley systems (Meyboom, 1966; Berthold et al., 2004; Cummings et al., 2012). In this study, the hydrogeology of the Sunset paleovalley was conceptualized using available hydrogeological data for buried-valley aquifer systems in northeastern BC and the WCSB, and with data from MWIP monitoring wells within the study area (Figure 1). This study focuses on a single, confined buried-valley/fractured-bedrock aquifer system, which is a hydrogeological setting common to northeastern BC (Hickin et al., 2008, 2016).

In most groundwater systems, the distribution and magnitude of recharge is predominantly dependent on climate (precipitation/evapotranspiration rates), geological framework (confining thickness/conductivity) and topography (runoff/infiltration ratio; Winter, 2001; Sanford, 2002). The dominant factor controlling recharge for this study area is assumed to be lithology, with most recharge likely originating where the confining till/clay is thinnest, resulting in a shorter travel time to assimilation and storage in aquifer material (Andriashek, 2003; Nastev et al., 2005; Cummings et al., 2012). Recharge into buried-valley aquifers depends greatly on the bulk permeability of the confining layer (e.g., till) and groundwater residence times in till material have been shown to range from thousands to tens of thousands of years (Keller et al., 1989). Although buried-valley aquifers are typically confined, localized heterogeneities and discontinuities can create 'windows' of unconfined conditions (Nastev et al., 2005). These windows can then provide hydrological pathways for recharge, which is focused toward weathered bedrock and buried-valley aquifers (Korus et al., 2017).

Using the U.S. Geological Survey's MODFLOW 6 software (Hughes et al., 2017), groundwater-flow models for the shallow (<200 m), regional, multilayered aquifer system were constructed and calibrated. Within the study area, the model quantitatively estimated the spatial distribution and magnitude of groundwater recharge and discharge, the water balance between defined hydrostratigraphic units and residence times of groundwater in aquifers.
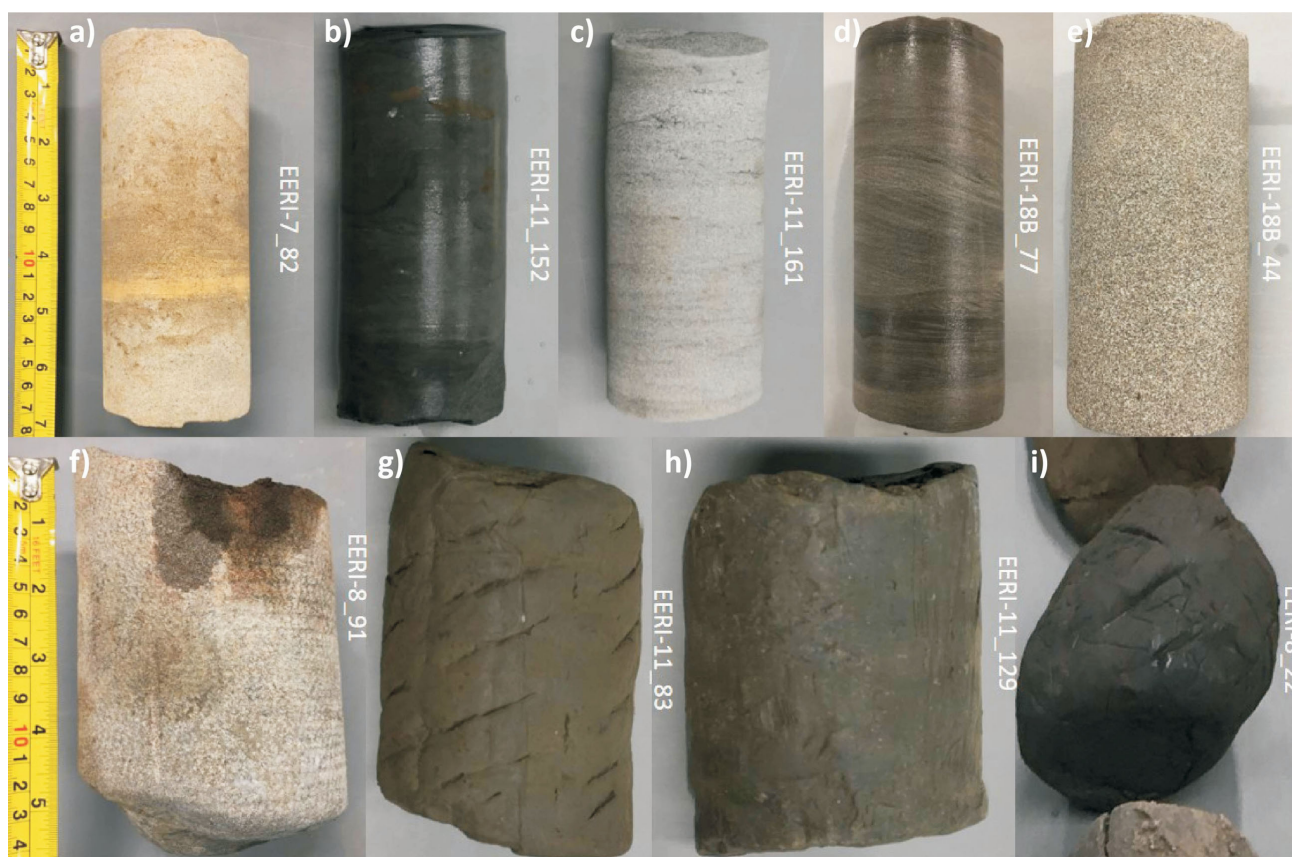
Figure 3. Examples of geological material encountered during the Monitoring Well Installation Project drilling campaigns: **a)** fine sandstone, rounded and well sorted; quartz and lithic (±10%) grains, with a few shaly patches and laminar stratification; **b)** dark massive mudstone with brown shaly patches and load-cast structures; fractures in horizontal disposition; **c)** very fine sandstone, rounded, well to moderately sorted; quartz, lithic and mica grains with a shaly matrix in a laminar stratification; **d)** very fine muddy sandstone, rounded and well sorted; quartz, lithic and mica grains with shaly horizons; cross-bedding stratification; **e)** massive medium sandstone, rounded and well sorted; quartz, lithic and mica grains well consolidated in a shaly matrix; **f)** massive medium sandstone, rounded to subrounded and well sorted; quartz, lithic and mica grains very well consolidated in matrix; **g)** clast-poor muddy diamict from the upper soil; **h)** clast-intermediate diamict from the upper soil; **I)** clast-poor diamict from the upper soil. Samples recovered from monitoring wells EERI-7, -8, -11 and -18B (see Figure 1 for locations).

Investigating Petrophysical Properties of Bedrock Strata in the Peace Region

During drilling for the MWIP, a series of core samples were recovered in order to characterize the bedrock's key petrophysical properties, which control the flow and migration of fugitive gas in the shallow subsurface within the Peace Region. Key core samples are undergoing porosity and permeability measurements as well as CT scan analyses to characterize the pore structure and inferflow properties. Figure 3 shows the range of geological material encountered during installation of the MWIP wells, including shale, siltstone and sandstone units in addition to the ubiquitous Quaternary diamict that prevails at surface throughout the region.

Initial results of petrophysical characterization suggest a large range in pore structure properties (i.e., pore-size distribution and mean pore diameter) based on sediment type. Consequently, this has resulted in a large range in key fluid flow parameters; meaning fugitive gas flow in the sub-

surface within the Peace Region is highly complex and dynamic. Figure 4 shows an example of mercury intrusion capillary porosimetry (MICP) data attained for a very tight mudstone (with thin fine sandstone interlayers) encountered in EERI-11 at a depth of 46.3 m (sample EERI-11_152; Figure 3b). Results show that 80% of the measured pore structure is composed of pores with a pore throat diameter of <0.1 μm. This indicates the strata will act as a robust capillary barrier to flow and significant entry pressures will be required for a gas phase to enter or move through it.

Geochemical Classification of Hydrogeochemical Units and Potential Degradation of Groundwater Quality from Interactions between Methane and Subsurface Materials

The occurrence of methane (CH_4) in shallow groundwater has seen increasing degrees of study in the past decades due to the surge of hydraulic fracturing practices, particularly in North America (Mason et al., 2015). Although methane is
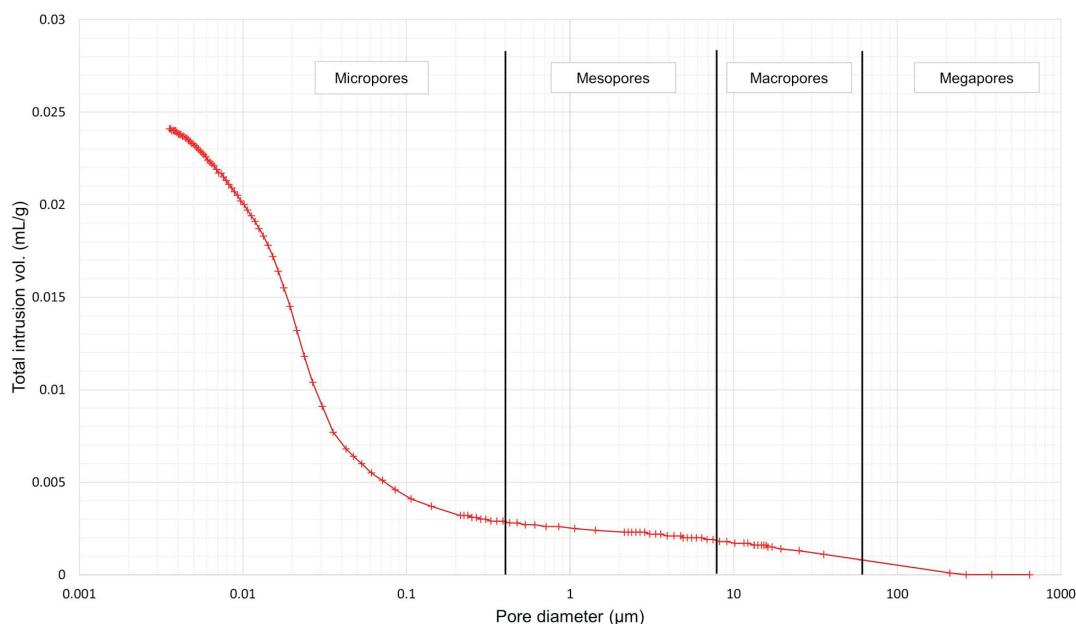
Figure 4. Graph showing percentage of total intrusion volume achieved versus calculated pore throat diameter for a sample of mudstone encountered in monitoring well EERI-11 at 46.3 m depth. Results show a very tight formation with very small pores dominating the pore structure, which infers that this unit would act as a robust capillary barrier to fugitive gas flow in the subsurface.

commonly present in many natural environments, high concentrations in groundwater can lead to detrimental effects on water quality not only as a combustion risk, but also through geochemical alteration of aquifer materials (Van Stempvoort et al., 2005). Characterizing the sediment and bedrock geochemistry of aquifer materials that may be exposed to increased concentrations of methane can provide insight toward assessing risk to the quality of groundwater in those aquifers. Additionally, identifying processes by which production and accumulation of methane occurs is an essential aspect of understanding the potential sources of the methane (Schoell, 1988). Investigating how elevated methane concentrations affect the hydrochemistry of groundwater and the subsequent interactions with geological aquifer materials may indicate specific hazards to groundwater quality.

In most subsurface environments, dissolved methane is relatively stable under anoxic conditions and can easily be advectively transported through groundwater without being involved in any reactions (Appelo and Postma, 2005). However, changes in water chemistry due to methane-related reactions can potentially occur where there are elevated methane concentrations and suitable electron-accepting species over relevant temporal and spatial scales. These can range from methane-oxidation–related processes, such as decreases in pH, increases in alkalinity and increases in trace metal concentrations (Cahill et al., 2017), to methane-driven reduction processes leading to elevated pH and alkalinity and mobilization of trace metals (Van Stempvoort et al., 2005; Schout et al., 2018). Change of pH in groundwa-

ter is one of the main driving forces behind mobilization of chemical species. When pH is considered with oxidation reduction potentials (Eh or pe), the stability fields for solids and aqueous phase chemical species can be defined (Faure, 1997; Appelo and Postma, 2005). Reductive dissolution or oxidation of minerals containing heavy and trace metals (such as Cd, Cr, Pb, Ni, Se, Hg, U, As), which can degrade groundwater quality, can occur when the redox conditions are altered. Substitution of heavy metals for primary metals in minerals is common, leading to varying compositions and the potential for release of heavy metals into the environment upon mineral dissolution. Heavy and trace metals may not always be directly incorporated into mineral structures; oxyanions and cations can be sorbed onto surface sites of oxides, clay minerals or organic matter, or within the structure of minerals such as iron and manganese oxides and oxyhydroxides. Changes in pH and Eh induced by methane-related redox reactions can result in mobilization of adsorbed species through ion exchange, desorption processes or dissolution, leading to significant water quality problems (Cullen and Reimer, 1989; Smedley and Kinniburgh, 2002; Appelo and Postma, 2005; Nesse, 2012). Characterizing the mineralogical and chemical composition of aquifer materials and determining the mineral fraction in which toxic metals reside, can aid in the prediction for mobilization of those contaminants into aquifer systems after changes in redox conditions caused by elevated methane concentrations.

The purpose of this study is to understand how dissolved methane in shallow aquifer systems can interact with geo-

logical materials leading to changes in groundwater quality. The study focuses on the Peace Region, using data from the recently installed EERI monitoring well network and the sediment and bedrock core and chip samples obtained during drilling.

The first objective is to characterize the geochemical composition of both unconsolidated and bedrock aquifer materials and surrounding subsurface materials. Borehole samples from areas both proximal and distal to oil and gas production will be analyzed. During drilling operations at the 29 EERI well locations, sediment and bedrock samples were obtained approximately every 1.5 m. Of these samples, a subset of 128 samples was chosen for bulk chemical analysis at ALS-Environmental (Vancouver, BC). Whole rock analysis by lithium metaborate fusion, trace element detection by four acid and aqua-regia digestion, and combustion analysis for carbon and sulphur will be completed. Statistical analysis of the bulk chemistry is being used to generalize subsurface materials, based on chemical composition, into hydrogeochemical stratigraphic units, with the aim of providing a predictive means of determining geochemical compositions of sediment and bedrock beyond point data sources, such as boreholes.

The second objective is to determine the potential interactions between methane-containing groundwater and subsurface materials, as well as investigate the subsequent detrimental effects on groundwater quality from water-rock interactions through laboratory experiments and numerical modelling. A smaller subset, 25 of the 128 bulk chemistry samples, have been subjected to a sequential extraction procedure (SEP) in the Aqueous Geochemistry Laboratory at Simon Fraser University (Burnaby, BC). This SEP targets nine separate mineral phases and chemical fractions including

1) water soluble and secondary sulphates,
2) weakly adsorbed fraction,
3) strongly adsorbed fraction, carbonates and monosulphides,
4) easily reducible oxides,
5) reducible oxides and low crystalline oxides,
6) crystalline oxides,
7) acid volatile sulphides,
8) organics and humic substances, and
9) sulphides.

Determining the abundance of potentially harmful chemical species in differently mobilized fractions of subsurface materials will allow for an investigation into the possible interactions between methane-containing groundwater and these materials. The associated risk of groundwater degradation may be approximated depending on the likelihood of species mobilization, which is dependent on the phase or fraction in which it occurs.

Summary

The Energy and Environment Research Initiative groundwater monitoring well network of 29 monitoring stations across the Peace Region has been installed. In 2019–2020, monitoring wells were sampled for inorganic and gas geochemical analysis and isotopic analysis as described in this paper. Hydrochemical analyses of water samples collected in summer 2020 are pending. The data provided by the monitoring well network will be synthesized into a peer-review publication, which is currently underway. Four separate student-led substudies have also been undertaken: i) an examination of the origin of methane in an aquifer located at Hudson's Hope, ii) an investigation of recharge processes and pathways in a typical buried-valley aquifer system in northeastern BC, iii) the petrophysical properties of near-subsurface aquifer materials in northeastern BC, and iv) geochemical classification of hydrogeochemical units and analysis of groundwater quality from interactions between methane and subsurface materials. These studies will first appear in student theses and then in peer-reviewed literature.

Acknowledgments

References

Andriashek, L.D. (2003): Quaternary geological setting of the Athabasca Oil Sands (in situ) area, northeast Alberta; Alberta Energy and Utilities Board, EUB/AGS Earth Sciences Report 2002-03, URL <http://wayback.archive-it.org/2901/20111212222052/http://www.ags.gov.ab.ca/publications/ESR/PDF/ESR_2002_03.pdf> [October 2020].

Appelo, C.A.J. and Postma, D. (2005): Geochemistry, Groundwater and Pollution (2nd edition); A.A. Balkema Publishers, Amsterdam, The Netherlands, 649 p.

Baye, A., Rathfelder, K., Wei, M. and Yin, J. (2016): Hydrostratigraphic, hydraulic and hydrogeochemical descriptions of Dawson Creek-Groundbirch areas, northeast BC; Province of British Columbia, Water Science Series 2016-04, 52 p.

Berthold, S., Bentley, L.R. and Hayashi, M. (2004): Integrated hydrogeological and geophysical study of depression-focused groundwater recharge in the Canadian Prairies; Water Resources Research, v. 40, issue 6, URL <https://doi.org/10.1029/2003WR002982>.

Bredehoeft, J.D. (2002): The water budget myth revisited: why hydrogeologists model; Groundwater, v. 40, no. 4, p. 340–345, URL <https://doi.org/10.1111/j.1745-6584.2002.tb02511.x>.

Brown, D., Fontaine, J., Hickin, A., Kerr, B., Serra-Sogas, N. and Beauchamp, M. (2011): Kiskatinaw River watershed, Montney Water Project; in Geoscience BC Report 2011-12, Geoscience BC, poster, URL <http://www.geoscience-bc.com/i/project_data/GBC_Report2011-12/GBCR2011-12_kiskatinaw20110531.pdf> [November 2020].

Cahill, A.G., Beckie, R., Ladd, B., Sandl, E., Goetz, M., Chao, J., Soares, J., Manning, C., Chopra, C., Finke, N., Hawthorne, I., Black, A., Mayer, K.U., Crowe, S., Cary, T., Lauer, R., Mayer, B., Allen, A., Kirste, D. and Welch, L. (2019): Advancing knowledge of gas migration and fugitive gas from energy wells in northeast British Columbia, Canada; Greenhouse Gases: Science and Technology, v. 9, no. 2, p. 134–151, URL <https://doi.org/10.1002/ghg.1856>.

Cahill, A.G., Steelman, C.M., Forde, O., Kuloyo, O., Emil Ruff, S., Mayer, B., Mayer, K.U., Strous, M., Ryan, M.C., Cherry, J.A. and Parker, B.L. (2017): Mobility and persistence of methane in groundwater in a controlled-release field experiment; Nature Geoscience, v. 10, no. 4, p. 289–294, URL <https://doi.org/10.1038/ngeo2919>.

Chao, J.T.-H., Cahill, A.G., Lauer, R.M., Van De Ven, C.J.C. and Beckie, R.D. (2020): Propensity for fugitive gas migration in glaciofluvial deposits: an assessment of near-surface hydrofacies in the Peace Region, northeastern British Columbia; Science of The Total Environment, v. 749, art. 141459, URL <https://doi.org/10.1016/j.scitotenv.2020.141459>.

Council of Canadian Academies (2014): Environmental impacts of shale gas extraction in Canada: the expert panel on harnessing science and technology to understand the environmental impacts of shale gas extraction; Council of Canadian Academies, Ottawa, Ontario, 262 p.

Cullen, W.R. and Reimer, K.J. (1989): Arsenic speciation in the environment; Chemical Reviews, v. 89, issue 4, p. 713–764, URL <https://doi.org/10.1021/cr00094a002>.

Cummings, D.I., Russell, H.A.J. and Sharpe, D.R. (2012): Buried-valley aquifers in the Canadian Prairies: geology, hydrogeology, and origin; Canadian Journal of Earth Sciences, v. 49, no. 9, p. 987–1004, URL <https://doi.org/10.1139/e2012-041>.

Esri Canada (2019): Canada hillshade; Esri Canada, URL <https://www.arcgis.com/home/item.html?id=558eb0df1e014-dc78b2c0fd30f4476b3> [November 2019].

Evans, R. (2017): Towards accurate in situ dissolved gas concentration estimations in gas-charged groundwater using field measured total dissolved gas pressure (PTDG); M.Sc. thesis, University of Calgary, 158 p., URL <https://doi.org/10.11575/PRISM/28476>.

Faure, G. (1997): Principles and Applications of Geochemistry (2nd edition); Prentice Hall, Upper Saddle River, New Jersey, 600 p.

Gardiner, L., Rhodes, R. and Geller, D. (2020): District of Hudson's Hope production well completion report; unpublished report prepared by Western Water Associates Ltd. (British Columbia).

Gentzis, T., Schoderbek, D. and Pollock, S. (2006): Evaluating the coalbed methane potential of the Gething coals in NE British Columbia, Canada: an example from the Highhat area, Peace River coalfield; International Journal of Coal Geology, v. 68, issue 3, p. 135–150, URL <https://doi.org/10.1016/j.coal.2006.02.001>.

Goetz, A.M. and Beckie, R.D. (2021): Groundwater recharge in a confined paleovalley setting, northeastern British Columbia (part of NTS 093P); in Geoscience BC Summary of Activities 2020: Energy and Water, Geoscience BC, Report 2021-02, p. 149–162, URL <http://geosciencebc.com/updates/summary-of-activities/> [January 2021].

Hartman, G.M.D. and Clague, J.J. (2008): Quaternary stratigraphy and glacial history of the Peace River valley, northeast British Columbia; Canadian Journal of Earth Sciences, v. 45, no. 5, p. 549–564, URL <https://doi.org/10.1139/E07-069>.

Hickin, A.S. and Fournier, M.A. (2011): Preliminary bedrock topography and drift thickness of the Montney play area; BC Ministry of Energy, Mines and Low Carbon Innovation, Energy Open File 2011-1 and Geoscience BC, Report 2011-07, 2 maps, scale 1:500 000, URL <http://cdn.geoscience-bc.com/project_data/GBC_Report2011-7/GBC_Report-2011-07_BCMEM%20OF2011-1.pdf> [November 2020].

Hickin, A.S., Best, M.E. and Pugin, A. (2016): Geometry and valley-fill stratigraphic framework for aquifers in the Groundbirch paleovalley assessed through shallow seismic and ground-based electromagnetic surveys; BC Ministry of Energy, Mines and Low Carbon Innovation, BC Geological Survey, Open File 2016-5, 46 p.

Hickin, A.S., Kerr, B., Turner, D.G. and Barchyn, T.E. (2008): Mapping Quaternary paleovalleys and drift thickness using petrophysical logs, northeast British Columbia, Fontas map sheet, NTS 94I; Canadian Journal of Earth Sciences, v. 45, no. 5, p. 577–591, URL <https://doi.org/10.1139/e07-063>.

Hirsche, T. and Mayer, B. (2009): A comprehensive literature review on the applicability of free and dissolved gas sampling for baseline water well testing: final report; prepared for Alberta Environment, 47 p.

Hughes, J.D., Langevin, C.D. and Banta, E.R. (2017): Documentation for the MODFLOW 6 framework; U.S. Geological Survey, Techniques and Methods, book 6, chap. A57, 42 p., URL <https://doi.org/10.3133/tm6A57>.

Keller, C.K., Van Der Kamp, G. and Cherry, J.A. (1989): A multiscale study of the permeability of a thick clayey till; Water Resources Research, v. 25, issue 11, p. 2299–2317, URL <https://doi.org/10.1029/WR025i011p02299>.

Korus, J.T., Joeckel, R.M., Divine, D.P. and Abraham, J.D. (2017): Three-dimensional architecture and hydrostratigraphy of cross-cutting buried valleys using airborne electromagnetics, glaciated Central Lowlands, Nebraska, USA; Sedimentology, v. 64, no. 2, p. 553–581, URL <https://doi.org/10.1111/sed.12314>.

Ladd, B., Cahill, A.G., Goetz, M., Allen, A., Welch, L., Mayer, B., van Geloven, C., Kirste, D. and Beckie, R. (2020): Installation of a purpose-built groundwater monitoring well network to characterize groundwater methane in the Peace Region, northeastern British Columbia (NTS 093P/09–16, 094A/01–08); in Geoscience BC Summary of Activities 2019: Energy and Water, Geoscience BC, Report 2020-02, p. 131–144, URL <http://www.geosciencebc.com/summary-of-activities-2019-energy-and-water/> [November 2020].

Mason, C.F., Muehlenbachs, L. and Olmstead, S.M. (2015): The economics of shale gas development; FEEM, Working Paper No. 017.2015, 38 p., URL <https://doi.org/10.2139/ssrn.2572269>.

Meyboom, P. (1966): Unsteady groundwater flow near a willow ring in hummocky moraine; Journal of Hydrology, v. 4, p. 38–62, URL <https://doi.org/10.1016/0022-1694(66)90066-7>.

Morgan, S.E., Allen, D.M., Kirste, D. and Salas, C.J. (2019): Investigating the hydraulic role of a large buried valley network on regional groundwater flow; Hydrogeology Journal, v. 27, no. 7, p. 2377–2397, URL <https://doi.org/10.1007/s10040-019-01995-0>.

Nastev, M., Rivera, A., Lefebvre, R., Martel, R. and Savard, M. (2005): Numerical simulation of groundwater flow in regional rock aquifers, southwestern Quebec, Canada; Hydrogeology Journal, v. 13, no. 5, p. 835–848, URL <https://doi.org/10.1007/s10040-005-0445-6>.

Nesse, W.D. (2012): Introduction to Mineralogy (2nd edition); Oxford University Press, Inc., New York, New York, 496 p.

Ryan, B. and Lane, B. (2006): Coal utilization potential of Gething Formation coals, northeast British Columbia; *in* Summary of Activities 2006, BC Ministry of Energy, Mines and Low Carbon Innovation, p. 49–72.

Ryan, B., Karst, R., Owsiacki, G. and Payie, G. (2005): Potential coalbed gas resource in the Hudson's Hope area of northeast British Columbia; *in* Summary of Activities 2005, BC Ministry of Energy, Mines and Low Carbon Innovation, p. 15–37.

Sanford, W. (2002): Recharge and groundwater models: an overview; Hydrogeology Journal, v. 10, no. 1, p. 110–120, URL <https://doi.org/10.1007/s10040-001-0173-5>.

Schoell, M. (1988): Multiple origins of methane in the Earth; Chemical Geology, v. 71, issues 1–3, p. 1–10, URL <https://doi.org/10.1016/0009-2541(88)90101-5>.

Schout, G., Hartog, N., Hassanizadeh, S.M. and Griffioen, J. (2018): Impact of an historic underground gas well blowout on the current methane chemistry in a shallow groundwater system; Proceedings of the National Academy of Sciences of the United States of America, v. 115, issue 2, p. 296–301.

Smedley, P.L. and Kinniburgh, D.G. (2002): A review of the source, behaviour and distribution of arsenic in natural waters; Applied Geochemistry, v. 17, issue 5, p. 517–568, URL <https://doi.org/10.1016/S0883-2927(02)00018-5>.

Statistics Canada (2017): Census profile, 2016 census, northeast [economic region], British Columbia and British Columbia [province]; Statistics Canada, URL <https://www12.statcan.gc.ca/census-recensement/2016/dp-pd/index-eng.cfm> [August 2020].

Van Stempvoort, D., Maathuis, H., Jaworski, E., Mayer, B. and Rich, K. (2005): Oxidation of fugitive methane in ground water linked to bacterial sulfate reduction; Groundwater, v. 43, issue 2, p. 187–199, URL <https://doi.org/10.1111/j.1745-6584.2005.0005.x>.

Winter, T.C. (2001): The concept of hydrologic landscapes; Journal of the American Water Resources Association, v. 37, no. 2, p. 335–349, URL <https://doi.org/10.1111/j.1752-1688.2001.tb00973.x>.

Controlled Natural Gas Release Experiment in a Confined Aquifer, Northeastern British Columbia (NTS 094A/04): Activity Report 2019–2020

C.J.C. Van De Ven, The University of British Columbia, Vancouver, British Columbia, colevandeven@eoas.ubc.ca

A.G. Cahill, The Lyell Centre, Heriot-Watt University, Edinburgh, Scotland

B. Ladd, The University of British Columbia, Vancouver, British Columbia

J. Chao, The University of British Columbia, Vancouver, British Columbia

J. Soares, The University of British Columbia, Vancouver, British Columbia

T. Cary, University of Calgary, Calgary, Alberta

N. Finke, The University of British Columbia, Vancouver, British Columbia

C. Manning, The University of British Columbia, Vancouver, British Columbia

A.L. Popp, University of Oslo, Oslo, Norway

C. Chopra, The University of British Columbia, Vancouver, British Columbia

K.U. Mayer, The University of British Columbia, Vancouver, British Columbia

A. Black, The University of British Columbia, Vancouver, British Columbia

R. Lauer, University of Calgary, Calgary, Alberta

C. van Geloven, British Columbia Ministry of Forests, Lands, Natural Resource Operations and Rural Development, Prince George, British Columbia

L. Welch, British Columbia Oil and Gas Commission, Kelowna, British Columbia

S. Crowe, The University of British Columbia, Vancouver, British Columbia

B. Mayer, University of Calgary, Calgary, Alberta

R.D. Beckie, The University of British Columbia, Vancouver, British Columbia

Introduction

As a result of petroleum resource development, a potential environmental concern exists in the form of fugitive gas (FG; Jackson et al., 2011; Vidic et al., 2013; Vengosh et al., 2014). Fugitive gas is natural gas that is able to escape from both production formations and intermediate gas-bearing formations in the subsurface (Council of Canadian Academies, 2014; Dusseault and Jackson, 2014). This gas can migrate vertically, as a result of density contrasts between the light natural gas (mainly methane) and heavier formation fluids, along two potential preferential pathways: 1) inside

a surface well casing that contains compromised cement (termed surface casing vent flow, SCVF) or 2) outside of a wellbore, along the adjacent formation (termed gas migration, GM). Gas migration presents environmental concerns because it may 1) cause the degradation of groundwater quality if natural gas dissolves into potable groundwater under certain conditions (e.g., microbial communities, redox conditions), 2) present risk of explosion due to the combustibility of natural gas, which may reach surface infrastructure such as houses and water wells, and/or 3) be a potential source of greenhouse gas emissions, if released to the atmosphere (Kelly et al., 1985; Van Stempvoort et al., 2005; Cahill et al., 2017; Forde et al., 2018; Van De Ven and Mumford, 2020a). The risks associated with these environmental expressions of GM require focused attention on the investigation of 1) mechanisms governing the migration of

free-phase and dissolved-phase gas, 2) biogeochemical processes affecting the fate of natural gas in both the saturated and unsaturated zones of the subsurface, and 3) the release of gas to the atmosphere.

Petroleum resource development is active in northeastern British Columbia (BC), where economic gas-bearing formations exist. There are some 25 000 gas wells in the region, of which 0.6% have exhibited visible signs of gas migration (Cahill et al., 2019a). The region is within the Western Canada Sedimentary Basin (WCSB), with a highly heterogeneous surficial geology composed of complex sequences of till, glaciolacustrine, glaciofluvial, fluvial and lacustrine deposits overlying bedrock (Shaw, 1982; Cahill et al., 2019a; Chao et al., 2020). Therefore, the region is complex in terms of understanding the impacts of GM on groundwater resources and the emissions of GM to the atmosphere because previous GM research has mainly focused on relatively homogeneous, sand and gravel aquifer systems (e.g., Roy et al., 2016; Cahill et al., 2017; Schout et al., 2019; Van De Ven and Mumford, 2020c). To address the knowledge gaps associated with GM in complex geological settings, the Hudson's Hope Field Research Station (HHFRS) was established in order to perform a controlled, synthetic natural gas injection in the shallow subsurface (Cahill et al., 2019a, b, 2020).

This paper presents a summary of the progress made with respect to the fieldwork undertaken at the HHFRS, which looks to advance the scientific understanding of GM in groundwater systems, the unsaturated zone and the atmosphere to reduce future risk. The principal objective of this research project is to provide scientific knowledge and understanding to inform the practice and management of resource development in BC. Ultimately, the aim of the project is to 1) characterize the physical and biogeochemical processes that control subsurface gas migration and impact, and quantify the amount of natural gas that remains, degrades or leaves the subsurface, 2) test a variety of FG monitoring and detection methodologies, and 3) inform regulations to facilitate safe and sustainable development of petroleum resources.

Background

For a detailed description of the mechanisms for gas flow, mass transfer and fate of methane in groundwater systems, refer to Cahill et al. (2019a, b, 2020). Generally, when GM occurs in a shallow groundwater system, the gas movement is governed by the rate at which the gas enters the system (leak rate), buoyancy of the gas, permeability and the variation in capillary forces associated with the porous media through which it flows (Ji et al., 1993; Brooks et al., 1999; Geistlinger et al., 2006; Selker et al., 2007; Van De Ven and Mumford, 2019). This results in an upward movement of gas through complex interconnected channels. However,

the flow can also be lateral if the gas is entering the system at a high leak rate, causing the gas to spread in all directions due to the high driving force. Flow is also directed laterally and forms pools due to both subtle (e.g., bedding structure) and stark (e.g., clay or silt lenses) contrasts in the permeability of the geological strata through which it flows (Kueper et al., 1993; Glass et al., 2000; Steelman et al., 2017; Cahill et al., 2018). This gas can either 1) span the subsurface system and be released at the surface (surface expression) causing potential safety concerns or be released as greenhouse gases to the atmosphere, and/or 2) dissolve into groundwater (aqueous expression) potentially causing water quality concerns (Cahill et al., 2017; Forde et al., 2019c; Van De Ven and Mumford, 2020a, b).

The ability for leaked gas to dissolve and be transported in groundwater depends on a variety of variables including the rate of groundwater flow, surface area of gas exposed to water, the heterogeneity of the system and chemical characteristics of the native groundwater and leaked gas (Powers et al., 1998; Cirpka and Kitanidis, 2001; Sale and McWhorter, 2001; Parker and Park, 2004; Koch and Nowak, 2015). Once dissolved, the components of natural gas (mainly methane and other hydrocarbons such as ethane and propane) are relatively benign to human health if consumed (McIntosh et al., 2014; Hamilton et al., 2015). However, as a result of secondary effects associated with microbial oxidation (i.e., the consumption of methane as a source of energy for microbes), which converts methane (CH_4) to carbon dioxide (CO_2), changes in water quality can occur, such as changes in alkalinity and pH, that can drive other geochemical processes (Kelly et al., 1985; Van Stempvoort et al., 2005; Roy et al., 2016; Forde et al., 2019b). These other processes can lead to further decline in water quality through the liberation of metals as a result of mineral dissolution.

If the leaked gas does not completely dissolve into groundwater, it may pass through the saturated groundwater zone and enter into the unsaturated zone above the water table (Bachu, 2017; Forde et al., 2018). This unsaturated zone is connected to the atmosphere and therefore presents a potential pathway for surface expression. The natural gas can also be oxidized to CO_2 in this zone, therefore changing the form of greenhouse gas emitted. The mechanisms for gas (natural gas or CO_2) entering the unsaturated zone then moving to the atmosphere are not well known. Previous work as part of this project has shown that gas reaching the unsaturated zone can migrate both by advection and diffusion and then be released to the atmosphere (Forde et al., 2019a). The flux of CH_4 and CO_2 was found to be dependent on atmospheric conditions (i.e., barometric pressure), which causes fluctuations in the amount of emitted greenhouse gas over time.

Understanding the amount of GM that will be present in the environment either in the groundwater zone, the unsaturated zone or released into the atmosphere is currently not well understood. Developing this knowledge is, however, pressing because the proportionality will determine, for example, how severe water quality impacts will be, the longevity of the impacts to groundwater systems, the potential contribution to greenhouse gas emissions and therefore global climate change, and what safety risks can be expected in proximity to sites impacted by GM. This project is actively addressing these questions, such that GM can be quantified and constrained.

Description of the Study Site and the Injection Experiment

The HHFRS is situated in the Peace Region just northeast of the town of Hudson's Hope, BC (Figure 1). The HHFRS is approximately 10 000 m^2, situated in a typical landscape of the WCSB. The site has a shallow piezometric surface, fluctuating between 1–1.5 m below ground surface (bgs). Near to the centre of the site, the screen of a gas injection well was placed 26 m bgs, and a comprehensive monitoring network was constructed around this injection point. The monitoring system (Figure 2) was designed to look specifically at
- near-surface geology—achieved by well core analysis and geophysical surveys;

- groundwater conditions—achieved by installing 24 monitoring wells, including 17 multilevel wells, allowing for groundwater samples to be collected for dissolved gas concentrations, geochemical parameters and stable isotopes analyses;

- vadose zone processes—achieved by placing 12 dynamic flux chambers at 100 locations for time-discrete flux survey measurements and 22 soil-gas wells for soil-gas collection for composition and stable isotopes analyses;

- atmospheric boundary layer—achieved by installing an eddy covariance station for sitewide gas emission measurements.

The injection of natural gas commenced on June 12, 2018 and continued for 66 days. Synthetic natural gas, designed to emulate the gas composition within the Montney Formation, was injected at a rate of 1.5 m^3/day, for a total injection volume of approximately 97 m^3 (standard temperature and pressure) of gas. Groundwater and surface zones were monitored prior to, during and following the completion of gas injection. Sampling has continued each year since the commencement of the experiment, allowing the long-term impact of the injection to be assessed. The most recent sampling event occurred on July 17, 2020. An in-depth description of the site, instrumentation and injection experiment can be found in Cahill et al. (2019a, b, 2020).
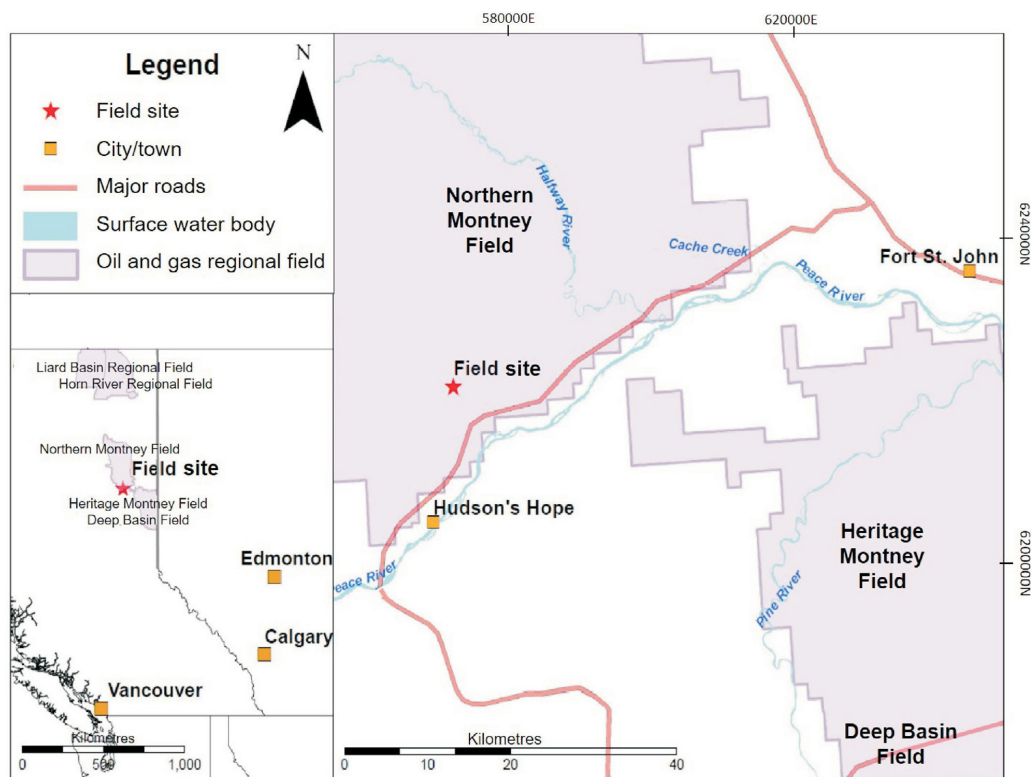
Figure 1. Location of the Hudson's Hope Field Research Station in northeastern British Columbia with regional oil and gas fields (DataBC, 2018). UTM Zone 10N, NAD 83.

Figure 2. The Hudson's Hope Field Research Station groundwater monitoring, surface flux monitoring and injection systems (photo taken September 28, 2018).

Summary of Activities and Progress

A variety of research objectives have been achieved over the last 12 months. These achievements include

1) characterization of the near-surface (above 30 m bgs) geology at the HHFRS, including publication of a journal article in *Science of The Total Environment* (Chao et al., 2020);

2) data analysis and interpretation of groundwater monitoring and geochemical data during and following the injection of synthetic natural gas;

3) data analysis and interpretation of surface flux data during and following the injection of synthetic natural gas; and

4) data analysis and interpretation of emissions data using eddy covariance during and following the injection of synthetic natural gas.

A summary of the progress and highlights of the findings for each of these activities is provided below.

Near-Surface Geology and Hydrostratigraphy

A key objective of this project was to characterize the near-surface geology at a scale relevant to understand gas flow, mass transfer and fate of GM in complex systems (centimetre to metre scale). This work has been completed and a peer-reviewed article has been published in *Science of The Total Environment* (Chao et al., 2020).

The near-surface geology at the HHFRS was characterized using a variety of tools including core profiles, cone-penetrometer testing (CPT), sediment samples and electrical resistivity surveys. Specific emphasis was placed on understanding the movement and resulting distribution of free-phase natural gas in the complex, interbedded systems expected in the WCSB. A conceptual hydrostratigraphic model of the site with respect to gas flow was developed, showing that the pattern of buoyancy-driven gas in glaciofluvial deposits can be complex and spatially heterogeneous (Figure 3). This layered system can cause both the vertical migration of gas (through the more permeable units 1 and 3; Figure 3) and lateral migration of gas due to capillary barriers (layers which impede gas flow due to high
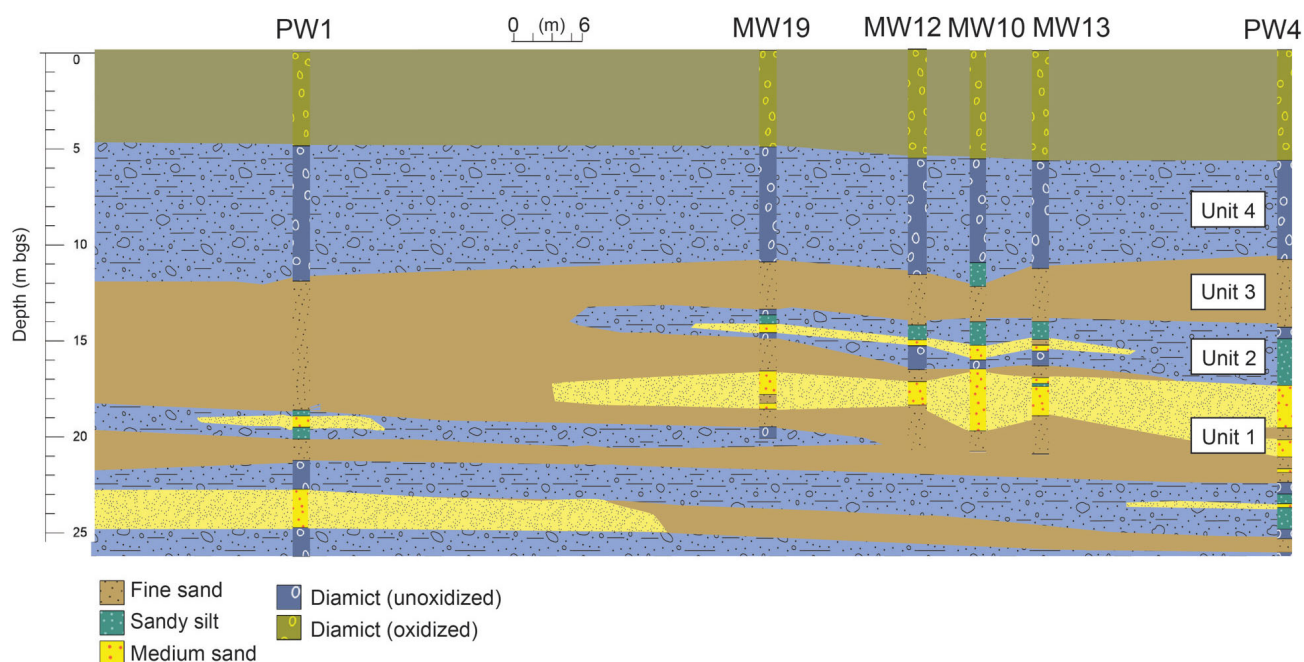
Figure 3. Hydrostratigraphic conceptual model developed for the near-surface geology at the Hudson's Hope Field Research Station (Chao et al., 2020). Abbreviations: bgs, below ground surface; MW, monitoring well; PW, pumping well.

pressure requirements to move gas through the tightly distributed pore space; units 2 and 4 in Figure 3). The local capillary barrier in the permeable zone (e.g., unit 2 in Figure 3) controls the lateral extent of gas migration, fostering significant gas pooling below the barrier. The surficial diamict (till; unit 4 in Figure 3; Figure 4), a feature common across the WCSB, can limit a significant portion of vertical gas migration from reaching the ground surface. In this system, the majority of natural gas is expected to be confined to aqueous expression because of high pressure requirements to pass through the upper diamict. The diamict was found to be oxidized between the surface and a depth of 3.5 to 5.7 m bgs then transitioned to unoxidized material (Figure 3). There was some evidence of till lenses observed embedded within the oxidized diamict. Both natural pathways and anthropogenically induced pathways (e.g., installed wells), which may have lower pressure requirements for gas to enter and flow through, could provide conduits for gas to move vertically toward the ground surface and into the atmosphere. If gas was able to enter the diamict unit, the oxidized portion might have greater capacity to degrade methane and convert it to CO_2 before reaching the surface.

One tool used to assess the near-surface geology and hydrostratigraphy was CPT. Traditionally, this approach is used in geotechnical applications, however, the properties of soil that allow differentiation between soil behaviour types (SBT) can be used to infer the hydrostratigraphic layers. That is, when coupled with soil samples collected from core, the CPT results can be used to understand the distribution of hydrofacies along a vertical profile (e.g., see Figure 5). This technique allowed for nine profiles over the extent of the HHFRS study area to be measured at the centimetre scale. This provides a very high-resolution means of constructing a conceptual site model where GM may occur.

Hydrogeology and Groundwater Monitoring

Understanding the dissolution of natural gas in the complex subsurface environment at the HHFRS is a key objective of the project. By measuring the evolution of dissolved gas using the groundwater monitoring network at the site (see Cahill et al., 2020), information on the magnitude, duration and extent of groundwater impacts can be assessed. Additionally, estimates of the amount of gas trapped in the subsurface can be assessed.

During the injection period, four sampling ports (out of 49 sampling ports in 19 wells) showed increases in concentrations of dissolved injected gas (mainly methane, ethane and propane). Approximately 40 days after the injection ceased, groundwater obtained from two more sampling ports across the site showed increases in dissolved methane (0.1–14 mg/L). The most recent measurements (490 days after the start of the injection) showed that elevated dis-


Figure 4. The upper diamict layer at the Hudson's Hope Field Research Station (unit 4) is a plasticine-like material that will limit gas flow through the layer.

solved methane appeared in 17 sampling ports in 10 wells (Figure 6). The most significant increase in dissolved methane (~1 to 27.1 mg/L) appeared at a depth of 18 m in monitoring well 9, representing a highly heterogeneous distribution of the gas. This depth corresponds to unit 1, as expected because this is a permeable unit that would allow for gas to migrate and accumulate. Moderate increases (~0.1–8.0 mg/L) in dissolved methane occurred at monitoring depths of 12 and 16 m (unit 3). No significant increases in dissolved gas concentrations were observed at the deepest monitoring depth of 20 m. Note that the measured concentrations are lower than the expected solubility of methane that varies with depth, ranging from 42 to 68 mg/L from 12 to 26 m bgs.

Sample collection (most recent field event was July 17, 2020) and analysis of groundwater for dissolved gas and isotope compositions of methane are ongoing. Currently, the focus is on understanding the rate of dissolution of free-phase gas trapped within the system. Using upscaled mass transfer approaches (Christ et al., 2006, 2010) and sitewide dissolved methane concentrations, the aim is to estimate the longevity of the free-phase gas within the system. Based on preliminary analysis, the time for complete dissolution of all injected gas will be on the order of tens of years. In addition to mass transfer considerations, the fate of natural gas is being assessed by analyzing degradation products associated with microbial oxidation (CO_2) coupled with isotopic analysis. The potential degradation of the injected gas can reduce the timescale of its presence in groundwater systems.

Soil Gas and Surface Efflux

To quantify the surface expression of GM at the HHFRS, the release of CH_4 and CO_2 to the surface was measured using a variety of soil flux techniques including dynamic long-term soil flux chambers, survey chamber measure-
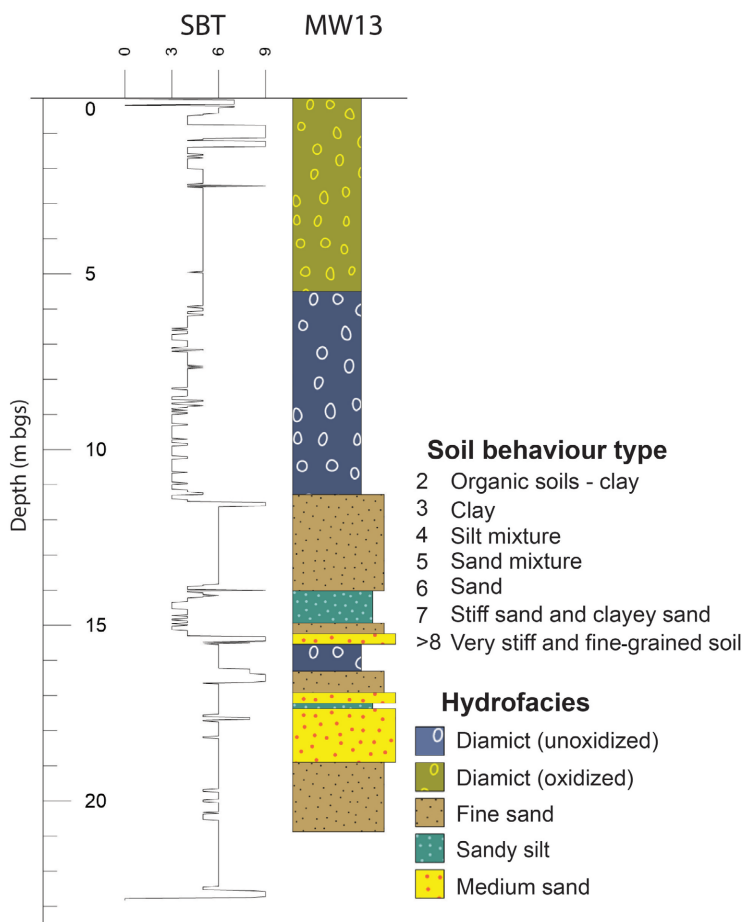
Figure 5. Vertical profile of soil behaviour types (SBT) for monitoring well (MW) 13 compared to the hydrofacies observed from the core log. Abbreviation: bgs, below ground surface.

ments and soil-gas wells distributed over the surface of the HHFRS (Figure 7a). The combination of these three monitoring approaches allowed for temporally and spatially expansive monitoring and for isotopic data to be collected to assess methane and ethane degradation in the subsurface. With these multiple lines of data, a better understanding of the surface expression of GM associated with a leaking energy well could be developed.
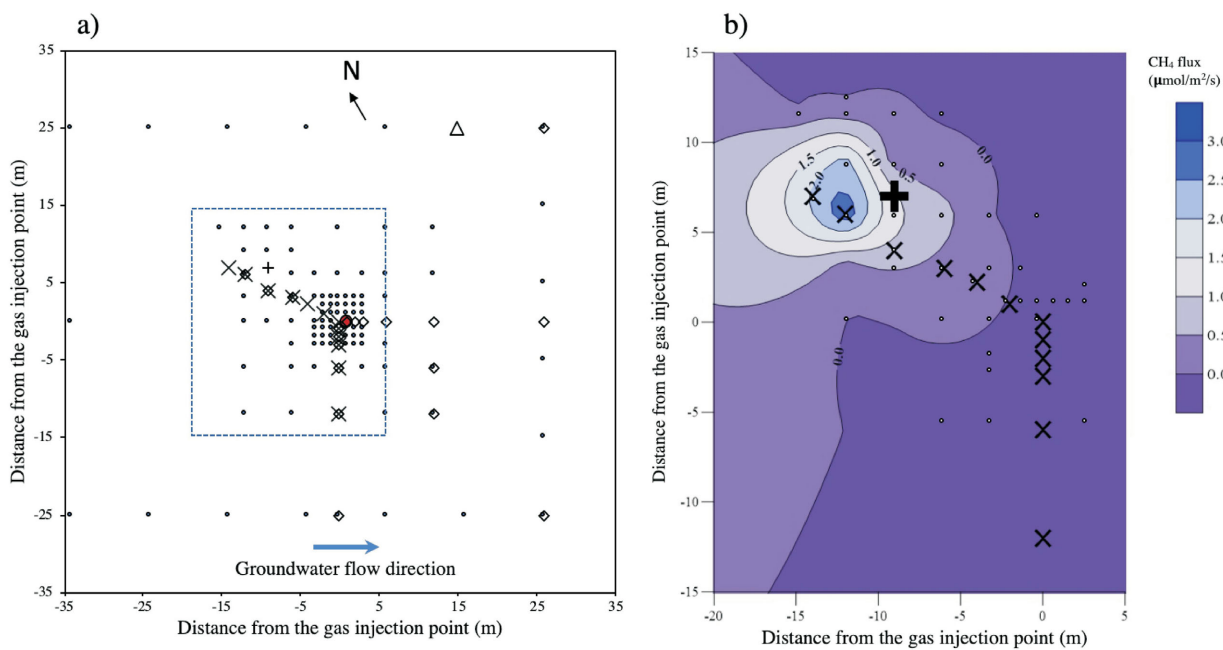
Methane fluxes above background levels were measured to the northwest of the injection point (approximately 16 m; Figure 7b). This location is upgradient of groundwater flow, suggesting that free-phase gas movement in the heterogeneous subsurface was governed by contrasts in entry pressure and permeability as opposed to groundwater flow. The CH_4 fluxes in the area of the release fluctuated between 0.1 and 8 $\mu mol/m^2/s$, suggesting that a preferential flow pathway developed between the saturated zone and the surface. The CO_2 fluxes were more challenging to interpret because natural increases of CO_2 fluxes from the subsurface due to increased root respiration associated with warmer summer months occurred concurrently with the release of the natural gas. Although an increase from background

CO_2 levels was observed, it is difficult to determine if this was the result of injected CH_4 being oxidized. Measurements using the survey chambers at 12 different time points (every 2–4 weeks following the initiation of gas injection) allowed for a larger area to be monitored to determine fluxes across the HHFRS. These measurements, however, confirmed that elevated CH_4 fluxes were localized to the area northwest of the injection point near to monitoring well (MW) 2 (Figure 7b). The flux data suggest that gas migration from the unsaturated zone to the surface is likely attributed to preferential flow paths through the upper diamict layer, described by Chao et al. (2020). This confirmatory evidence of the localized fluxes reiterates the findings of Chao et al. (2020), and suggests that gas will reach the surface only through naturally formed pathways in the diamict (e.g., fractures in the material, seams of coarse-grained sediments) or as a result of anthropogenic-formed pathways (e.g., along installed wells).

In addition to the flux data, soil-gas compositions (CH_4, CO_2, N_2, Ar) and isotope ratios provide further insights on the mechanisms of surface expression at the HHFRS. The carbon isotopic composition ($\delta^{13}C$) of CH_4 present in the
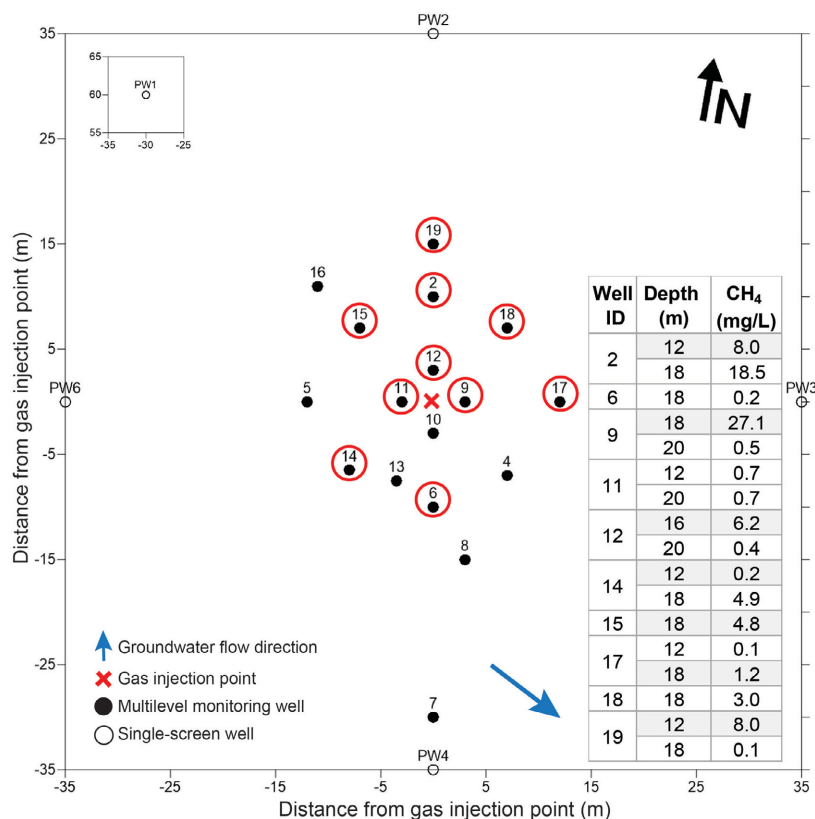
Figure 6. Groundwater monitoring well locations, including sampling locations that showed elevated dissolved methane (CH$_4$) concentrations (red circles) 490 days after the injection began at Hudson's Hope Field Research Station. Abbreviation: PW, pumping well.

Well ID	Depth (m)	CH$_4$ (mg/L)
2	12	8.0
	18	18.5
6	18	0.2
9	18	27.1
	20	0.5
11	12	0.7
	20	0.7
12	16	6.2
	20	0.4
14	12	0.2
	18	4.9
15	18	4.8
17	12	0.1
	18	1.2
18	18	3.0
19	12	8.0
	18	0.1

· Survey collar location   ✕ Long-term chamber   + MW2   ● Gas injection point   ◇ Soil-gas well   △ EC system

Figure 7. a) Location of surface flux monitoring equipment at the Hudson's Hope Field Research Station and **b)** methane (CH$_4$) flux using an integrated interpolation of long-term soil flux chambers and survey chamber measurements, 45 days after the beginning of injection. Dashed box in a) represents the area presented in b). Abbreviations: EC, eddy covariance; MW, monitoring well.
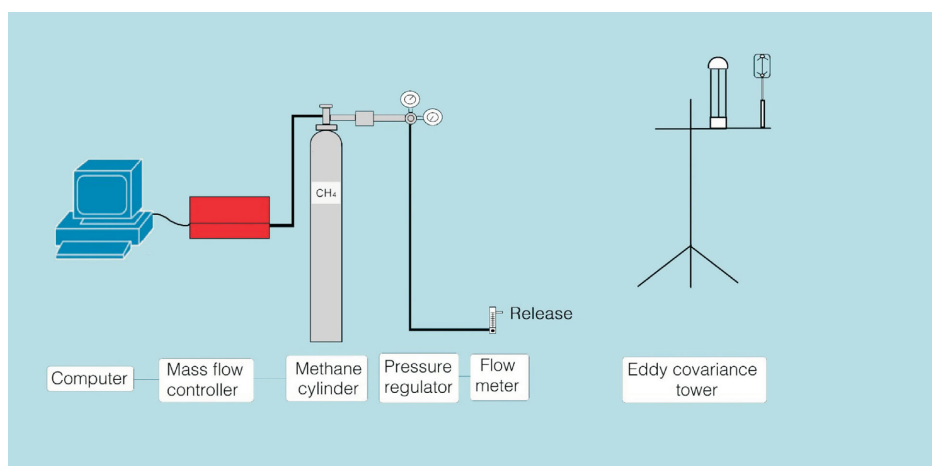
Figure 8. Schematic diagram showing the experimental setup of the controlled gas release experiments at Hudson's Hope Field Research Station.

unsaturated zone is less negative than that of the injected CH_4 and $\delta^{13}C$ of CO_2 is more negative than is typical for background conditions. This suggests that oxidation of the injected CH_4 is occurring facilitated by microbes. With further investigation, the rate of oxidation of the injected CH_4 can be determined when coupled with investigation of the microbial community structure and activity at the site.

Eddy Covariance and Micrometeorology

The eddy covariance (EC) tower was deployed prior to and during the natural gas release in the subsurface at the site in 2018 (see Cahill et al., 2020 for a detailed description). The EC system was redeployed to the site in the summer of 2019. During this time a controlled release at the surface was conducted to better constrain the results from the subsurface release (described below), after which the EC system was decommissioned. A comprehensive analysis of the dataset collected over the injection experiment enabled the gathering of knowledge about gas leakage to the atmosphere (location and volume).

The controlled surface release experiments were of paramount importance, and helped confirm and validate: 1) the flux footprint model to be used for data analysis, and 2) the methodology of data analysis to be followed, that is, converting the EC measurements to values that are more representative of gas leakage to the atmosphere. During the surface release experiments, CH_4 was released using a mass flow controller under varying conditions and was measured using the EC system (Figure 8). Various factors associated with the gas source, such as along-wind distance from the tower, the height of the source from the surface and release rates, were tested to understand the dependence of the flux footprint model on these factors. All the controlled releases indicated that the flux footprint model of Kljun et al. (2015) performed the best under the conditions of this project.

The approaches for flux footprint analysis included 1) down-scaling the EC measurements to the surface measurements by knowing the location and nature of the leak as informed by the chambers, and 2) demonstrating an inversion approach (based on Lewicki et al., 2009) to independently use EC measurements to obtain a surface flux distribution over the domain of the field site, and identify the location of the leak. The data analysis is complete and the results will be described in detail in a peer-reviewed publication.

Conclusions and Ongoing Work

Field activities at the Hudson's Hope Field Research Station have been completed with the exception of annual groundwater sampling events to monitor continued dissolution and degradation of the injected natural gas. Long-term groundwater monitoring infrastructure will remain for this purpose, whereas other systems such as the eddy covariance and solar power stations have been decommissioned. In addition to the publication of the near-surface geology and hydrostratigraphy investigation results in *Science of The Total Environment*, several other manuscripts are in preparation detailing 1) the surface flux monitoring and the key findings of these efforts, 2) the evolution of dissolved gas at the site, and 3) the geochemical processes occurring at the site as a result of the controlled gas release. Further dissemination of this research has occurred through conferences including GeoConvention, the American Geophysical Union Fall Meeting and The Geological Society of America Annual Meeting.

Acknowledgments

References

Bachu, S. (2017): Analysis of gas leakage occurrence along wells in Alberta, Canada, from a GHG perspective – gas migration outside well casing; International Journal of Greenhouse Gas Control, v. 61, p. 146–154, URL <https://doi.org/10.1016/j.ijggc.2017.04.003>.

Brooks, M.C., Wise, W.R. and Annable, M.D. (1999): Fundamental changes in in situ air sparging flow patterns; Groundwater Monitoring & Remediation, v. 19, p. 105–113.

Cahill, A.G., Beckie, R., Ladd, B., Sandl, E., Goetz, M., Chao, J., Soares, J., Manning, C., Chopra, C., Finke, N., Hawthorne, I., Black, A., Mayer, K.U., Crowe, S., Cary, T., Lauer, R., Mayer, B., Allen, A., Kirste, D. and Welch, L. (2019a): Advancing knowledge of gas migration and fugitive gas from energy wells in northeast British Columbia, Canada; Greenhouse Gases: Science and Technology, v. 9, issue 2, p. 134–151, URL <https://doi.org/10.1002/ghg.1856>.

Cahill, A.G., Ladd, B., Chao, J., Soares, J., Cary, T., Finke, N., Manning, C., Chopra, C., Hawthorne, I., Forde, O.N., Mayer, K.U., Black, A., Crowe, S., Mayer, B., Lauer, R., van Geloven, C., Welch, L. and Beckie, R.D. (2019b): Implementation and operation of a multidisciplinary field investigation involving a subsurface controlled natural gas release, northeastern British Columbia; in Geoscience BC Summary of Activities 2018: Energy and Water, Geoscience BC, Report 2019-02, p. 95–104, URL <http://cdn.geoscience-bc.com/pdf/SummaryofActivities2018/EW/2016-043_SoA2018_EW_Cahill_ControlledGasRelease.pdf> [November 2020].

Cahill, A.G., Ladd, B., Chao, J., Soares, J., Cary, T., Finke, N., Manning, C., Popp, A.L., Chopra, C., Mayer, K.U., Black, A., Lauer, R., van Geloven, C., Welch, L., Crowe, S., Mayer, B. and Beckie, R.D. (2020): Controlled natural gas release experiment in a confined aquifer, northeastern British Columbia (NTS 094A/04): activity report 2018–2019; in Geoscience BC Summary of Activities 2019: Energy and Water, Geoscience BC, Report 2020-02, p. 145–160, URL <http://www.geosciencebc.com/i/pdf/SummaryofActivities2019/EW/Project%202016-043_EW%20SOA-2019.pdf> [November 2020].

Cahill, A.G., Parker, B.L., Mayer, B., Mayer, K.U. and Cherry, J.A. (2018): High resolution spatial and temporal evolution of dissolved gases in groundwater during a controlled natural gas release experiment; Science of The Total Environment, v. 622–623, p. 1178–1192, URL <https://doi.org/10.1016/j.scitotenv.2017.12.049>.

Cahill, A.G., Steelman, C.M., Forde, O., Kuloyo, O., Emil Ruff, S., Mayer, B., Mayer, K.U., Strous, M., Ryan, M.C., Cherry, J.A. and Parker, B.L. (2017): Mobility and persistence of methane in groundwater in a controlled-release field experiment; Nature Geoscience, v. 10, no. 4, p. 289–294, URL <https://doi.org/10.1038/ngeo2919>.

Chao, J.T.-H., Cahill, A.G., Lauer, R.M., Van De Ven, C.J.C. and Beckie, R.D. (2020): Propensity for fugitive gas migration in glaciofluvial deposits: an assessment of near-surface hydrofacies in the Peace Region, northeastern British Columbia; Science of The Total Environment, v. 749, art. 141459, URL <https://doi.org/10.1016/j.scitotenv.2020.141459>.

Christ, J.A., Ramsburg, C.A., Pennell, K.D. and Abriola, L.M. (2006): Estimating mass discharge from dense nonaqueous phase liquid source zones using upscaled mass transfer coefficients: an evaluation using multiphase numerical simulations; Water Resources Research, v. 42, p. 1–13, URL <https://doi.org/10.1029/2006WR004886>.

Christ, J.A., Ramsburg, C.A., Pennell, K.D. and Abriola, L.M. (2010): Predicting DNAPL mass discharge from pool-dominated source zones; Journal of Contaminant Hydrology, v. 114, p. 18–34, URL <https://doi.org/10.1016/j.jconhyd.2010.02.005>.

Cirpka, O.A. and Kitanidis, P.K. (2001): Transport of volatile compounds in porous media in the presence of a trapped gas phase; Journal of Contaminant Hydrology, v. 49, p. 263–285, URL <https://doi.org/10.1016/S0169-7722(00)00196-0>.

Council of Canadian Academies (2014): Environmental impacts of shale gas extraction in Canada: the expert panel on harnessing science and technology to understand the environmental impacts of shale gas extraction; Council of Canadian Academies, Ottawa, Ontario, 262 p.

DataBC (2018): B.C. Data Catalogue; Government of British Columbia, URL <https://catalogue.data.gov.bc.ca> [September 2018].

Dusseault, M. and Jackson, R. (2014): Seepage pathway assessment for natural gas to shallow groundwater during well stimulation, in production, and after abandonment; Environmental Geosciences, v. 21, p. 107–126, URL <https://doi.org/10.1306/eg.04231414004>.

Forde, O.N., Cahill, A.G., Beckie, R.D. and Mayer, K.U. (2019a): Barometric-pumping controls fugitive gas emissions from a vadose zone natural gas release; Scientific Reports, v. 9, p. 1–9, URL <https://doi.org/10.1038/s41598-019-50426-3>.

Forde, O.N., Cahill, A.G., Mayer, K.U., Mayer, B., Simister, R.L., Finke, N., Crowe, S.A., Cherry, J.A. and Parker, B.L. (2019b): Hydro-biogeochemical impacts of fugitive methane on a shallow unconfined aquifer; Science of The Total Environment, v. 690, p. 1342–1354, URL <https://doi.org/10.1016/j.scitotenv.2019.06.322>.

Forde, O.N., Mayer, K.U., Cahill, A.G., Mayer, B., Cherry, J.A. and Parker, B.L. (2018): Vadose zone gas migration and surface effluxes after a controlled natural gas release into an unconfined shallow aquifer; Vadose Zone Journal, v. 17, issue 1, p. 1–16, URL <https://doi.org/10.2136/vzj2018.02.0033>.

Forde, O.N., Mayer, K.U. and Hunkeler, D. (2019c): Identification, spatial extent and distribution of fugitive gas migration on the well pad scale; Science of The Total Environment, v. 652, p. 356–366, URL <https://doi.org/10.1016/j.scitotenv.2018.10.217>.

Geistlinger, H., Krauss, G., Lazik, D. and Luckner, L. (2006): Direct gas injection into saturated glass beads: transition from incoherent to coherent gas flow pattern; Water Resources Research, v. 42, p. 1–12, URL <https://doi.org/10.1029/2005WR004451>.

Glass, R.J., Conrad, S.H. and Peplinski, W. (2000): Gravity-destabilized nonwetting phase invasion in macroheterogeneous porous media: experimental observations of invasion dynamics and scale analysis; Water Resources

Research, v. 36, p. 3121–3137, URL <https://doi.org/10.1029/2000WR900152>.

Hamilton, S.M., Grasby, S.E., McIntosh, J.C. and Osborn, S.G. (2015): The effect of long-term regional pumping on hydrochemistry and dissolved gas content in an undeveloped shale-gas-bearing aquifer in southwestern Ontario, Canada; Hydrogeology Journal, v. 23, p. 719–739, URL <https://doi.org/10.1007/s10040-014-1229-7>.

Jackson, R.B., Pearson, B.R., Osborn, S.G., Warner, N.R. and Vengosh, A. (2011): Research and policy recommendations for hydraulic fracturing and shale-gas extraction; Duke University, Center on Global Change, Durham, North Carolina, 11 p., URL <https://nicholas.duke.edu/cgc/HydraulicFracturingWhitepaper2011.pdf> [November 2020].

Ji, W., Dahmani, A., Ahlfeld, D.P., Lin, J.D. and Hill, E. (1993): Laboratory study of air sparging: air flow visualization; Groundwater Monitoring & Remediation, v. 13, p. 115–126, URL <https://doi.org/10.1111/j.1745-6592.1993.tb-00455.x>.

Kelly, W.R., Matisoff, G. and Fisher, J.B. (1985): The effects of a gas well blow out on groundwater chemistry; Environmental Geology and Water Sciences, v. 7, p. 205–213, URL <https://doi.org/10.1007/BF02509921>.

Kljun, N., Calanca, P., Rotach, M.W. and Schmid, H.P. (2015): A simple two-dimensional parameterisation for Flux Footprint Prediction (FFP); Geoscientific Model Development, v. 8, p. 3695–3713, URL <https://doi.org/10.5194/gmd-8-3695-2015>.

Koch, J. and Nowak, W. (2015): Predicting DNAPL mass discharge and contaminated site longevity probabilities: conceptual model and high-resolution stochastic simulation; Water Resources Research, v. 51, p. 806–831, URL <https://doi.org/10.1002/2014WR015478>.

Kueper, B.H., Redman, D., Starr, R.C., Reitsma, S. and Mah, M. (1993): A field experiment to study the behavior of tetrachloroethylene below the water table: spatial distribution of residual and pooled DNAPL; Groundwater, v. 31, p. 756–766, URL <https://doi.org/10.1111/j.1745-6584.1993.tb-00848.x>.

Lewicki, J.L., Hilley, G.E., Fischer, M.L., Pan, L., Oldenburg, C.M., Dobeck, L. and Spangler, L. (2009): Eddy covariance observations of surface leakage during shallow subsurface CO 2 releases; Journal Geophysical Research, Atmospheres, v. 114, art. D12302, URL <https://doi.org/10.1029/2008JD011297>.

McIntosh, J.C., Grasby, S.E., Hamilton, S.M. and Osborn, S.G. (2014): Origin, distribution and hydrogeochemical controls on methane occurrences in shallow aquifers, southwestern Ontario, Canada; Applied Geochemistry, v. 50, p. 37–52, URL <https://doi.org/10.1016/j.apgeochem.2014.08.001>.

Parker, J.C. and Park, E. (2004): Modeling field-scale dense nonaqueous phase liquid dissolution kinetics in heterogeneous aquifers; Water Resources Research, v. 40, p. 1–12, URL <https://doi.org/10.1029/2003WR002807>.

Powers, S.E., Nambi, I.M. and Curry, G.W., Jr. (1998): Non-aqueous phase liquid dissolution in heterogeneous systems: mechanisms and a local equilibrium modeling approach; Water Resources Research, v. 34, p. 3293–3302, URL <https://doi.org/10.1029/98WR02471>.

Roy, N., Molson, J., Lemieux, J.M., Van Stempvoort, D. and Nowamooz, A. (2016): Three-dimensional numerical simulations of methane gas migration from decommissioned hydrocarbon production wells into shallow aquifers; Water

Resources Research, v. 52, p. 5598–5618, URL <https://doi.org/10.1002/2016WR018686>.

Sale, T.C. and McWhorter, D.B. (2001): Steady state mass transfer from single-component dense nonaqueous phase liquids in uniform flow fields; Water Resources Research, v. 37, p. 393–404, URL <https://doi.org/10.1029/2000WR-900236>.

Schout, G., Griffioen, J., Hassanizadeh, S.M., Cardon de Lichtbuer, G. and Hartog, N. (2019): Occurrence and fate of methane leakage from cut and buried abandoned gas wells in the Netherlands; Science of The Total Environment, v. 659, p. 773–782, URL <https://doi.org/10.1016/j.scitotenv.2018.12.339>.

Selker, J.S., Niemet, M., Mcduffie, N.G., Gorelick, S.M. and Parlange, J.-Y. (2007): The local geometry of gas injection into saturated homogeneous porous media; Transport in Porous Media, v. 68, p. 107–127, URL <https://doi.org/10.1007/s11242-006-0005-0>.

Shaw, J. (1982): Melt-out till in the Edmonton area, Alberta, Canada; Canadian Journal of Earth Sciences, v. 19, p. 1548–1569, URL <https://doi.org/10.1139/e82-134>.

Steelman, C.M., Klazinga, D.R., Cahill, A.G., Endres, A.L. and Parker, B.L. (2017): Monitoring the evolution and migration of a methane gas plume in an unconfined sandy aquifer using time-lapse GPR and ERT; Journal of Contaminant Hydrology, v. 205, p. 12–24, URL <https://doi.org/10.1016/j.jconhyd.2017.08.011>.

Van De Ven, C.J.C. and Mumford, K.G. (2019): Characterization of gas injection flow patterns subject to gravity and viscous forces; Vadose Zone Journal, v. 18, no. 1, p. 1–11, URL <https://doi.org/10.2136/vzj2019.02.0014>.

Van De Ven, C.J.C. and Mumford, K.G. (2020a): Aqueous and surface expression of subsurface GHGs: subsurface mass transfer effects; Water Research, v. 170, art. 115327, URL <https://doi.org/10.1016/j.watres.2019.115327>.

Van De Ven, C.J.C. and Mumford, K.G. (2020b): Intermediate-scale laboratory investigation of stray gas migration impacts: methane source architecture and dissolution; Environmental Science & Technology, v. 54, p. 6299–6307, URL <https://doi.org/10.1021/acs.est.0c00456>.

Van De Ven, C.J.C. and Mumford, K.G. (2020c): Intermediate-scale laboratory investigation of stray gas migration impacts: transient gas flow and surface expression; Environmental Science & Technology, v. 54, p. 11641–12806, URL <https://doi.org/10.1021/acs.est.0c03530>.

Van Stempvoort, D., Maathuis, H., Jaworski, E., Mayer, B. and Rich, K. (2005): Oxidation of fugitive methane in ground water linked to bacterial sulfate reduction; Groundwater, v. 43, p. 187–199, URL <https://doi.org/10.1111/j.1745-6584.2005.0005.x>.

Vengosh, A., Jackson, R.B., Warner, N., Darrah, T.H. and Kondash, A. (2014): A critical review of the risks to water resources from shale gas development and hydraulic fracturing in the United States; Environmental Science & Technology, v. 15, p. 8334–8248, URL <https://doi.org/10.1021/es405118y>.

Vidic, R.D., Brantley, S.L., Vandenbossche, J.M., Yoxtheimer, D. and Abad, J.D. (2013): Impact of shale gas development on regional water quality; Science, v. 340, issue 6134, art. 1235009, URL <https://doi.org/10.1126/science.1235009>.

Pilot Collaborative Water Monitoring Program, Northeastern British Columbia (NTS 094A, Parts of 093P, O, 094B, G, H): An Overview

S.L. Lapp, British Columbia Oil and Gas Commission, Fort St. John, British Columbia, suzan.lapp@bcogc.ca

D.L. Cottrell, Shell Canada Ltd., Calgary, Alberta

E.G. Johnson, British Columbia Ministry of Energy, Mines and Low Carbon Innovation, Victoria, British Columbia

W.T. Van Dijk, Matrix Solutions Inc., Edmonton, Alberta

L.G. Wytrykush, Geoscience BC, Vancouver, British Columbia

Project Background

Northeastern British Columbia (BC) is an area of active and historical natural gas development, mining, forestry and other activities. Projects such as the Province of BC's Northeast Water Strategy (NEWS) and Regional Strategic Environmental Assessment (RSEA) and results of the Scientific Review of Hydraulic Fracturing in British Columbia (Scientific Hydraulic Fracturing Review Panel, 2019) have identified the need to

- increase water monitoring in BC's Northeast region,
- address Treaty 8 First Nations' concerns over water quantity and quality, and
- combine Traditional Knowledge with scientific data to better understand local water resources.

Over the past 100 years, the Water Survey of Canada has monitored streamflow at 54 stations in northeastern BC, however, only 29 stations are active today. Both surface and groundwater quality have been monitored randomly and inconsistently at numerous locations across the northeast; historically, there was little effort to correlate water quantity with water quality. This lack of baseline data, particularly in some of the smaller watersheds, makes it a challenge to manage water. Several needs have been identified in northeastern BC, specifically, the collection of scientific data to improve the understanding of surface water flow and correlated surface water quality and the collection of groundwater and climate monitoring data to 1) assess groundwater–surface water interaction, 2) assess groundwater quality and 3) improve watershed water balances. There is also an overarching need to develop a framework that relates the wealth of First Nations Traditional Knowl-

edge to scientific data. This will begin bridging the data gap between these two methods of assessment.

In recognition of these needs, Geoscience BC initiated three overlapping projects summarized under the title of Pilot Collaborative Water Monitoring Program, Northeast B.C. (Figure 1):

1) Northeast B.C. Hydrometric Monitoring Project
   a) install four to six hydrometric stations to measure surface water quantity
2) Groundwater Quantity and Quality, Surface Water Quality and Climate Monitoring Project
   a) install groundwater monitoring well(s) to monitor quantity and quality
   b) install surface water quality monitoring sites, which will align with the hydrometric station locations to be installed as part of the Northeast B.C. Hydrometric Monitoring Project
   c) install climate stations to monitor local weather in the vicinity of groundwater and surface water monitoring sites
3) Traditional Knowledge Project
   a) gather Traditional Knowledge at each station/site to incorporate with Western science data

The three projects will be conducted in unison, were started in the fall of 2020 and will end by March 2023.

Program Description

The three projects will be conducted in collaboration with the Treaty 8 First Nations; all Treaty 8 First Nations have been invited to participate in the program. The first online meeting was held in December 2020. As part of the ongoing meetings with the First Nations communities, four to six hydrometric station locations will be selected within the pilot study area (Figure 2), ideally within medium to high disturbance watersheds (Johnson, 2015), which will align
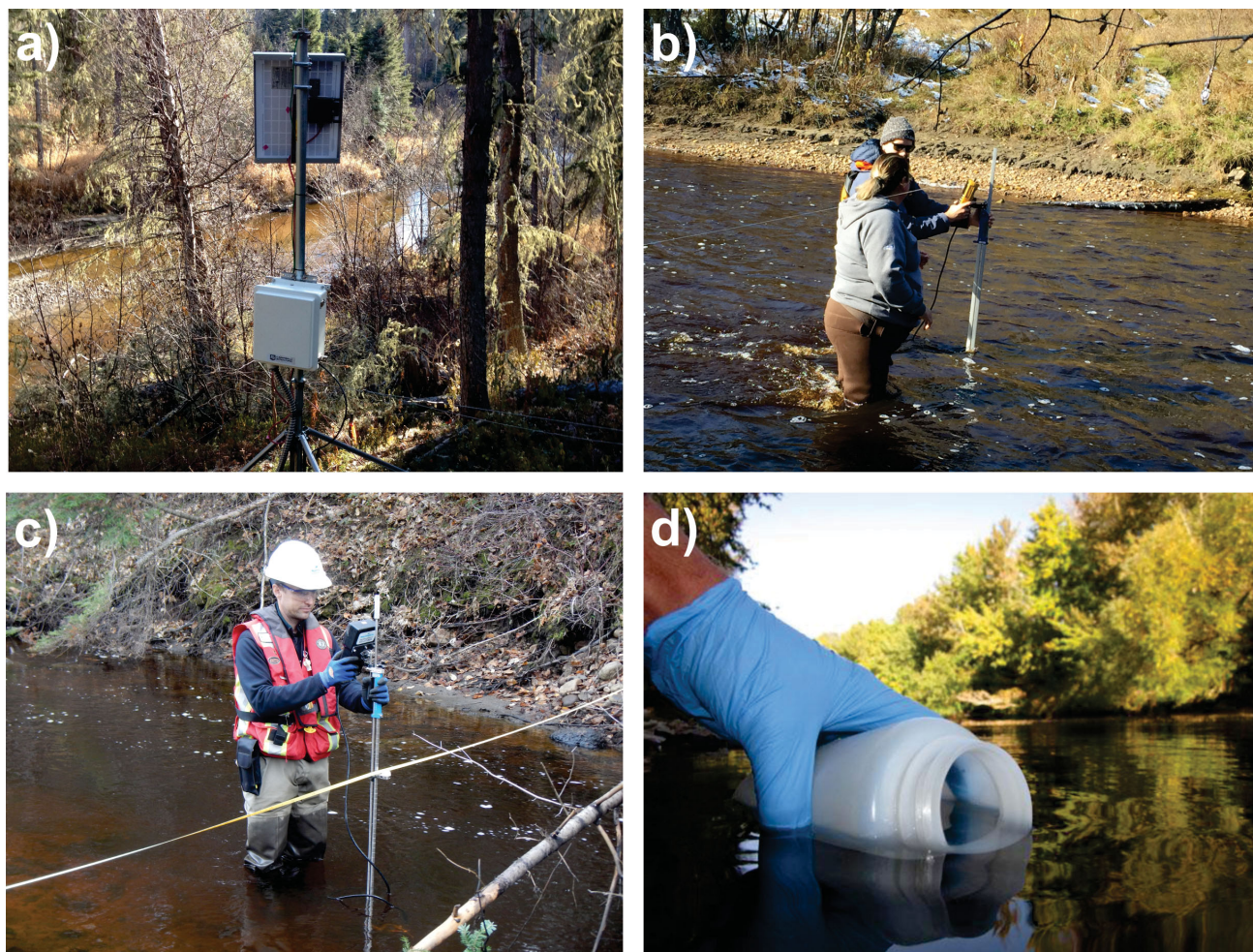
Figure 1. A selection of the equipment to be installed and data to be collected at the chosen sampling sites: **a)** data communication equipment, **b)** First Nations training, **c)** streamflow measurement and **d)** water quality sampling.

with the RSEA process. Sites will initially be selected through a desktop review and confirmed through field site visits in the spring/early summer of 2021. The equipment will be installed during the field season of 2021 and data collection and associated sampling will continue through to the end of 2022 to capture two full seasons of data. Hydrometric stations to measure surface water quantity will be installed at all the selected sites, and surface water quality sampling will be conducted where possible. Groundwater wells (for groundwater quantity and quality monitoring) and climate monitoring equipment will be installed at selected sites where possible.

The Treaty 8 First Nations will be invited to be a part of the entire process, from selecting the station locations to installing the equipment to collecting the data. In addition, First Nations will be invited to share their Traditional Knowledge at each site. This collaborative program is designed to be a two-way learning process—capturing data with a study design that will build scientific knowledge and

including Traditional Knowledge to help bridge the gap between the learnings gained from monitoring and Indigenous values, which will then be conserved. The program is scheduled to wrap up in 2023 with a final report. However, conversations have been initiated with industry and government to continue this project beyond 2023.

Summary

This pilot water monitoring study takes a collaborative approach with First Nations, government and consultants working together to select water and climate monitoring locations in northeastern British Columbia. The combining of Traditional Knowledge and Western science can be used to inform decisions and support the rights of the Treaty 8 First Nations. By collecting the different types of surface water, groundwater and climate data, it will hopefully lead to a better understanding of the health of the study area watersheds and the overall water balance.
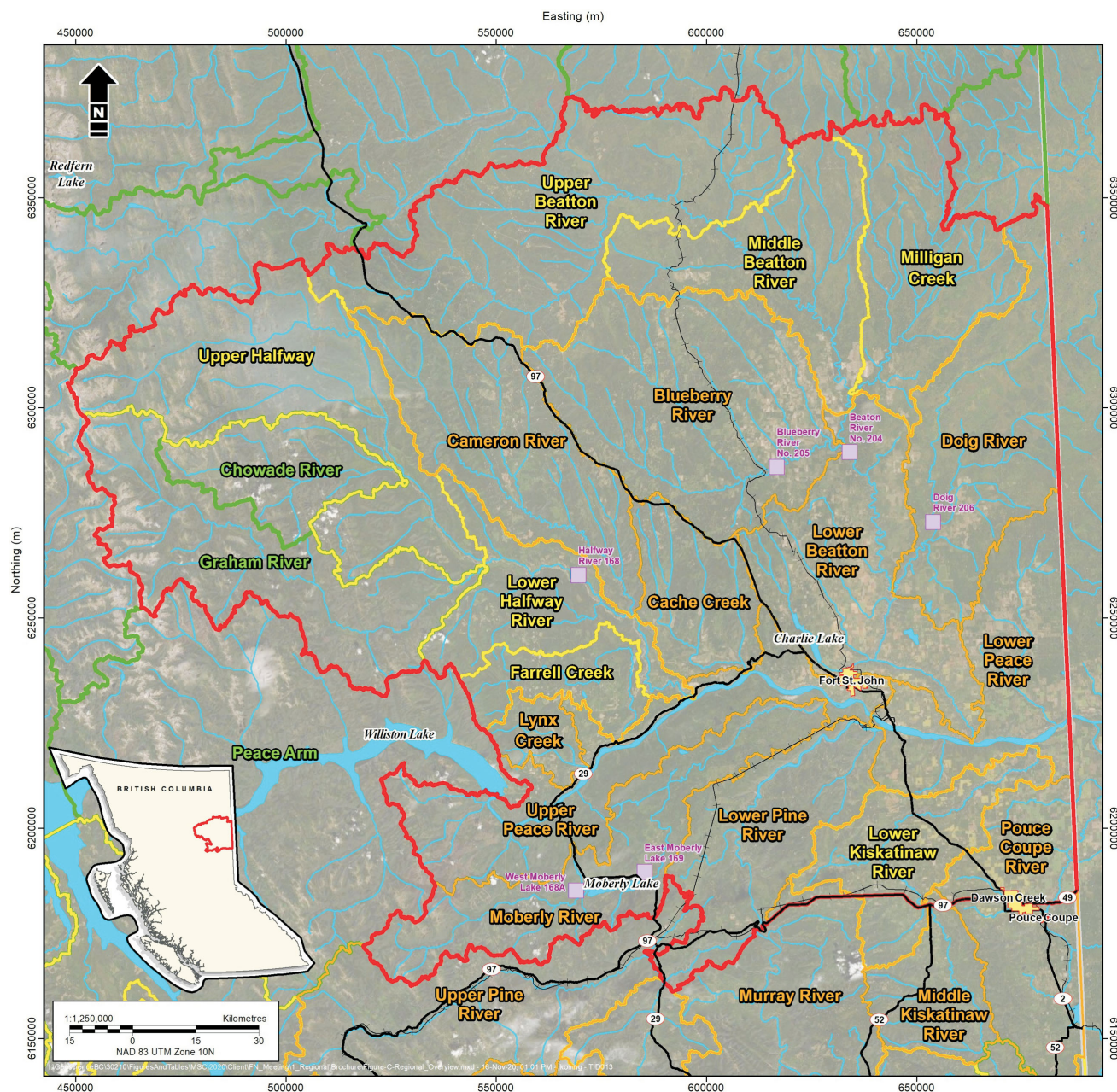
Figure 2. The proposed Pilot Collaborative Water Monitoring Program study area in northeastern British Columbia is outlined in red. First Nation communities are indicated by purple squares. Each of the watersheds has been ranked based on disturbance levels, which align with the Regional Strategic Environmental Assessment process. The colour of the watershed boundaries and names indicate the level of disturbance: orange is high, yellow is medium and green is low.

The long-term goals of the program are to

- expand surface water, groundwater and climate monitoring across northeastern British Columbia,

- continue collaborating with First Nations to build water and climate monitoring capacity,

- increase common understanding of water at several key locations and develop better tools for cross-cultural dialogue about shared waters, and

- develop an effective monitoring approach to assist with watershed health assessments and identify changes in watershed health.

Acknowledgments

also thank C. van Geloven for his constructive comments on this manuscript.

References

Johnson, E.G. (2015): Disturbance-sensitivity based approach to prioritizing monitoring in northeast B.C.; BC Ministry of Forests, Lands, Natural Resource Operations and Rural Development, 79 p., URL <https://www2.gov.bc.ca/assets/gov/environment/air-land-water/water/northeast-water-strategy/disturbance_sensitivity_based_approach.pdf> [January 2019].

Scientific Hydraulic Fracturing Review Panel (2019): Scientific review of hydraulic fracturing in British Columbia; BC Ministry of Energy, Mines and Low Carbon Innovation, final report, 220 p., URL <https://www2.gov.bc.ca/assets/gov/farming-natural-resources-and-industry/natural-gas-oil/responsible-oil-gas-development/scientific_hydraulic_fracturing_review_panel_final_report.pdf> [October 2020].

Groundwater Recharge in a Confined Paleovalley Setting, Northeastern British Columbia (Part of NTS 093P)

A.M. Goetz[1], The University of British Columbia, Vancouver, British Columbia, mgoetz@eoas.ubc.ca

R.D. Beckie, The University of British Columbia, Vancouver, British Columbia

Introduction

The Peace Region in northeastern British Columbia (BC) is located on the western edge of the Western Canada Sedimentary Basin (WCSB), bordering the Canadian Rocky Mountains (Figure 1). The hydraulic characteristics of major aquifers of the Peace Region in northeastern BC have been the subject of increasing interest over the last decade (Foundry Spatial Ltd., 2011; Baye et al., 2016; Morgan et al., 2019; Chao et al., 2020). Although groundwater is not the main source of drinking water for the over 60 000 residents of the Peace Region, as most large communities source their water supply from major rivers, nonetheless understanding sustainable yield of groundwater is important for domestic, industrial, agricultural and environmental purposes (Bredehoeft, 2002; Baye et al., 2016; Statistics Canada, 2017). Most groundwater wells in northeastern BC are constructed with a well screen installed in weathered/fractured bedrock, with fewer having the screen installed in buried-valley sand/gravel aquifers (Baye et al., 2016). Buried-valley, or paleovalley, aquifers commonly host significant sources of groundwater in those areas where they are thick and laterally continuous (Hickin et al., 2008). For example, a buried-valley aquifer located in the Peace River paleovalley near Hudson's Hope, BC was shown to yield 31.5 L/s (600 gal/min) during a 72-hour constant-rate pumping test (Gardiner et al., 2020).

The objective of this study is to determine dominant recharge pathways through low-permeability, confining layers to both weathered bedrock and buried-valley aquifers in the Sunset paleovalley, an archetypical groundwater system that is located in the southern Peace Region, west of Dawson Creek, BC (Figure 1). The spatial distribution of recharge values, residence times of aquifers and the steady-state water balance of the system are analyzed using a groundwater-flow model.

The distribution and magnitude of recharge is dependant on climate (precipitation/evapotranspiration rates), geological framework (confining thickness/conductivity) and topography (runoff/infiltration ratio; Winter, 2001; Sanford, 2002). Over much of the study area, the aquifers are confined by low-permeability tills, which limit recharge rates, but protect the aquifers from potentially degrading surficial processes such as drought and contamination (Cummings et al., 2012). The dominant factor controlling recharge for the Sunset paleovalley system is assumed to be lithology, with most recharge likely originating where 'windows' of thin surficial confining material (e.g., Quaternary diamict) exist, resulting in a shorter travel time to the aquifer below (Andriashek, 2003; Nastev et al., 2005; Cummings et al., 2012). These windows can provide pathways for focused recharge to weathered bedrock and buried-valley aquifers (Korus et al., 2017). Recharge dynamics in buried-valley aquifers depend greatly on the bulk permeability of the confining layer and groundwater residence times in till material has been shown to range from thousands to tens of thousands of years (Keller et al., 1989). The flow regime through surficial tills depends on vertical groundwater flux, depth to the water table and depth of the weathered/unweathered boundary (Keller et al., 1988).

There are no modelling studies with a primary focus on groundwater recharge of buried-valley settings in northeastern BC. This region is distinct from those of most other studies in the WCSB; it is characterized by undulating terrain near the Rocky Mountain Foothills and a lack of features common to the Prairie Pothole Region, which are hypothesized to be the dominant recharge mechanism found in many WCSB buried-valley systems (Meyboom, 1966; Berthold et al., 2004; Cummings et al., 2012).

Paleovalley systems are common in glaciated terrain and numerous other local (1–5 km scale) buried-valley systems have been studied using numerical models (Shaver and Pusc, 1992; Seifert et al., 2008; Seyoum and Eckstein, 2014). Morgan et al. (2019) used MODFLOW 6 software developed by the U.S. Geological Survey to simulate regional (60 km) groundwater flow for a paleovalley system in northeastern BC located in the Halfway River area, focusing on the continuity of buried-valley aquifers and their

---
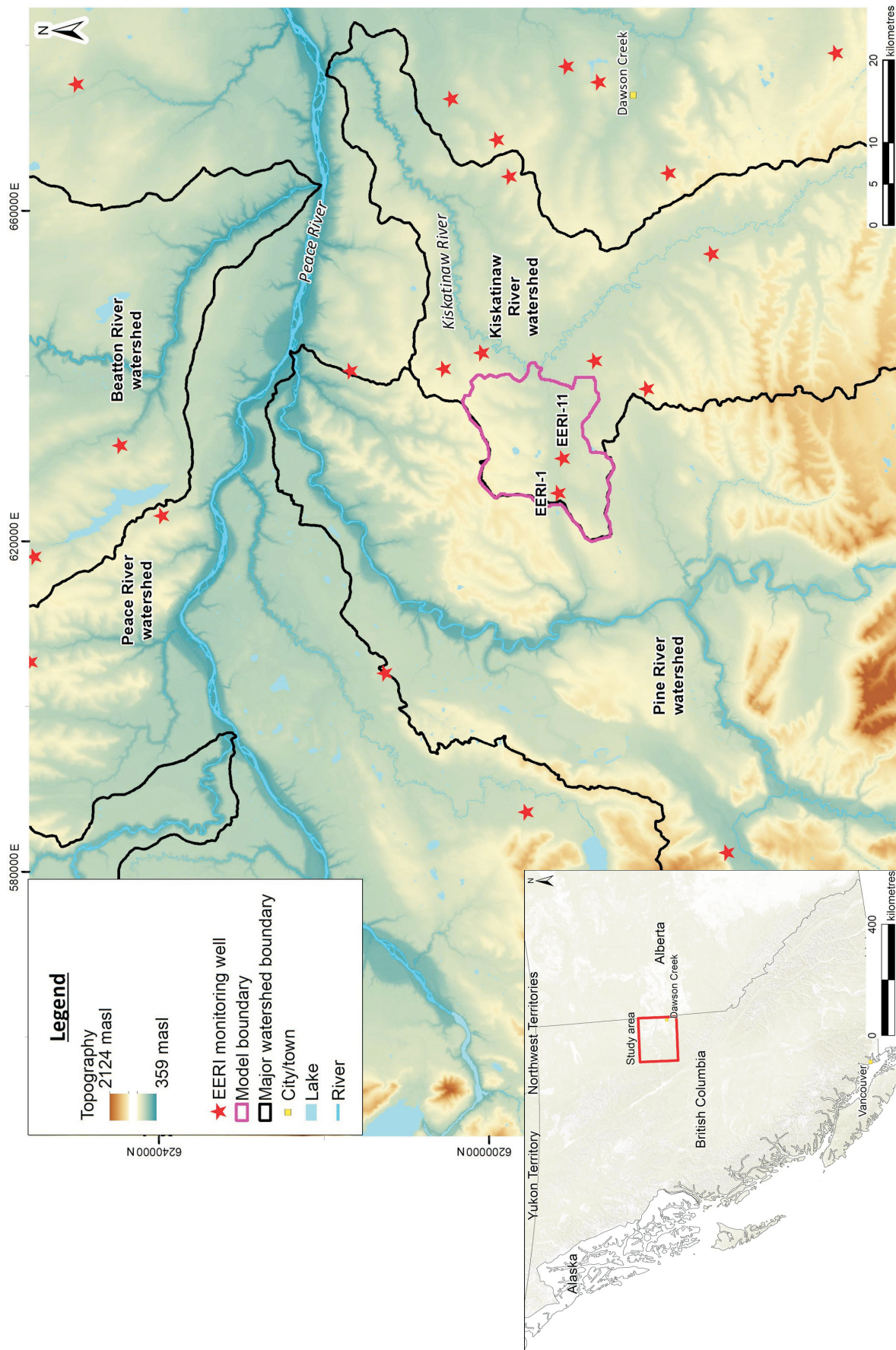
Figure 1. Digital elevation model of the study area in the southern Peace Region, showing major watershed boundaries. Inset shows the location of the study area in British Columbia. Abbreviations: EERI, Energy and Environment Research Initiative; m asl, metres above sea level.

importance on regional groundwater flow. Comparatively, this study by Morgan et al. (2019), focusing on a larger area, covered several distinct paleovalleys, had a large unconfined-aquifer component and described aquifers that were conceptualized to have considerable connection to surface water.

Since recharge is a major component of the groundwater budget, the interpreted model results will help inform sustainable extraction of this finite groundwater supply and have implications for advective transport of solutes and/or contaminants, such as dissolved fugitive gas being released from compromised energy wells (Bredehoeft, 2002; Cahill et al., 2019; Chao et al., 2020). As the Sunset paleovalley system is in an area of unconventional-gas development, it is important to understand typical regional-scale groundwater-flow patterns that will control the movement of potential dissolved-phase contaminants, including fugitive dissolved gases.

The first step consisted in developing the hydrogeological framework and conceptual model of the system, focusing on the shallow (<200 m), regional (~15 km) groundwater flow of the multilayered aquifer system. Next, a 3-D, steady-state, saturated-flow model of the system using MODFLOW 6 software was developed (Hughes et al., 2017). The system was then modelled using methods that yielded a steady-state model, since only two long-term monitoring points were available within the model domain, and since the longer term flow dynamics and water balance of the near-surface potable or near-potable water aquifers were the principal focus.

This modelling study complemented a larger regional characterization of shallow groundwater in the Peace Region described in Allen et al. (2021). In 2018–2019, 29 monitoring-well stations were installed in various aquifer types throughout the Peace Region as part of the Energy and Environment Research Initiative (EERI), a component of the Monitoring Well Installation Project of The University of British Columbia. These stations provided high-quality lithological and hydrogeological data on Quaternary and bedrock material. Monitoring wells EERI-1 and EERI-11 are located within this study's model domain and provided key data to construct the conceptual hydrogeological model (Figure 2).
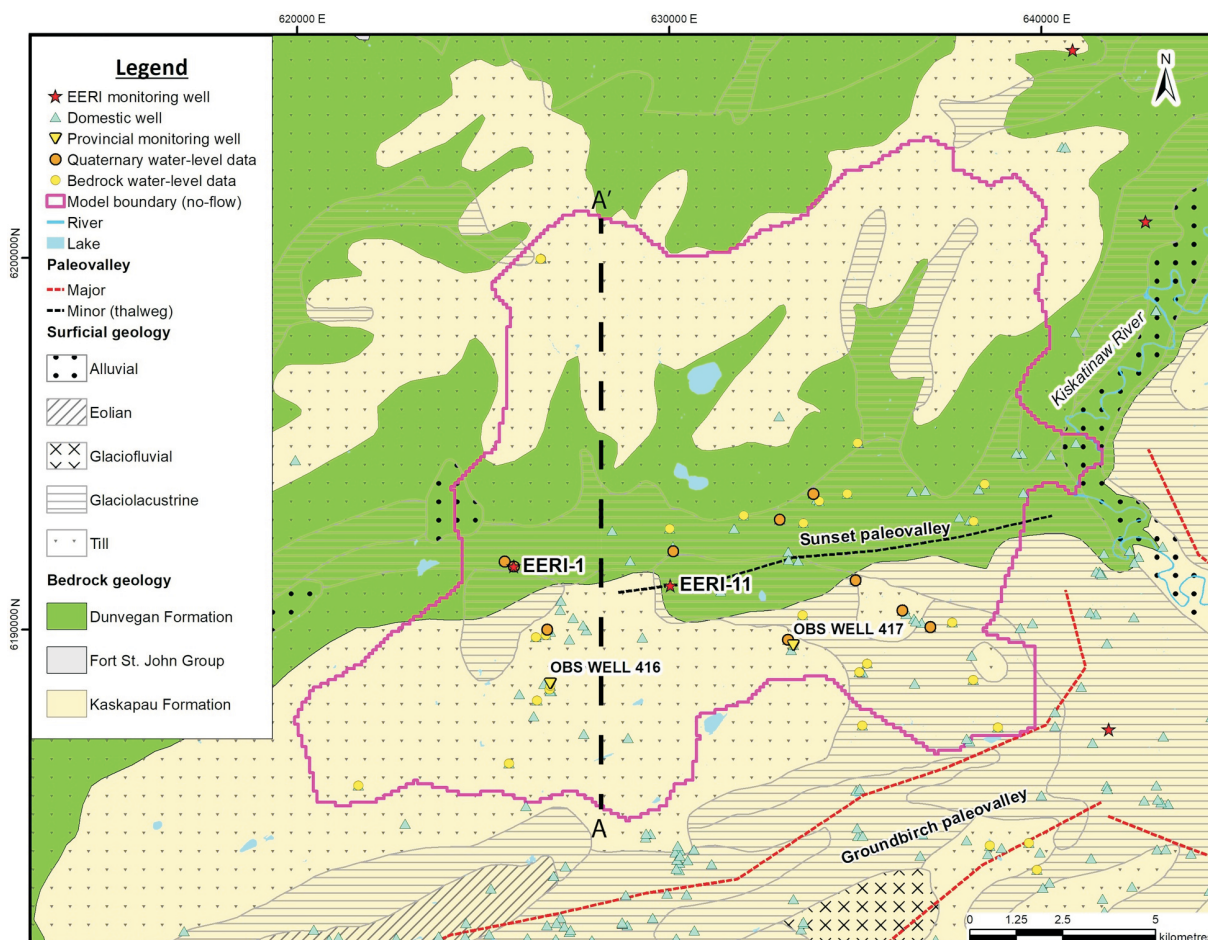
Figure 2. Surficial, bedrock and water well data of the study area in the southern Peace Region, west of Dawson Creek. The model area is outlined in pink and the vertical black dashed line represents a transect (A–A') indicating the location of the conceptual model cross-section shown in Figure 4. Abbreviation: EERI, Energy and Environment Research Initiative.

Study Area

Physiology

The Sunset paleovalley is a minor paleovalley (Figure 2) delineated by Hickin et al. (2008), with an elevation ranging from 660 to 900 m above sea level (asl). It is considered part of the Alberta Plateau of the Interior Plains physiographic region of BC (Holland, 1964).

The climate of the study area has mean annual temperatures below 0°C, with daily average temperatures ranging between -17°C and 22°C. Average annual precipitation ranges from 350 to 500 mm, approximately 200 mm of which falls as snow (Environment and Climate Change Canada, 2020). Peak freshet due to snowpack melting occurs in the spring, with most meltwater coming from mountainous regions to the west of the study area. A generally rural region, the dominant land usages within the study area include agriculture, timber harvesting and energy development (Baye et al., 2016).

The study area is located in the Sunset Creek sub-basin of the Kiskatinaw River watershed, with the river forming the eastern drainage for surface water (Figure 1). Originating in the foothills of the Rocky Mountains, the Kiskatinaw is a groundwater-fed, drought-stressed river with a mean baseflow index ranging between 58 and 75% (2007–2011; Saha et al., 2013). Groundwater contribution to the Kiskatinaw River is highest during drought and snowfall events, and lowest during wet seasons and freshet. Average annual runoff for the Kiskatinaw River Basin (1966–2008) comes from precipitation (14.2%), with the remainder consisting of evapotranspiration and groundwater recharge (Foundry Spatial Ltd., 2011). The flow rate of the Kiskatinaw River varies greatly, averaging 10 m^3/s and dropping to 0.052 m^3/s during the winter months (Saha et al., 2013). It is important to understand groundwater contribution to this river, as it is the most important source of water to the communities of Dawson Creek and Pouce Coupe as well as to thousands of rural residents of the Peace Region. Dawson Creek water demand increases by 3.2% per year on average (Saha et al., 2013).

Regional Geology

Located near the western limits of the WCSB, the shallow geology of the Sunset Creek valley generally consists of glaciogenic Quaternary sediments that overlie the topmost, southwest-dipping, Upper Cretaceous sedimentary bedrock strata (Figure 2; Hickin and Fournier, 2011a; Riddell, 2012). The shallow bedrock formations are interpreted as the result of successive marine transgressive-regressive cycles (Riddell, 2012). There are two bedrock formations of interest mapped within the study area: the Dunvegan and Kaskapau formations (BC Ministry of Energy Mines and Low Carbon Innovation, 2020). The Dunvegan Formation is an Upper Cretaceous nonmarine to marine deltaic sandstone/siltstone that is primarily mapped in low-elevation parts of the study area. This formation is the most important shallow reservoir for freshwater domestic groundwater in northeastern BC (Riddell, 2012). The overlying Kaskapau Formation shale/siltstone is more regionally extensive, but also hosts aquifer potential to some degree (Lowen Hydrogeology Consulting Ltd., 2011; Riddell, 2012). The uppermost bedrock strata are often observed as being weathered/fractured, which is likely the result of long-term mechanical weathering of bedrock surfaces caused by Pleistocene glacial erosion (Imrie, 1991; Gao, 2011). This secondary-fracture enhancement of the permeability has created observed hydraulic conductivities orders of magnitude greater than those observed in underlying competent bedrock counterparts (Riddell, 2012).

The extent, composition, lithology and genesis of major Quaternary paleovalley stratigraphy has been thoroughly studied in the Peace Region (Catto, 1991; Hartman and Clague, 2008; Hickin et al., 2008, 2016; Lowen Hydrogeology Consulting Ltd., 2011; Hickin and Best, 2013), where the paleovalleys were carved and filled by various glacially related processes, such as preglacial rivers, and further incised by proglacial or subglacial channels (Cummings et al., 2012). Valley shape, specifically depth-to-width ratio, can vary greatly, with larger paleovalleys being broad and shallow, and smaller paleovalleys being narrow and deep (Andriashek, 2003; Pugin et al., 2014). Created glacially or interglacially, these paleovalleys sometimes mimic the shape of modern major river valleys, such as the Peace, Pine and Kiskatinaw paleovalleys. Others, such as the Groundbirch and Sunset paleovalleys, are completely blanketed by till and glaciolacustrine deposits, leaving little surface expression.

EERI Wells

The Quaternary and shallow bedrock geology of the Sunset paleovalley was broadly conceptualized using lithological data from 85 registered domestic-well records entered in the WELLS database, two provincial monitoring wells and two EERI monitoring wells newly installed within the study area. Unfortunately, the lithological logs of most of the domestic wells are of extremely poor quality, providing little descriptive information and often lumping units together (Baye et al., 2016). Therefore, the only highly detailed logs in the paleovalley, obtained from EERI-1 and EERI-11, were key to the development of the hydrogeological conceptual model. The monitoring wells were installed using the sonic drilling method through Quaternary sediment and diamond coring through bedrock. The sonic drilling method uses high-frequency vibrations to drive the drill bit downward, retrieving high-quality unconsolidated sediment core in the process. Combining these two drilling methods made it possible to retrieve much more detailed

and higher quality logs than would have been possible relying solely on air rotary drilling. Both EERI wells are located in topographic lows, near the Sunset paleovalley thalweg (Figure 2). The sequence stratigraphy of EERI-1 and EERI-11 were determined with the aid of detailed descriptions from a study on the Quaternary stratigraphy of the adjacent Groundbirch paleovalley (Hickin et al., 2016). It was assumed that through lateral continuity, given that the Sunset and Groundbirch paleovalleys share a similar elevation, the stratigraphic interpretations of the study by Hickin et al. (2016) could be applied to the Sunset paleovalley depositional setting. The generalized sequence stratigraphy of the Late Wisconsinan Sunset paleovalley is interpreted as glaciolacustrine sediments deposited by glacial advance, which were overlain by ice-contact sediments, in turn overlain by retreat-phase glaciolacustrine sediments.

Monitoring well EERI-1 consists of ~66 m of mainly till and sand/gravel intervals and does not reach bedrock (Figure 3). The top ~13 m is a sequence of coarse sharp sand, overlain by diamict interbedded with a thin clay layer, overlain by continuous clay interpreted as sediments deposited by retreat-phase glacial Lake Peace, a proglacial lake which typically formed the surface units in areas of northeastern BC with elevations less than 1000 m asl (Hickin et al., 2016). The subglacial till below this unit (~13–42 m) is a poorly sorted, silt- to clay-rich, matrix-supported diamict with granule- to boulder-sized clasts of western provenance (chert and quartzite), indicative of Cordilleran ice-sheet transport. This subglacial till forms an abrupt contact with the underlying glaciofluvial sandy gravel, which consists of a poorly sorted and clast-supported gravel, with minor sand interbeds. Underlying the glaciofluvial gravel is a fining-upward sequence of laminated silty clay to diamict, interpreted as deposits associated with the advance-phase glacial Lake Mathews (Hartman and Clague, 2008).

Monitoring well EERI-11 extends through 40 m of clay, diamict and sand overlying 37 m of medium sandstone interlayered with siltstone. Like EERI-1, the uppermost 10 m consist of fining-upward glaciolacustrine clay indicative of retreat-phase glacial Lake Peace. Below this, lies subglacial till (10–27 m) consisting mainly of poorly sorted, silt- to clay-rich matrix-supported diamict with granule- to boulder-sized clasts. Below this, a massive fine-sand unit (27–37 m) is interpreted to be of glaciofluvial origin. The lowermost portion (37–40 m) consists of a thin layer of diamict interpreted as deposits associated with glacial Lake Mathews. These Quaternary sediments lie unconformably atop the Cretaceous bedrock, which is composed of medium-grained sandstone interlayered with siltstone that matches the Dunvegan Formation bedrock mapped at this location.

Groundwater Flow

Hydraulic-head data was available from 35 groundwater wells, made up of domestic, provincial observation and EERI wells. Although 85 domestic well records entered in the WELLS database are located within the model domain, head data from only 31 wells were used to calibrate the numerical-model study since these were the only wells providing both reliable lithological and static-water records (22 in bedrock and 9 in Quaternary units).

The newly installed EERI monitoring wells provided more recent (2019–2020) and reliable hydraulic-head measurements than domestic wells. Most EERI monitoring wells located across the Peace Region were equipped with data-logged pressure transducers to record head through time. Monitoring well EERI-1 is a nested multilevel well, with screens installed in the deeper glaciofluvial gravel and shallower sand units; both these screened units are artesian. Consequently, no data loggers were installed, and transient-head data is therefore unavailable. Monitoring well EERI-11 is a multilevel well developed by Westbay® Instruments and equipped with nine pressure-measurement ports, all located in the weathered bedrock Dunvegan Formation; all nine showed artesian pressure when measured during two sampling events in 2019 and 2020. At both sampling times, the vertical gradient between consecutive ports was less than ±0.02 m/m in seven of the nine ports. This small vertical gradient is within the ±0.01 m error tolerance of the Westbay pressure-profile tool (Meyer et al., 2008, 2014), and indicates horizontal flow along these intervals, relatively high vertical hydraulic conductivity (Kv) and good vertical connection in this section of weathered bedrock (Meyer et al., 2014). The hydraulic head at the bottom port was 12 cm greater than at the top port, with a vertical separation of 25 m, corresponding to a total vertical gradient of 0.0048 m/m downward (Figure 3). The lack of large resolvable head changes between ports indicates the absence of aquitard units within this section of sandstone interlayered with siltstone. It is important to note that the top 4 m of bedrock (directly underlying the Quaternary units) are not screened by Westbay ports. Without head measurements in the top 4 m, it is difficult to interpret the vertical-flow direction through the bedrock/overburden interface.

Conceptual Model

Hydrostratigraphy

A conceptual model, which identifies the most important hydrogeological processes, was developed considering the available information. A schematic hydrostratigraphic section for the Sunset paleovalley model is shown in Figure 4. The Sunset paleovalley has similar morphology and geology and, therefore, expected flow patterns similar to those identified in the study by Nastev et al. (2005). Precipitation
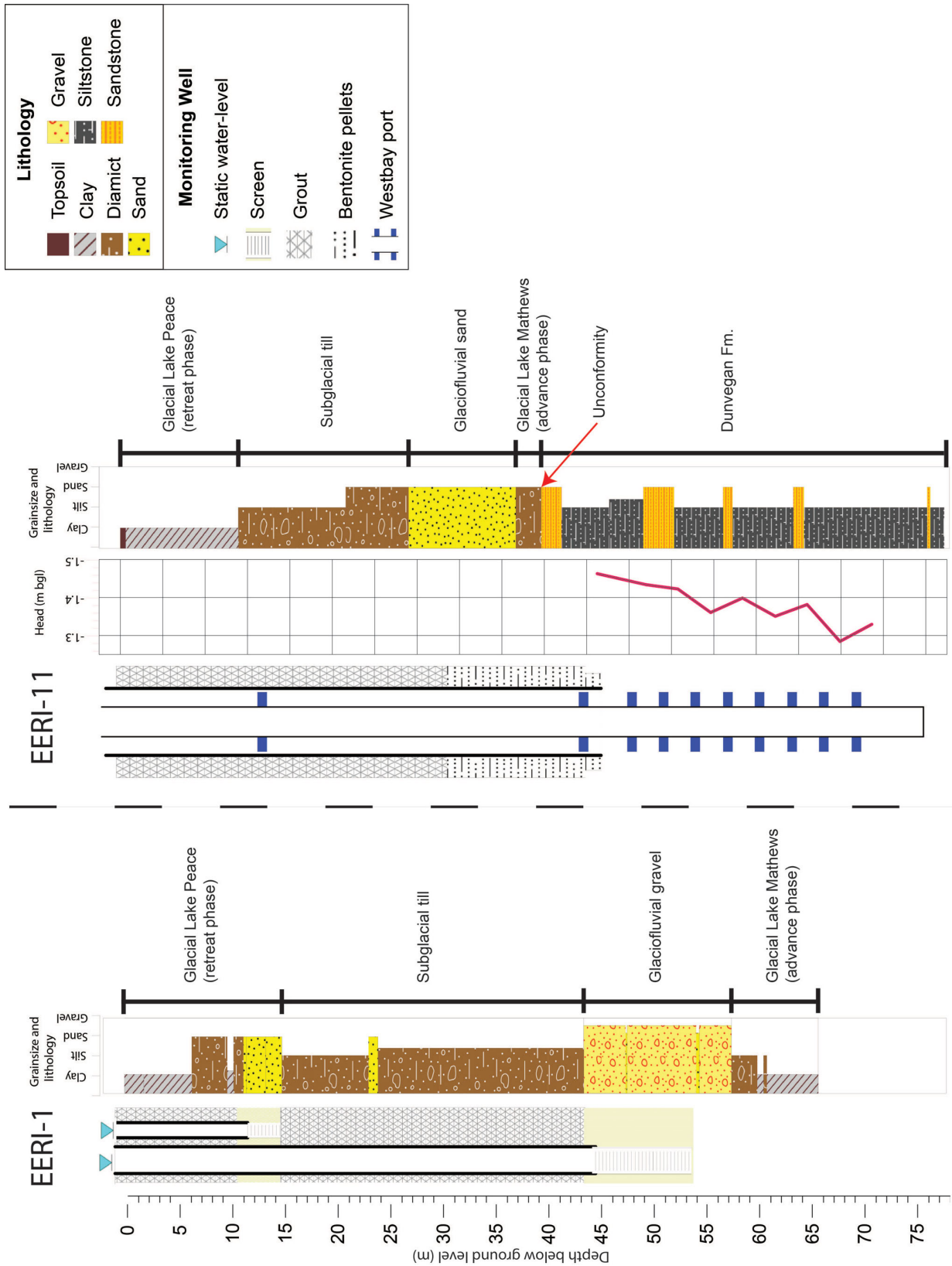
Figure 3. Well completion, hydraulic head, highly detailed lithological logs and depositional interpretation of monitoring wells EERI-1 and EERI-11 in the southern Peace Region, west of Dawson Creek. Abbreviations: EERI, Energy and Environment Research Initiative; Fm., Formation; m bgl, metres below ground level.

is expected to infiltrate to groundwater mostly in topographic highs, where impermeable till/clay is thin or absent. Infiltrated water then flows into the regional weathered-bedrock aquifer, with the flow direction mimicking bedrock topography toward the valley centre. From this point, the groundwater will either continue to flow in the weathered bedrock toward groundwater discharge points, flow upward into more permeable buried-valley sand/gravel aquifers due to strong hydraulic-conductivity contrasts, or travel downward to recharge deep groundwater. Groundwater flow in both gravel and bedrock aquifers is expected to ultimately flow roughly parallel to the long axis of the bedrock valley (Shaver and Pusc, 1992) toward outflow points, such as springs, or into regional drains, such as the Kiskatinaw River.

Eight hydrostratigraphic units (HSUs) have been identified for the conceptual model of the Sunset paleovalley: five Quaternary hydrofacies (weathered till/clay, alluvium, unweathered till, buried-valley sand/gravel and basal till) and three bedrock hydrofacies (weathered-bedrock Dunvegan Formation sandstone, weathered Kaskapau Formation shale and competent shale).

Aquifer Properties

The hydraulic conductivity of each of the eight HSUs is based on estimates from various sources: range of values from the literature, grain-size distribution results and pumping tests (Table 1). In all units, Kx is assumed equal to Ky. A vertical anisotropy factor of Kh/Kv = 10 is set for the alluvial, buried-valley sand/gravel and all bedrock HSUs to demonstrate the horizontal preferential permeability common to sedimentary rocks (Freeze and Cherry, 1979). The three till HSUs are assumed to be isotropic based on the assumption that both vertical and horizontal fractures are equally common, in combination with extremely low expected matrix permeability. However, it is expected that flow-through till material will always be vertical due to flow-line refraction.

Grain-size distribution was analyzed using a Mastersizer particle-size analyzer developed by Malvern Panalytical Ltd. on select Quaternary samples from EERI-1. The hydraulic conductivity of two samples within the EERI-1 buried-valley sand/gravel was estimated using the Kozeny-Carman and Terzaghi equations (Odong, 2007), with values ranging between 60 and 130 m/d.
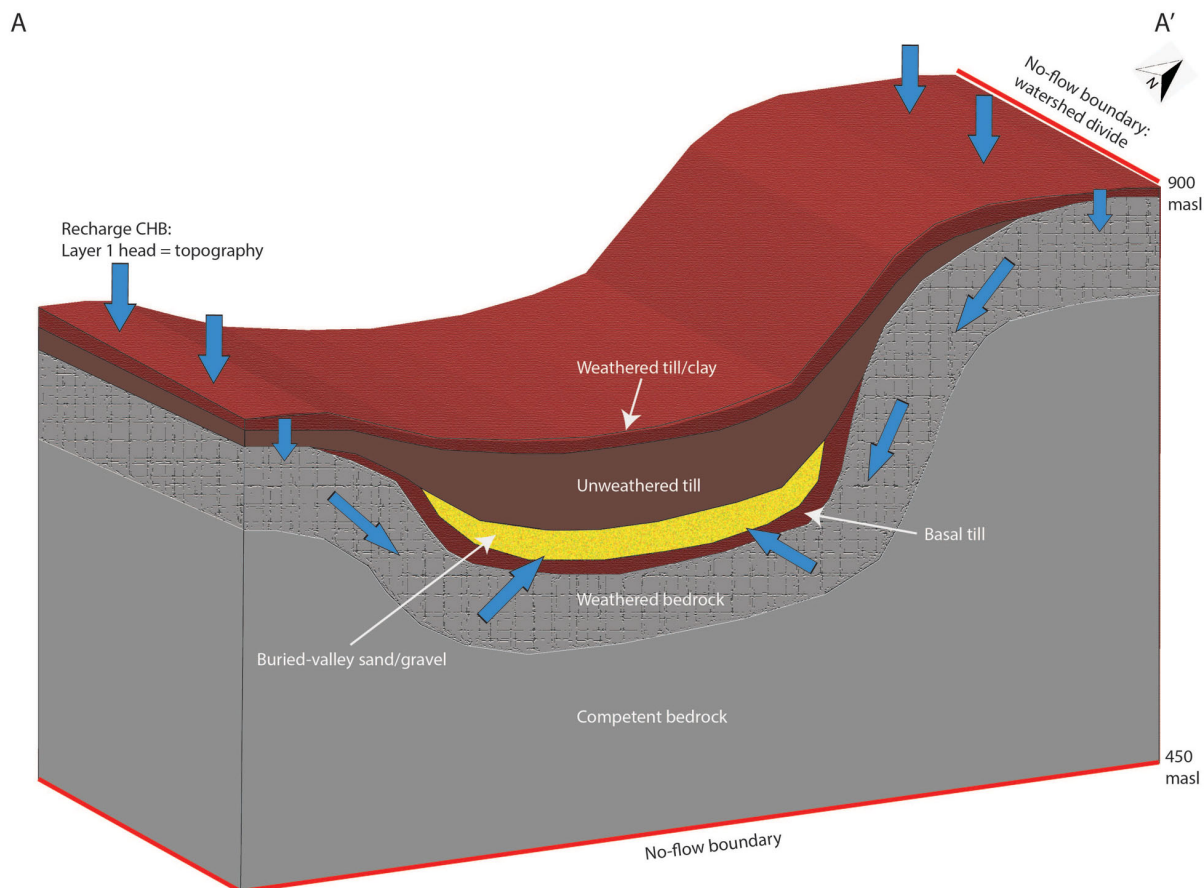
Figure 4. Conceptual block model of the hydrostratigraphy of the Sunset paleovalley study area, along transect A–A' shown in Figure 2. Hydrostratigraphic units are labelled, along with hypothesized recharge flow path (blue arrows) from surface to buried-valley sand/gravel aquifer and approximate locations of some of the boundary conditions. Abbreviations: CHB, constant-head boundary; m asl, metres above sea level.

Table 1. Hydrostratigraphic units, with corresponding layer number, calibrated hydraulic conductivities and range of values from the literature. Shaded hydrostratigraphic units represent aquifer material.

Hydrostratigraphic unit	Model layer no.	Model Kx/Ky (m/d)	Model Kz (m/d)	Literature range Min (m/d)	Max (m/d)
Weathered till/clay[1]	1	1.5×10^{-3}	1.5×10^{-3}	1.6×10^{-4}	1.7×10^{-2}
Alluvial[2]	1	430	43	260	8.6×10^{-4}
Unweathered till[1]	2	8.6×10^{-6}	8.6×10^{-6}	4.3×10^{-6}	8.6×10^{-5}
Buried-valley sand/gravel[1,3]	3	110	11	1	140
Basal till[1]	4	1.5×10^{-3}	1.5×10^{-3}	1.6×10^{-4}	1.7×10^{-2}
Dunvegan Fm. sandstone (weathered)[2,4]	5	8	0.8	8.6×10^{-5}	8.6
Kaskapau Fm. shale (weathered)[2,4]	5	0.1	1.0×10^{-2}	8.6×10^{-9}	8.6×10^{-5}
Shale (competent)[2]	6	1.0×10^{-7}	1.0×10^{-8}	8.6×10^{-9}	8.6×10^{-5}

[1]Estimated from literature values (Cummings et al., 2012)

[2]Estimated from literature values (Freeze and Cherry, 1979)

[3]Estimated from grain size analysis (A.M. Goetz, unpublished data, 2020)

[4]Estimated from pumping-test analysis (Baye et al., 2016)

In a prior study by Baye et al. (2016), 24-hour pumping tests were performed at the provincial monitoring wells within the model domain. Using the Theis, Cooper-Jacob and recovery analyses (Theis, 1935; Cooper and Jacob, 1946), provincial monitoring well OBS 416 presented a range of hydraulic conductivities between 9.0 and 30 m/d and well OBS 417 ranged between 0.70 and 0.81 m/d. These values are representative of both the weathered-bedrock Dunvegan Formation and weathered Kaskapau Formation.

Groundwater-Flow Modelling

Model Structure

The grid of this model is formed of gridblocks each measuring 100 by 100 m; it consists of 23 448 gridblocks per layer and the active model domain covers approximately 235 km[2] (Figure 5). The gridblock size was chosen to adequately represent variations in hydraulic properties, while maintaining a manageable run time (Reilly and Harbaugh, 2004). All gridblocks are set to 'convertible' as the default value, with the wetting option enabled for all layers. The model is made up of six layers, extending from ground surface to a planar, horizontal base at an elevation of 450 m asl. The top four layers represent Quaternary HSUs and the bottom two layers represent bedrock HSUs.

The upper surface of the grid was interpolated from digital elevation data (DEM; Government of British Columbia, 2020) and the top of the bedrock was interpolated using an existing bedrock topography DEM (Hickin and Fournier, 2011b). In a previous study of drift thickness in the Peace Region, Hickin and Fournier (2011b) digitized a bedrock DEM using primarily lithological descriptions from water well driller logs, oil and gas petrophysical logs, and surface exposures. Both bedrock and surface topography DEMs were reclassified (Resample raster function in ArcMap) to the same 100 m cell size. Since the DEMs came from different sources, bedrock elevations at some spots were greater than surface elevations. To eliminate this incongruence, Raster Calculator was used in ArcGIS to locate cells where bedrock DEM elevation was greater than ground surface DEM elevation. The bedrock elevation in these selected cells was set to 1 m deeper than the surficial DEM. The resulting DEMs were then imported into MODFLOW 6 as layer boundaries.

It was not possible to define precise lithological contacts based on the few lithology logs publicly available for the model domain area (Seyoum and Eckstein, 2014; Morgan et al., 2019). In an attempt to approximate as precisely as possible the thicknesses of the overburden layers (layers 1–4), each layer was assigned a constant fraction of the total drift thickness dependent on spatial location. These constant fractions for the four Quaternary layers were estimated based primarily on hydrogeological interpretations from monitoring wells EERI-1 and EERI-11. The surficial geology of layer 1 at the surface is based on mapped surficial geology data from Hickin and Fournier (2011a) and consists of either weathered till/clay or the alluvial HSU. The thickness of this layer accounts for 13% of the total drift-thickness value. Layer 2 is composed entirely of unweathered till, representing the main confining unit of the model. The thickness of this layer corresponds to 52% of the total drift thickness. Layer 3 is defined as buried-valley sand/gravel HSU, if within the thalweg shape, or unweathered till, if it lies outside the thalweg shape (yellow outline on Figure 5). The thickness of this layer is 25% of the total drift thickness. Layer 4 consists entirely of basal till HSU and accounts for 10% of the total drift thickness. Layer 5 is defined as either weathered bedrock Dunvegan Formation sandstone or Kaskapau Formation shale, depending on mapped bedrock (BC Ministry of Energy, Mines and Low Carbon Innovation, 2020). The thickness of this layer is uniformly set at 20 m. Layer 6 is entirely composed of competent-bedrock shale HSU (layer 6), ranging from the bottom of the weathered bedrock to 450 m asl.
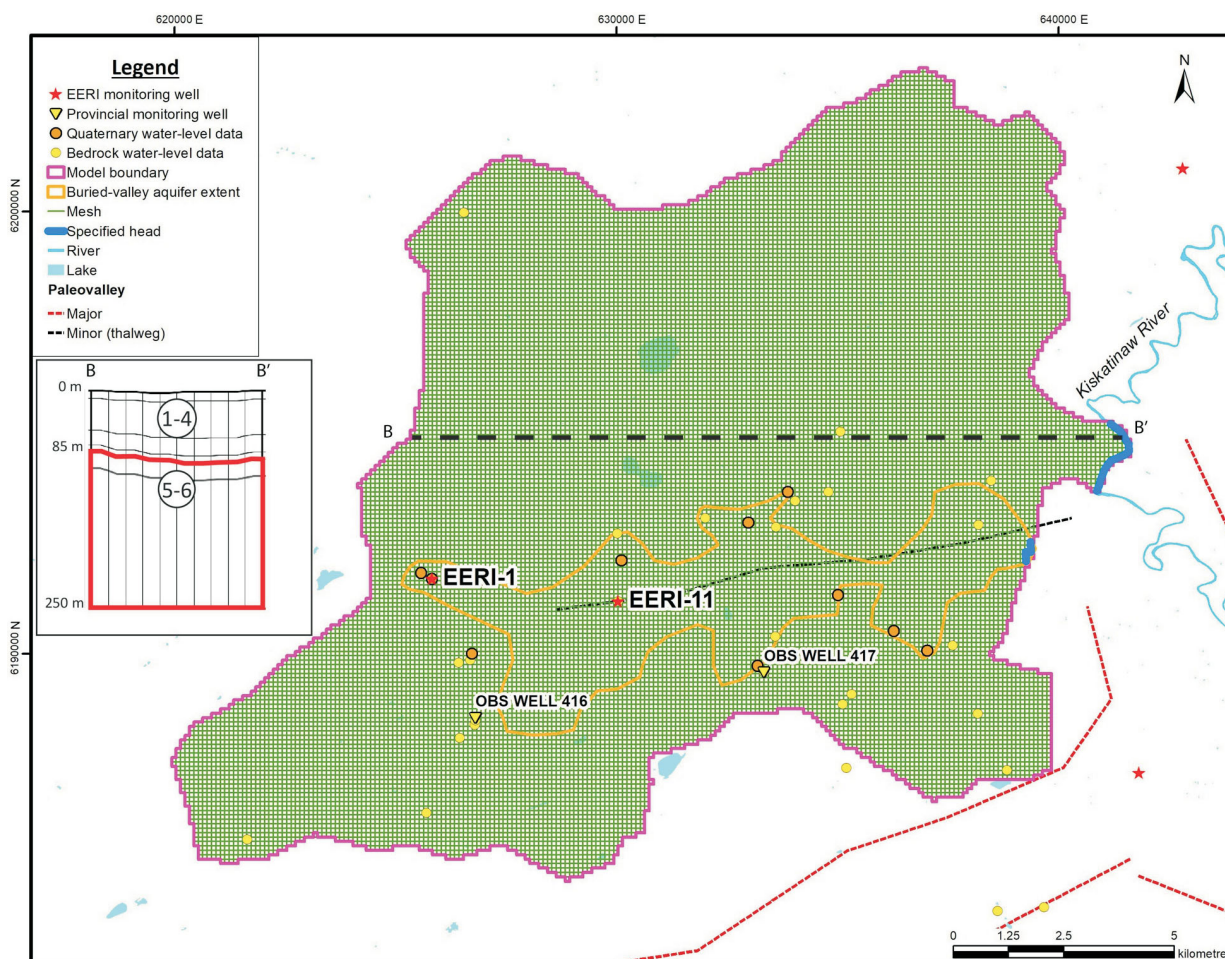
Figure 5. Model grid with boundary conditions built using MODFLOW 6 software (Hughes et al., 2017). Inset showing a simple cross-section (B–B') of layers 1–4 (Quaternary HSUs) and layers 5, 6 (bedrock HSUs). Abbreviations: EERI, Energy and Environment Research Initiative; HSU, hydrostratigraphic unit.

Boundary Conditions

In the case of the lateral limits of the model domain, no-flow boundaries were primarily defined by major regional watershed divides, with some boundaries being interpreted as flow divides between the Sunset Creek, Groundbirch and Kiskatinaw River valleys (Figure 2). A reasonable approximation is that these three valleys are likely separated by groundwater divides, with no interbasin groundwater flow. The northern and western no-flow boundaries follow the boundary between the Pine River and Kiskatinaw River watersheds (Figure 1). The Pine River likely acts as a groundwater divide, blocking the influence from the Rocky Mountain "water towers", which store and release large volumes of groundwater in 'pulses' during freshet (Viviroli and Weingartner, 2008; Marques et al., 2013). The southern no-flow boundary was determined using the particle-tracking program in MODFLOW 6. A larger model domain was established and the groundwater-divide boundaries between Sunset and Groundbirch paleovalleys identified by the particle tracks.

No-flow boundaries were applied to the bottom section of the model. This boundary is not associated with a specific lithological change, but rather was set at a depth great enough to avoid it influencing the simulation of flow in the shallow aquifers.

Hydrological data within the study area show hydraulic heads are close to the topographic surface, suggesting infiltration rates exceed recharge rates. The thickness and the low hydraulic conductivity of the confining-layer till (the conductance of the unit) is assumed to act as a major control on the recharge rate. Under the assumption that recharge was largely limited by surface hydraulic conductivity (lithology-controlled recharge), a constant-head boundary (CHB) condition was applied to the top of layer 1, except for areas mapped as alluvial HSU (Sanford, 2002). The head in layer 1 was set equal to the elevation of the model top. This boundary condition allowed the model to implicitly calculate recharge rates and actually identify preferential pathways through confining layers. This boundary condition is beneficial in cases such as this study, where spatial

measurements of rainfall, runoff and evapotranspiration data are unknown (Sanford, 2002).

A constant-rate–recharge boundary condition of 68 mm/a was applied to the alluvial HSU, which corresponded to the rate resulting from a recharge study based on material type by Baye et al. (2016). This boundary condition specific to the alluvial HSU was implemented due to the excessive amount of water entering this very permeable material (43 m/d) with the CHB applied, a value greater than precipitation, which was unrealistic.

To allow water to flow out of the model, specified head boundaries were applied to two of the aquifer layers (3 and 5) at the presumed paleovalley outflow point, where the Sunset paleovalley meets the Kiskatinaw River valley.

The specified head value for the buried-valley sand/gravel aquifer (layer 3) was estimated based on the head gradient of gravel-thalweg domestic wells west of the outflow boundary. This specified head value was estimated to be 693 m asl at the outflow boundary.

The specified head in the weathered-bedrock aquifer (layer 5) was set at the estimated Kiskatinaw River elevation (665 m) near the model outflow point, since this represented bedrock outcropping at this boundary and groundwater flowing into the Kiskatinaw River according to drift-thickness data. The outflow boundary for layer 5 was defined as the intersection of the Sunset paleovalley bedrock catchment with the Kiskatinaw River. No stream-gauge data were available on the Kiskatinaw River near the Sunset paleovalley outflow point to constrain the head or flux value.

Results

Simulated recharge at each surface gridblock within the model domain is shown in Figure 6. Gridblocks in orange/red represent recharge areas, whereas those in different shades of green represent modelled discharge areas (negative values). The observed spatial pattern of recharge/discharge gridblocks agrees with the hypothesis of highland recharge and valley discharge, except for several localized
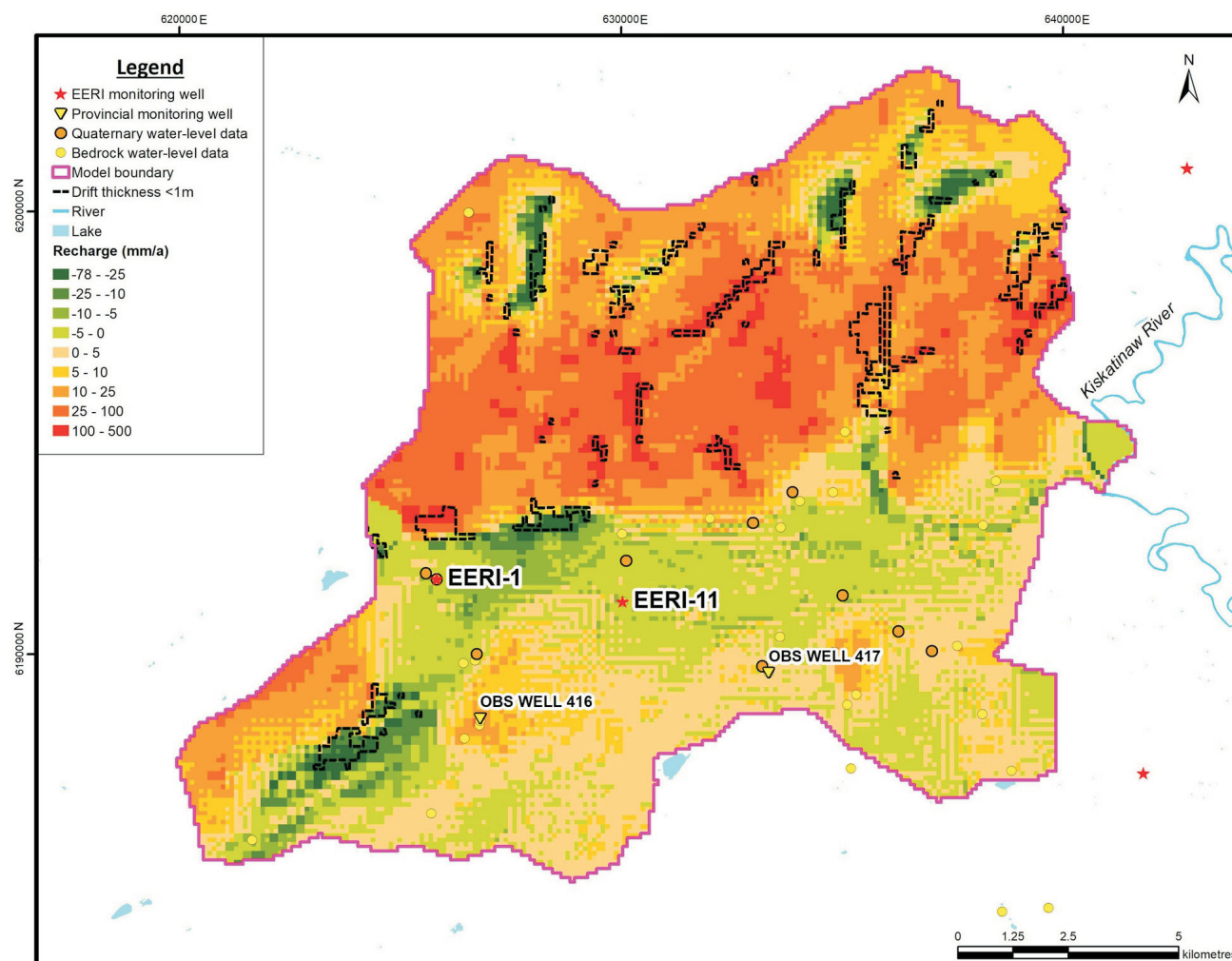
Figure 6. Spatial distribution of recharge/discharge rates in hydrostratigraphic unit layer 1 in the Peace Region, west of Dawson Creek. Dotted black lines indicate zones of thinnest drift (<1 m). Abbreviation: EERI, Energy and Environment Research Initiative.

discharge areas associated with topographic lows in the northern part of the model. The spatial average recharge rate of the model is 16 mm/a, with a standard deviation of 32 mm/a and values ranging from -78 to 500 mm/a. As this is a steady-state simulation, these values represent temporal averages and instantaneous values will vary about them. The maximum value of steady-state–gridblock discharge (78 mm/a) is lower than the 400 mm/a evapotranspiration rate estimated for the Kiskatinaw River watershed (Foundry Spatial Ltd., 2011). The difference between discharge and evapotranspiration suggests that discharge areas would not result in groundwater-fed creeks within the model domain. This is consistent with the ephemeral nature of the mapped streams in the model area. Extreme outlier gridblocks with high recharge values (>100 mm/a) are unrealistic given the low hydraulic-conductivity values of layer 1 and are likely numerical artifacts caused by misalignment of adjacent gridblocks with large differences in elevation, as explained in Hughes et al. (2017, p. 54). These outlier values could likely be dealt with by refining the grid mesh of these areas. Outlier recharge values occur mostly within regions with <10 m of Quaternary cover (total thickness of layers 1–4).

Recharge values based on surficial confining material in the region were studied by Baye et al. (2016) using the hydrologic evaluation of landfill performance (HELP) model developed for the Environmental Protection Agency by the U.S. Army Corps of Engineers Waterways Experiment Station. They calculated average annual recharge rates for vadose zones of till (33 mm/a), glaciolacustrine (2 mm/a) and alluvial (46–68 mm/a) materials. Since layer 1 in the Sunset paleovalley model domain consists primarily of till and glaciolacustrine material, the results of this study are consistent with the range of values presented in the Baye et al. (2016) study.

Discussion

Steady-state groundwater flow in the Sunset Creek valley groundwater system was analyzed. The simulation results were consistent with the general conceptual model, showing relatively low recharge rates, constrained by the low hydraulic conductivity of the surface diamict. Given the limited information, a pragmatic choice was made to assign uniform, effective properties to the units in the simulation domain, whereas the real system is heterogeneous at both the unit and subunit scale. Effective medium properties will likely yield reasonable predictions for total fluxes but will not properly account for rapid travel that can occur through fractures or other preferential pathways.

Finer mesh size, leading to longer run times, could have helped improve spatial recharge-rate resolution and potentially deal with the large outlier values seen in the model. The model domain could be expanded to incorporate adjacent Kiskatinaw and Groundbirch paleovalleys to gain a better understanding of the flow budget between these regional features.

Although difficult to accurately conceptualize, intertill aquifers could be included to simulate potential permeable pathways through confining unweathered till. These interconnected permeable lenses within the confining layer have been hypothesized as potential pathways for buried-valley recharge (Cummings et al., 2012).

Conclusion

A regional groundwater-flow model of a paleovalley-based confined-aquifer system in northeastern BC was constructed with the purpose of simulating the spatial distribution of recharge and discharge. This modelling study synthesized available hydrogeological data for buried-valley aquifer systems in northeastern BC and the WCSB, with data from newly installed monitoring wells, to construct a simplified conceptualization of the Sunset paleovalley. Using MODFLOW 6 software, groundwater-flow models were constructed and calibrated, adjusting parameters within the range of values identified in the literature. Within the study area, the model quantitatively estimated the spatial distribution and magnitude of groundwater recharge and discharge, the water balance between HSUs and residence times of aquifers. The average recharge in the study area was estimated at 16 mm/a, which falls within the range of results from another study in the same region (Baye et al., 2016).

In future work, the model's water budget will be analyzed to investigate flow volumes between HSUs and to compare model outflow to estimates of Kiskatinaw River baseflow, as determined from hydrometric data. Using the particle-tracking program of MODFLOW 6, average residence times for the aquifers will be calculated and evaluated based on residence times from similar paleovalley studies.

The model results add to the understanding of buried-valley aquifer systems and their recharge. These hydrogeological settings are common to the Interior Plains region of North America and are important sources of water used for domestic, agricultural and industrial purposes. As a next step, modelled flow-budget results can be used as a basis for groundwater-management strategies within the region.

Acknowledgments

References

Allen, A., Goetz, A.M., Gonzalez, P.S., Ladd, B., Cahill, A.G., Welch, L., Mayer, B., van Geloven, C., Kirste, D. and Beckie, R.D. (2021): Installation of a purpose-built groundwater monitoring well network to characterize groundwater methane in the Peace Region, northeastern British Columbia (NTS 093P/09–16, 094A/01–08: activity report 2019–2020; *in* Geoscience BC Summary of Activities 2020: Energy and Water, Geoscience BC, Report 2021-02, p. 123–134, URL <http://geosciencebc.com/updates/summary-of-activities/> [January 2021].

Andriashek, L.D. (2003): Quaternary geological setting of the Athabasca Oil Sands (in situ) area, northeast Alberta; Alberta Energy and Utilities Board, EUB/AGS Earth Sciences Report 2002-03, 286 p., URL <https://static.ags.aer.ca/files/document/ESR/ESR_2002_03.pdf> [July 2020].

Baye, A., Rathfelder, K., Wei, M. and Yin, J. (2016): Hydrostratigraphic, hydraulic and hydrogeochemical descriptions of Dawson Creek-Groundbirch areas, northeast BC; Province of British Columbia, Water Science Series 2016-04, 52 p.

BC Ministry of Energy, Mines and Low Carbon Innovation (2020): Bedrock geology; BC Ministry of Energy, Mines and Low Carbon Innovation, BC Geological Survey, Data Catalogue, URL <https://catalogue.data.gov.bc.ca/dataset/bedrock-geology> [July 2020].

Berthold, S., Bentley, L.R. and Hayashi, M. (2004): Integrated hydrogeological and geophysical study of depression-focused groundwater recharge in the Canadian Prairies; Water Resources Research, v. 40, issue 6, 14 p., URL <https://doi.org/10.1029/2003WR002982>.

Bredehoeft, J.D. (2002): The water budget myth revisited: why hydrogeologists model; Groundwater, v. 40, no. 4, p. 340–345, URL <https://doi.org/10.1111/j.1745-6584.2002.tb-02511.x>.

Cahill, A.G., Beckie, R., Ladd, B., Sandl, E., Goetz, M., Chao, J., Soares, J., Manning, C., Chopra, C., Finke, N., Hawthorne, I., Black, A., Mayer, K.U., Crowe, S., Cary, T., Lauer, R., Mayer, B., Allen, A., Kirste, D. and Welch, L. (2019): Advancing knowledge of gas migration and fugitive gas from energy wells in northeast British Columbia, Canada; Greenhouse Gases: Science and Technology, v. 9, no. 2, p. 134–151, URL <https://doi.org/10.1002/ghg.1856>.

Catto, N.R. (1991): Quaternary geology and landforms of the eastern Peace River region, British Columbia, NTS 94A/1, 2, 7, 8; BC Ministry of Energy, Mines and Low Carbon Innovation, BC Geological Survey, Open File 1991-11, 19 p.

Chao, T.-H., Cahill, A.G. and Lauer, R. (2020): Propensity for fugitive gas migration in glaciofluvial deposits: an assessment of near-surface hydrofacies in the Peace Region, northeastern British Columbia; Science of The Total Environment, v. 749, art. 141459, URL <https://doi.org/10.1016/j.scitotenv.2020.141459>.

Cooper, H.H. and Jacob, C.E. (1946): A generalized graphical method for evaluating formation constants and summarizing well-field history; Eos, Transactions of the American Geophysical Union, v. 27, no. 4, p. 526–534, URL <https://doi.org/10.1029/TR027i004p00526>.

Cummings, D.I., Russell, H.A.J. and Sharpe, D.R. (2012): Buried-valley aquifers in the Canadian Prairies: geology, hydrogeology, and origin; Canadian Journal of Earth Sciences, v. 49, no. 9, p. 987–1004, URL <https://doi.org/10.1139/e2012-041>.

Environment and Climate Change Canada. (2020): Canadian climate normals 1981–2010 station data: Dawson Creek; Government of Canada, URL <https://climate.weather.gc.ca/climate_normals/results_1981_2010_e.html> [July 2020].

Foundry Spatial Ltd. (2011): Montney Water Project: watershed posters; Geoscience BC, Geoscience BC Report 2011-12, 8 posters, URL <http://www.geosciencebc.com/s/Report-2011-12.asp> [July 2020].

Freeze, R.A. and Cherry, J.A. (1979): Groundwater; Prentice-Hall, Englewood Cliffs, New Jersey, 624 p.

Gao, C. (2011): Buried bedrock valleys and glacial and subglacial meltwater erosion in southern Ontario, Canada; Canadian Journal of Earth Sciences, v. 48, no. 5, p. 801–818, URL <https://doi.org/10.1139/e10-104>.

Gardiner, L., Rhodes, R. and Geller, D. (2020): District of Hudson's Hope production well completion report; unpublished report prepared by Western Water Associates Ltd. (British Columbia)

Government of British Columbia (2020): Digital Elevation Model; Government of British Columbia, URL <https://www2.gov.bc.ca/gov/content/data/geographic-data-services/topographic-data/elevation/digital-elevation-model> [September 2020].

Hartman, G.M.D. and Clague, J.J. (2008): Quaternary stratigraphy and glacial history of the Peace River valley, northeast British Columbia; *in* Geology of northeastern British Columbia and northwestern Alberta: diamonds, shallow gas, gravel, and glaciers; Canadian Journal of Earth Sciences, v. 45, no. 5, p. 549–564, URL <https://doi.org/10.1139/E07-069>.

Hickin, A.S. and Best, M.E. (2013): Mapping the geometry and lithostratigraphy of a paleovalley with a time-domain electromagnetic technique in an area with small resistivity contrasts, Groundbirch, British Columbia, Canada; Journal of Environmental and Engineering Geophysics, v. 18, no. 2, p. 119–135, URL <https://doi.org/10.2113/JEEG18.2.119>.

Hickin, A.S. and Fournier, M.A. (2011a): Compilation of Geological Survey of Canada surficial geology maps for NTS 94A and 93P; BC Ministry of Energy, Mines and Low Carbon Innovation, Energy Open File 2011-2, Geoscience BC Map 2011-08-1, scale 1:250 000, URL <https://cdn.geosciencebc.com/project_data/GBC_Report2011-8/GBC_Map2011-08-1_BCMEMOF2011-2.pdf> [October 2020].

Hickin, A.S. and Fournier, M.A. (2011b): Preliminary bedrock topography and drift thickness of the Montney Play area; BC Ministry of Energy, Mines and Low Carbon Innovation, Energy Open File 2011-1, Geoscience BC Report 2011-07, 2 maps, scale 1:500 000, URL <https://geosciencebc.com/project_data/GBC_Report2011-7/GBC_Map2011-07_BCMEM%20OF2011-1.pdf> [October 2020].

Hickin, A.S., Best, M.E. and Pugin, A. (2016): Geometry and valley-fill stratigraphic framework for aquifers in the Groundbirch paleovalley assessed through shallow seismic and ground-based electromagnetic surveys; BC Ministry of Energy, Mines and Low Carbon Innovation, BC Geological Survey, Open File Report 2016-05, 46 p.

Hickin, A.S., Kerr, B., Turner, D.G. and Barchyn, T.E. (2008): Mapping Quaternary paleovalleys and drift thickness using petrophysical logs, northeast British Columbia, Fontas map sheet, NTS 94I; *in* Geology of northeastern British Columbia and northwestern Alberta: diamonds, shallow gas,

gravel, and glaciers, Canadian Journal of Earth Sciences, v. 45, no. 5, p. 577–591, URL <https://doi.org/10.1139/e07-063>.

Holland, R. (1964): Landforms of British Columbia: a physiographic outline; BC Ministry of Energy, Mines and Low Carbon Innovation, Bulletin No. 48, 138 p., URL <https://ci.nii.ac.jp/naid/10018003680/> [July 2020].

Hughes, J.D., Langevin, C.D. and Banta, E.R. (2017): Documentation for the MODFLOW 6 framework; U.S. Geological Survey, Techniques and Methods, book 6, chap. A57, 42 p., URL <https://doi.org/10.3133/tm6A57>.

Imrie, A.S. (1991): Stress-induced response from both natural and construction-related processes in the deepening of the Peace River valley, B.C.; Canadian Geotechnical Journal, v. 28, no. 5, p. 719–728, URL <https://doi.org/10.1139/t91-086>.

Keller, C.K., Van Der Kamp, G. and Cherry, J.A. (1988): Hydrogeology of two Saskatchewan tills, I. Fractures, bulk permeability, and spatial variability of downward flow; Journal of Hydrology, v. 101, issue 1, p. 97–121, URL <https://doi.org/10.1016/0022-1694(88)90030-3>.

Keller, C.K., Van Der Kamp, G. and Cherry, J.A. (1989): A multiscale study of the permeability of a thick clayey till; Water Resources Research, v. 25, issue 11, p. 2299–2317, URL <https://doi.org/10.1029/WR025i011p02299>.

Korus, J.T., Joeckel, R.M., Divine, D.P. and Abraham, J.D. (2017): Three-dimensional architecture and hydrostratigraphy of cross-cutting buried valleys using airborne electromagnetics, glaciated Central Lowlands, Nebraska, USA; Sedimentology, v. 64, no. 2, p. 553–581, URL <https://doi.org/10.1111/sed.12314>.

Lowen Hydrogeology Consulting Ltd. (2011): Aquifer classification mapping in the Peace River region for the Montney Water Project; report prepared for Geoscience BC by Lowen Hydrogeology Consulting Ltd., 51 p., URL <http://a100.gov.bc.ca/appsdata/acat/documents/r23247/aq_class_peace_riv_re_june_2011_1308845969283_d0546dd6b5818f205e6a3613d94555e8b28a4ee32529a427b4d1ac6b05311258.pdf> [September 2020].

Marques, J.E., Marques, J.M., Chaminé, H.I., Carreira, P.M., Fonseca, P.E., Monteiro Santos, F.A., Moura, R., Samper, J., Pisani, B., Teixeira, J., Carvalho, J.M., Rocha, F. and Borges, F.S. (2013): Conceptualizing a mountain hydrogeologic system by using an integrated groundwater assessment (Serra da Estrela, Central Portugal): a review; Geosciences Journal, v. 17, no. 3, p. 371–386, URL <https://doi.org/10.1007/s12303-013-0019-x>.

Meyboom, P. (1966): Unsteady groundwater flow near a willow ring in hummocky moraine; Journal of Hydrology, v. 4, p. 38–62, URL <https://doi.org/10.1016/0022-1694(66)90066-7>.

Meyer, J.R., Parker, B.L. and Cherry, J.A. (2008): Detailed hydraulic head profiles as essential data for defining hydrogeologic units in layered fractured sedimentary rock; Environmental Geology, v. 56, no. 1, p. 27–44, URL <https://doi.org/10.1007/s00254-007-1137-4>.

Meyer, J.R., Parker, B.L. and Cherry, J.A. (2014): Characteristics of high resolution hydraulic head profiles and vertical gradients in fractured sedimentary rocks; Journal of Hydrology, v. 517, p. 493–507, URL <https://doi.org/10.1016/j.jhydrol.2014.05.050>.

Morgan, S.E., Allen, D.M., Kirste, D. and Salas, C.J. (2019): Investigating the hydraulic role of a large buried valley network on regional groundwater flow; Hydrogeology Journal, v. 27, no. 7, p. 2377–2397, URL <https://doi.org/10.1007/s10040-019-01995-0>.

Nastev, M., Rivera, A., Lefebvre, R., Martel, R. and Savard, M. (2005): Numerical simulation of groundwater flow in regional rock aquifers, southwestern Quebec, Canada; Hydrogeology Journal, v. 13, no. 5, p. 835–848, URL <https://doi.org/10.1007/s10040-005-0445-6>.

Odong, J. (2007): Evaluation of empirical formulae for determination of hydraulic conductivity based on grain-size analysis; Journal of American Science, v. 3, no. 3, p. 54–60.

Pugin, A.J.-M., Oldenborger, G.A., Cummings, D.I., Russell, H.A.J. and Sharpe, D.R. (2014): Architecture of buried valleys in glaciated Canadian Prairie regions based on high resolution geophysical data; Quaternary Science Reviews, v. 86, p. 13–23, URL <https://doi.org/10.1016/j.quascirev.2013.12.007>.

Reilly, T.E. and Harbaugh, A.W. (2004): Guidelines for evaluating ground-water flow models; U.S. Geological Survey, Scientific Investigations Report 2004-5038, 30 p., URL <https://pubs.usgs.gov/sir/2004/5038/PDF/SIR2004-5038_ver1.01.pdf> [September 2020].

Riddell, J. (2012): Potential for freshwater bedrock aquifers in northeast British Columbia: regional distribution and lithology of surface and shallow subsurface bedrock units (NTS 093I, O, P; 094A, B, G, H, I, J, N, O, P); BC Ministry of Energy, Mines and Low Carbon Innovation, Geoscience Reports 2012-04, p. 65–78.

Saha, G.C., Paul, S.S., Li, J., Hirshfield, F. and Sui, J. (2013): Investigation of land-use change and groundwater–surface water interaction in the Kiskatinaw River watershed, northeastern British Columbia (parts of NTS 093P/01, /02, /07–/10); in Geoscience BC Summary of Activities 2012, Geoscience BC, Report 2013-1, p. 139–148, URL <https://cdn.geosciencebc.com/pdf/SummaryofActivities2012/SoA2012_Saha.pdf> [November 2020].

Sanford, W. (2002): Recharge and groundwater models: an overview; Hydrogeology Journal, v. 10, no. 1, p. 110–120, URL <https://doi.org/10.1007/s10040-001-0173-5>.

Seifert, D., Sonnenborg, T.O., Scharling, P. and Hinsby, K. (2008): Use of alternative conceptual models to assess the impact of a buried valley on groundwater vulnerability; Hydrogeology Journal, v. 16, no. 4, p. 659–674, URL <https://doi.org/10.1007/s10040-007-0252-3>.

Seyoum, W.M. and Eckstein, Y. (2014): Hydraulic relationships between buried valley sediments of the glacial drift and adjacent bedrock formations in northeastern Ohio, USA; Hydrogeology Journal, v. 22, no. 5, p. 1193–1206, URL <https://doi.org/10.1007/s10040-014-1128-y>.

Shaver, R.B. and Pusc, S.W. (1992): Hydraulic barriers in Pleistocene buried-valley aquifers; Groundwater, v. 30, no. 1, p. 21–28, URL <https://doi.org/10.1111/j.1745-6584.1992.tb00807.x>.

Statistics Canada (2017): Census Profile, 2016 Census—Northeast [Economic region], British Columbia and British Columbia [Province]; Statistics Canada, URL <https://www12.statcan.gc.ca/census-recensement/2016/dp-pd/index-eng.cfm> [September 2020].

Theis, C.V. (1935): The relation between the lowering of the Piezometric surface and the rate and duration of discharge of a well using ground-water storage; Eos, Transactions of the American Geophysical Union, v. 16, no. 2, p. 519–524, URL <https://doi.org/10.1029/TR016i002p00519>.

Viviroli, D. and Weingartner, R. (2008): "Water Towers"—a global view of the hydrological importance of mountains; *in* Mountains: Sources of Water, Sources of Knowledge, E. Wiegandt (ed.), Springer, Dordrecht, Netherlands, Advances in Global Change Research, v. 31, p. 15–20, URL <https://doi.org/10.1007/978-1-4020-6748-8_2>.

Winter, T.C. (2001): The concept of hydrologic landscapes; Journal of the American Water Resources Association, v. 37, no. 2, p. 335–349, URL <https://doi.org/10.1111/j.1752-1688.2001.tb00973.x>.

Geoscience BC

t: 604 662 4147
e: info@geosciencebc.com

SUITE 1101–750 WEST PENDER ST
VANCOUVER, BC V6C 2T7 CANADA

www.geosciencebc.com